The background of the slide is a dark field filled with a dense distribution of small, bright, golden-yellow particles. These particles are scattered across the entire frame, with a higher concentration in the lower-left and lower-right areas, creating a sense of depth and texture. The overall appearance is that of a microscopic view of a material composed of many small, spherical or sub-spherical particles.

Gold/Silica Particles for Various Applications in (CLEM) Microscopy

Jantina Fokkema

Gold/Silica Particles for Various Applications in (CLEM) Microscopy

PhD thesis, Utrecht University, the Netherlands, 2020

ISBN: 978-94-6416-159-5

Cover design: Mirelle van Tulder, persoonlijkproefschrift.nl

Print: Ridderprint | www.ridderprint.nl

Gold/Silica Particles for Various Applications in (CLEM) Microscopy

Goud/Silica Deeltjes voor Verschillende
Toepassingen in (CLEM) Microscopie

(met een samenvatting in het Nederlands)

Proefschrift

ter verkrijging van de graad van doctor aan de Universiteit Utrecht
op gezag van de rector magnificus, prof. dr. H.R.B.M. Kummeling,
ingevolge het besluit van het college voor promoties in het openbaar
te verdedigen op woensdag 21 oktober 2020 des middags te 12.45 uur

door

Jantje Fokkema

geboren op 29 januari 1991 te Leeuwarden

Promotor: Prof. dr. H.C. Gerritsen

Copromotor: Dr. G.A. Blab

This work is part of Microscopy Valley with project number 12715 which is partly financed by the Netherlands Organisation for Scientific Research (NWO).

Contents

| | | |
|----------|---|------------|
| 1 | Introduction | 1 |
| 2 | A Study of Fluorophore Labelling Density Effects | 17 |
| 3 | Fluorescently Labelled Silica Coated Gold Nanoparticles as Fiducials | 45 |
| 4 | 3D (i)CLEM: Endocytosed Fiducials as Dual-Modality Probes | 77 |
| 5 | A Single Sample to Check the Performance of a Light Microscope | 105 |
| | Bibliography | 131 |
| | Summary | 147 |
| | Samenvatting voor een breder publiek | 151 |
| | Dankwoord | 155 |
| | List of Publications | 159 |
| | About the Author | 161 |

Introduction

In this chapter, a general introduction to the work presented in this thesis is given. As most of the work in this thesis focuses on light, electron, or a combination of light and electron microscopy, these techniques are introduced first. To fully understand why the combination of light and electron microscopy proves so valuable, the advantages and disadvantages of the two complementary techniques are discussed as well. From there, it is explained how correlative measurements can be used to combine the benefits of both types of microscopy. A major challenge in correlative microscopy, the registration of images or data, is illustrated by studying HT1080 cells stably expressing LAMP-1-GFP with light and an electron microscopy. Using this example, it is explained how particles or fiducial markers that are clearly visible in both modalities can be used to correlate light and electron microscopy images.

As many studies base their conclusions on results from light microscopy, it is of utmost importance that these measurements are of excellent quality. This makes it crucial that microscopes are performing at their best. Moreover, for reliable quantitative measurements the calibration of the microscope is of importance as well. Therefore, strategies, challenges and the need for new test targets for the calibration and alignment purposes are discussed in the following section of this chapter.

The chapter finishes by giving an outline of the work presented in this thesis.

1.1 Light and fluorescence microscopy

In light or optical microscopy, a technique that lies at the heart of the work presented in this thesis, photons are used to create a magnified image of a specimen [1]. In its simplest form, a single-lens microscope is used as a magnifying glass to create a magnified image of an object. Though, for practical reasons, most microscopes used in research at present are so called "compound microscopes" and contain at least two (sets of) lenses. In figure 1.1a schematic illustration of a compound microscope with two lenses, the objective and the eyepiece, is included. In this setup, a light source and a condenser lens are used to homogeneously illuminate a specimen from behind. The light passing through the specimen is collected by the objective lens that creates an intermediate magnified image of the specimen. The eyepiece lens is now used to further magnify this image and creates the final image that can be viewed by the user [2, 3].

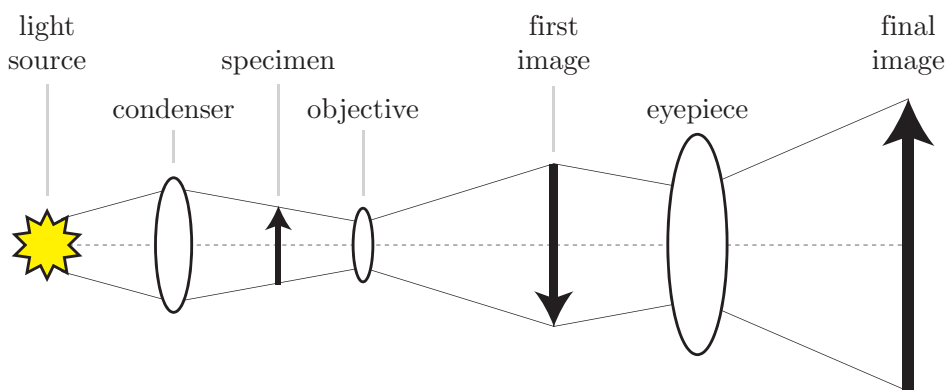


Figure 1.1: Schematic illustration of the most commonly used type of light microscope, the compound microscope [2].

Fluorescence Microscopy (FM) is an example of a more sophisticated light microscopy technique that can be used to (selectively) detect fluorescence from a specimen. This fluorescence originates from fluorescent species or substances that emit light, or photons, after the absorption of light. The emitted photons contain the same or a smaller amount of energy compared to the photons that were initially absorbed. To clarify this, an energy or Jablonski diagram and corresponding excitation and emission spectra of this process are included in figure 1.2. In the Jablonski diagram, S_0 and S_1 correspond to the singlet ground and first and excited electronic state. The vibrational energy levels of these states are also included in the figure. For fluorescence to occur, a photon is absorbed first as indicated by the blue or purple arrow. This photon excites the fluorophore from its ground state (S_0) to a higher vibrational level of the S_1 state. Within (several) picoseconds (10^{-12} s) or less, the fluorophore relaxes to the lowest vibrational level of the S_1 state via a process called internal conversion (grey arrow). From this state the fluorophore returns to one of the vibrational states of the ground state under the emission of a photon (green arrow). The lifetime related to this process is referred to as the radiative lifetime and is typically in the order of 10^{-9} – 10^{-8} s. After further internal conversion, the fluorophore finally returns to the lowest vibrational level of the ground state [4].

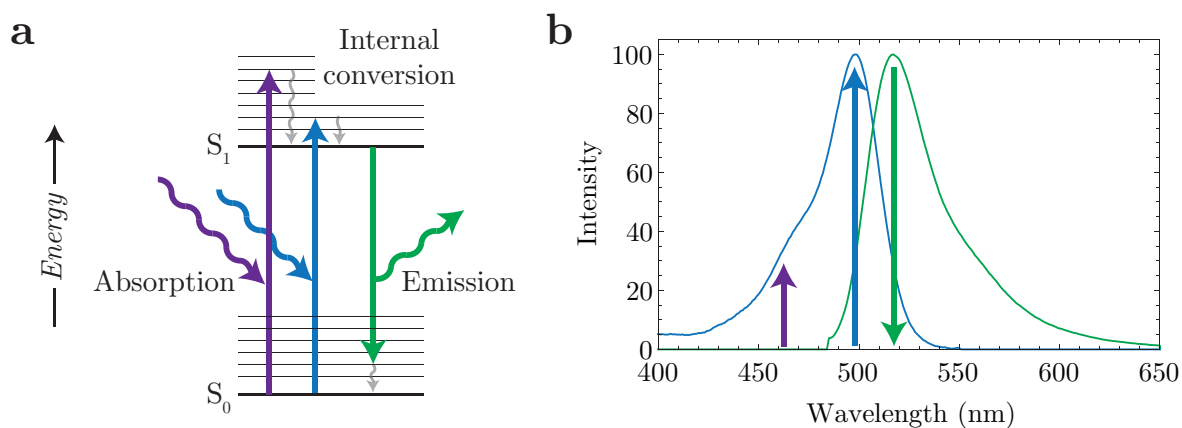


Figure 1.2: In (a) an energy or Jablonski diagram and in (b) corresponding excitation (blue) and emission (green) spectra of a fluorescent molecule.

Fluorescence can occur in molecules, fluorescent proteins, minerals or nanomaterials such as quantum dots. In figure 1.3 for example, pictures of jellyfish under the illumination of non-visible UV light are shown. After absorption of the UV light, visible green or pink/red light is emitted by the fluorescent proteins present in the two types of jellyfish. In this work we will mainly focus on fluorescent molecules or fluorophores and fluorescent proteins where fluorescence typically originates from aromatic domains within the molecule or protein.

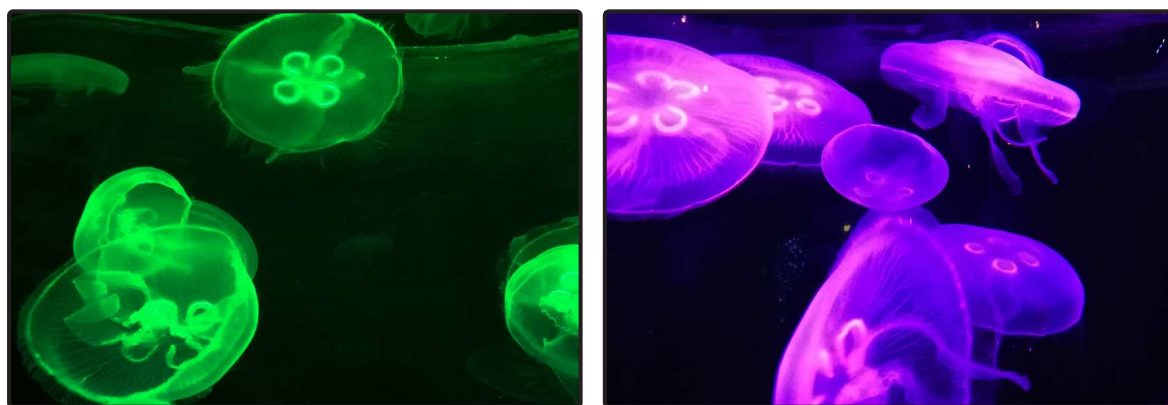


Figure 1.3: Two types jellyfish under illumination with UV. Pictures were taken at the aquarium facility of the Loro Parque zoo (Tenerife, Spain).

To use a light microscope for the selective detection of fluorescence, a dichroic mirror and excitation and emission filters are introduced as illustrated in figure 1.4. The key-component in this design is the dichroic mirror. This mirror reflects short-wavelength light that is used for excitation of the specimen, while allowing the longer wavelength fluorescence emission to pass [2]. The excitation and emission filters are for additional filtering of the excitation and emission light, respectively. This additional filtering reduces the amount of detected background signal and opens up the possibility to selectively detect fluorescent species within a specimen.

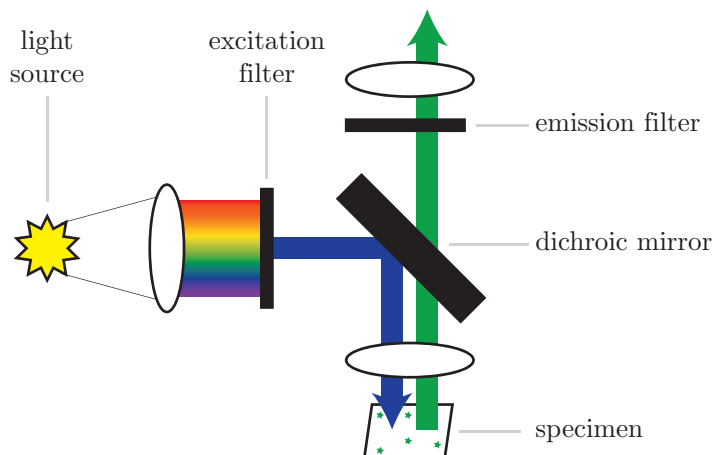


Figure 1.4: Schematic illustration of a fluorescence microscope [2].

Fluorescence microscopy is a very sensitive technique and under good imaging and labelling conditions, single fluorescent molecules can be visualized within a specimen. This high sensitivity in combination with the large field of view of FM techniques enables the visualization of rare transient events or specific cells within complex tissues [5, 6]. Also, measurements can be performed both *in situ* and *in vivo* because data can be collected very fast and under physiological, non-harmful or toxic conditions. This opens up the possibility to, for example, study dynamic processes within cells in live-cell experiments [7].

Despite all great properties, FM also comes with some limitations. First of all, the resolution of FM is limited to a few hundred nanometers for standard confocal and widefield microscopes. This limit is imposed by the diffraction limit and is large compared to the size of biomolecules. With super-resolution techniques it is possible to overcome the diffraction limit [8, 9]. However, the possibility of performing super-resolution microscopy measurement remains limited for a lot of researchers as it requires dedicated setups and/or labelling strategies. Another important disadvantage of FM is that only fluorescent or fluorescently tagged molecules or proteins are visible in FM. As most materials are non-fluorescent and therefore not visible, information about surrounding tissue or materials is missing.

1.1.1 Time resolved measurements to study fluorophores and their fluorescence

For FM measurements, it is crucial that fluorophores are performing well. Therefore, the performance of fluorophore is frequently studied with time-resolved measurements. One of the important parameters that can be deduced from the fluorescence decay curve is the fluorescence lifetime of a fluorophore. This lifetime determines how many times a fluorophore can cycle between its excited state and is ground state per second. Apart from the fluorescence lifetime, time traces contain far more information. It is for example also possible to study fluorescence quenching and enhancement. Because of

the importance of time resolved measurements throughout the work presented in this thesis, some basics are explained in the following section.

Fluorescence always starts with the excitation of a fluorophore from its ground state to an excited state. After excitation, the excited fluorophore will return to its ground state at some point in time. This can occur via the emission of a photon, a process referred to as radiative decay, or non-radiatively as indicated in figure 1.5. In the absence of external effects, the rates of both processes are characteristics of a fluorophore and determine the time the fluorophore on average remains in its excited state. This time is referred to as the fluorescence lifetime or the radiative decay time (τ) and is determined by the radiative decay rate (k_r) and the non-radiative decay rate (k_{nr}) as indicated in the equation below. Here, all possible non-radiative decay processes are grouped and represented by a single rate constant (k_{nr}) [4].

$$\tau = \frac{1}{k_r + k_{nr}} \quad (1.1)$$

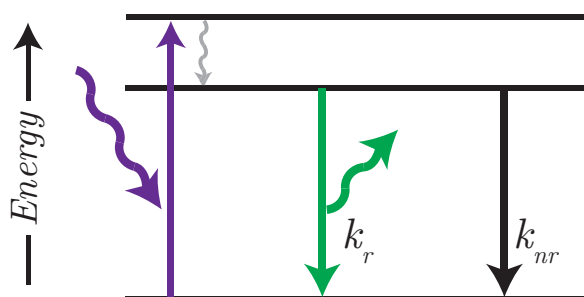


Figure 1.5: A simplified Jablonski diagram representing that following excitation (purple arrow) a fluorophore can return to its ground state radiatively (green arrow) or non-radiatively (black arrow). The rate constants k_r and k_{nr} are related to these processes and determine the fluorescence lifetime (τ) and the quantum efficiency of a fluorophore.

Radiative and non-radiative decay are two competing processes. Therefore, not only the fluorescence lifetime but also the probability that excitation of a fluorophore is followed by the emission of a photon is determined by the rate constants related to these processes (k_r and k_{nr}). k_r and k_{nr} can be used to calculate the quantum efficiency (QE) or quantum yield of a fluorophore. As the name suggests, the QE is defined as the number of emitted divided by the number of absorbed photons and is therefore a measure of the fluorescence efficiency of a fluorophore. It can be calculated as follows:

$$QE = \frac{\text{Number of emitted photons}}{\text{Number of absorbed photons}} = \frac{k_r}{k_r + k_{nr}} = \tau k_r \quad (1.2)$$

From this equation, it can be concluded that the QE of a fluorophore decreases when the non-radiative decay rate, k_{nr} , increases. This is exactly what happens when fluorophores are quenched, for example by nearby heavy metals. As the quantum efficiency is related to the fluorescence lifetime (equation 1.2), this is accompanied by a decrease in the fluorescence lifetime.

Fluorescence lifetimes can be determined by performing time resolved or radiative decay measurements. Time-correlated single photon counting (TCSPC) [10] is frequently used for this purpose. In these measurements, time traces or decay curves are obtained by the detection of single photons after excitation of fluorophores by a very short laser pulse. This process is repeated many times and decay curves are obtained by correlating the time of arrival of each photon (t) with the timing of the laser pulse ($t=0$), see figure 1.6a.

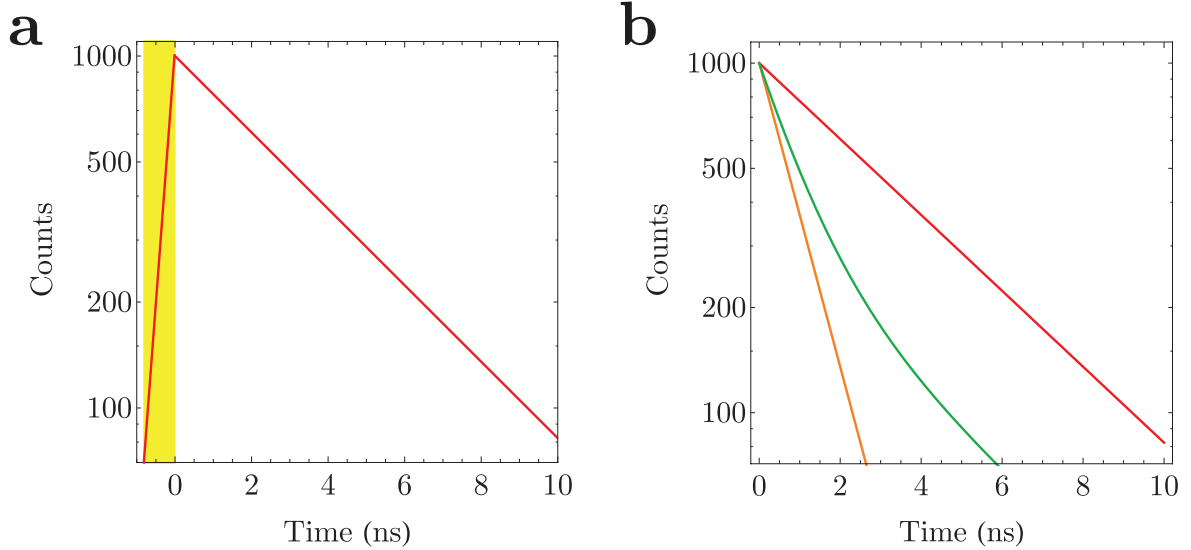


Figure 1.6: In (a) the laser pulse that is used for excitation of the fluorophores is indicated by the yellow bar (not on scale) and the red curve represent the recorded time trace. In (b) single-exponential decay curves of a fluorophore with a fluorescent lifetime of 4 ns (red) and 1 ns (orange) and a multi-exponential decay curve (green) are simulated. The multi-exponential decay curve contains two fluorescent components with fluorescent lifetime of 4 ns (30%) and 1 ns (70%).

When decay curves of a single fluorophore, with a single fluorescence lifetime are recorded, they can be fitted with a single-exponential function (equation 1.3). In this equation, I_0 corresponds to the intensity (or number of counts) immediately following the excitation pulse and τ corresponds to the fluorescence lifetime of the fluorophore.

$$I(t) = I_0 \exp\left(\frac{-t}{\tau}\right) \quad (1.3)$$

If fluorophores with different lifetimes are present within an ensemble of fluorophores, the situation becomes more complex as this result in multi-exponential decay curves. This can occur for example when a fraction of the fluorophores within the measurement is affected by a quencher. Fluorescence quenching introduces an additional non-radiative pathway and therefore lowers the radiative lifetime as well as the QE of fluorophores. An example of such a double-exponential decay curve is indicated by the green line in figure 1.6b.

1.2 Electron microscopy

In Electron Microscopy (EM), the second important technique used in this thesis, electrons are used for imaging instead of photons. As the wavelength of an electron is much smaller than the wavelength of a photon, EM techniques have a far greater resolution. Achievable resolutions are in the order of nanometers for regular EM microscopes and in the order of tens of picometers for dedicated high-resolution systems.

In figure 1.7 a schematic representation of the two most commonly used types of electron microscopes are shown: the transmission electron microscope or TEM and the scanning electron microscope or SEM. The design of a TEM (a) is very similar to that of the light microscope included in figure 1.1. The most important difference is the presence of an electron source instead of a light source. Furthermore, lenses are of electromagnetic origin as they are designed to focus and manipulate an electron beam, and images are collected on a fluorescent screen and the entire setup, or ‘column’, is placed into a sealed chamber under high vacuum. This high vacuum is necessary as the electrons would otherwise collide with atoms/molecules present in air before reaching the specimen and/or fluorescent screen.

The scanning electron microscopy or SEM setup in (b) on the other hand looks very different as images are collected in a different manner. Apart from the lenses that are used to create a very narrow electron beam, this setup contains a scanning coil or beam deflector. This beam deflector is used to change the x/y position of the beam so that it is possible to scan the surface of the specimen with a focused beam of electrons. While scanning, a detector is used to collect a fraction of the electrons that is scattered or released by the specimen. Images are created by correlating this signal with the position of the electron beam.

The high resolution in EM is great but also comes at a price as the field of view of an electron microscope is typically very small. This limits the possibility to image large volumes or areas. Another disadvantage is that the grey scale images collected with EM do not contain any functional information about the observed structures. Additionally, under the high vacuum conditions that are encountered in EM, *in vivo* or *in situ* imaging is no longer possible.

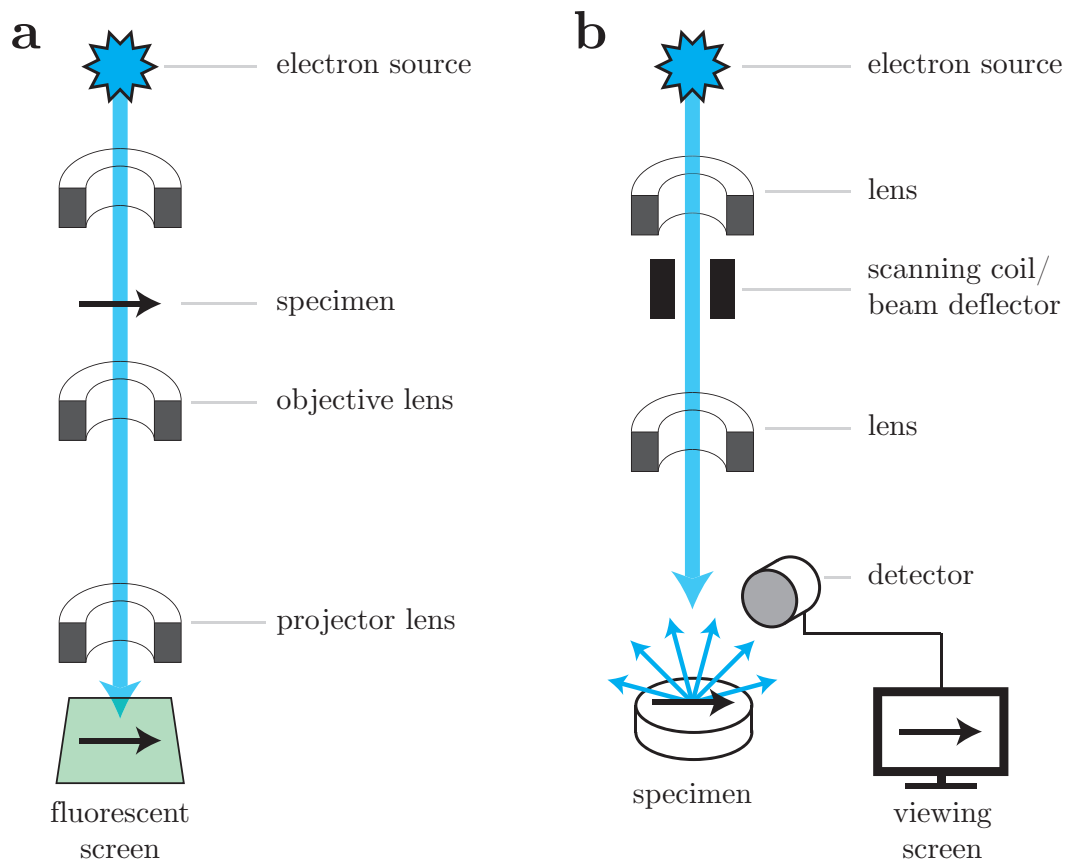


Figure 1.7: Schematic illustration of (a) a transmission and (b) a scanning electron microscope [2].

1.3 Correlative Light & Electron Microscopy

In Correlative Light and Electron Microscopy (CLEM), a combination of light and electron microscopy is used to explore a single specimen. This combination proves valuable because it combines the advantages of FM and EM [11]. First, FM is used to visualize, localize and track specific fluorescent molecules in cells over large areas or volumes with high sensitivity and specificity. Next, EM is used to gather high resolution structural information of regions of interest identified by FM. At present, most CLEM experiments are performed in a non-integrated fashion; FM and EM data is collected sequentially using two dedicated setups. In this approach, FM data is collected first because most fluorophores or fluorescent proteins degrade upon interaction with an electron beam. Also, not all fluorophores and fluorescent proteins remain fluorescent under the dry and vacuum conditions encountered in an electron microscope. Because the heavy metals that are introduced to provide EM contrast quench most fluorescence, FM data is often recorded before specimen are prepared for EM. Another advantage of this non-integrated CLEM is that the great variety of well-developed labelling agents, protocols and setups for FM and EM is accessible without having to compromise on one of them.

An obvious disadvantage of non-integrated CLEM is the need to transfer specimen from the first to the second microscope. During this transfer, specimens are easily contaminated or damaged. For cryo measurements, in which the sample has to remain stable at a temperature around 4 K, this becomes even more challenging as the cryo conditions should be maintained when the sample is transferred from microscope to microscope. If a sample is successfully transferred to the second microscope another challenge appears. Retrieving a region of interest in EM that was first imaged in FM is not always straight-forward and can be time consuming as the orientation of the sample changes when the sample is transferred.

To tackle these challenges, various alternative routes were developed by the integration of a fluorescence microscope in an electron microscope. We refer to this as integrated CLEM or iCLEM. The first integrated microscope was already presented in the 1982 by Wouters and Koerten et al. [12]. Together they managed to integrate a light microscope in a scanning electron microscope. From there on, great developments were made, see the reviews by Timmermans and Otto [13] and Ando et al. [14]. Two important developments will be addressed in the following section.

The first important development was presented by Agronskaia [15] and co-workers in 2008 when a fluorescence microscope was successfully integrated in a transmission electron microscopy. In the design of this microscope a long working distance, low-NA objective is placed between the pole pieces of the TEM lens. To switch between FM and EM, the sample is tilted 90 degrees as illustrated in figure 1.8. The iLEM prototype of this microscope was commercialized by FEI (now ThermoFisher Scientific) as the iCorr. This setup is the first commercially available iCLEM microscope. Recently the work by Agronskaia et al. was extended by Hendriks, Mohammadian and co-workers [16] who demonstrated that it is also possible to perform integrated correlative super-resolution measurements with the iLEM setup via single-molecule fluorescence measurements.

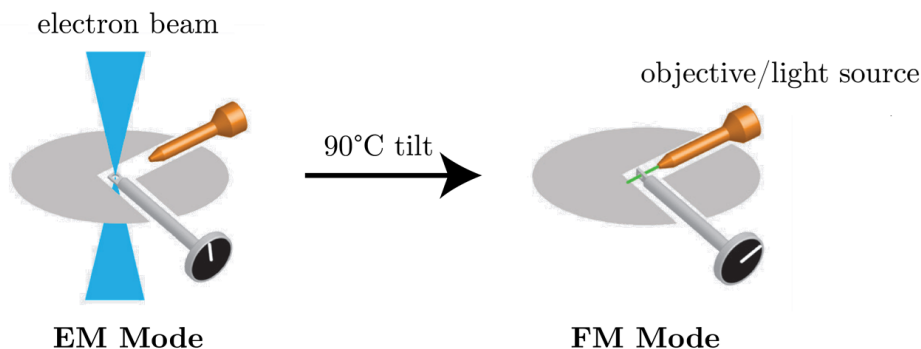


Figure 1.8: The iLEM/iCorr design: an objective is placed between the pole pieces of the TEM lens. To switch between FM and EM imaging, the sample is tilted. Image was taken from ref [16].

The second iCLEM setup that is addressed here was presented in 2013 by Zonneville [17] and co-workers. This microscope is an improvement on the work of Wouters and Koerten as it also integrates a light microscope in a scanning electron microscope. In the design of this microscope, a high-NA objective lens is placed below the sample, paraxial to the SEM as illustrated in figure 1.9. This geometry allows for simultaneous collection of FM and EM data [18] and allows for sub-5 nm image registration [19]. This microscope was commercialized by Delmic as the SECOM microscope. Nowadays also the SECOM-SR, a microscope that combines super-resolution (SR) optical microscopy and electron microscopy, is also commercially available.

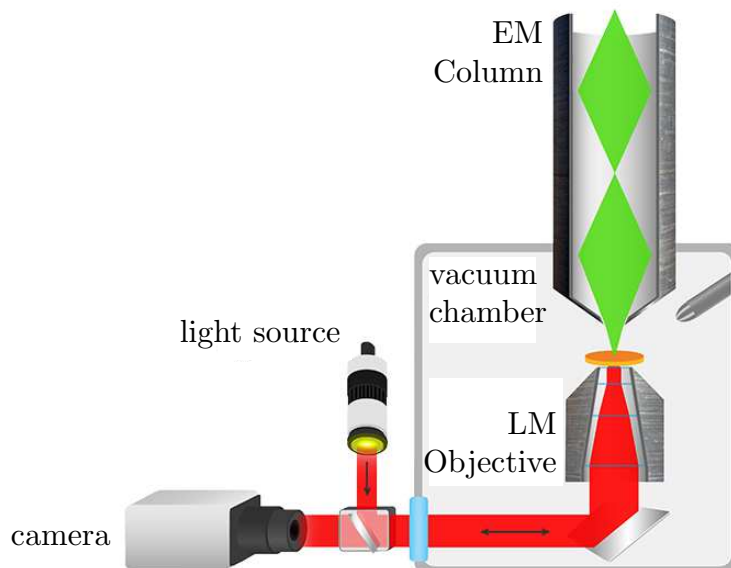


Figure 1.9: The SECOM design: a high-NA objective is placed below the sample, paraxial to the SEM. Image was taken from the Delmic website.

The iCLEM techniques are all based on a 2D electron microscopy technique, i.e. scanning or transmission electron microscopy. Within the TTW Microscopy Valley programme, progress has been made to develop the first 3D iCLEM setup by integrating a confocal microscope in a focused ion beam scanning electron microscope. After the confocal microscope is used to obtain 3D FM data that can be used to rapidly locate regions of interest, the system is capable of producing high resolution 3D EM images by repetitively removing layers by ion-beam milling and recording SEM images (slice and view). The possibility to only image predefined regions of interest in EM will significantly speed-up the 3D CLEM workflow.

1.3.1 The challenge of data registration

To gain additional information from CLEM experiments, it is very important to properly overlay or register (stacks of) images obtained in the two modalities. How challenging this registration can be is demonstrated by the example CLEM data included in figure 1.10. In this figure, FM and EM images of a 70 nm thick cryosection of HT1080 cells stably expressing LAMP-1-GFP are included. The first thing to notice from these images is that the FM and EM images look completely different. In FM, fluorescence coming from LAMP-1, DAPI and SiR-Lysosomes is recorded in three separate channels, depicted in green, blue and magenta. All other cellular structures are non-fluorescent and therefore not visible. The grey scale image recorded in EM, on the other hand, shows the entire cellular structure but does not contain any information about the presence of DAPI, LAMP-1 or SiR-lysosomes. In this example, the unusual shape of the DAPI labelled nuclei can be recognized in both modalities. This shape can be used to identify the region imaged in EM and/or to create a first rough overlay; but often such features are not present. Other possible issues apparent from the images which can make image registration more difficult are the large difference in scale, field of view and resolution.

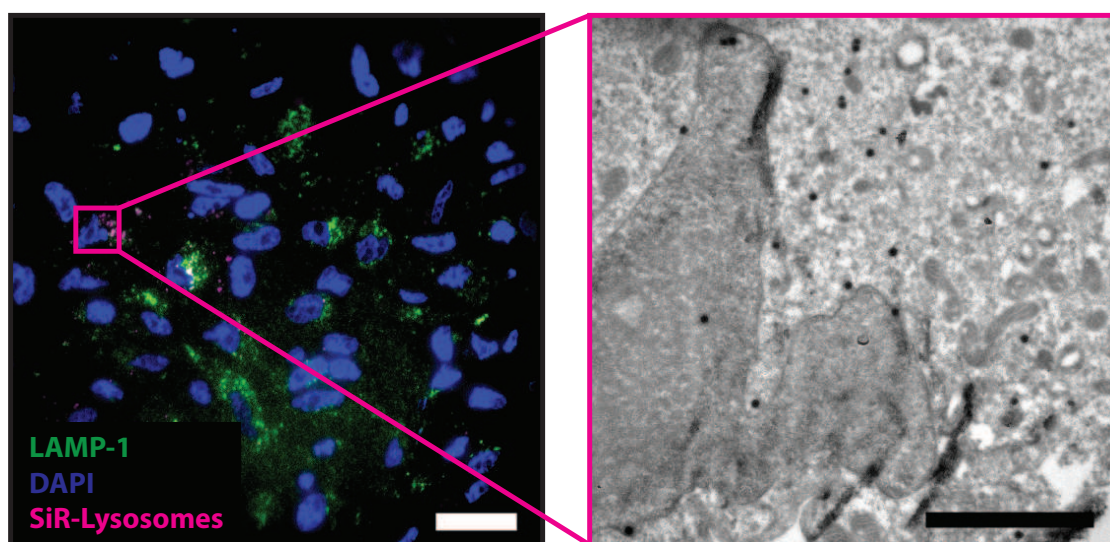


Figure 1.10: FM (left) versus EM (right) images of a 70 nm thick cryosection of HT1080 cells stably expressing LAMP-1-GFP. Scale bars indicate 20 and 2 μm .

One of the ways to overcome the challenge of image registration is the introduction of particles or fiducial markers that are clearly visible in both modalities. Positions of the fiducial markers can then be used as reference points to overlay the data obtained in the two modalities, as shown in figure 1.11.

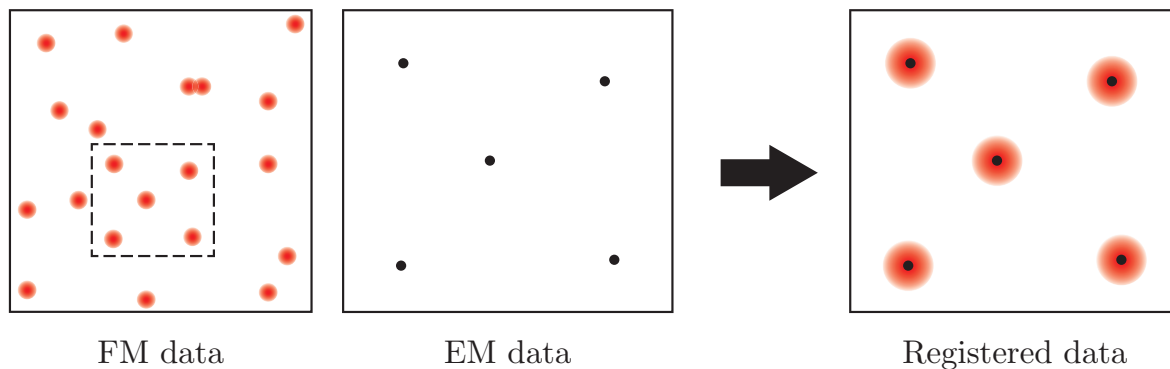


Figure 1.11: Particles or fiducials markers visible in both, FM and EM, can be used as anchor points to register data obtained in the two modalities.

Such fiducial markers have to meet several requirements. For EM, it is important that the particle or nanocomposite has a high EM contrast with respect to the surrounding (biological) specimen, background or support. For FM it is also important that the particle is bright and photostable. For an integrated approach, the fluorescence must be preserved even under the vacuum and/or cryo conditions of an electron microscope. A final and very important requirement is the size of the particle. For particles that are used only as fiducial markers, a relatively large particle diameter of 50-100 nm would be acceptable. However, if the particles are also used for (immuno)labelling, the total diameter should be as small as possible, ideally below 50 nm.

1.4 Evaluating the quality of a light microscope

Much of the work presented in this thesis relies on the quality of light microscopy measurements. The quality of these measurements is determined by the performance of the microscope that is used. Therefore, it is important that good methods and standards are available to quantify and optimize the performance of the microscope. The performance is not only determined by the specifics of the setup but also highly depends on the alignment of the optical components within the microscope. Because microscope alignment can vary over time, the performance should be evaluated on a regular basis to guarantee a high level of quality of all measurements.

For quantitative measurements, besides performance and alignment, it is also important that a microscope is well calibrated. Calibration of the lateral dimensions (x and y) of the field of view is reasonably straightforward as calibrated stage micrometers or test targets that are specifically designed for this purpose are commercially available. In figure 1.12 images of such a test target are included, the different patterns on this grid can be used for calibration purposes or to for example measure image distortions, to identify focus errors or to evaluate resolution in two dimensions [20]. Scaling and calibration of the axial direction (z) on the other hand, is more challenging and easy commercial solutions are not available.

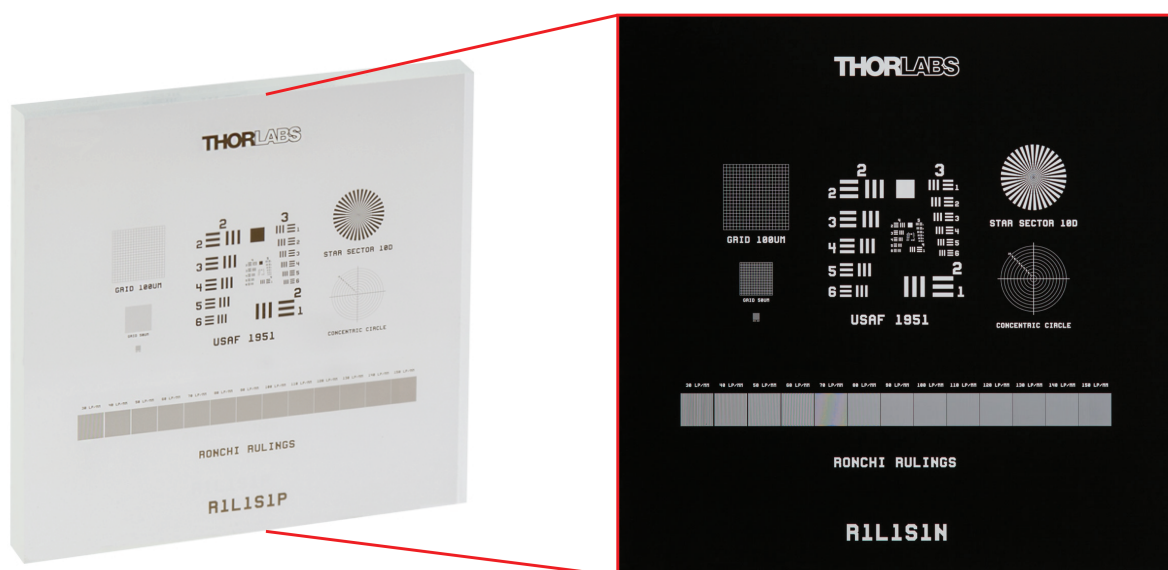


Figure 1.12: Thorlabs R1L1S1P combined resolution and distortion test targets, 18 mm x 18 mm [20].

Some clever solutions for this are presented in literature. An example of this is the generally applicable procedure for the axial calibration of a confocal microscope presented by Besseling et al. [21]. Besseling and co-workers demonstrated that a sample cell built from ordinary glass cover slips can be used for the axial calibration of a confocal microscope. This was achieved by accurately measuring the height of the empty cell. Next, confocal stacks of the cell filled with solvents with different refractive indices

and fluorescent dye were recorded. For each refractive index, the measured cell height was different as changing the refractive index results in linear shrinkage or elongation of images in the axial direction. By comparing this confocal height with the actual height of the (empty) cell the axial scaling factor could be deduced as a function of the refractive index.

A good way to determine how well a microscope performs is by recording the Point Spread Function (PSF) of the setup [22]. The PSF is obtained by recording a 3D image of a single sub-resolution object and basically shows the blurring of a point object by the microscope. By comparing the recorded PSF to a theoretical PSF it is possible to deduce how well a microscope is performing and/or aligned as distortions or misalignment effects are absent in the theoretical PSF. Deformations, (large) differences in size or sudden changes in the experimental PSF are all indications that a setup is misaligned or not performing as it should.

With the advent of (3D) super-resolution microscopy techniques such as stimulated emission depletion (STED) microscopy, calibration, alignment and therefore the possibility to record PSFs became even more critical. The success and achievable resolution of STED measurements strongly depend on the size and shape of the PSF. As this PSF is the product of the interaction of two laser beams with the specimen, the excitation and depletion beam, it is important to also determine how these beams are aligned with respect to one another. Gold beads are frequently imaged in reflection to study and improve the alignment of the two beams and to increase the quality of the final PSF.

Another reason to collect PSFs is their use in image post-processing. Experimentally obtained PSFs are frequently used to increase the resolution of images by deconvolution techniques. This is a mathematical process that (partially) corrects for the response of the microscope to an object, thereby deblurring images [23]. The observation that image restoration with an experimentally measured PSF allows for better image restoration than deconvolution with a theoretical PSF [24] stresses how important it is that methods are available to reliably measure the PSF of a setup.

At present, good tools are available to measure PSFs and to align (3D) STED beams close to the cover glass. This used to be sufficient as the majority of images was collected close to the cover glass. Though, with the development of high-end objectives that can be used to collect images far away from the cover glass [25] this is no longer sufficient. To use these objectives at their maximum capacity, it becomes a necessity to also develop methods to reliably characterise PSFs far away from the cover glass. To meet this need, test targets should be developed that can be used for calibration and alignment of (STED) microscopes in three dimensions. Ideally, this would substitute the multitude of samples that is currently needed to check the full performance of such a microscope. This could be achieved for example by placing various materials in a smart (nano)geometry.

1.5 Outline of this thesis

Throughout this thesis, nanocomposite particles are used for various applications in (correlative light and electron) microscopy. To facilitate further reading, a brief outline of the thesis is given below.

Chapter 2 starts with a discussion of the importance of fluorophore labelling density. Silica particles labelled with different fluorophore densities are used to study how labelling density and the brightness and bleaching behaviour of the particles relate to each other. To explain and learn from this experimental work, simulations are included as well.

In **Chapter 3** nanocomposite particles based on a gold core and a fluorescently labelled silica shell are presented as fiducial markers for correlative light and electron microscopy. Within this nanocomposite particle, the gold core provides contrast for EM and fluorophores covalently incorporated in the silica shell provide fluorescence for FM.

Chapter 4 elaborates on the previous chapters as the fiducial markers are tested in an iCLEM experiment. To this end, cells are labelled in three dimensions by endocytosis of the fiducial markers. Following uptake, the cells are prepared for EM following the extremely thin layer plastification protocol. Throughout this procedure the fluorescence of the fiducial markers is monitored as it is crucial that (enough) fluorescence is preserved for iCLEM compatibility. In the final section, 3D iCLEM measurements of the obtained cellular samples are included. This data is recorded on an integrated setup that was developed by co-workers within this project.

In **Chapter 5** a single sample is presented to check the full performance of a 3D (super-resolution) light microscope. This sample is composed of a refractive index matched colloidal crystal of silica beads with a fluorescent or a gold core. The periodicity of this sample can be used to calibrate the microscope in three dimensions; alignment of laser lines can be checked using the reflection of the gold cores; and the point spread function (PSF) can be measured at multiple positions and depths using the fluorescent cores.

2

A Study of Fluorophore Labelling Density Effects

In this chapter, theory, measurements and simulations are presented to get a better understanding of the effects of fluorophore labelling density on brightness and bleaching of fluorescently labelled particles. In the theoretical model, a combination of energy transfer and quenching is considered to explain labelling density effects on fluorescence behaviour. Next, particles labelled with different fluorophore labelling density are synthesized and characterized to validate the presented model. The fluorophore of choice for this is rhodamine B as this is a very popular, well studied and commercially available fluorophore. Silica is chosen as a host material as good methods are available to synthesize fluorescently labelled, spherical and monodisperse silica particles.

2.1 Introduction

When fluorescently labelled particles are used in fluorescence microscopy, it is important that the particles are well visible. The particles should be so bright that their fluorescence intensity is well above any background signal. In addition, the particles should remain visible over a longer period over time, so the bleaching behaviour of the particles is of importance as well. Because both, brightness and bleaching, depend on the density or number of fluorophores in the particles, optimization of the labelling density is necessary. This chapter focusses on optimization of the labelling density of fluorescently labelled particles.

2.2 Brightness and labelling density

First, we will consider how labelling density affects the brightness of a fluorescently labelled particle. As a starting point, it seems reasonable to assume that the brightness of a particle scales with the number of fluorophores within the particle. This assumption would hold if fluorophores can be viewed as independent molecules but in reality, the situation is much more complex. If the distances or separations between fluorophores become short enough, fluorophores can sense each other and interactions between fluorophores come into play. As short-range interactions between fluorophores often result in fluorescence quenching, increasing the number of fluorophores often does not result in the expected (linear) increase of the fluorescence intensity [4, 26, 27, 28, 29, 30]. Concentration-quenching and self-quenching are frequently used terms to refer to this effect. In the following section, an explanation for this observation is given by considering which distance dependent interactions can occur between fluorophores. Generally speaking, three regimes can be identified:

1. Large distances (> 10 nm)
Fluorophores do not sense each other, and the intensity scales with the number of fluorophores in a particle;
2. Intermediate distance ($\sim 1-10$ nm)
When separations are in this range, Förster Resonant Energy Transfer (FRET) between fluorophores can take place and allows the excited state to migrate between fluorophores. The intensity again scales with the number of fluorophores in a particle;
3. Close distance (< 1 nm)
Overlap of the electron clouds or orbitals results in strong quenching effects. The linear relation between intensity and the number of fluorophores in a particle no longer holds.

In the particles used in this thesis, fluorophores are expected to be randomly distributed throughout the particles. Therefore, a distribution of distances between fluorophores will be present in every particle. In figure 2.1, a schematic 2D representation

of randomly distributed fluorophores is shown; here, labelling density increases from (a) to (c). If we simplify the system by assuming that all fluorophores have a 100% quantum efficiency, there are different possibilities after the excitation of a fluorophore for the different labelling densities.

In (a) there are no interactions between fluorophores because distances between fluorophores are large (> 10 nm). Excitation of one of the fluorophores will therefore always result in the emission of a photon. In (b) separations are within the range of Förster energy transfer. This allows the excited state to migrate between fluorophores until a photon is emitted by one of the fluorophores. In (c1 & c2) many of the fluorophores are within the range of Förster energy transfer and some of the fluorophores are at close distance so that self-quenching takes place. The latter fluorophores act as quenching centers and are often dimers. After excitation there are two options: the excited state can either migrate until a photon is emitted (c1) or it can migrate until it reaches one of the quenching centers (c2). If the excited state reaches a quenching center, no photon is emitted which reduces the number of emitted photons and thereby the fluorescence intensity or brightness of the particles.

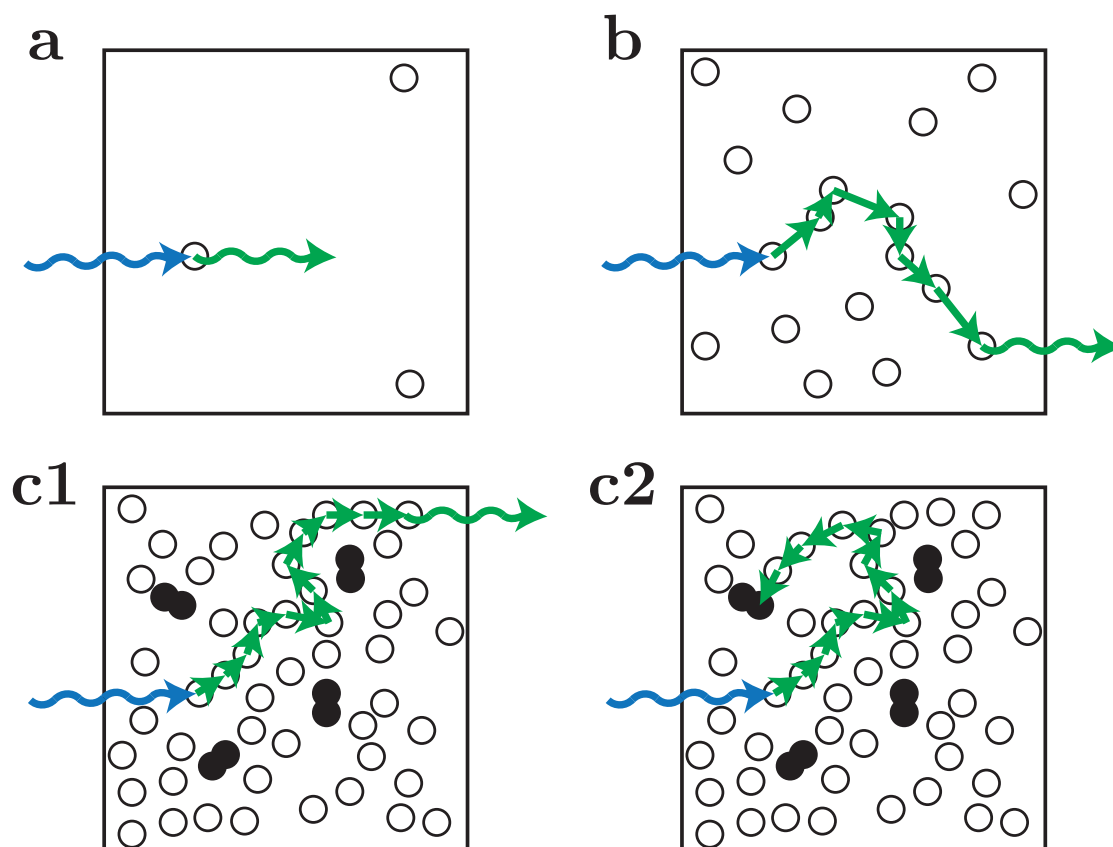


Figure 2.1: A schematic illustration of the three labelling density regimes. White and black spheres represent fluorophores and quenching centers respectively. The wavy blue and green arrows indicate excitation by and emission of a photon, the straight green arrows indicate that the excited state is transferred non-radiatively from fluorophore to fluorophore.

This figure illustrates how important it is to optimize the labelling density to obtain bright particles. At low labelling densities, increasing the number of fluorophores results in an increase in the brightness of the particles. When the labelling density becomes higher, this increase is (partially) counterbalanced because some of the fluorescence is quenched. At very high labelling densities, the probability of formation of quenching centers (dimers) can be high and the fluorescence can be strongly quenched. In the following sections, a combination of theory, measurements and simulations is presented to gain more insight in labelling density effects.

2.2.1 Energy transfer at intermediate distances ($\sim 1-10$ nm)

Energy can be transferred non-radiatively between fluorophores via Förster Resonance Energy Transfer by dipole-dipole interaction. A schematic representation of this process is shown in figure 2.2. In this representation, a donor is excited by a photon. This donor returns to its ground state by transferring its energy non-radiatively to a nearby acceptor. Finally, the now excited acceptor returns to its ground state by the emission of a photon or via a non-radiative decay process. For FRET to occur, three requirements must be fulfilled.

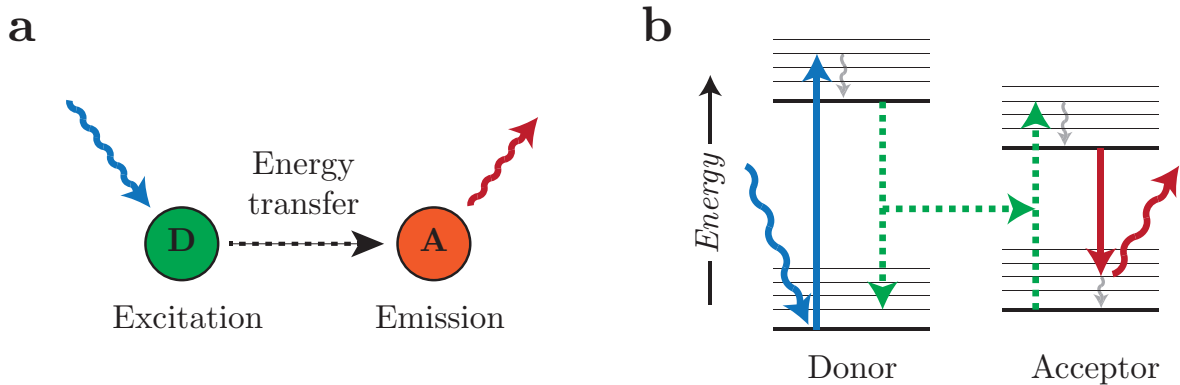


Figure 2.2: In (a) A schematic representation of FRET, in (b) the Jablonski diagram for this process.

1. The distance between the donor and acceptor

This first requirement is that the donor and the acceptor are in close proximity, typically within ~ 10 nm. The distance dependency of the energy transfer efficiency, E_{FRET} is given by:

$$E_{FRET} = \frac{R_0^6}{R_0^6 + r^6} \quad (2.1)$$

Here, r corresponds to the distance between the donor and the acceptor and R_0 is the Förster distance of the FRET pair. This Förster distance is defined as the distance where $E_{FRET} = 50\%$ and depends on the photophysical properties of donor

and acceptor. Förster distances of commonly used fluorophores are between ~ 3 and ~ 7 nm [4, 31]. The equation shows that the FRET efficiency is inversely proportional to the sixth power of the donor-acceptor separation. Therefore, this process is very sensitive to small changes in donor-acceptor separation. This is clearly visible in figure 2.3 where the energy transfer efficiency is shown as a function of the donor-acceptor separation, r/R_0 . FRET occurs when the distance between the donor and the acceptor is less than approximately two times the Förster radius. When r/R_0 is between 0.5 and 1.5, small variations in the donor-acceptor distance have a large effect on the FRET efficiency. This strong distance dependency makes FRET ideal to, for example, study protein folding, dynamics or interactions between molecules [32, 33, 34].

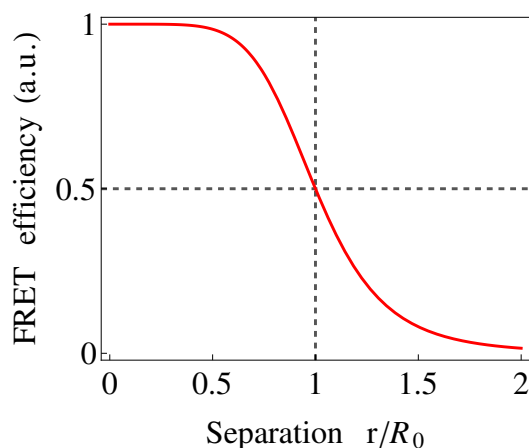


Figure 2.3: FRET efficiency as a function of the separation (r/R_0) between a single donor and a single acceptor molecule. R_0 is the Förster distance of the donor-acceptor pair.

The same r^{-6} distance dependency is found in the expression for the energy transfer rate, k_{FRET} , from a donor to a nearby acceptor:

$$k_{FRET} = \frac{1}{\tau_D} \left(\frac{R_0}{r} \right)^6 \quad (2.2)$$

Here, r and R_0 again correspond to the distance between the donor and the acceptor and the Förster radius and τ_D is the decay time of the donor.

2. Spectral overlap of donor emission and acceptor absorption

The donor emission spectrum and the acceptor absorption spectrum should overlap to make energy transfer energetically possible. This shows up in more detail in the expression for the Förster radius:

$$R_0^6 = \frac{9000(\ln 10)\kappa^2 Q_D}{128\pi^5 N n^4} J(\lambda) \quad (2.3)$$

Here, Q_D is the quantum yield of the donor in absence of the acceptor, n is the refractive index of the medium, N is Avogadro's number, κ^2 the orientation factor (see

below). The overlap integral, $J(\lambda)$, is a measure for the degree of spectral overlap between the donor emission and acceptors absorption. This number is calculated as follows:

$$J(\lambda) = \int_0^{\infty} F_D(\lambda)\epsilon_A(\lambda)\lambda^4 d\lambda \quad (2.4)$$

Here, $F_D(\lambda)$ is the corrected fluorescence intensity of the donor and $\epsilon_A(\lambda)$ is the extinction coefficient of the acceptor at a given wavelength λ . The corrected fluorescence intensity is obtained from the emission spectrum by normalizing its total area to unity.

In figure 2.4a spectra of a fictional FRET-pair are shown. Here, the area in grey corresponds to the area where there is spectral overlap between donor emission and acceptor absorption. This is an example of hetero-FRET as energy is transferred between non-identical fluorophores. Though, FRET can also occur between two identical fluorophores as long as there is significant spectral overlap between the absorption and emission spectra. This is illustrated in figure 2.4b where the absorption and emission spectra of the donor in (a) are included. In this example there is significant spectral overlap between the spectra. If two of these molecules are within the FRET-range and one molecule is excited, it can also transfer its energy, as a donor, to another fluorophore, now acting as an acceptor and vice versa. We refer to this as homo-FRET because energy is transferred between identical fluorophores.

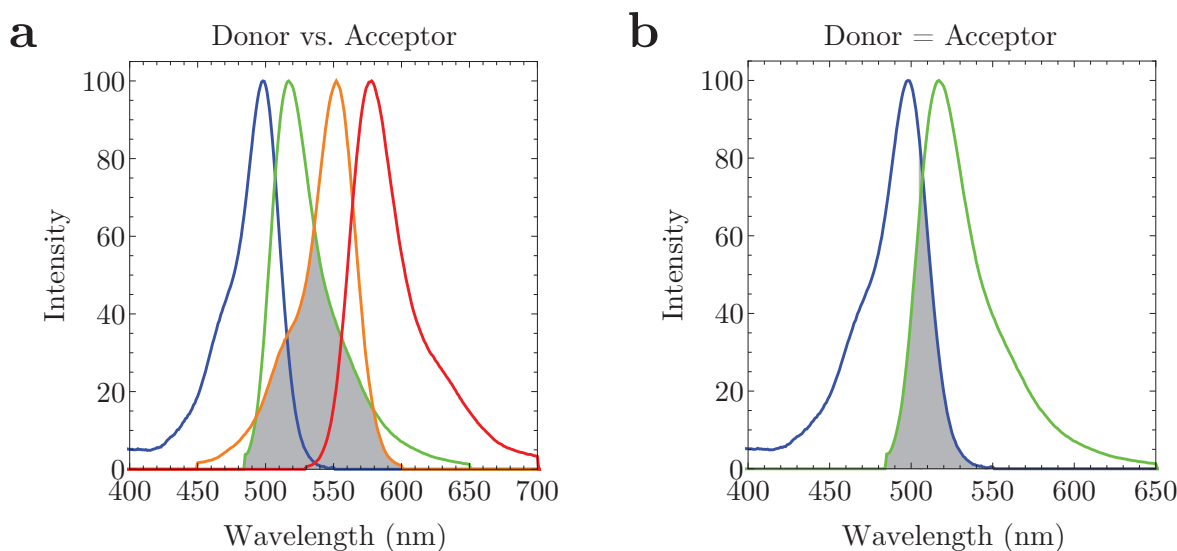


Figure 2.4: Absorption (blue/orange) and emission (green/red) spectra for (a) hetero- and (b) homo-FRET. Spectral overlap is indicated by the grey area.

3. The relative orientations of donor and acceptor transition dipole moments

The relative orientations of the transition dipole moments of the donor and acceptor also plays a role in the energy transfer probability. This effect is usually expressed by the orientation factor, κ^2 , which depends on the relative orientations of the donors emission dipole moment and the acceptors absorption dipole moment. In this work, we assume the dipole moments to be randomly oriented and that spatial averaging takes place of their orientations. This results in a κ^2 value of 2/3.

2.2.2 Dexter quenching at close distances ($< 10 \text{ \AA}$)

When the distance between two fluorophores becomes small enough, their electron clouds will overlap. This overlap allows an excited electron to transfer non-radiatively from an excited to an unexcited fluorophore. This type of energy transfer is often referred to as "Dexter electron transfer" (DET) and results in a high probability of fluorescence quenching. Therefore it is also referred to as "Dexter quenching". Dexter proposed a theory for this mechanism in 1953 when he was studying sensitized luminescence of atoms in solids [35]. According to this theory, the rate or probability of energy exchange between an excited and an unexcited atom is given by:

$$k_{DET} = A \exp\left[-\frac{2r}{L}\right] \propto J(\lambda) \exp\left[-\frac{2r}{L}\right] \quad (2.5)$$

Here, k_{DET} is the transfer rate or probability of energy transfer, A is the Dexter amplitude, r is the distance between the atoms and L is the effective average Bohr radius for the excited and unexcited states of the atoms. As we are studying fluorophores instead of atoms, the van der Waals radius (r_w) of the fluorophore is used instead of the average Bohr radius (L). The dimensions of rhodamine B and its electron cloud, the fluorophore used in this study, is reported to be around 4 by 10 by 17 \AA [36, 37, 38]. Therefore, overlap of the electron clouds and quenching is expected when the separation between fluorophores is below 10-20 \AA .

It is good to finalize this section by stressing that Dexter electron transfer and FRET (section 2.2.1) are two different mechanisms for the transfer of energy between fluorophores [4]. For Dexter electron transfer close molecular contact is required as this type of energy transfer originates from a quantum mechanical effect. Energy transfer via FRET on the other hand finds its origin in dipole-dipole coupling of fluorophores which is a through-space interaction.

2.3 Photobleaching and labelling density

When fluorescent probes are excited repeatedly, they tend to lose their ability to fluoresce over time [39, 40]. Therefore, FM images fade in time during fluorescence measurements up to the point where fluorescence is completely lost. This fading is caused by chemical alterations in the fluorescent molecule that result in an often permanent loss of the ability to fluoresce, a process referred to as photobleaching or bleaching. The photobleaching rate depends on various factors such as the type of fluorophore, the illumination intensity, time and wavelength and the environment of the fluorophore. The presence of oxygen, for example, speeds up the process of photobleaching. Therefore, anti-fading agents are often used that inhibit the generation and diffusion of reactive oxygen species [40, 41, 42, 43].

Besides the previously stated factors, the photobleaching rate also depends on the fluorophore labelling density. Imhof et al. reported a decrease in the photobleaching rate of fluorescein labelled silica particles with increasing fluorophore labelling density [27]. A possible explanation for this was given by considering the decrease in radiative lifetime with increasing labelling density. The shorter lifetime results in faster depopulation of the excited state, which lowers the probability of bleaching via excited state reactions.

Another effect that can occur is that quenching of a fluorophore by a neighbouring bleached fluorophore becomes less efficient. Bleaching would therefore be counterbalanced by an increase in the fluorescence intensity of neighbouring fluorophores. In the work by Genovese et al., such a mechanism is used to explain the observed reduction in photobleaching of pluronic silica particles labelled with increasing fluorophore (rhodamine B) labelling densities [44]. For the highest labelling densities, this mechanism could even explain the unexpected observation of initial photo brightening of the particles upon illumination. Acceptor-photobleaching FRET studies are also based on this principle. In this technique, it is assumed that fluorophores are completely destroyed upon permanent photobleaching. Therefore, after selective photobleaching of the acceptor, FRET is no longer possible which results in an increase of the donor intensity. Despite the successes of this method, the possibility that light absorbing species act as “dark quenchers” is not taken into account. This leads to a possible underestimation of the unquenched donor fluorescence [45].

In this chapter, the relationship between photobleaching and labelling density of fluorescent nanoparticles is studied using photobleaching and radiative lifetime measurements.

2.4 The distribution of fluorophores

When fluorophore labelling densities are considered, one often refers to the "average" fluorophore separation. This value corresponds to the average separation between fluorophores in case of a fully homogeneous distribution. A schematic representation of such a homogenous distribution in three dimensions is included in figure 2.5. In this ordering, the separation between all nearest neighbour fluorophores is the same.

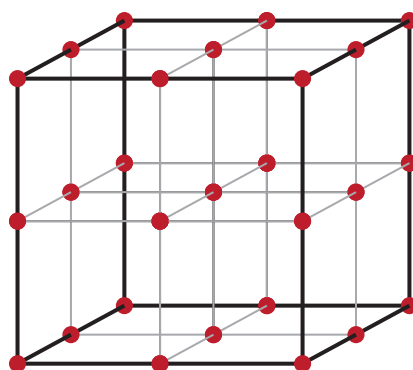


Figure 2.5: A 3D representation of a fully homogenous distribution of fluorophores. Red spots correspond to fluorophores and all lines are of equal length.

In reality, a more or less random distribution of fluorophores throughout the volume is expected. This results in the presence of a distribution of fluorophore separations. If for example the average fluorophore to fluorophore separation is estimated to be around 10 nm, distances smaller as well as larger than 10 nm will be present. This can be demonstrated by Monte Carlo simulations of fluorophores randomly placed inside the volume of a sphere, see figure 2.6. This data was obtained by placing 523 fluorophores inside the volume of a 100 nm diameter sphere. With this number of fluorophores and volume, a volume of $10 \times 10 \times 10 \text{ nm}^3$ is available per fluorophore and an average fluorophore separation of 10 nm.

To visualize the range of fluorophore separations, nearest neighbour distances were calculated for all fluorophores. By repeating the simulation, statistically relevant data was obtained. An example of a simulated distribution is plotted in figure 2.6. This figure shows that the average nearest neighbour distance is shorter than the average separation. Another important observation is that distances in both the Förster and the Dexter regime are present. This reveals that, at this dye concentration, both homo-FRET and quenching via Dexter electron transfer can take place in the particles. Homo-FRET now allows the excited state to migrate from an unquenched to a (nearby) quenched fluorophore, thereby contributing to quenching.

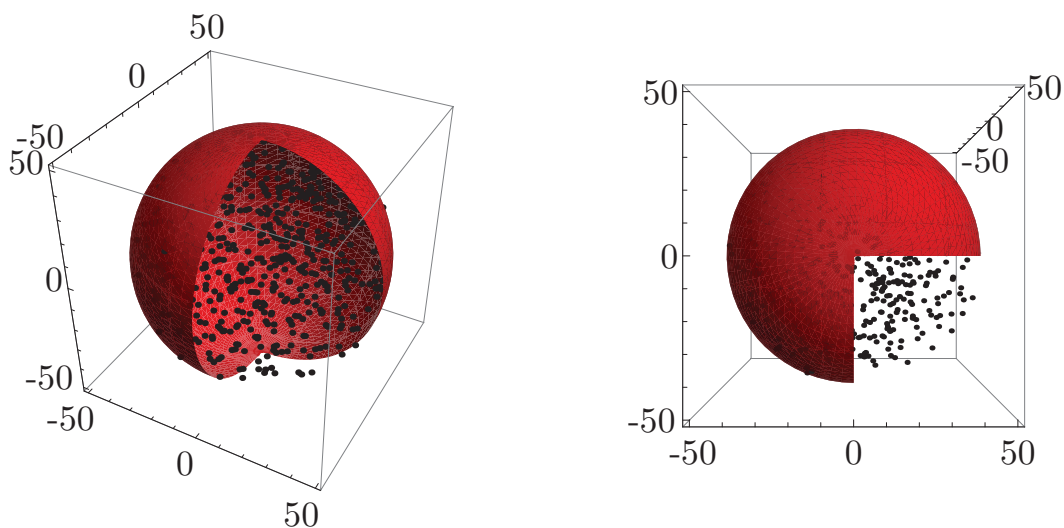


Figure 2.6: Sample data of Monte Carlo simulations where points, representing fluorophores, are positioned inside the volume of a 100 nm diameter sphere. Here, 523 fluorophores were placed inside the sphere corresponding to an average separation of 10 nm.

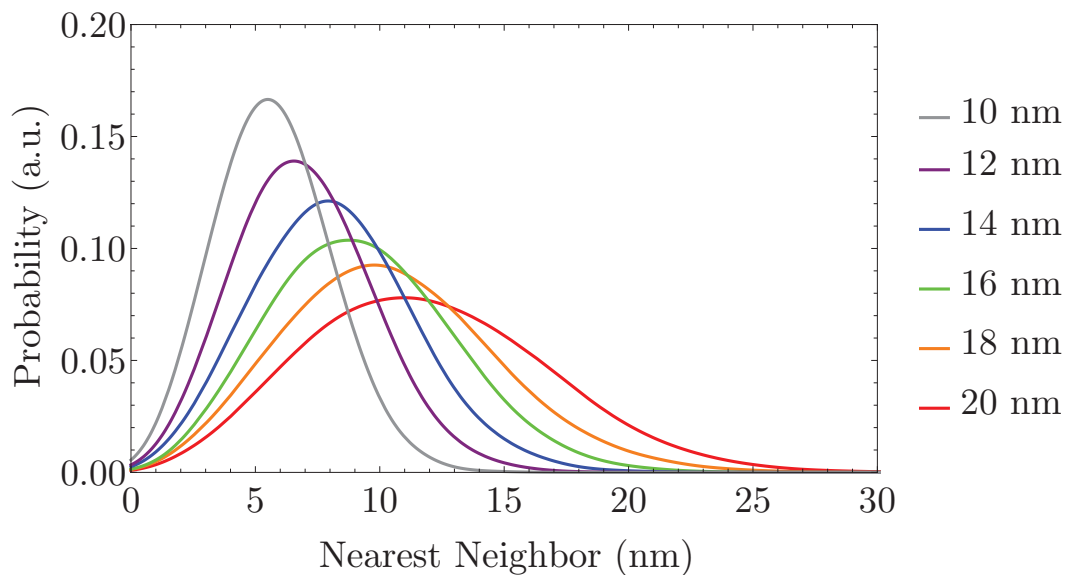


Figure 2.7: Histograms of the nearest neighbour distance between fluorophores inside a 100 nm diameter sphere obtained from Monte Carlo simulations. Distances in the legend correspond to average fluorophore separations.

2.5 Experimental details

2.5.1 Synthesis of the rhodamine B labelled silica particles

The particles were synthesized via the procedure depicted schematically in figure 2.8. In the first step, non-fluorescent silica cores with a diameter of approximately 30 nm were synthesized as described by Karg et al. [46] and Reculosa et al. [47]. In the next step, these cores were used as seeds and coated with a layer of rhodamine B labelled silica. Seeded growth was the preferred method because this method can be used to synthesize spherical monodisperse silica particles of any desired size below a micron [48, 49]. By using the same seeds and by keeping all reactions conditions except for the fluorophore concentration equal during this seeded growth step, particles of the same size labelled with different fluorophore densities were synthesized. After growth of the rhodamine B labelled silica layer, a second seeded growth step was performed to grow an additional non-fluorescent silica layer. This layer is added for stabilization since it prevents aggregation of the particles.

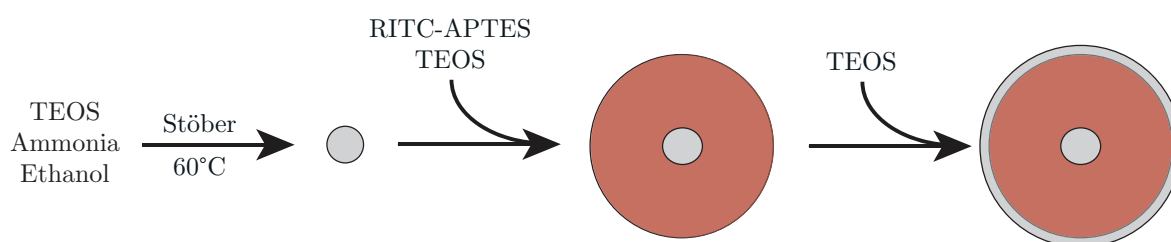


Figure 2.8: A schematic representation of the synthesis of rhodamine B labelled silica nanoparticles. By varying the amount of RITC-APTES added in the first seeded growth step, particles with different fluorophore labelling densities can be obtained.

Materials

Tetraethyl orthosilica or TEOS (reagent grade, 98%), ammonium hydroxide solution (ACS reagent, 28-30% NH₃ basis), rhodamine B isothiocyanate (mixed isomers) or RITC, 99% (3-aminopropyl)-triethoxysilane or APTES, sodium hydroxide pellets (ACS reagent, >97.0%) and Vivaspin 20 centrifugal concentrator tubes (MWCO 100.000 Da) were purchased from Sigma-Aldrich. Absolute ethanol was purchased from Merck. All glassware was extensively cleaned with soap, water and ethanol prior to use. Milli-Q water was used in all experiments.

Synthesis of the non-fluorescent silica cores

50 mL ethanol and 3.75 mL ammonia were transferred to a round bottomed flask equipped with a condenser. The solution was placed in a 60°C preheated oil bath for 30 minutes under constant stirring at 300 rpm. After 30 minutes, the stirring speed was increased to 500 rpm followed by the injection of 1.5 mL TEOS. 10 minutes after

this addition, the stirring speed was reduced to 300 rpm and stirring and heating was continued. After approximately 16 hours, the now slightly turbid solution was cooled down to room temperature and stored in the refrigerator.

Growth of the rhodamine B labelled silica layer

Prior to the seeded growth, RITC-APTES coupling was performed by transferring 10 mg RITC and 1 mL absolute ethanol to a vial. Under constant stirring, 83 μL APTES was added to this solution. The vial was closed and wrapped in aluminium foil to protect the fluorophore from photo bleaching and stirred for another 16 hours. After 16 hours, different dilutions ranging from 0 to 40 vol% of the RITC-APTES solution in ethanol were prepared. These solution were used to synthesize particles with relative dye concentrations ranging from 0 to 40 (labelled as $[\text{Dye}] = 0 - 40$).

For growth of the rhodamine B labelled silica layer, 180 mL ethanol and 1.8 mL of the solution of non-fluorescent silica cores were transferred to a vial and sonicated for 15 minutes to ensure homogenization. 15 mL of the obtained solution was transferred to vials A-J. Under continuous stirring at 600 rpm, 1.5 mL ammonia and 15 μL of a 10 vol% solution of TEOS in ethanol was added to all vials to grow a first thin layer of non-fluorescent silica. The growth of this layer helps to stabilize the particles before growth of the rhodamine B labelled silica layer is started. After 90 minutes, growth of the rhodamine B labelled silica layer was started by the addition of 60 μL of the diluted rhodamine B solution and 60 μL of 10 vol% TEOS solution to all vials. The different dilutions of RITC-APTES in ethanol were used for vials A-J to obtain particles labelled with various rhodamine B concentrations. Both additions were repeated with 180, 500 and 800 μL with time intervals of 90 minutes to grow the entire fluorescently labelled silica layer. 90 minutes after the last addition, a second stabilization layer was grown by the addition of 300 μL 10 vol% TEOS solution. 60 minutes after this final addition, the reaction mixtures were transferred to a dialysis bag that was placed inside a 40 mL vial filled with ethanol. The solution were gently stirred and the ethanol was replaced three times over a time span of 36 hours. Further cleaning of the particles was performed via repeated centrifugation in 100.000 MWCO vivaspin tubes.

2.5.2 Characterization of the particles

Determination of the fluorophore incorporation efficiency

Immediately after synthesis of the particles, 3 mL of the reaction mixtures was transferred to 5 mL Eppendorf tubes. These solutions were centrifuged 10 minutes at 10.000 RCF to separate the particles from the reaction mixture. The supernatants were collected and stored; next the particles were redispersed in 3 mL ethanol. Centrifugation and redispersion in ethanol was repeated two more times to remove all non-incorporated fluorophore from the solutions.

The particles were dissolved by transferring 1.5 mL particle solution and 1.5 mL of a 0.4 M sodium hydroxide solution in water to a clean 5 mL Eppendorf tube. The supernatants were diluted following the exact same procedure to obtain a set of reference

samples. 48 hours after homogenization of the solutions, transparent solutions ranging from colourless ($[\text{Dye}] = 0$) to pink ($[\text{Dye}] = 40$) were obtained. Absorption spectra of all solutions were recorded on a HP8953A spectrophotometer in 1 cm quartz cuvettes. If necessary, samples were diluted with a 1:1 (volume) mixture of ethanol and 0.4 M sodium hydroxide solution.

Spectral and radiative decay measurements

Bulk excitation and emission spectra of the particles suspended in ethanol were recorded in 1 cm quartz cuvettes using an Edinburg Instruments FLS920 fluorescence spectrometer. In all measurements, fluorescence was detected at an angle of 90° to the exciting beam. A 530 nm long pass filter was placed between the sample and the detector in all measurements to remove residual excitation light. To record excitation and emission spectra, a 450 W xenon lamp and a double excitation monochromator with a grating blazed at 500 nm was used for excitation. Spectra were recorded with a Hamamatsu H74220-60 photo sensor module.

Radiative decay measurements of the particles suspended in ethanol were recorded in 1.50 mm quartz ultra-micro-cuvettes on a homebuilt setup. Briefly, a 20 MHz ps pulsed supercontinuum STC-500 laser (Fyla, Valencia) in combination with a monochromator tuned to 525 nm, a 515/30 bandpass filter and a vertical polarizer were used for excitation of the sample. The emitted light was filtered with a 532 longpass and a 590/60 bandpass filter. In addition, an emission polarizer placed under the magic angle was used to remove polarization artefacts. Emitted photons were detected with a microchannel plate photomultiplier tube (MCP-PMT, Hamamatsu R3809U-50) and time correlated spectra were recorded with a TCSPC-module (SPC-150 Becker & Hickl GmbH). Decay spectra were analysed using an up to 3 exponential Levenberg-Marquardt fit. The homemade analyses software (TRIX), includes iterative deconvolution to account for the effect of the Instruments Response Function (IRF). The Full Width Half Maximum of the IRF amounted to 100 ps.

Single particle intensity and bleaching measurements

Fluorescence intensity images were acquired using a Nikon Eclipse Ti widefield microscope equipped with a 40x 0.75 NA Nikon air objective. The accessory perfect focus unit was used to retain sample focus during the measurements. A mercury arc lamp in conjunction with a 510-560 nm excitation filter, a 565 nm long pass dichroic mirror and a 590 nm long pass emission filter were used to select excitation and detection wavelength bands. An excitation intensity of 12.8 mW was used in all experiments, corresponding to an intensity of 6.0 W/cm^2 in the object plane. Finally, a NEO sCMOS camera (Andor, Belfast) was used to record images.

Single particle intensities were determined using ThunderSTORM software [50]. For the single particle intensity measurements, the obtained data (a list of fitted intensities for every fluorescent spot) was directly analysed in Mathematica. To obtain the average single particle intensities, for every sample, data obtained from at least 20 images was plotted in a histogram. The first peak in this histogram was attributed to the single

particle intensity and a normal distribution was fitted to this peak to obtain the mean intensity and the standard deviation.

To study bleaching, a series of images of a selected region of a specimen were recorded over time. Bleaching curves were obtained by plotting the average intensity of every image as a function of time.

To gain more insight into the bleaching behaviour of the particles, radiative decay measurements were conducted at fixed time intervals over the course of bleaching. These measurements were carried out on a different microscope, a Nikon Eclipse TE2000-S. All other experimental conditions were chosen to match the experimental conditions that were used to obtain the bleaching curves. Briefly, the microscope was equipped with the same 40x 0.75 NA Nikon air objective and a mercury lamp in conjunction with the same 510-560 nm excitation filter, 565 nm long pass dichroic mirror and 590 nm long pass emission filter was used for repeated bleaching. With two additional neutral density filters, an intensity of 11.9 mW was measured, matching to the widefield measurements mentioned above fairly well

Following bleaching for a fixed amount of time, radiative decay curves were recorded using a fluorescence lifetime module (LiMo) coupled to a Confocal Laser Scanning Microscope (CLSM, Nikon Instruments Europe BV, Amsterdam) [51]. For these measurements, a 80 MHz ps pulsed supercontinuum Koheras SuperK laser (NKTphotonics, Birkerød) was used for excitation of the sample. An Acousto Optical Tunable Filter (AOTF) tuned to 525 nm in combination with a 535/40 nm bandpass filter and the CLSM 532 nm longpass dichroic was used to select the excitation wavelength. The excitation power at the specimen was 3-10 μ W. A GaAsP photomultiplier tube (PMT, Hamamatsu, Germany) in combination with a 532 nm longpass and a 590/60 nm bandpass filter were used for detection.

The time-gated LiMo (Nikon Instruments, Europe BV, Amsterdam) captures four intensities per pixel representing the total fluorescent intensity in four consecutive time gates of approximately 2 ns each. These four-gate intensity decays were fitted with a monoexponential decay using the LiMo software to generate lifetime images (160x160pixels). The pixel fluorescence lifetimes were plotted in a histogram and fitted with a Gaussian function to obtain the radiative decay values.

2.6 Simulations

Simulations were performed to gain more insight in the fluorescence behaviour of the nanoparticles. Particles with a geometry that mimics the core-shell geometry of the synthesized particles were used in all simulations. The size of the non-fluorescent core was set at 27.4 nm, the TEM diameter of the non-fluorescent silica cores, and the total particle diameter was set at 81 nm. This total diameter corresponds to the average particle size after growth of the fluorescently labelled silica shell that was determined in TEM measurements. The following processes were included in the simulations:

- Radiative decay (k_r);
- Non-radiative decay (k_{nr});
- Energy transfer between identical fluorophores via homo-FRET (k_{FRET} , section 2.2.1);
- Quenching via Dexter energy transfer (k_{DET} , section 2.2.2);
- The presence of dimers.

For the fluorophore used here, rhodamine B, a single exponential decay with a fluorescence lifetime of 3.2 ns and a quantum efficiency of 0.6 was assumed [52]. This quantum efficiency is determined by the ratio between the radiative decay rate and the sum of the radiative and non-radiative decay rates. For homo-FRET it is required to calculate the Förster radius (R_0). For this quantum efficiency, a Förster radius of 4.5 nm was calculated based on the spectral overlap between the absorption and emission spectra of the fluorophore. The van der Waals radius (r_w) for Dexter energy transfer was assumed to be 1 nm, which reasonably matches the dimensions of rhodamine B and its electron cloud, see section 2.2.2. The strength of the Dexter energy transfer is not available from literature and is hard to estimate. Therefore, the value of A in equation 2.5 was varied in the simulations.

Spectral measurements, see 2.7.3, revealed clear indications of the presence of rhodamine B dimers in the particles. Dimers of fluorescent molecules are known to have low quantum efficiencies and short lifetimes [4, 30, 53, 54, 55, 56, 57]. Here, we assumed that the radiative rate of the rhodamine B is not affected by dimerization and that the short lifetime and low quantum efficiency are caused by quenching. Effectively this results in an increase in the non-radiative rate. To implement dimers in the simulations, it was assumed that dimers consist of two molecules sitting at the same position. Furthermore, we assume that once a dimer dye is excited no energy transfer to other dyes takes place. Therefore, dimers effectively result in traps with low emission and short lifetimes. In addition, it was assumed that the formation of dimers is a first order chemical reaction governed by a single chemical equilibrium constant. This constant was varied in the simulations.

After defining all input parameters, a particle was generated by placing a certain number of fluorophores randomly inside the volume of the fluorescently labelled shell. Furthermore, randomly placed dyes within a distance of 0.2 nm from each other were

assumed to be dimers sitting at the same position. Next, the rates of all processes were calculated for all fluorophores, including processes internal to the molecule (k_r , k_{nr}) and transfer processes to all neighbouring molecules (k_{FRET1} , k_{DET1} ; k_{FRET2} , k_{DET2} ; ...). To simplify the simulations, energy transfer between fluorophores was only considered for fluorophores within $< 3R_0$ of one another. This assumption is reasonable as energy transfer to fluorophores that are further apart is negligible ($E_{FRET}(3R_0) \sim 0.1\%$). The simulations were initiated by the excitation of a randomly picked fluorophore within the particle. After excitation, the cumulative rate of all processes related to this particular fluorophore ($k_{tot} = k_r + k_{nr} + \sum k_{FRET} + \sum k_{DET}$) was used to calculate the time (t) at which one of the possible processes takes place. Here, we assumed an exponential probability distribution, $P(t) = \exp(-t/k_{tot})$. Next, to determine which processes takes place, a random number was generated between 0 and k_{tot} to select the process. Here, the strength of the process ($k_{process}$) is taken into account as weight factor.

Depending on the type of process that was selected, the molecule may return to its ground state (radiatively, non-radiatively, Dexter) or transfer its excited state to another dye molecule (homo-FRET). In the case of homo-FRET, the selection of a new time and process is repeated until an excited molecule returns to its ground state. The simulation of a complete excitation-decay path may involve multiple homo-FRET steps at high dye concentrations.

Each randomly generated particle configuration was excited 5000 times to assure averaging over all dyes in the particle. Furthermore, 1000 particle configurations were simulated for each dye concentration, to average over different dye distributions. The timing of all radiative decay events is used to construct radiative decay curves whereas the number of homo-FRET steps shows to which extend the excited state can migrate within the particles.

The amplitude for Dexter electron transfer, the fluorescence lifetime of the dimers and the chemical equilibrium constant for dimer formation were varied in the simulations to find acceptable agreement between simulations and experiments for the whole dye concentration range used in the experiments. The simulations were carried out on a PC and usually took between seconds and minutes per set of input parameters. To enable comparison between the simulated and measured decay curves, the simulated curves were convoluted with the experimental IRF. Average decay times were obtained from the simulated curves by fitting using the TRIX software.

2.7 Results

2.7.1 Synthesis of the particles

In figure 2.9 and table 2.1 representative TEM images and the average diameter and standard deviations of the synthesized particles are shown. From the TEM image in (a), it can be concluded that fairly monodisperse (st. dev. $\sim 10\%$) non-fluorescent and almost spherical silica cores with an average diameter of 27.4 nm were successfully synthesized. In (b) a representative TEM image of the particles after growth of the rhodamine B labelled silica shell is included. This figure shows that the silica grows selectively on the existing cores as no secondary nucleation is observed. There are also no indications of the formation of aggregates during silica growth as nearly spherical particles are obtained and the particle size of the different samples is almost identical. On average, the diameter of the particles increases from 27.4 nm to 84 nm. This increase is accompanied by a decrease in polydispersity as the size standard deviation drops from $\sim 10\%$ to $\sim 5\%$. A further increase in size is observed after growth of the second stabilization layer, see 2.9c. The average diameter of the particles after the final growth steps is 102 nm.

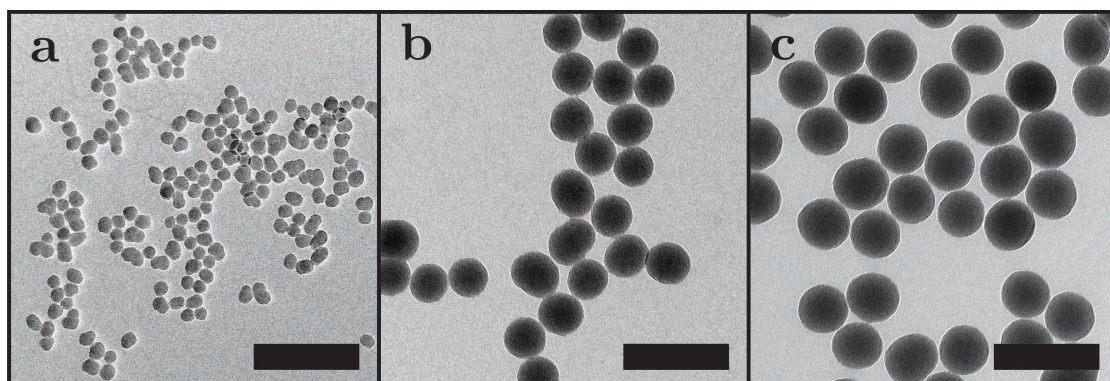


Figure 2.9: Representative TEM images of the particles at the different stages of the synthesis; (a) the non-fluorescent silica cores used to synthesize all samples after growth of the first stabilization layer; (b) after growth of the rhodamine B labelled silica layer; (c) after growth of the second non-fluorescent stabilization layer. All scale bars indicate 200 nm.

| [Dye] | Total particle diameter | | | |
|-------|-------------------------|---------------|-------------|---------------|
| | RITC layer | | Stab. layer | |
| | d (nm) | σ (nm) | d (nm) | σ (nm) |
| 40 | 84.4 | 5.0 | 102.5 | 3.9 |
| 35 | 85.2 | 5.1 | 107.4 | 5.2 |
| 25 | 85.7 | 4.6 | 101.1 | 5.3 |
| 20 | 84.2 | 4.6 | 101.4 | 5.7 |
| 12.5 | 83.1 | 3.7 | 106.0 | 4.8 |
| 7.5 | 82.1 | 4.1 | 102.8 | 4.9 |
| 5 | 83.8 | 2.7 | 100.9 | 5.5 |
| 2.5 | 85.1 | 4.1 | 102.3 | 6.3 |
| 1 | 83.5 | 4.9 | 103.6 | 5.8 |
| 0 | 80.8 | 3.8 | 97.3 | 5.3 |

Table 2.1: Particle sizes determined from TEM images after growth of the rhodamine B labelled silica layer and the second stabilization layer. All samples were based on 27.4 nm ($\sigma = 2.8$ nm) non-fluorescent silica cores. In this table, d is the average particle diameter and σ is the standard deviation of this average value, both determined by measuring diameters of 100 particles.

2.7.2 The labelling density

To calculate the average fluorophore separations and number of fluorophores per particle, the fluorophore labelling efficiency during the growth of the fluorescently labelled silica was determined. This was performed via absorption measurements after dissolution of the silica particles as described by Imhof et al. [27]. In figure 2.10 absorption spectra of the sample after silica dissolution and of the supernatant are shown. The spectra are obtained after a baseline correction that was performed and after subtraction of the reference sample ([Dye]=0).

The observed maximum in the absorption spectra around 550 nm were used to calculate the fluorophore incorporation efficiency according to the formula below. The outcome of this calculation is listed in table 2.2.

$$\text{Incorporation efficiency} = \frac{\text{Abs. sample}}{\text{Abs. sample} + \text{Abs. supernatant}} \times 100\% \quad (2.6)$$

The outcome of these calculations is listed in table 2.2 and shows that the labelling efficiency is approximately 2.5% for all samples. This results in a calculated average separation ranging from 7.7 nm for the highest to 24.9 nm for the lowest labelling density. This separation in combination with the TEM size of the particles was used to estimate the average number and corresponding error (\sqrt{N}) of fluorophores per particle. This number ranges from 19 for the lowest to 553 for the highest labelling density.

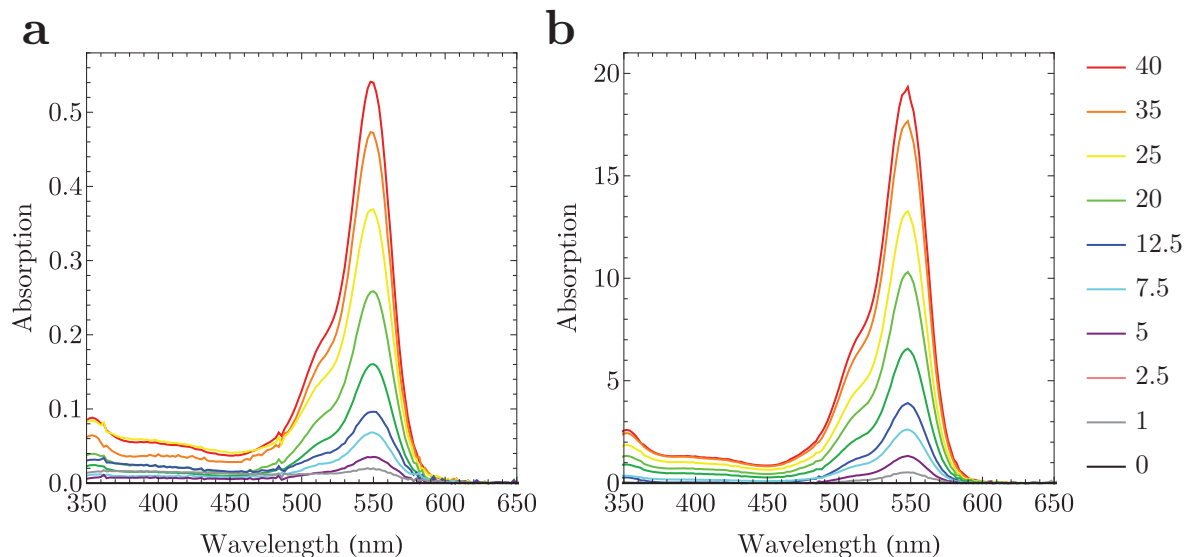


Figure 2.10: Absorption spectra of the samples after silica dissolution (a) and corresponding supernatants (b). The numbers in the legend correspond to the relative dye concentration ($[\text{Dye}]$) that was used to synthesize the particles

| Dye | Labelling efficiency (%) | Average separation (nm) | Fluorophores per particle (a.u.) |
|------|--------------------------|-------------------------|----------------------------------|
| 40 | 2.7 | 7.7 | 553 ± 24 |
| 35 | 2.6 | 8.2 | 472 ± 22 |
| 25 | 2.7 | 9.1 | 351 ± 19 |
| 20 | 2.4 | 10.1 | 290 ± 17 |
| 12.5 | 2.4 | 11.9 | 158 ± 13 |
| 7.5 | 2.4 | 14.1 | 105 ± 10 |
| 5 | 2.5 | 15.8 | 83 ± 9 |
| 2.5 | 2.6 | 19.8 | 33 ± 6 |
| 1 | 3.7 | 24.0 | 19 ± 4 |

Table 2.2: The fluorophore labelling efficiency, average separation and the estimated number of fluorophores per particle for the different samples.

2.7.3 Spectral and radiative decay measurements

Spectral and radiative decay measurements were carried out to investigate labelling density effects in the fluorescence of the particles. Excitation and emission spectra were recorded and show clear labelling density effects even at low dye concentrations, see figure 2.11. The first indication is the shift of both spectra towards shorter wavelengths with increasing labelling density. This shift is accompanied by an increase in the height of the shoulder (peak) in the excitation spectra around 520 nm. Both observations are indicative for an increase of the number of dimers present in the particles [53, 58, 59, 60, 61, 62, 63].

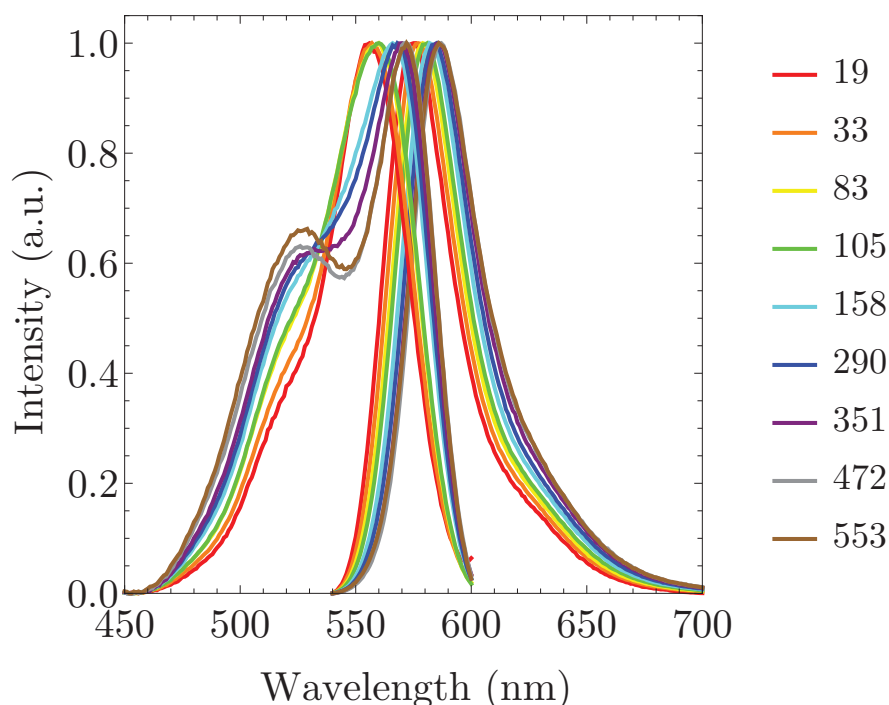


Figure 2.11: Emission spectra recorded after excitation at 520 nm (right) and excitation spectra recorded at 620 nm emission (left). The numbers in the legend corresponds to the estimated number of fluorophores per particle.

A second indication for the presence of labelling density effects can be found in the radiative decay curves included in figure 2.12. The curves reveal faster decay with increasing fluorophore labelling density. This can be attributed to an increase in quenching as the fluorescence lifetime is directly related to the quantum yield of a fluorophore, see sections 2.2 and 1.1.1. It is important to note that fluorophores that are completely quenched do not emit photons and are therefore not visible in the decay curves. It is therefore only possible to use the decay curves as an indication for the increase in quenching as the severity of quenching is easily underestimated.

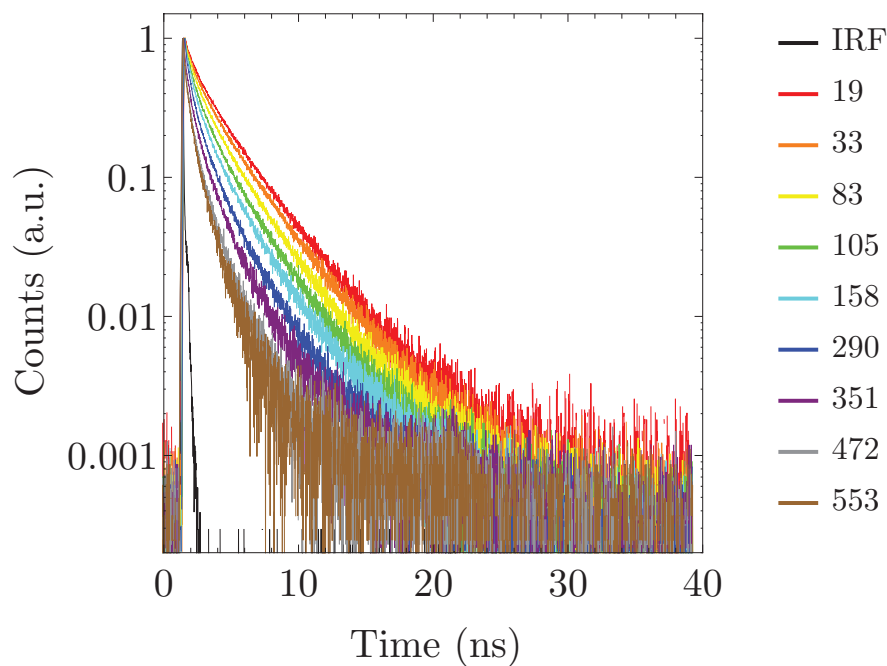


Figure 2.12: Radiative decay curves after pulsed excitation at 525 nm. The numbers in the legend corresponds to the estimated number of fluorophores per particle.

2.7.4 Single particle intensities and bleaching

In figure 2.13 the average single particle intensity, determined from wide field fluorescence microscopy measurements, is plotted versus the number of fluorophores per particle. In this figure, the single particle intensity initially increases almost linearly when the number of fluorophores increases from 0 to 83. At higher numbers of fluorophores per particle, the increase becomes (strongly) non-linear. Increasing the number of fluorophore per particles is now clearly counterbalanced by a decrease in the fluorescence intensity per fluorophore by quenching effects. Note that care was taken to avoid bleaching effects during these measurements.

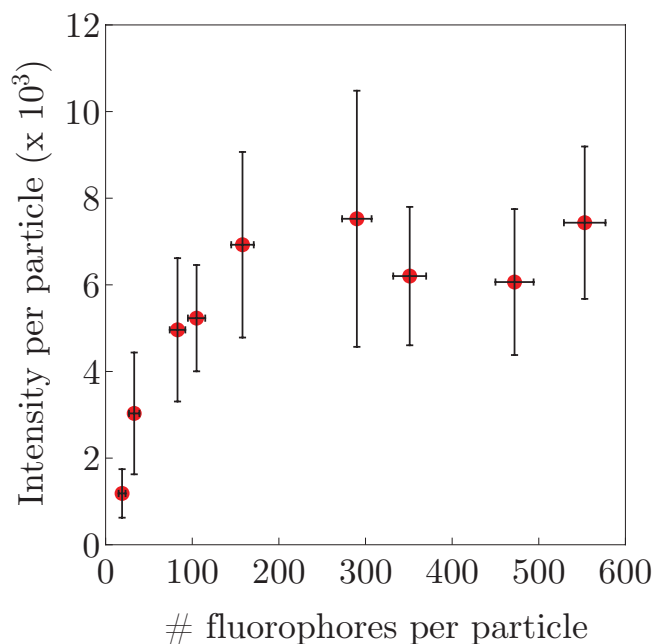


Figure 2.13: Average single particle intensity plotted as a function of the estimated number of fluorophores per particle. The standard deviation in this plot corresponds to the standard deviation of the normal distribution that was fitted to the data to obtain the mean intensity.

From the normalized bleaching curves in figure 2.14 it can be seen that bleaching rate strongly depends on the fluorophore labelling density. Generally speaking, the bleaching rate reduces when the number of fluorophores per particle increases. As explained in section 2.3, a possible explanation for this is that the degree of self-quenching reduces when more and more fluorophores are bleached. This explanation is partially confirmed by the radiative decay measurements that are included in figure 2.15. These measurements demonstrate that the shortened fluorescence lifetime of all particles recovers over the course of bleaching. This effect becomes more and more pronounced with increasing labelling density as the degree of self-quenching is higher for these particles. The easiest way to understand this effect, is by considering bleaching as the removal of a fluorophore. These measurements however prove that quenched fluorophores are still contributing to the degree of quenching as the increase or recovery in the fluorescence lifetime flattens out over the course of bleaching.

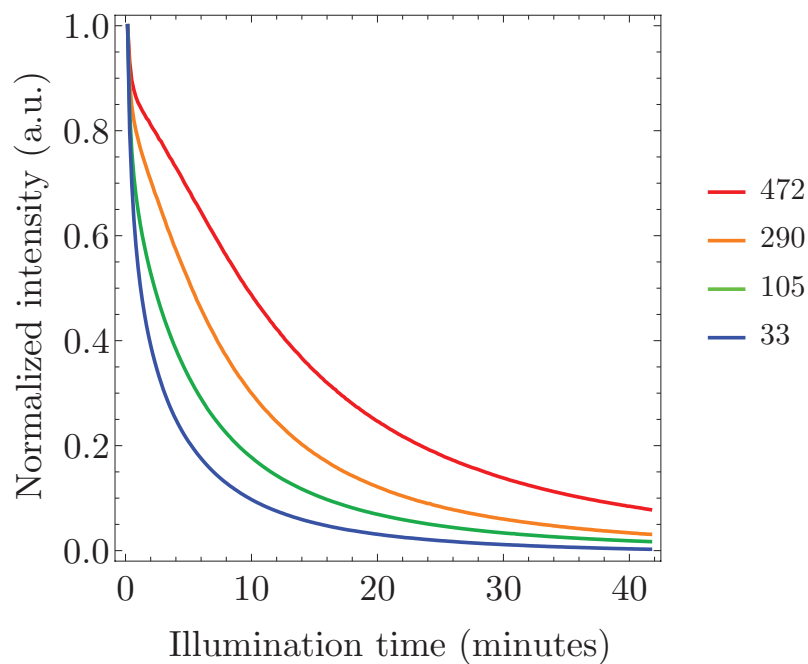


Figure 2.14: Normalized bleaching curves measured at an excitation intensity of 6.0 W cm^{-2} . The numbers in the legend corresponds to the estimated number of fluorophores per particle.

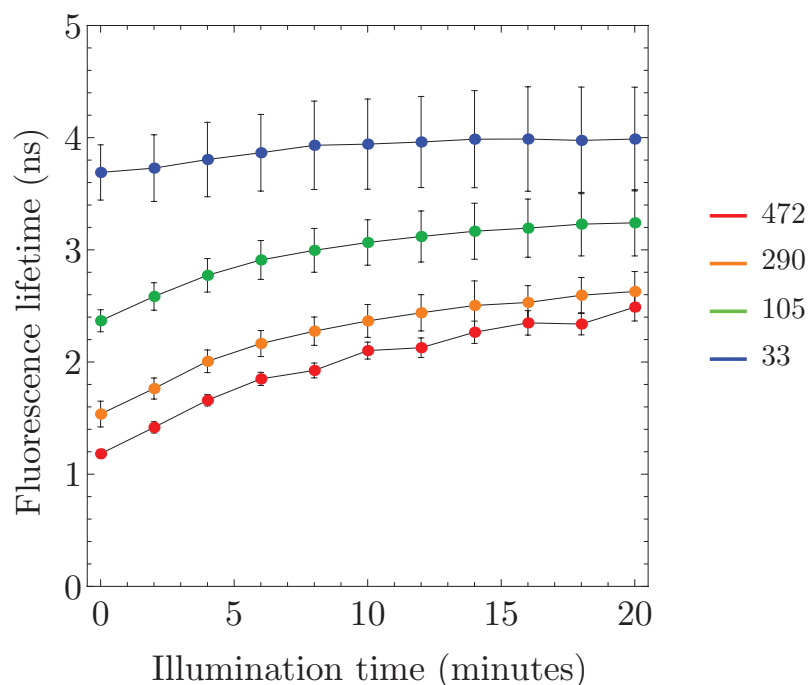


Figure 2.15: Average decay times plotted as a function of the bleaching time. The conditions that were used for bleaching closely match the conditions that were used to obtain the bleaching curves included in figure 2.14. The numbers in the legend corresponds to the estimated number of fluorophores per particle.

2.7.5 Simulations

The amplitude of the Dexter energy transfer turned out to be the parameter with the biggest impact on the simulations. Values between $A = 100$ and 250 gave acceptable results. The example presented in this section is based on a value of 150 . The other two parameters that were varied are both related to the dimers, the equilibrium constant for dimer formation and the fluorescence lifetime of the dimers. These parameters both affect the average simulated lifetime, but much less strongly than A . Their effect mainly shows up in the shape of the fluorescence decay curves. Here, a value for the equilibrium constant of $3.3 \cdot 10^{-3}$ and a lifetime of 0.4 ns for the dimers gave good agreement for the fluorescence decay curves. For this equilibrium constant a particle containing 553 dye molecules is expected to have ~ 165 dimers and ~ 223 monomers. This sizable number of dimers is expected from the clearly visible dimer contribution in the emission spectrum in figure 2.11. We note that the dimer fluorescence lifetime of 0.4 ns corresponds with a quantum efficiency of ~ 0.08 .

Figure 2.16 shows measured and simulated average fluorescence lifetimes as a function of the number of fluorophores per particle. Overall, there is reasonable agreement between the measurements and the simulations.

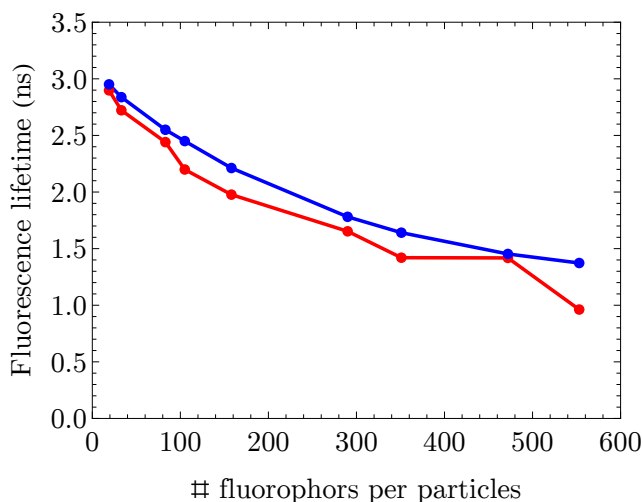


Figure 2.16: Measured (red) and simulated (blue) average fluorescence lifetimes as a function of the number of fluorophores per particle. In the simulations, single exponential decay of rhodamine B with a fluorescence lifetime of 3.2 ns and a quantum efficiency of 0.6 was assumed. The equilibrium constant for dimer formation and the lifetime of the dimers were fixed at $3.3 \cdot 10^{-3}$ and 0.4 ns. The amplitude of the Dexter transfer, A , was fixed at 150 .

In figure 2.17, the simulated and measured radiative decay curve of particles with an estimated number of fluorophores of 553 is shown. The input parameters as indicated above were used in the simulations. The correspondence is very good. Here, it was essential to convolute the simulated decay curves with the instrument response function of the setup.

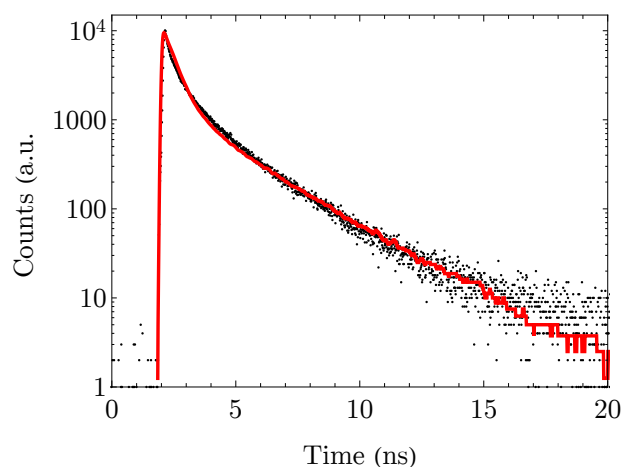


Figure 2.17: Measured (dots) and simulated (drawn) radiative decay curves of particles with an estimated number of fluorophores of 553 per particles. The simulated curve was convoluted with the experimental IRF. The input parameters listed in figure 2.16 were used for the simulation.

The simulations also yield the number of energy transfer steps before a photon is emitted. In figure 2.18, the number of energy transfer steps is shown for $A = 150$, with and without the presence of dimers. Without dimers, the number of energy transfer steps rapidly increases with the number of fluorophores per particle. In the presence of dimers, however, the increase in the number of energy transfer steps is very limited and levels off.

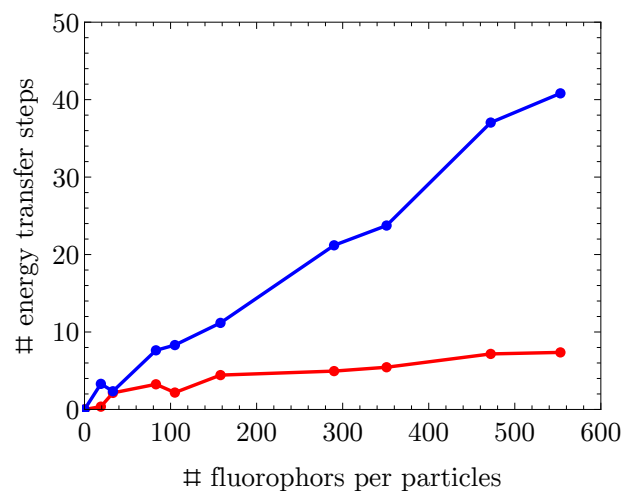


Figure 2.18: Simulated number of energy transfer steps with (red) and without (blue) the presence of dimers as a function of the number of fluorophores per particle. The input parameters listed in figure 2.16 were used for the simulations.

2.8 Conclusion & Outlook

Monodisperse and spherical core-shell-shell silica particles with different fluorophore labelling densities were successfully synthesized. These particles consist of a 27 nm diameter non-fluorescent core and were coated with a rhodamine B labelled silica layer to obtain a total diameter of ~ 83 nm. The number of fluorophores within this shell varied from 19 for the lowest labelling density to 553 for the highest labelling density. This corresponds to an average fluorophore-to-fluorophore separation from 24.0 to 7.7 nm. For stabilization an additional non-fluorescent layer was added to obtain a total diameter of ~ 100 nm.

Spectral and radiative decay measurements revealed clear indications for labelling density effects. First of all, the spectral measurements reveal that more and more dimers are formed when the labelling density becomes higher. This is accompanied by a decrease in the fluorescence lifetime of the fluorophores which is indicative for quenching. This increased quenching is confirmed in the single particle intensity measurements. At first, the fluorescence intensity increases linearly with increasing fluorophore labelling density as the number of fluorophores per particles becomes higher. However, below an average separation of ~ 15 nm the relationship between the number of fluorophores and the fluorescence intensity become (strongly) non-linear. Now, the addition of fluorophores is counter-balanced by an increase in fluorescence quenching as a result of concentration- or self-quenching.

The rate at which fluorophore are bleached also shows a strong dependence on the labelling density. Generally speaking, a reduction in the bleaching rate with increased labelling densities was observed. Radiative decay measurements confirmed that the degree of self-quenching decreases over the course of bleaching, thereby confirming that bleaching is partially counterbalanced by a decrease in fluorescence quenching.

Simulations were conducted to better understand the observed labelling density effects. Radiative decay, non-radiative decay, homo-FRET, quenching via Dexter energy transfer and dimer formation were all taken into consideration in these simulations. Despite the complexity of the system, it proved to be possible to reproduce the radiative decay curves, and radiative decay times of the fluorescently labelled particles. The simulations thereby confirm that a combination of energy transfer via homo-FRET, Dexter quenching and dimer formation can account for the observed labelling density effects.

The number of energy transfer steps that occurred within a particle before a photon is emitted could also be deduced from these measurements. This number showed a very strong dependence on the number of dimers present in the particles. In the absence of dimers, the number of energy transfer steps rapidly increases when the number of fluorophores inside a particles increases. In the presence of dimers the number of steps is limited and levels off.

The most important recommendation for future research is to expand the simulations included in this chapter. As a starting point, one could for example try to reproduce the relationship between the labelling density and the single particle intensity. From there on, also the relationship between the bleaching rate and the labelling density can be theoretically studied. Such data can be used for example to determine optimum labelling densities of rhodamine B in different host materials.

In the result presented in this chapter, the simulations were performed repeatedly to determine the input parameters that resulted in good agreement between measurements and simulations. The development of methods to predict the input parameters for the simulations is therefore another important recommendation for future research. By developing methods to for example determine how the Dexter amplitude, A , varies from fluorophore to fluorophore it would be possible to develop a model that is applicable to a great variety of fluorophores.

2.9 Acknowledgements

First of all, I would like to thank and acknowledge Hans Gerritsen for the simulations included in this chapter. I also thank Dave van den Heuvel for his help with the radiative decay, the single particle intensity and the bleaching measurements. I am also grateful for Daves valuable input on the topics presented in this chapter. Finally, I thank Dave van den Heuvel, Gerhard Blab and Hans Gerritsen for critical reading of the chapter.

Fluorescently Labelled Silica Coated Gold Nanoparticles as Fiducials

In this chapter, gold nanoparticles coated with a fluorescently labelled (rhodamine B) silica shell are presented as fiducial markers for Correlative Light and Electron Microscopy (CLEM). Prior to the synthesis of the fiducial markers, the distance dependency of the influence of the gold nanoparticles on the fluorophores incorporated in the silica shell is studied. This study shows that the influence of the gold can be neglected when the separation between the fluorophores and the gold core is large enough (>15 nm). Next, the synthesis of the fluorescently labelled gold particles is optimized to obtain homogeneous, spherical core-shell particles of arbitrary size. Particles labelled with different fluorophore densities are characterized to determine under which conditions bright and (photo)stable particles are obtained. 2D and 3D CLEM examples are presented where optimized particles are used for correlation. In the 2D example, fiducials are added to a cryosection of cells whereas in the 3D example cells are imaged after endocytosis of the fiducials. Both examples demonstrate that the particles are clearly visible in both modalities and can be used for correlation. Additionally, the recognizable core-shell structure of the fiducials proves to be very useful in electron microscopy: it makes it possible to irrefutably identify the particles and makes it easy to accurately determine the center of the fiducials.

3.1 Introduction

The field of Correlative Light and Electron Microscopy, or CLEM, has expanded rapidly during the last decade. Especially in biology it turns out to be very useful to combine these two techniques. Light microscopy or Fluorescence Microscopy (FM) is used to visualize, localize, and track specific fluorescent molecules in cells over large areas with high sensitivity, while Electron Microscopy (EM) provides high resolution ultra-structural information of cells and materials [11, 64]. This opens up the possibility to visualize rare transient events or specific cells within complex tissues [5, 6].

For the best results in CLEM experiments, data from the different modalities should be registered with the highest possible precision. This is complicated by the vastly different fields of view of FM and EM, as well as the different contrast mechanisms of these techniques. FM requires bright and stable fluorophores, while EM relies on differences in electron density for contrast, and frequently requires heavy metal staining to visualize biological structures. Since fluorescent probes (i.e. molecules, proteins) are typically not electron dense, fluorescent labels can generally not be used for correlation.

Particles visible in both modalities (fiducial markers) can be used to overcome this problem. The viability of this approach has been demonstrated in literature by using fluorescent latex beads [65, 66, 67] or quantum dots [68, 69, 70]. However, a shared problem of these candidate particles is their relatively low EM contrast, making visualization and localization in heavily EM stained samples difficult or even impossible. An alternative approach to register data between modalities is via a double labelling procedure. Here, proteins of interest are labelled with a fluorescent probe, followed by labelling with antibodies or protein A conjugated with colloidal gold [71]. A disadvantage of this approach is that correlation is indirect and based on the assumption that both labels fully colocalise. Despite great successes achieved by this approach, Miles *et al.* [72] and van Elsland *et al.* [73] recently demonstrated that this assumption not always holds true, thereby stressing the importance of finding a more direct way for registering FM and EM data.

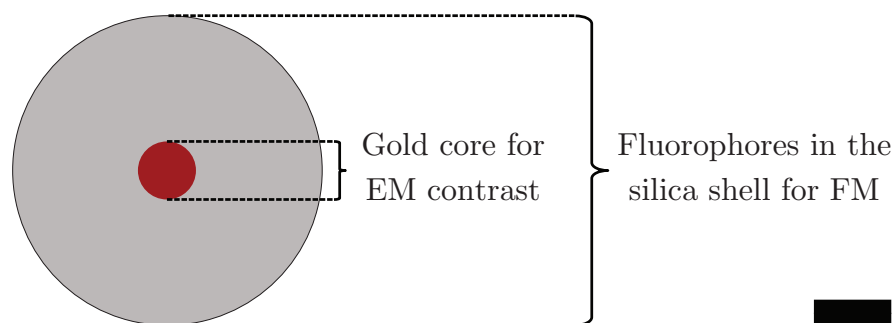


Figure 3.1: A schematic representation of the here presented fiducial markers. The scale bar indicates 20 nm.

In this chapter, nanocomposite core-shell particles based on a gold core and a fluorescently labelled silica shell (figure 3.1) are deployed as fiducial markers. The gold core provides contrast for EM and fluorophores covalently incorporated in the silica

shell provide fluorescence for FM. Rhodamine B is chosen as fluorophore because it was demonstrated by Karreman *et al.* [74] that rhodamine like fluorophores behave well under the dry and vacuum conditions encountered in EM. Using a red emitting fluorophore is also advantageous because excitation at longer wavelengths results in reduced autofluorescence [75].

Before the fiducials are presented, the distance dependency of the interactions between the gold core and the fluorophores incorporated in the silica shell is studied. This is important as the presence of the gold core can result in quenching of fluorescence. Core-shell-shell particles based on a gold core, a non-fluorescent silica shell and a fluorescently labelled silica shell are specifically designed and synthesized for this. In this geometry, the non-fluorescent silica layer is used as a spacer between the gold core and the fluorescently labelled silica layer. Next, to obtain the fiducials, an optimized synthesis of the nanocomposite particles to obtain spherical and highly monodisperse core-shell particles of arbitrary size is presented. A thorough study is performed to optimize the fluorophore labelling density within the silica shell to obtain bright and (photo)stable particles. Finally, particles labelled with this optimum fluorophore labelling density are tested as fiducials in a 2D and a 3D CLEM experiment.

3.2 Experimental details

3.2.1 Synthesis of the nanocomposite gold-silica particles

In this section, the synthesis and characterization of the particles that are presented throughout this chapter is described. Next, a description of the 2D and 3D CLEM experiments that were conducted to test the particles as fiducial markers is included.

Materials

Hydrogen tetrachloroaurate(III)trihydrate or chloroauric acid (ACS reagent) and sodium hydroxide pellets were obtained from ACROS Organics. Sodium citrate tribasic dihydrate, sodium silica solution (wt 26.5% in water) or water glass, amberlite cation exchange resin, tetraethyl orthosilica or TEOS (reagent grade, 98%), ammonium hydroxide solution (ACS reagent, 28-30% NH_3 basis), rhodamine B isothiocyanate (mixed isomers) or RITC, 99% (3-aminopropyl)triethoxysilane or APTES, polyvinylpyrrolidone or PVP (Average Mw 10.000 g mol⁻¹), dialysis tubing cellulose membrane (av. flat width 33 mm) and Vivaspin 20 centrifugal concentrator tubes (MWCO 100.000 Da) were purchased from Sigma-Aldrich. Absolute ethanol was purchased from Merck.

All glassware and stirring beans used for the gold synthesis were rinsed with aqua regia and mili-Q water prior to use. All remaining glassware was extensively cleaned with soap, water and ethanol prior to use. Milli-Q water was used in all the experiments.

Synthesis of 15 nm diameter citrate stabilized gold particles

All gold particles presented in this chapter were synthesized via the extensively studied citrate reduction or Turkevich method [76, 77], see figure 3.2. Particles obtained via this procedure are spherical, charge (citrate) stabilized and have a diameter of approximately 15 nm.

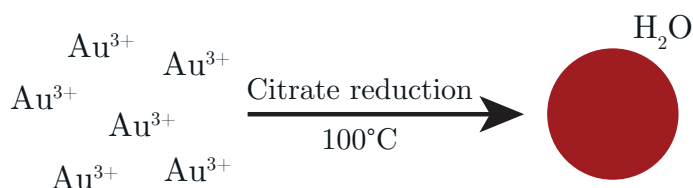


Figure 3.2: A schematic representation of the synthesis of the gold nanoparticles.

Gold and citrate stock solutions were prepared by transferring 0.1 g chloroauric acid and 0.1 g sodium citrate to two separate vials. 10 mL water was added to both vials to obtain 1% (w/v) stock solutions. In a typical synthesis, 300 mL water and 3 mL of the 1% (w/v) gold solution were transferred to a two necked round bottomed flask equipped with a condenser. This flask was placed in a 140°C oil bath to ensure homogeneous heating and was heated until boiling under constant vigorous stirring (600 rpm). When boiling commenced, 9 mL of the 1% (w/v) sodium citrate solution

was added. Within the first few minutes after the sodium citrate addition, the color of the solution gradually changed from blue to purple to deep red indicating particle formation. After 15 minutes boiling no change in color was observed anymore and the deep red solution was cooled down to room temperature.

Particles to study gold-fluorophore interactions

To study distance dependent gold-fluorophore interactions, the previously obtained citrate stabilized gold particles were coated with a very thin and dense silica layer following the procedure by Liz-Marzán *et al.* [78]. Next, a seeded growth procedure was used to coat these particles with a non-fluorescent and a rhodamine B labelled silica layer, see figure 3.3. The non-fluorescent silica layer in this core-shell-shell geometry was used as a spacer layer. By varying the thickness of this layer the distance dependency of the gold fluorophore interactions were studied.

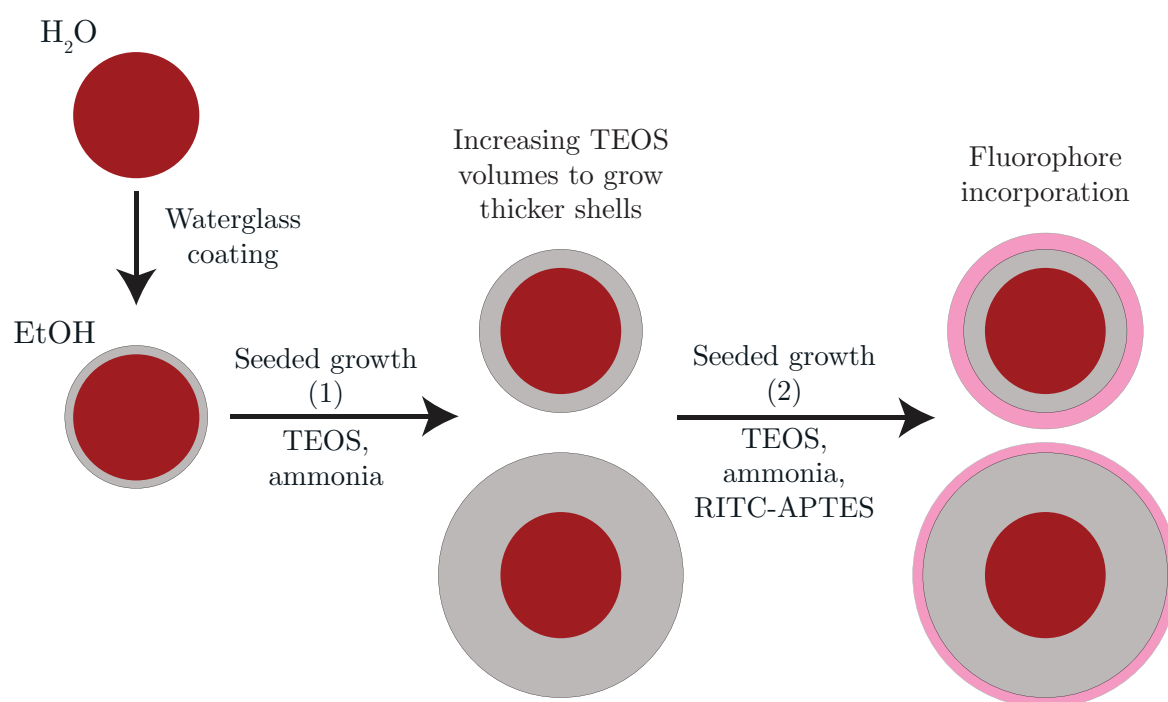


Figure 3.3: A schematic representation of the synthesis of the rhodamine B labelled silica coated gold nanoparticles to study distance dependent gold-fluorophore interactions. By varying the amount of silica precursor, TEOS, added in the first seeded growth steps, the thickness of the non-fluorescent silica layer, and thereby the spacing between the gold core and the fluorescently labelled silica layer, was varied.

Prior to the first silica coating step, the gold particles were APTES functionalized by transferring 25 mL citrate stabilized gold particles and 187.5 μL of a 1 mM solution of APTES in water to a vial. The obtained solution was stirred to ensure complete complexation of the amine groups with the gold surface. After 30 minutes, a solution

of active silica was prepared by lowering the pH of a 0.53 wt% sodium silica solution in water to 10-11 by progressive addition of amberlite cation exchange resin. pH indicator paper was used to check the pH between additions. 750 μL of the obtained solution was added to the 25 mL of APTES functionalized gold nanoparticles under constant stirring. After one minute, the obtained solution was allowed to stand, so that the active silica could polymerize onto the particles. After 16 hours, the solution was centrifuged 15 minutes at 15.000 rcf in 5 mL eppendorf tubes. The supernatant (water) was removed and the particles were redispersed in an equal amount of ethanol. Homogenization of the solution was ensured by placing the obtained solution in a sonication bath (~ 1 minute).

Prior to the silica shell growth, APTES-dye coupling was performed by transferring 10 mg RITC and 1 mL absolute ethanol to a vial. This solution was stirred and 8.3 μL APTES was added. The vial was wrapped in aluminum foil to protect the fluorophore from photobleaching and stirred for 16 hours. Next, 2.4 mL of the gold particle solution in ethanol was transferred to vials A-G. Under constant stirring, 100 μL ammonia was added to all solutions followed by the addition of various amounts (0-200 μL) of 10 vol% TEOS solutions in ethanol to grow the non-fluorescent silica shell. After 90 minutes, 20 μL of 10 vol% TEOS solution in ethanol and 20 μL of a ten times diluted solution of the APTES-RITC solution in ethanol was added to the particles to grow the rhodamine B labelled silica layer. 90 minutes after this addition, the particles were cleaned by repeated centrifugation and redispersion in ethanol to remove all non-incorporated rhodamine B from the solution.

Synthesis of the fiducial markers

To synthesize the fiducial markers, the citrate stabilized gold particles were coated with a nonionic polymer, polyvinylpyrrolidone or PVP, so that they could be transferred into ethanol following the procedure described by Graf *et al.* [79]. Once the particles were transferred to ethanol, they were coated with a fluorescently labelled silica shell via a seeded growth procedure similar to the procedure described by H. Giesche [48, 49]. This seeded growth procedure is based on the traditional Stöber method [80] to synthesize silica particles of a specific size obtained via the addition of silica precursor, TEOS, to mixtures of water, ammonia and alcohol.

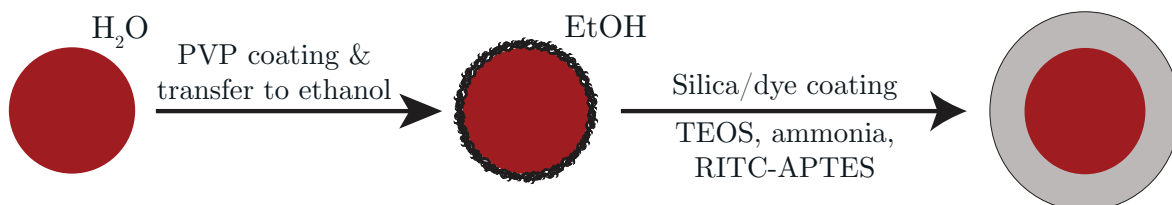


Figure 3.4: A schematic representation of the synthesis of the (rhodamine B labelled) silica coated gold nanoparticles.

Fluorescent dyes were covalently incorporated within the silica matrix during shell growth following the procedures described by A. Imhof *et al.* [27] for fluorescein isothiocyanate (FITC) and Verhaegh *et al.* [81] for rhodamine B isothiocyanate (RITC). Covalent incorporation is ensured by linking a fluorophore with an active amine reactive group such as an isothiocyanate group with an aminosilane; (3-aminopropyl)triethoxysilane or APTES. After coupling, this complex was introduced during the silica shell growth and part of it was incorporated within the silica shell.

For PVP functionalization of the gold particles, 120 μL of a 10 vol% (w/v) PVP solution (1 g in 10 mL water) was added per 5 mL of gold nanoparticle solution under constant stirring. The obtained solution was stirred for at least 12 hours to ensure functionalization of the gold nanoparticles. After 12 hours, the solution was centrifuged 15 minutes at 15.000 rcf in 5 mL eppendorf tubes. The supernatant (water) was removed as much as possible with a glass pipette and the particles were redispersed in an equal amount of ethanol. Homogenization of the sample was ensured by placing the obtained solution in a sonication bath (~ 1 minute).

APTES-dye coupling was performed by transferring 10 mg RITC and 1 mL absolute ethanol to a vial. This solution was stirred and 8.3 μL APTES was added. The vial was wrapped in aluminum foil to protect the fluorophore from photobleaching and stirred for 16 hours. The APTES-dye ratio during this coupling reaction was calculated such that there was a two times excess of APTES compared to the amount of fluorophore. Different dilutions of this dye solution in absolute ethanol were used to synthesize particles labelled with different dye labelling densities. Solutions with relative dye concentrations ranging from 0 to 30 (labelled as [Dye] = 0 - 30) were prepared by preparing dilutions of 0 to 30 vol% of APTES-dye solution in ethanol. For example, to obtain a relative dye concentration of 30, 300 μL APTES-dye solution (30 vol%) and 700 μL absolute ethanol (70 vol%) were transferred to a vial.

To coat the gold particles with a fluorescently labelled silica shell, 15 mL solution of PVP stabilized gold nanoparticles was transferred to a 20 mL closed vial. Under continuous stirring (700 rpm), 1500 μL 28-30% ammonium hydroxide solution was added to this solution. Next, 30 μL of a 10 vol% of TEOS solution in absolute ethanol was added to grow a first, very thin, silica layer. This layer helps to stabilize the particles since the immediate addition of APTES-dye solution results in the formation of clusters of gold nanoparticles. This layer also serves as a spacer layer between the gold cores and the fluorophores embedded in the silica shell. 60 minutes after the first TEOS addition an additional 150 μL of the 10 vol% TEOS solution was added. After approximately one minute of stirring, 150 μL of diluted APTES-dye solution was added as well. Both additions were repeated with 300 μL after 90 minutes of stirring. Finally, after another 90 minutes, 60 μL of 10 vol% TEOS was added to grow a final stabilization layer around the fluorescently labelled particles. 60 minutes after the final addition, the reaction mixture was transferred to a dialysis bag that was placed inside a 40 mL vial filled with ethanol. The solution was gently stirred and the ethanol was replaced three times over a time span of 36 hours. Further cleaning of the particles was performed via repeated centrifugation in 100.000 MWCO vivaspin tubes.

3.2.2 Characterization of the particles

Determination of the fluorophore incorporation efficiency

Immediately after synthesis of the particles, 3 mL of the reaction mixture was transferred to a 5 mL eppendorf tube. This solution was centrifuged 15 minutes at 15.000 rcf to separate the particles from the reaction mixture. The supernatant or reaction mixture, that contained all non-incorporated rhodamine B, was collected and stored. The particles were redispersed in 3 mL absolute ethanol and centrifugation and redispersion in ethanol was repeated two more times. 1.5 mL particle solution and 1.5 mL of a 0.4 M sodium hydroxide solution in water were transferred to a clean 5 mL eppendorf tube. After homogenization, solutions were stored for 48 hours to ensure complete dissolution of the silica shell of the particles. Next, the solutions were centrifuged 30 minutes at 20.000 rcf to remove the non-dissolved gold cores from the solution. Solutions ranging from transparent and colorless for the blanco ($[Dye] = 0$) to transparent pink for high labelling densities ($[Dye] = 30$) were separated from the red to black pellets and stored. Absorption spectra of all solutions were recorded on a HP8953A spectrophotometer in 1 cm quartz cuvettes. If necessary, samples were diluted with a 1:1 (volume) mixture of ethanol and 0.4 M sodium hydroxide solution.

Spectral and radiative decay measurements

Bulk excitation and emission spectra and radiative decay measurements of the particles suspended in ethanol were recorded in 1 cm quartz cuvettes using an Edinburgh Instruments FLS920 fluorescence spectrometer. In all measurements, fluorescence was detected at an angle of 90° to the exciting beam. Furthermore, a 530 nm longpass filter was placed between the sample and the detector in all measurements to remove residual excitation light. To record excitation and emission spectra, a 450 W xenon lamp and a double excitation monochromator with a grating blazed at 500 nm was used for excitation. Spectra were recorded with a Hamamatsu H74220-60 photo sensor module with a grating blazed at 500 nm. For the radiative decay measurements a picosecond pulsed diode laser (EPL-515) emitting at 509.8 nm with a 50 ns pulse period and a 204.4 ps pulse width was used for excitation. Radiative decay curves were recorded with a Hamamatsu R928 PMT detector with a grating blazed at 500 nm.

Single particle measurements

Measurements were carried out on a Nikon Eclipse Ti widefield microscope equipped with a 40x 0.75 NA Nikon air objective. A Nikon TI-ND6-PFS perfect focus unit was used to retain sample focus during the measurements. A mercury arc lamp in conjunction with a 510-560 nm excitation filter, a 565 nm long pass dichroic mirror and a 590 nm long pass emission filter ensured proper illumination and detection wavelengths. An excitation intensity of 6.0 W/cm^2 was used in all experiments. Finally, an Andor NEO sCMOS camera was used to record images. Single particle intensities were determined using ThunderSTORM [50]. For the single particle intensity measurements, the obtained data was directly analyzed in Mathematica. To obtain the average sin-

gle particle intensities, for every sample, data obtained from at least 20 images was plotted in a histogram. The first peak in this histogram was attributed to the single particle intensity and a normal distribution was fitted to this peak to obtain the mean intensity and the standard deviation. For the bleaching measurements, a second analysis was performed in MatLab to trace the intensity of single particles from frame to frame. Furthermore, the data was filtered based on the single particle intensities determined from the first frame to remove clusters from the data set. The filtered data was averaged per frame to obtain bleaching curves.

3.2.3 CLEM experiments

Cell culture

HeLa cells and HT1080 cells stably expressing LAMP-1-GFP were cultured in a 37°C, 5% CO₂ incubator, in T75 culture bottles (Corning). Cells were maintained in Dulbecco's Modified Eagle's Medium (DMEM; Gibco) supplemented with 10% fetal bovine serum, 2 mM L-glutamin, 100 U/mL penicillin, 100 µg/mL streptomycin (referred to as complete DMEM). Cells were passaged when confluency reached 85% to 90%.

2D CLEM: Widefield and TEM imaging of fiducials on thin cryosections

HT1080 cells stably expressing LAMP-1-GFP were incubated in complete DMEM containing 5 nm diameter colloidal gold particles conjugated to bovine serum albumin (BSA-Au⁵) for 3 hours. Following incubation, cells were processed for cryosectioning according to previous protocol [82]. Briefly, cells were chemically fixed using formaldehyde and glutaraldehyde, scraped from the culture substrate and pelleted in 12% gelatin. Samples were infiltrated overnight in 2.3 M sucrose for cryoprotection, and plunge frozen in liquid nitrogen. 70 nm thick cryosections were sectioned and picked up on copper support grids coated with formvar and carbon. Sections were treated with DAPI (4 µg/mL) diluted in PBS to label nuclei. After labelling, sections were washed with PBS, incubated with a diluted solution (1/500) of the fiducial markers in water, followed by rinses with PBS and dH₂O. The grids were sandwiched between a microscope slide and a #1.5 coverslip in a drop of 50% glycerol in dH₂O. Fluorescence imaging for DAPI, GFP and the fluorescent nanoparticles was performed with a Deltavision RT Core widefield microscope (GE Healthcare) equipped with a Cascade II EM-CCD camera (Photometrics), using a 100x/1.4 NA objective. Following fluorescent imaging, the sections were washed in dH₂O, stained with uranyl acetate and embedded in methylcellulose as previously described [82]. ROIs determined in FM were retraced and imaged in a Tecnai T12 TEM (Thermo Scientific). Following imaging, the x and y positions of the fiducials in fluorescence data were registered using ThunderSTORM [50]. Fiducials not properly resolved in ThunderSTORM were not considered as reference points for registration of data. In TEM data, positions of the fiducials were registered manually using the center of the gold core. Correlation of fluorescence and TEM data based on the positions of the particles was performed using eC-CLEM [83].

3D CLEM: Confocal and FIB-SEM imaging of endocytosed nanoparticles

HeLa cells were grown on gridded glass coverslips, prepared as described by Fermie *et al.* [84]. Cells were incubated with fiducial markers at a concentration of 1 $\mu\text{g}/\text{ml}$ dissolved in complete DMEM and incubated for 3 hours, and fixed overnight in 1x PHEM buffer (60 mM PIPES, 25 mM HEPES, 10 mM EGTA, 2 mM MgCl_2 , pH = 6.9) containing 4% paraformaldehyde (Sigma) and 0.1% glutaraldehyde (Merck) at 4°C. Following fixation, coverslips with cells were washed in 1x PHEM buffer and mounted in live-cell coverslip holders filled with 1x PHEM buffer to prevent dehydration of the samples. Fluorescence imaging was performed using a Zeiss LSM700 CLSM equipped with 63x/1.4 NA oil immersion objective. Nanoparticles were excited using the 555 nm laser line at 2% power. Z-stacks were collected with 200 nm step size. The position of cells relative to the grid of the coverslips was recorded using polarized light. Cells were prepared for electron microscopy according to a protocol described earlier [85], with minor modifications. Briefly, samples were postfixed using 1% osmium tetroxide (w/v) with 1.5% potassium ferrocyanide (w/v) for 1 h on ice, incubated with 1% thiocarbonylhydrazide in dH_2O (w/v) for 15 min, followed by 1% osmium tetroxide in dH_2O for 30 min. Samples were en-bloc stained with 2% uranyl acetate in dH_2O for 30 minutes and stained with Waltons lead aspartate for 30 min at 60°C. Dehydration was performed using a graded ethanol series. Samples were embedded in Epon resin and polymerized for 48-60 h at 65°C. Polymerized resin blocks were removed from the glass coverslips using liquid nitrogen, mounted on aluminum stubs and rendered conductive using conductive carbon paint and a sputter coated layer of 5 nm Pt. Following sample preparation, automated serial imaging was performed using a Scios FIB-SEM (Thermo Scientific), according to a previously described workflow [84]. Briefly, trenches were prepared surrounding the region of interest using the FIB, after which automated serial imaging was performed using 5 nm isotropic voxels. Electron microscopy images were collected at an acceleration voltage of 2kV and a current of 0.2 nA, using the T1 backscattered electron detector. Following imaging, correlation of fluorescence and FIB-SEM data was achieved by manual registration using Fiji and eC-CLEM [83]. FIB-SEM images are presented with inverted contrast, to resemble TEM contrast.

3.3 Results

3.3.1 Distance dependent gold-fluorophore interactions

In figure 3.5 TEM images of the as-synthesized gold particles after growth of the first non-fluorescent silica layer are included. From these images it can be seen that the gold particles are homogeneously coated with a very thin silica layer. The gold particles have an average diameter of 17 nm and the thickness of the first silica layer is approximately 4 nm.

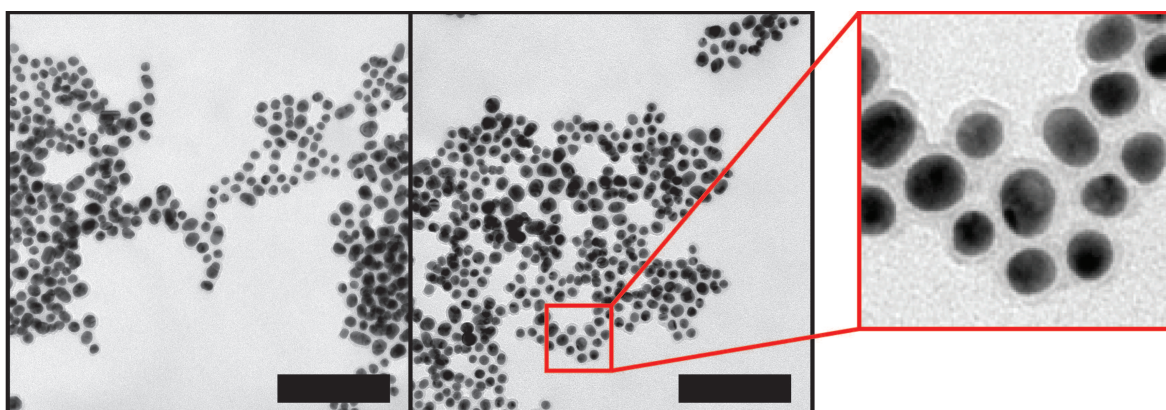


Figure 3.5: Representative TEM images of gold particles after growth of a very thin silica layer. The scale bars indicate 200 nm.

TEM images of some of the samples after growth of the non-fluorescent and the rhodamine B labelled silica shell in ethanol are included in figure 3.6 a, b and c. From these images it becomes clear that the silica grows homogeneously and selectively on the existing particles (i.e. no secondary nucleation is observed). These images also demonstrate that particles of different sizes can be synthesized. After growth of the rhodamine B labelled silica shell around the particles in a, b and c the slightly larger particles included in d, e and f were obtained.

In figure 3.7 the thickness of the silica shell is plotted against the volume of added 10 vol% TEOS for samples A-G. In this figure, the red line corresponds to the shell thickness before growth of the rhodamine B labelled silica layer and the blue line corresponds to the shell thickness after growth of this layer. The shaded area between these two lines now corresponds to the rhodamine B labelled silica shell. This data was used to calculate the average distance between the gold core and the fluorophores incorporated in the silica shell. This average separation was found to range from 7.0 (A) to 23.3 nm (G) and is indicated by the black line in the figure. It is important to note that a homogeneous distribution of fluorophores throughout this silica shell is assumed for this calculation.

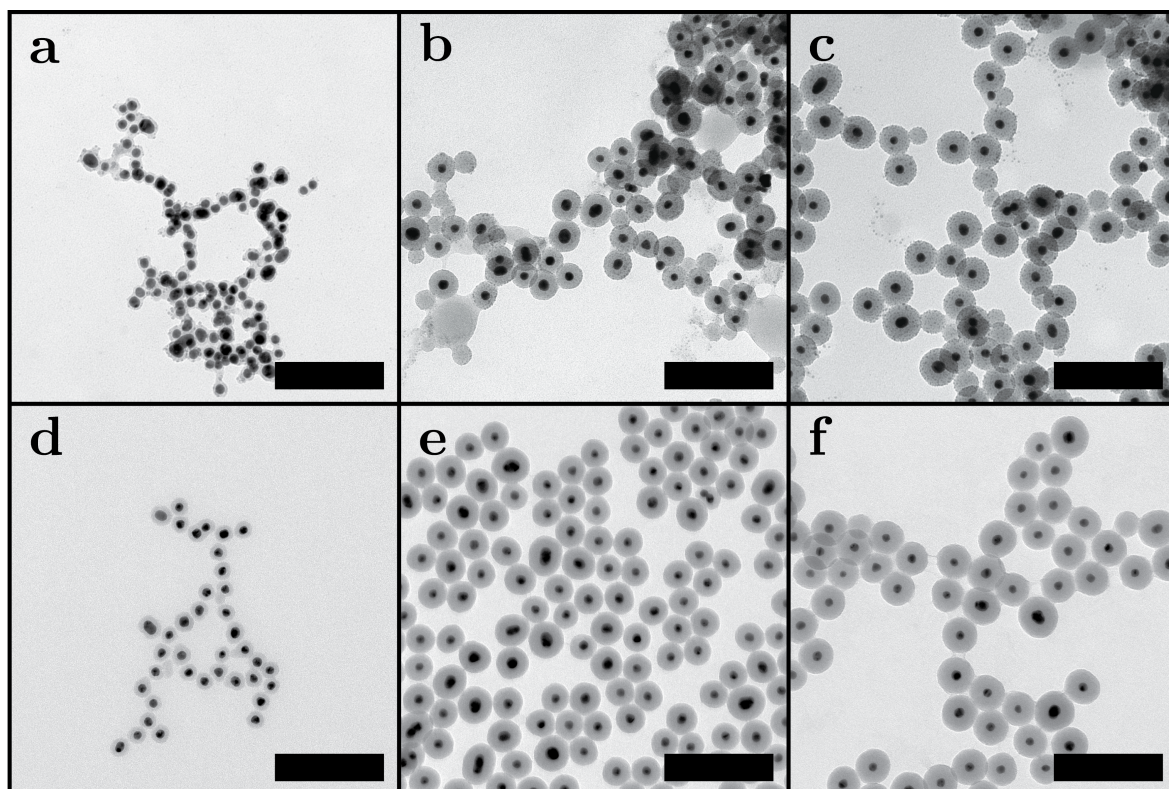


Figure 3.6: Representative TEM images of the gold particles after growth of the non-fluorescent silica layer (a-c) and growth of the rhodamine B labelled silica layer (d-f). The scale bars indicate 200 nm.

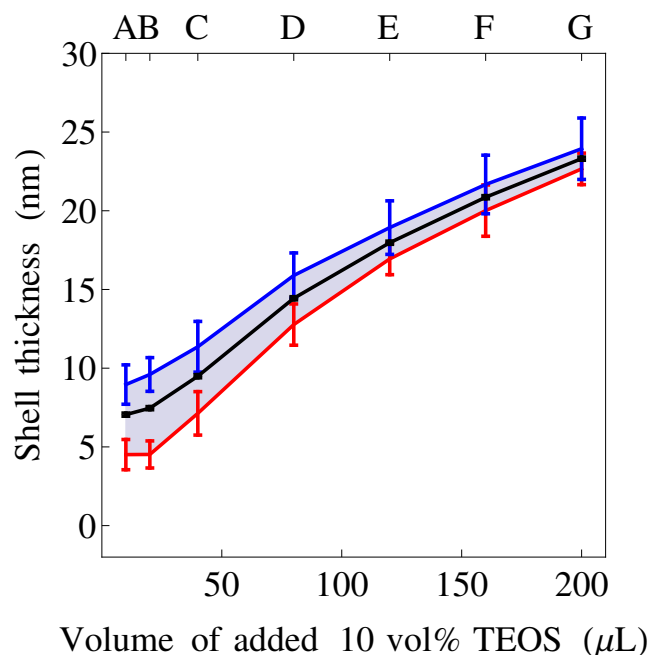


Figure 3.7: The average shell thickness of samples A-G is plotted versus the volume of added 10 vol% TEOS. Red and blue lines correspond to shell thicknesses before and after growth of the rhodamine B labelled silica layer. The black line corresponds to the average gold to fluorophore distance.

To determine whether the gold has any influence on the fluorophores incorporated in the silica shell, the excitation and emission spectra included in figure 3.8a were recorded. These measurements do not show any indications of any distance dependent influence of the gold core as no spectral changes are observed. This in line with expectations as quenching and/or enhancement of fluorescence by the gold core does not necessarily cause spectral changes.

The radiative decay curves included in figure 3.8b do reveal a distance dependency as faster decay curves are recorded when the average fluorophore to gold distance becomes shorter. The biggest effect is observed when the separation between the gold and the fluorophores is below 10 nm (red, orange and yellow curves). Above 18.0 nm no significant changes in the radiative decay curves are observed anymore. An explanation for this behavior can be found by taking in consideration the possibility of fluorescence quenching by the gold core. This quenching occurs because the energy of the excited fluorophore can be transferred non-radiatively to the gold particles when the distance between the two are in close proximity [86, 87, 88, 89].

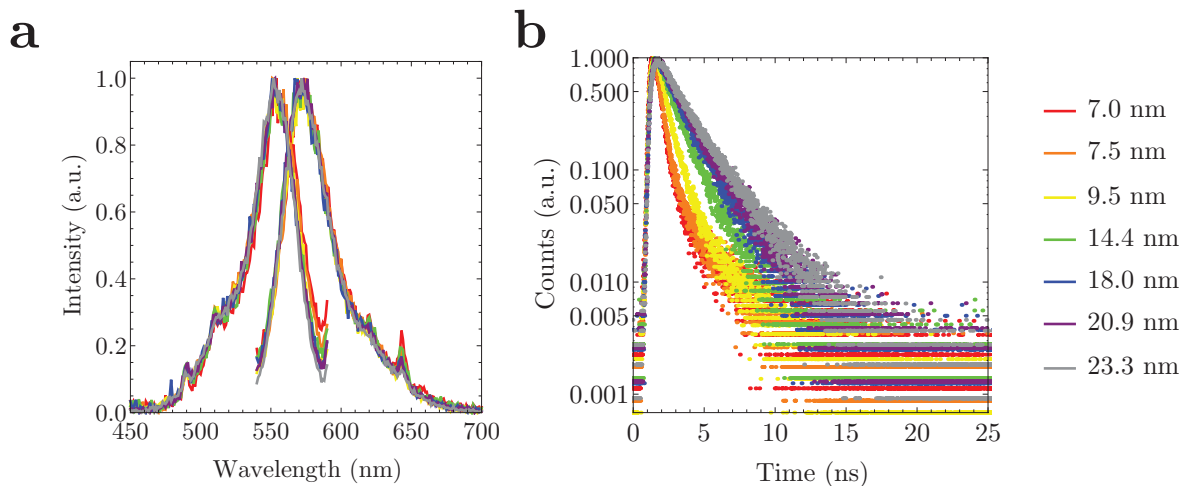


Figure 3.8: (a) Emission spectra recorded after excitation at 525 nm (right) and excitation spectra recorded at 600 nm (left). (b) Radiative decay curves after pulsed excitation at 509 nm and detection at maximum emission. The distances indicated in the legend correspond to the average distance between the edge of the gold core and the fluorophores incorporated in the silica shell.

It is beyond the scope of this thesis to fully characterize this distance dependent quenching. However, a brief explanation based on the work by Reineck *et al.* [86] is given because it is important to realize how severe quenching by the gold core can be. In this work the distance and spectral dependence of fluorescence quenching of fluorophores by similarly sized gold is studied. Similar gold-silica nanocomposite particles with fluorophores attached to the outer surface are used here to study the distance and spectral dependence of fluorescence quenching. It is experimentally and theoretically demonstrated that fluorescence is almost fully quenched for distances below 10 nm. Additionally, it is demonstrated that for a rhodamine B like fluorophore, ATTO565, quenching becomes negligible for gold to fluorophore distances above 20 nm, see figure 3.9. From this figure it can also be appreciated how well the relative intensity of the fluorophores scale with the relative fluorescence lifetime. This confirms that (more) shortening of the radiative decay curves corresponds to (more) quenching of fluorescence.

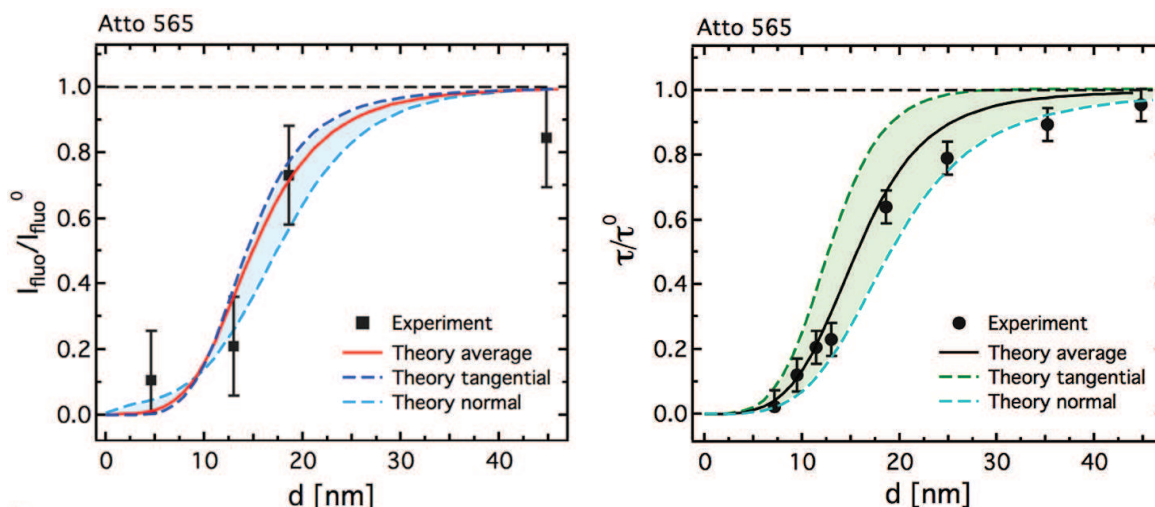


Figure 3.9: Experimental (black squares) and theoretical results (solid and dashed lines) for the relative fluorescence intensity (left) and the relative fluorescence lifetime τ/τ^0 (right) of Atto565 as a function of the nanoparticle-dye separation. Here τ^0 is the fluorescence lifetime of the dye molecule bound to a silica nanoparticle, which is slightly shorter than the lifetime of the free dye in solution (right). Images were taken from ref [86].

3.3.2 A calibration line to synthesize particles of a desired size

To synthesize particles of a desired size, a multistep silica coating of the gold nanoparticles was performed. Increasing volumes of TEOS were added to 5 mL of PVP functionalised gold nanoparticles in a solution of water, ammonia and absolute ethanol. 90 minutes after every addition, TEM samples were prepared, see figure 3.10.

From the TEM images it becomes clear that the silica shell is already homogeneous after the first TEOS addition (b). Furthermore, one can conclude that the thickness of the silica shell is increasing from (b) to (f) after every TEOS addition. Average particle diameters of all samples were determined by measuring the diameter of 100 particles, corresponding size histograms are presented in figure 3.11a.

In figure 3.11b the average particle diameters are plotted versus the cube root of the total volume of added 10 vol% TEOS. From this plot it becomes evident that there is a linear relationship between these two parameters after the first TEOS addition. This is in line with expectations since TEOS is converted directly into silica. Therefore, if silica grows only on the existing particles, there should be a linear relationship between the volume of added TEOS and the increase in volume of the particles. This linear relationship demonstrates that particles with every desired size can be synthesized with high control simply by varying the amount of added TEOS. From figure 3.11b it can be derived how much TEOS should be added to synthesize particles of a desired size starting from the same solution of gold particles.

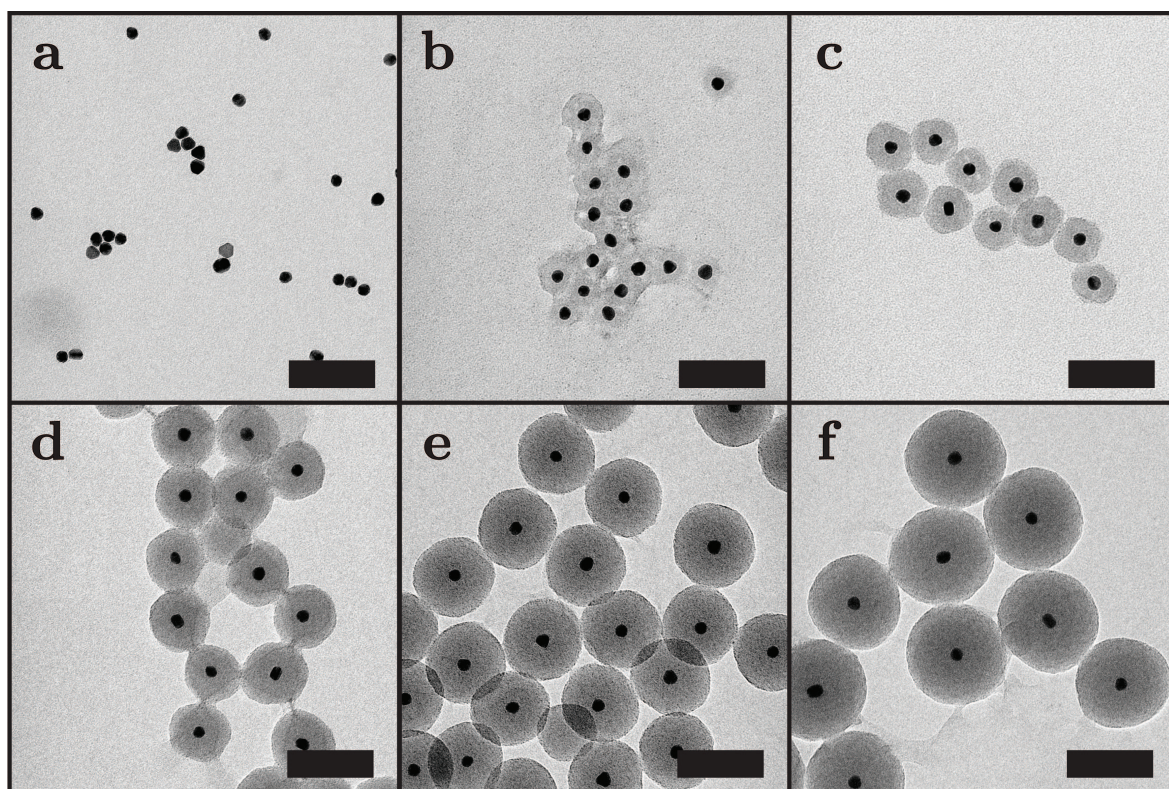


Figure 3.10: Representative TEM images of samples taken at different stages of silica coating. Sample (a) is prepared before TEOS addition. From (b) to (f) volumes of 20, 40, 80, 160 and 320 μL of 10 vol% TEOS are added. The scale bars indicate 100 nm.

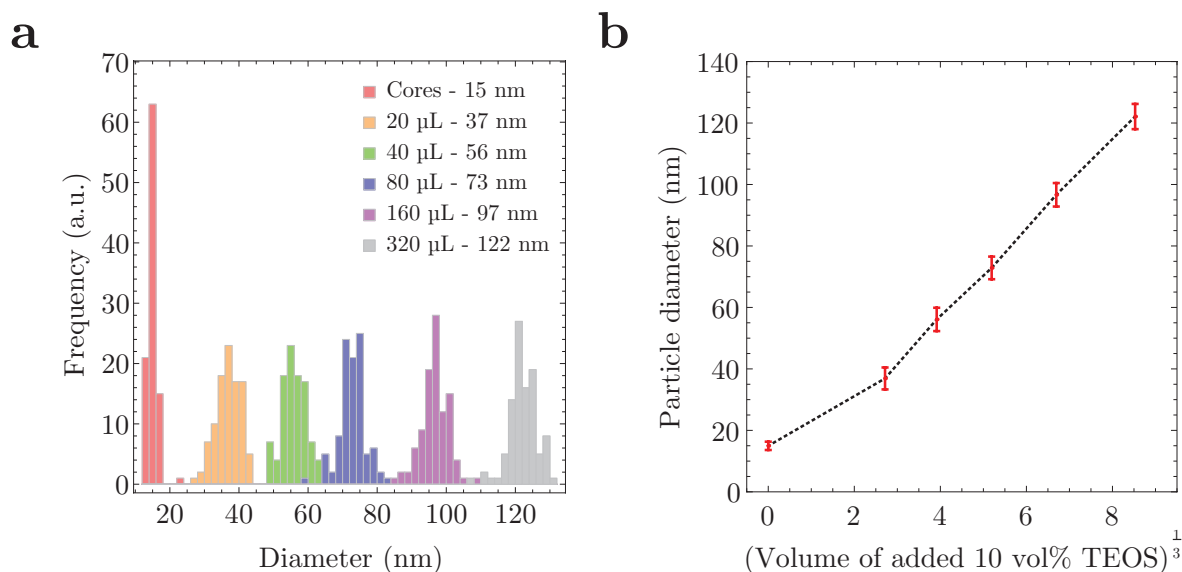


Figure 3.11: In (a) size histograms of particles synthesized by the addition of different TEOS volumes are included. The added volume of 10 vol% and the average particle diameters are indicated in the legend. In (b) the added volume of 10 vol% TEOS is plotted versus the average particle diameter.

3.3.3 Optimization of the fluorophore labelling density

A series of ~ 90 nm diameter particles with relative dye concentrations from 0 to 30 were synthesized, see table 3.1. Transmission Electron Microscopy (TEM) measurements were carried out to determine particle sizes at different stages of the synthesis. Representative images of particles are shown in figure 3.12. The images illustrate that the particles are successfully coated with a very thin silica layer after the first growth step (a). The silica layer becomes thicker and more homogeneous after growth of the rhodamine B labelled silica layer (b) and the second stabilization layer (c). It is important to note that silica grows selectively onto the existing particles, i.e. no secondary nucleation takes place. Average particle diameters and standard deviations at the different stages of the synthesis were determined from TEM images. Average particle sizes are almost identical for all samples at different stages of the reaction justifying the assumption that the volume of rhodamine B labelled silica per particle is similar for all samples. By ensuring that the number of particles is the same in all reactions, it is ensured that we are truly studying fluorophore labelling density effects.

| [Dye] | Total particle diameter | | | |
|-------|-------------------------|---------------|-------------|---------------|
| | RITC layer | | Stab. layer | |
| | d (nm) | σ (nm) | d (nm) | σ (nm) |
| 30 | 79 | 4.5 | 89 | 4.9 |
| 25 | 86 | 5.4 | 88 | 4.8 |
| 20 | 83 | 5.0 | 88 | 5.4 |
| 15 | 82 | 4.3 | 88 | 4.8 |
| 12.5 | 82 | 4.3 | 87 | 5.0 |
| 10 | 82 | 4.7 | 89 | 4.5 |
| 7.5 | 83 | 4.8 | 89 | 4.7 |
| 5 | 81 | 4.7 | 88 | 5.1 |
| 2.5 | 83 | 5.6 | 89 | 5.3 |
| 1 | 82 | 4.8 | 89 | 4.5 |
| 0 | 76 | 4.8 | 89 | 5.4 |

Table 3.1: Particle sizes determined from TEM after growth of the rhodamine B labelled silica layer and growth of the second stabilization layer. All samples were based on 15 nm ($\sigma = 1.4$ nm) diameter gold cores coated with a thin silica shell to obtain a total diameter of 25 nm ($\sigma = 2.7$ nm). In this table, d is the average particle diameter and σ is the standard deviation of this average value, both were determined by measuring diameters of 100 particles.

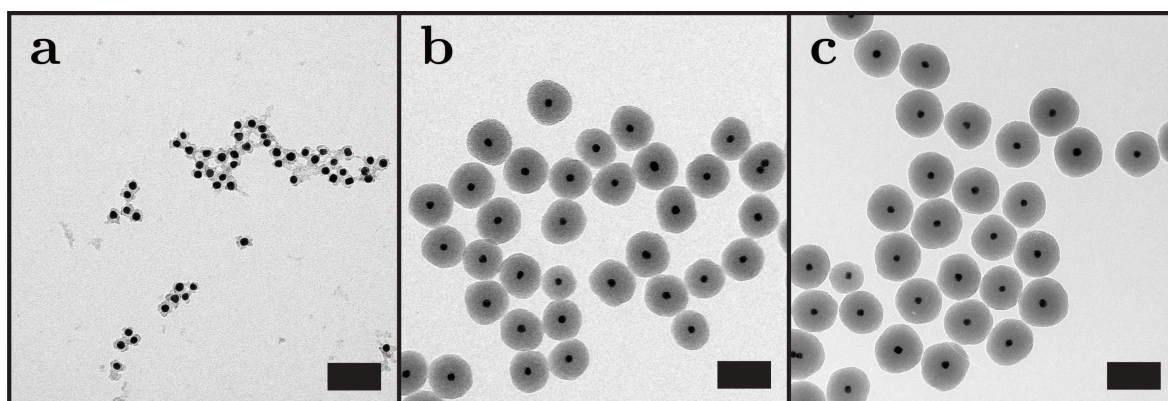


Figure 3.12: Representative TEM images at different stages of the silica coating procedure; (a) after growth of the first stabilization layer; (b) after growth of the rhodamine B labelled silica layer; (c) after growth of the second stabilization layer. The scale bars indicate 100 nm.

Determination of the fluorophore labelling density

To calculate the average fluorophore separations, fluorophore labelling efficiencies were determined. This was performed via absorption measurements after dissolution of the silica shell of the particles as described by Imhof *et al.* [27]. In figure 3.13 absorption spectra of the samples after silica dissolution and of the supernatant (the reaction mixture that contains all non-incorporated rhodamine B) are included. These spectra are obtained after a baseline correction was performed and after subtraction of the reference sample ($[Dye]=0$).

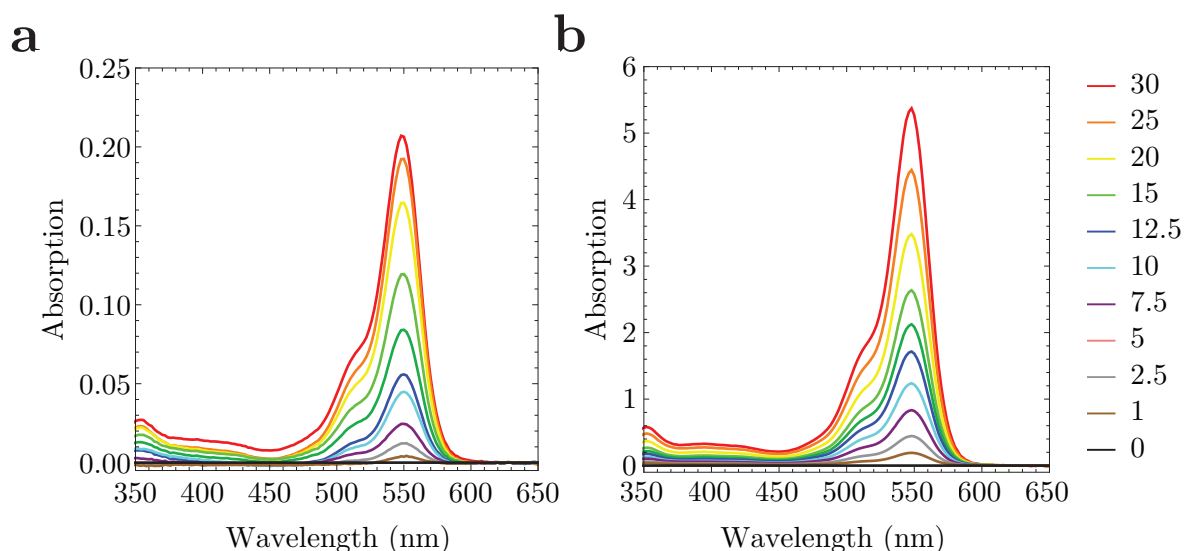


Figure 3.13: Absorption spectra of (a) the samples after silica dissolution and (b) corresponding supernatants. The numbers in the legend correspond to the relative dye concentration ($[Dye]$) that was used to synthesize the particles.

The observed maximum in the absorption spectra in figure 3.13 around 550 nm were used to calculate the incorporation efficiencies according to the formula below. All values used in the calculation and the calculated fluorophore labelling efficiencies are listed in table 3.2.

$$\text{Incorporation efficiency} = \frac{\text{Abs. sample}}{\text{Abs. sample} + \text{Abs. supernatant}} \times 100\% \quad (3.1)$$

Next, the average separation between fluorophores was calculated as the cube root of volume available per fluorophore. This value increases from 7.7 nm for the highest to 28.5 nm for the lowest labelling density (see table 3.2). The estimated average number and corresponding error (\sqrt{N}) of fluorophores per particle ranges from 12 for the lowest to 558 for the highest labelling density and is also included in this table.

| [Dye] | Max. absorption | | Labelling efficiency (%) | Average separation (nm) | Fluorophores per particle (a.u.) |
|-------|-----------------|--------------------|--------------------------|-------------------------|----------------------------------|
| | Sample (a.u.) | Supernatant (a.u.) | | | |
| 30 | 0.21 | 5.37 | 3.7 | 7.7 | 558 ± 24 |
| 25 | 0.19 | 4.45 | 4.1 | 7.9 | 662 ± 26 |
| 20 | 0.16 | 3.48 | 4.5 | 8.2 | 530 ± 23 |
| 15 | 0.12 | 2.64 | 4.3 | 9.2 | 358 ± 19 |
| 12.5 | 0.08 | 2.12 | 3.8 | 10.2 | 265 ± 16 |
| 10 | 0.06 | 1.72 | 3.2 | 11.7 | 175 ± 13 |
| 7.5 | 0.04 | 1.24 | 3.5 | 12.4 | 151 ± 12 |
| 5 | 0.02 | 0.83 | 2.9 | 15.2 | 77 ± 9 |
| 2.5 | 0.01 | 0.44 | 2.7 | 19.6 | 39 ± 6 |
| 1 | 0.004 | 0.19 | 2.2 | 28.5 | 12 ± 4 |

Table 3.2: Absorption maxima around 550 nm and calculated fluorophore labelling efficiencies, average separation between fluorophores and the number of fluorophores per particle for samples labelled with different relative dye concentrations.

Spectral measurements and radiative decay curves

To study fluorophore density effects, excitation and emission spectra and radiative decay curves were recorded (see figure 3.14a and b). Both spectra exhibit a small blue shift with increasing fluorophore density that is accompanied by an increase in the height of the shoulder around 520 nm in the excitation spectrum. Radiative (or fluorescence) decay curves were measured using the time-correlated single-photon counting technique after excitation with a pulsed laser [4]. These curves reveal faster decays with increasing labelling density which is indicative for fluorescence quenching. The radiative decay of particles labelled with the lowest dye labelling density, [Dye] = 2.5, is already slightly faster than the decay of the fluorophore, rhodamine B isothiocyanate (RITC), in ethanol. This can be attributed to a change in the local medium of the fluorophores, silica versus ethanol, and the APTES-dye coupling.

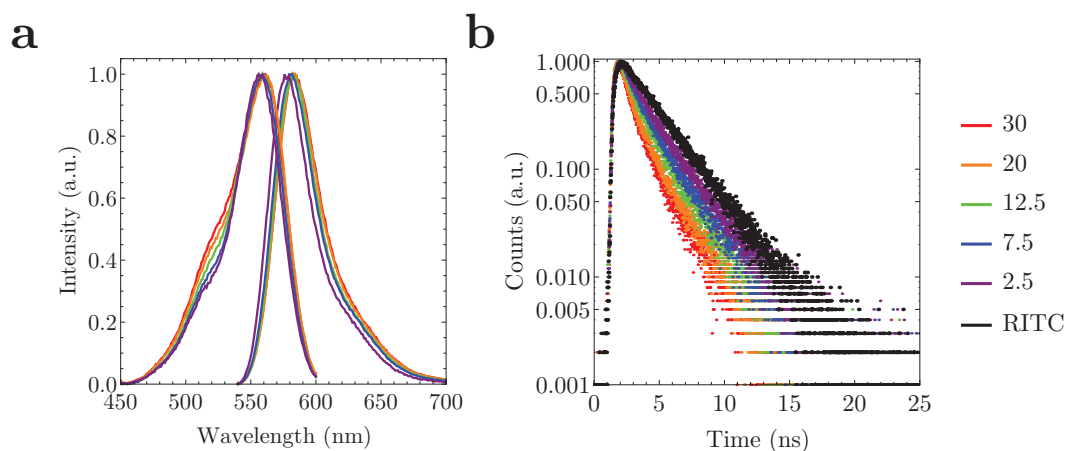


Figure 3.14: (a) Emission spectra recorded after excitation at 520 nm (right) and excitation spectra recorded at 610 nm (left). (b) Radiative decay curves after pulsed excitation at 509 nm and detection at maximum emission. The numbers in the legend correspond to the relative dye concentration ($[\text{Dye}]$) that was used to synthesize the particles.

Similar observations at increasing fluorophore densities in solid matrices were made by Genovese *et al.* [44] (rhodamine B in pluronic silica) and Imhof *et al.* [27] (fluorescein in Stöber silica) and for fluorophores on antibodies by Szabó *et al.* [26]. An explanation for these observations can be found by taking into account concentration effects including self quenching. Increasing the fluorophore density results in the formation of an increased number of dimers [53, 58] or other species acting as quenching centers. Additionally, resonance energy transfer (homo-FRET) between fluorophores becomes more efficient because the average separation between fluorophores shortens [4]. This combination of energy transfer and quenching successfully explains the effects of fluorophore concentration on the fluorescence quantum yield of fluorophores in solution [55, 56] and can also be applied to the work presented here. When increasing the fluorophore density in the particles, energy transfer between fluorophores becomes possible and the number of quenching centers within the particles increases. This energy transfer allows the excited state to migrate within the particle which makes it possible for the excited state to migrate from an unquenched fluorophore to a nearby quenching center, thereby contributing to quenching of fluorescence.

Single particle intensity and (photo)chemical stability

Widefield fluorescence microscopy measurements were performed to determine the single particle intensity and photostability of the particles. In figure 3.15a the average single particle intensity is plotted as a function of the number of dyes per particles. It can be seen that initially the single particle intensity increases when the number of dyes per particles increases. After this first increase, the single particle intensity remains more constant and eventually a small drop in intensity is observed. This optimum can be explained by the counterbalance between increasing the number of fluorophores versus

the increase in self quenching. This becomes more evident when the single particle intensity is plotted as a function of the average fluorophore separation, see figure 3.15b. At large separations (> 15 nm) the single particle intensity increases when the number of fluorophores per particle increases (i.e. shortening of the average separation) because the fluorophores do not sense each other. Next, a more constant regime between 10-15 nm with an optimum around 12 nm is observed. In this regime, the addition of fluorophores is counterbalanced by an increase in self quenching. Finally, when average separations drop below 10 nm self quenching becomes dominant which results in the aforementioned drop of intensity.

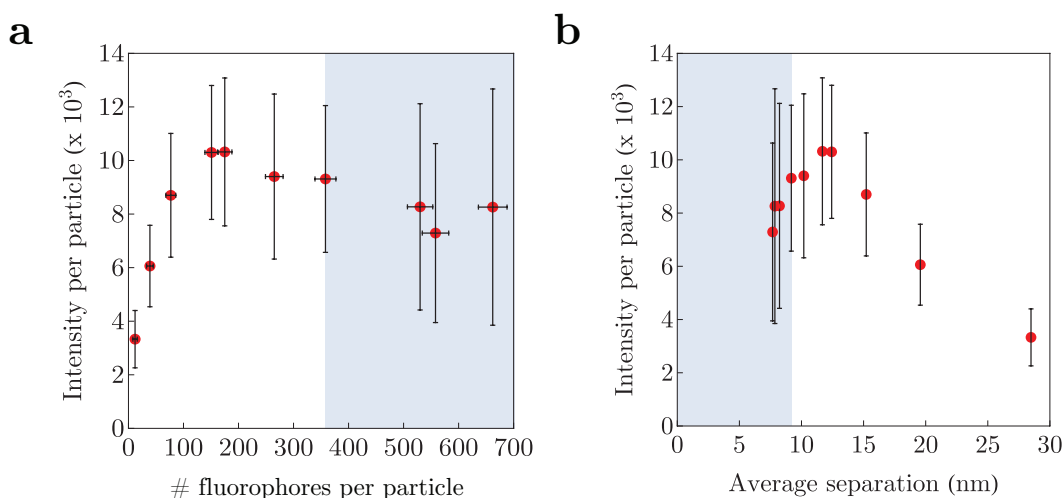


Figure 3.15: Average single particle intensity plotted as a function of the number of dyes per particle (a) and as a function of the average fluorophore separation (b). The standard deviation in the intensity per particle in this plot corresponds to the standard deviation of the normal distribution that was fitted to the data to obtain the mean intensity. The area in gray corresponds to non-stable particles.

The photostability of the particles was studied by measuring their photobleaching behavior. From the photobleaching curves in figure 3.16 it becomes clear that, generally speaking, the intensity loss reduces when the fluorophore density increases. This can be explained by the shortening of the radiative decay lifetime at higher fluorophore densities. The fluorophores spend less time in the excited state, thereby decreasing the bleach rate. In addition, photobleaching reduces the effective dye concentrations which decreases the effect of concentration quenching thereby counterbalancing bleaching.

Another observations made throughout the experiments was that particles with a relative dye concentration above 15 tend to cluster over time (gray area, figure 3.15). This clustering can result from a reduction of the negative zeta potential caused by the incorporation of positively charged fluorophores and amine groups. For CLEM applications non-clustered particles are preferred, therefore these high concentrations should be avoided.

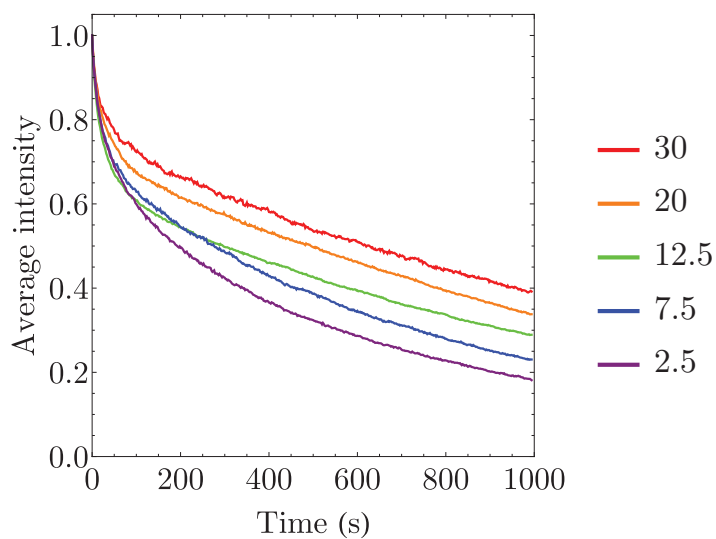


Figure 3.16: Normalized bleaching curves measured at an excitation intensity of 6.0 W cm^{-2} . The numbers in the legend correspond to the relative dye concentration ($[\text{Dye}]$) that was used to synthesize the particles.

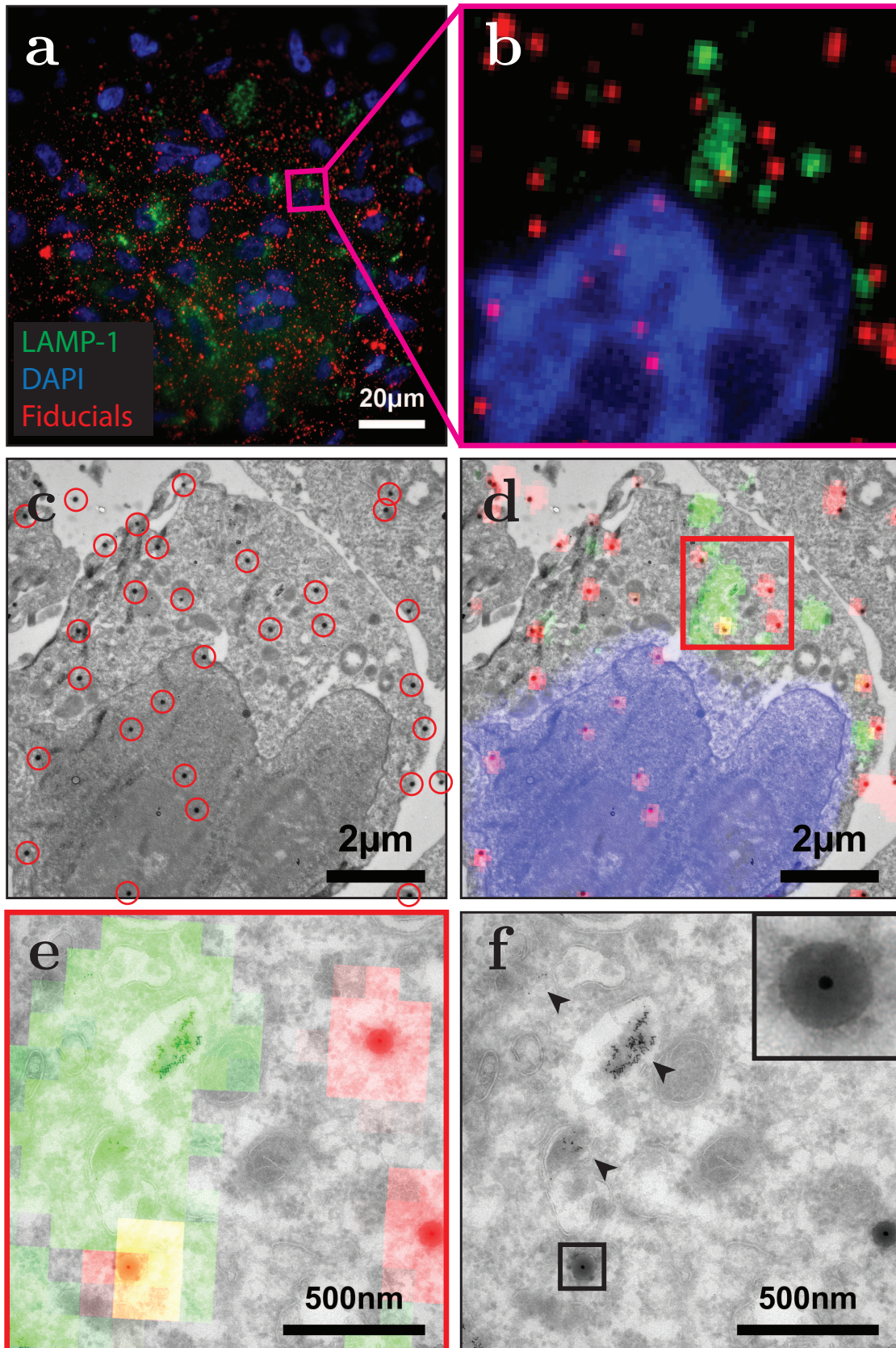
Based on the results included in this section, a relative fluorophore concentration of 10 (separation 11.7 nm) was chosen as the optimum labelling density. The average single particle intensity is maximum around this concentration. In terms of bleaching, it might be desirable to go for a higher labelling density. However, because of particle stability, a relative fluorophore concentration well below 15 (separation 9.2 nm) is desired.

3.3.4 2D CLEM experiment: Widefield and TEM imaging of fiducials on thin cryosections

The nanocomposite particles with the optimum dye concentration were first tested as fiducials in a 2D CLEM experiment. This experiment was performed by the addition of the particles to a cryosection of cells on a TEM grid in a correlative workflow. Results of this experiment are included in figure 3.17 and demonstrate that the fiducials are clearly visible in both modalities. The FM/EM overlay included in (d) and (e) is purely based on the positions of the fiducials and is used to correlate LAMP-1-GFP fluorescence to the ultrastructure of late endosomes and lysosomes. The inset in figure 3.17f clearly shows the core-shell structure of the fiducials. This core-shell structure was also apparent at the lower magnification TEM image in figure 3.17 and proved to be very useful to identify the fiducials. The core-shell also proved to be very useful to accurately determine the center of the fiducials and having a distinguishable well defined structure opens up possibilities for automatic registration of the particles. It should be noted that the EM magnification should be high enough to observe the core-shell structure of the fiducials. At too low magnifications, the core-shell structure is no longer visible which complicates discriminating fiducials from dirt and automatic registration of the fiducials.



Figure 3.17: 2D CLEM experiment of 81.9 nm diameter fiducials on top of a 70 nm thick cryosection of HT1080 cells stably expressing LAMP-1-GFP. (a) Widefield fluorescence microscopy image. (b) Region selected for TEM imaging. (c) TEM image of the selected region (fiducials encircled in red). (d) Overlay of FM and EM data based on the positions of the particles. In (e) and (f) higher magnification CLEM and TEM images of the in (d) highlighted region are included. The GFP fluorescence perfectly overlaps with the position of late endosomes and lysosomes, which were identified in TEM by their ultrastructural characteristics and the presence of endocytosed BSA-Au⁵ (arrowheads). In the inset of (f) one of the fiducials is enlarged, highlighting the core-shell structure of the particles.



Recognition of the fiducials

In this section it is demonstrated how the unique signature of the particles can be used to identify the fiducials in EM. To do so, specific areas of the EM image of the 2D-CLEM example presented in the main text are enlarged in figure 3.18. This demonstrates that already in this low magnification image the core-shell structure can be used to distinguish between fiducials (encircled in green) and other dark spot that are excluded as fiducials (encircled in orange). This is also confirmed by FM data since no fluorescence is observed from the dark spots that are excluded as fiducials.

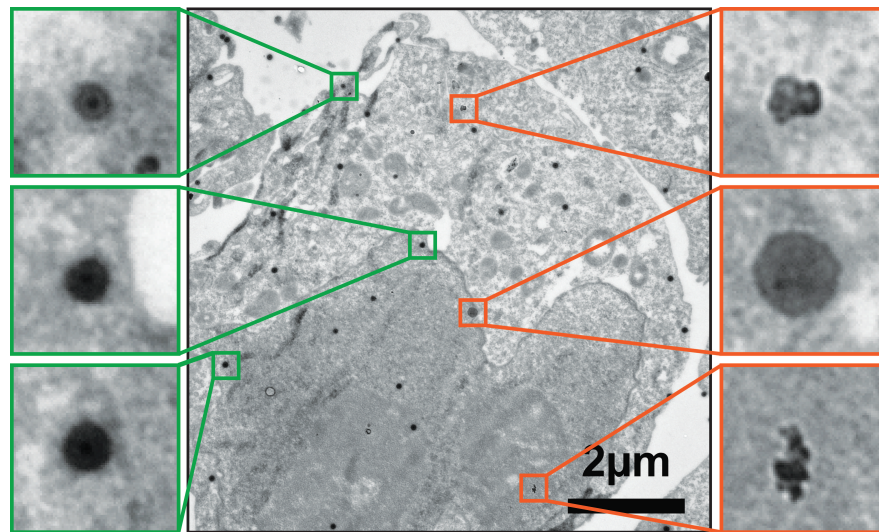


Figure 3.18: Low Magnification TEM image of 81.9 nm diameter fiducials on top of a 70 nm thick cryosection of HT1080 cells stably expressing LAMP-1-GFP.

This becomes even more apparent in the higher magnification EM image of the same region of interest included in figure 3.19. Again, the particles encircled in green correspond to fiducials whereas regions encircled in orange are excluded as fiducials because of the absence of the distinct core-shell structure.

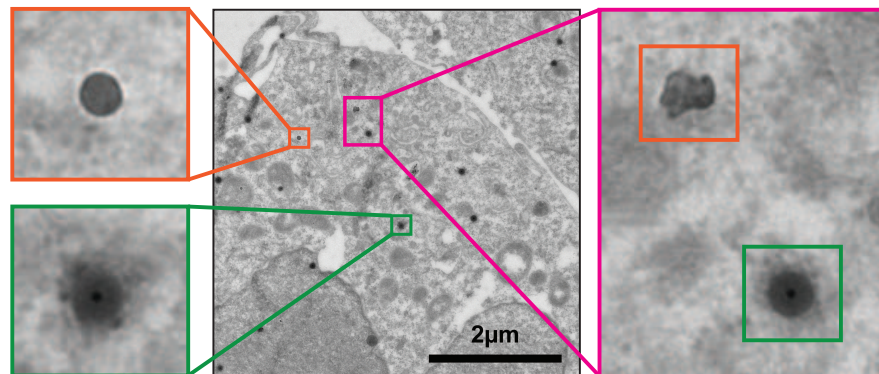


Figure 3.19: TEM image of 81.9 nm diameter fiducials on top of a 70 nm thick cryosection of HT1080 cells stably expressing LAMP-1-GFP.

3.3.5 3D CLEM experiment: Endocytosed nanoparticles as fiducials for correlative confocal fluorescence and 3D electron microscopy

In biological samples, correlating regions of interest (ROIs) between fluorescence and electron imaging can prove challenging due to the heterogeneous content of the cell and limited resolution of fluorescence imaging. Several organelles can be located within the same fluorescent spot, causing the risk of misidentification. The use of fiducials improves the registration accuracy between FM and EM, and can aid in alleviating this issue, especially when imaging in 3D. Due to their unique gold core silica shell architecture, we hypothesized that the nanoparticles could function as well-defined fiducials to correlate fluorescence and 3D electron imaging data. Previous research on silica particles has demonstrated that, under the right conditions, cells readily take up silica particles through endocytosis without cytotoxic effects [90, 91, 92, 93], indicating that endocytosed particles could serve as a useful and functional fiducial.

To examine the viability of the nanoparticles as 3D fiducials, we incubated HeLa cells with the nanoparticles diluted in medium, allowing uptake of the particles into the cells. After three hours the samples were fixed and imaged using confocal fluorescence microscopy. Endocytosed nanoparticles were detected throughout the cells (figure 3.20a), indicating successful endocytosis. Following fluorescence imaging, we selected a region of a cell containing both large, bright spots and smaller, dimly fluorescent spots for FIB-SEM imaging (figure 3.20a, inset). Samples were postfixated, stained and embedded for imaging by focused ion beam scanning electron microscopy (FIB-SEM). In FIB-SEM, samples are imaged by scanning the surface of a ROI using the electron beam, after which a thin layer is ablated from the surface using the FIB. This cycle is repeated until the ROI has been imaged, allowing 3D reconstruction of a sample. FIB-SEM on biological samples requires relatively severe staining with heavy metals to obtain sufficient detail of cellular structures, which comes at the risk of obscuring fiducials, and exaggerating biological features that may be mistaken for fiducials. In our FIB-SEM data, we found that the combination of the electron-dense gold core and the electron-lucent silica shell made for easy, unequivocal identification of the compartments containing nanoparticles, even in heavily stained samples, allowing easy correlation of fluorescence and FIB-SEM data.

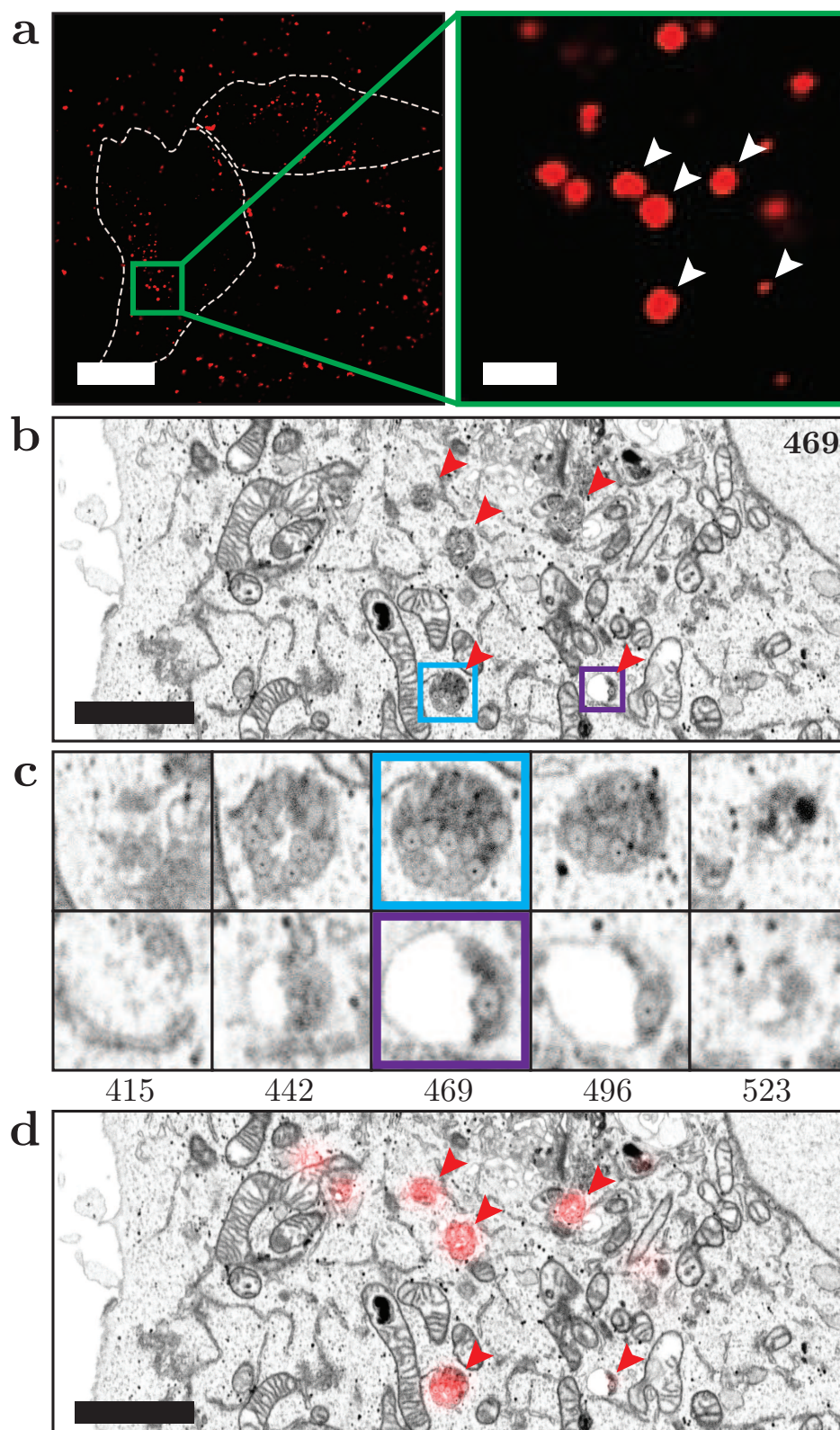
The nanoparticles were found in endocytic compartments (figure 3.20b), and could be resolved at an individual particle level. The unique structure of the particles proved helpful in identification, meaning that any fluorescent spot seen in the confocal data could be linked to corresponding particles detected using FIB-SEM (figure 3.20b). Interestingly, brightly fluorescent spots were correlated to compartments containing up to 40 particles (figure 3.20c, blue outline), whereas only 1 or 2 nanoparticles could be found in compartments corresponding to dimly fluorescent spots (figure 3.20c, purple outline), indicating a high level of sensitivity. Thanks to the high resolution and small sectioning distance employed by FIB-SEM, even single particles could be detected, and fitted to the fluorescent data.

In the FM (figure 3.20a) and FIB-SEM data, particles, and clusters of particles were

also observed outside the cells. Thorough testing, including Dynamic Light Scattering measurements, proved that initially non-clustered particles were presented to the cells. The observation of clusters outside the cells can be explained by taking into account that this data is recorded after 3 hours of uptake, after the addition of fixative and after overnight fixation. Within this time frame, particles still present in the medium can aggregate, in particular after the addition of fixative. This aggregation is not expected to affect the initial uptake of the particles but this could complicate automatic registration strategies.

Combined, our data shows that the nanoparticles are taken up by HeLa cells and are useable as 3D fiducials, owing to their bright fluorescence and ease of identification in FIB-SEM data.

Figure 3.20: 3D CLEM experiment of 99.2 nm diameter fiducials after cellular uptake in HeLa cells. (a) Confocal fluorescence microscopy slice of cells after fixation. White areas indicate coarse outlines of two cells. The enlarged region highlighted in green is chosen as ROI for FIB-SEM imaging. The white arrowheads indicate fiducials visible in the corresponding FIB-SEM slice shown in (b). (b) Virtual slice of the reconstructed FIB-SEM data, corresponding to the focal plane used for fluorescence imaging. Red arrowheads indicate compartments visualized in fluorescence microscopy, which contain various amounts of fiducials. The organelles encircled in blue and purple containing fiducials are enlarged in (c). (c) FIB-SEM slices through organelles of interest at different heights of both compartments, clearly showing the different amounts of fiducials present. The numbers below the figures correspond to the number of the FIB-SEM slices. (d) Overlay of FM and EM data based on the positions of the fiducials indicated by the arrowheads in (a) and (b). The scale bars in (a) correspond to 20 and 2 μm , the scale bars in (b) and (d) correspond to 2 μm .



3.4 Conclusions and outlook

15 nm gold particles coated with a fluorescently labelled silica shell (rhodamine B isothiocyanate) were successfully synthesized. A relative dye concentration of 10, corresponding to an average fluorophore-fluorophore separation of 11.7 nm yielded optimum brightness and (photo)stability. Particles labelled with this optimum dye concentration were successfully used as fiducials in a 2D CLEM experiment to correlate widefield FM and TEM images by addition of the fiducials to a cryosection of cells on a TEM grid, demonstrating high registration accuracy in both FM and EM. After endocytosis of the fiducials by HeLa cells, the particles could also be used as well-defined fiducials to correlate confocal FM and FIB-SEM. In both experiments, the unique core-shell signature of the fiducials proved very useful to identify the fiducials and to accurately determine the center of the fiducials. This was especially evident in the FIB-SEM data, where a fiducial with only an electron-lucent shell or only a small electron-dense core would be at risk of being misidentified as a cellular structure.

In future research, automatic registration procedures can be explored where the distinct core-shell structure of the here presented particles can be used to detect the fiducials in EM. Furthermore, we plan to use the offset between EM and FM positions of the fiducials to correct for FM/EM sample distortions. This opens up the possibility to use the fiducials to test and quantify the accuracy of different data correlation methods. Such a method can for example include nonlinear effects such as sample deformation caused by shrinkage of the sample in EM. Furthermore, the unique architecture of the nanoparticles can aid in devising automated correlation strategies, based on accurate localization of the nanoparticles within complex biological specimens. Finally, we note that due to the silica shell the particles are non-toxic and compatible with live cell imaging experiments, opening up imaging strategies for live-cell correlative imaging.

3.5 Acknowledgements

I would like to thank and acknowledge the following persons for their contributions: Dave van den Heuvel for his help with the single particle measurements; Tom Konings and Gerhard Blab for their help with the analysis of this data; Job Fermie and Nalan Liv for the 2 and 3D CLEM experiments and Cilia de Heus for her help with the preparation of EM samples. Finally, I would like to thank Job Fermie and Nalan Liv for their input on this manuscript and I thank them together with Dave van Den Heuvel, Judith Klumperman, Gerhard Blab and Hans Gerritsen for critical reading of the manuscript.

3D (i)CLEM: Endocytosed Fiducials as Dual-Modality Probes

In this chapter, the potential of the fluorescently labelled silica coated gold nanoparticles presented in chapter 3 for three dimensional iCLEM measurements is explored. To this end, entire HeLa cells and P388D1 mouse macrophages were labelled via endocytosis of the fiducial markers. The fluorescence intensity of the particles was monitored while the samples were prepared for EM. This was important as the procedure contained various fixation, staining and embedding steps that are expected to reduce the fluorescence intensity of the particles. Following this procedure, heavily stained, thin-layer plastic embedded cells were obtained. We observed that, despite a large decrease in fluorescence intensity, the fiducial markers remained visible in FM which makes them well suited for iCLEM measurements.

In the final section of this chapter, 3D iCLEM measurements of cellular samples with endocytosed fiducial markers are presented. It is demonstrated how the fiducial markers can be used to identify and target regions of interest in FM for further study by EM. A brief description of the iCLEM setup used for these measurements is also included. This setup was developed by co-workers within the same project.

4.1 Introduction

The success of iCLEM experiments, where a light (fluorescence) microscope is integrated in an electron microscope, strongly depends on the availability of good performing integrated microscopes. On the other hand, the compatibility of samples, labels and the procedures to prepare samples for both FM and EM are also of great importance. It is not straightforward to prepare samples that can be imaged with both modalities. Extensive protocols involving many steps are required to prepare biological sample for EM. These protocols all aim at the preservation of cellular ultra-structures and ensuring that samples show good contrast and are conductive enough to prevent charging effects during EM measurements [13, 94, 95, 96, 97, 98]. Often there is a trade off between FM and EM compatibility of samples at some point in these procedures. To get a better understanding of this trade off, the most important EM sample preparation steps and their effect on the FM compatibility of samples is discussed below.

The visibility of materials in an electron microscope (TEM or SEM) is mainly determined by the atomic number of the elements present in the material. Generally speaking, heavy elements, i.e. atoms with a high atomic number, scatter electrons more efficient than lighter elements (low atomic number) and are therefore better visible. This difference can be explained by the difference in size of the nucleus of these elements as it is the nucleus that scatters most of the electron that are used to collect images. To maximize contrast, it is best to have regions of heavy elements next to regions with light elements [99]. Following the same reasoning, black ink on a white paper is better visible than grey ink. EM staining protocols therefore always aim at providing a well-balanced mix between these regions.

Biological tissue is almost exclusively comprised of comparatively light elements and thus barely visible in an electron microscope. Therefore, a wide variety of protocols to add contrast to specific regions of tissues has been developed. This is achieved by the addition of heavy metals that specifically bind or enhance contrast of various macromolecular components of cells such as lipids, proteins, polysaccharides, nucleoproteins, or lipoproteins [100, 101]. We refer to this process as staining and osmium, uranyl and lead are examples of heavy metals that are frequently used for this [97]. Osmium, added as osmium tetroxide, is widely used for fixation and staining of lipid-containing membranes as it is known to react with the double bonds present in lipid molecules [96, 100, 102, 103, 104, 105]. Uranyl on the other hand, added as uranyl acetate, is mainly associated with staining of proteins but also interacts with lipids [96]. Finally, lead, which can be added as lead citrate or aspartate, enhances contrast of a wide range of cellular structures such as ribosomes, lipid membranes, cytoskeleton and other compartments of the cytoplasm [106]. Lead also interacts with uranyl acetate thereby enhancing the contrast of uranyl stained materials if it is added after materials are stained with uranyl acetate [96].

The heavy metals added for staining are known to be incompatible or only partially compatible with fluorophores and other labels for FM as they quench most fluorescence [15, 74, 107, 108, 109]. This quenching makes it impossible to detect fluorescent proteins or tags after samples are prepared for EM via standard protocols. Apart

from this heavy metal quenching, also the number of suitable fluorophores and fluorescent proteins is limited as not all of them remain fluorescent under the dry vacuum conditions encountered in standard electron microscopes [74, 110, 111].

Despite these challenges it has been demonstrated that it is possible to produce biological samples that are suitable for iCLEM measurements. This can be achieved by choosing the right fluorophores and/or fluorescent proteins and labelling procedure and by minimizing heavy metal staining to yield maximum fluorescence. Karreman et al. [74], for example, demonstrated that it is possible to perform two dimensional iCLEM measurements on sections of EM stained resin embedded cells immuno-labelled with fluorophores. After a careful evaluation of fluorophores and labelling procedures in combination with milder heavy metal staining she managed to prepare sections that were well contrasted for EM and remained fluorescent under the vacuum conditions of the TEM.

In this chapter, the possibility to use the fiducial markers presented in chapter 3 in three dimensional iCLEM measurements is explored. For iCLEM, it is important that (enough) fluorescence of the fiducial markers is preserved after samples are prepared for EM. To test this, the fluorescence intensity of cellular samples with endocytosed fiducial markers is monitored during a procedure to prepare cellular samples for FIB-SEM measurements. To this end, first the endocytosis itself is followed and optimised in two types of cells; HeLa cells and macrophages. Next, cells with endocytosed fiducial markers are fixed, stained and embedded following the procedure developed by van Donselaar and co-workers [98]. The cells are embedded in an extremely thin layer of plastic, and heavily stained with heavy metals to yield optimal imaging conditions for EM.

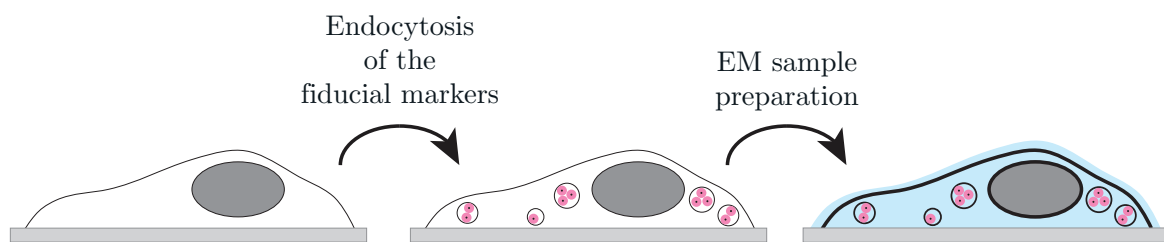


Figure 4.1: A schematic representation of the procedure to obtain iCLEM samples by endocytosis of the fiducial markers. After endocytosis, the first FM data is collected. Next, samples are prepared for EM while monitoring the fluorescence intensity of the endocytosed particles.

Not all plastics are suitable for iCLEM measurements and thin-layer embedding of biological tissue. Therefore, three frequently used plastics were tested prior to the experiments presented in this chapter: Epon, Lowicryl HM20 and Spurr's resin. The first one, Epon, is known to be very robust and proved to be very stable throughout the FIB-SEM measurements. However, the high viscosity and autofluorescence made this material unsuitable for thin-layer embedding and FM measurements. The second one, Lowicryl HM20, was nearly transparent which is advantageous for FM but

was not stable during FIB-milling and EM imaging. Also, a lot of structural defects were introduced as the plastic was too viscous to uniformly cover all biological tissue throughout the embedding procedure. The final one, Spurr's resin can be considered a good compromise: it is robust enough for FIB-SEM imaging and its autofluorescence is low enough for FM imaging. Moreover, it has a good viscosity for thin-layer embedding of biological tissue which makes it possible to reproducibly produce high quality iCLEM compatible samples.

In the final section of this chapter, 3D iCLEM measurements of the cellular samples with endocytosed fiducial markers are presented. It is demonstrated how the fiducial markers can be used to identify and target regions of interest in FM for further EM imaging. A brief description of the iCLEM setup that is used for these measurements is also included. This setup was developed by co-workers within this project.

4.2 Experimental details

4.2.1 Endocytosis of the fiducial markers

In this section, the possibility to use the fiducial markers for three-dimensional labelling of cells via endocytosis is explored. This approach was tested in two cell lines: P388D1 mouse macrophage and HeLa cells. Macrophages are a type of white blood cell and are known as "big eaters". The cells are specialized to engulf and kill pathogens like bacteria and viruses [112]. Uptake of (large) particles by these cells is frequently reported [113, 114, 115]. As the P388D1 cells exhibit characteristics typical for macrophages, rapid uptake of the fiducial markers by these cells is expected. HeLa cells on the other hand, are a type of cancer cells and are the most studied human cells [116]. For these cells, the size of particles in uptake studies is more critical but endocytosis of particles by HeLa cells is also reported [91, 117].

In figure 4.2 representative TEM images of the fiducial markers that were used for the cellular uptake experiments are included. These particles were synthesized following the procedures described in chapter 3. For cellular uptake by macrophages, the 128.8 ± 5.8 nm diameter particles in (a) were used whereas the smaller, 90.8 ± 4.9 nm diameter, particles in (b) were used for uptake by the HeLa cells. The number of fluorophores scales with the volume of rhodamine B labelled silica. Therefore, the larger particles are brighter than the smaller particles.

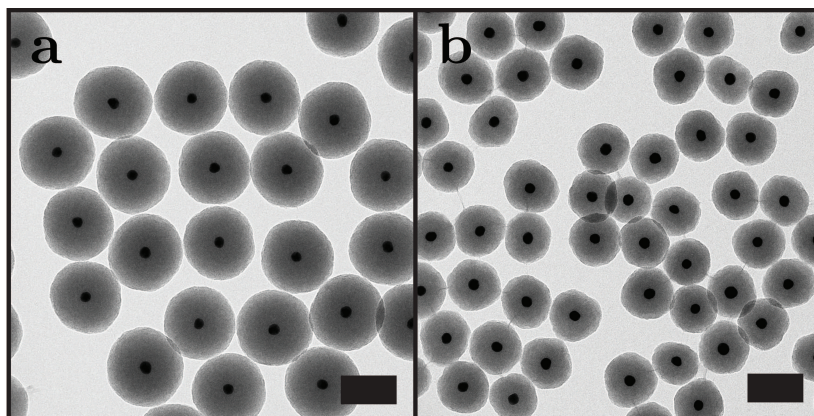


Figure 4.2: TEM images of the fiducial markers for cellular uptake by (a) P388D1 mouse macrophages and (b) HeLa cells. Both scale bars indicate 100 nm.

Cellular uptake experiments

HeLa cells were cultured in a 37°C, 5% CO₂ incubator, in T75 culture bottles (Corning). Cells were maintained in Dulbecco's Modified Eagle's Medium (DMEM; Gibco) supplemented with 10% fetal bovine serum, 2 mM L-glutamin, 100 U/mL penicillin, 100 µg/mL streptomycin (referred to as complete DMEM). Cells were passaged when confluency reached 85% to 90%. For cellular uptake, HeLa cells were grown on gridded glass coverslips, prepared as described by Fermie *et al.* [84].

Cells from the P388D1 mouse macrophage cell line were cultured in RPMI1640 medium supplemented with 10% fetal bovine serum, 2 mM L-glutamin, 100 U/mL penicillin and 100 µg/mL streptomycin, under 37°C, 5% CO₂ conditions. For time-lapse imaging, P388D1 cells were seeded in 8-well chambered microscope slides (Ibidi GmbH, #80826) coated with poly-L-lysine.

Both cell types were incubated with various concentrations of fiducial markers dissolved in complete DMEM for a fixed amount of time.

Live-cell imaging and in situ fixation

Live imaging was performed on a Deltavision RT widefield microscope (GE Healthcare) equipped with a conditioned imaging chamber set to 37°C and 5% CO₂. Time-lapse imaging was performed using a 100X/1.4 numerical aperture (NA) oil immersion objective and images were recorded using a Cascade II EM-CCD camera (Photometrics) with a gain value of 290 using the Acquire3D module in Softworx 6.5.2. To evaluate the endocytosis of the fiducial markers, fluorescence images of the particles were recorded every 2 s with an exposure time of 50 ms. A rhodamine B filter set was used to selectively excite (555/25 bandpass) and detect (605/52 bandpass) the particles. In addition, differential imaging contrast (DIC) images were collected simultaneously.

Cells were fixed in situ by the addition of 1 mL of fixative containing 4% paraformaldehyde (Sigma) and 0.05% glutaraldehyde (25% solution in dH₂O, Merck) in 1X PHEM buffer (60 mM PIPES, 25 mM HEPES, 10 mM EGTA, 2 mM MgCl₂, pH=6.9) to the coverslip holder. Movement in cells ceased within several seconds after addition of the fixative. After 10 minutes, cells were stored in fresh buffer with fixative.

Confocal imaging

After fixation and/or storage, coverslips were washed three times with 1x PHEM buffer to remove excess fixative, followed by two washes with dH₂O. Next, the coverslips were mounted on standard microscope slides using Prolong Gold antifade mountant containing DAPI (Thermo Fisher, P36930) which was cured overnight.

Fluorescence confocal imaging was performed using a Zeiss LSM700 CLSM equipped with 63x/1.4 NA oil immersion objective. The fiducial markers were excited using the 555 nm laser line at 2% power, while DAPI was visualized using the 405 nm laser line at 2% laser power. Z-stacks were collected with 200 nm step size. The position of cells relative to the grid of the coverslips was recorded using polarized light.

4.2.2 EM sample preparation: postfixation, dehydration and resin embedding

In this section, the procedure to prepare cellular samples with endocytosed fiducial markers is described. HeLa cells and macrophages were incubated for 3 hours with 10 $\mu\text{g}/\text{mL}$ solutions of 90.8 ± 4.9 nm and 128.8 ± 5.8 nm diameter fiducial markers respectively and used in all experiments described here. The aim of the experiments is to determine how the fluorescence intensity of the fiducial markers is affected by the different steps of the EM preparation procedure. Therefore, samples were prepared at different points in time within the EM sample preparation procedure (EM step 1-5). At these points, the fluorescence intensity of the fiducial markers was monitored. Radiative decay curves of the fiducial markers were recorded as well, as these can provide additional insight in the quenching of the fluorophores incorporated in the fiducial markers.

EM sample preparation

After primary (in situ) fixation of the cells, the coverslips were transferred to 35 mm dishes. Next, the cells were postfixated in 2.5% glutaraldehyde and 2% paraformaldehyde in 0.1 M sodium cacodylate buffer (CB) (EM step 1).

The samples were prepared for EM according to the extremely thin layer plastification or ETLP protocol that was developed by van Donselaar et al. [98]. Briefly, samples were contrasted using 1% osmium tetroxide (w/v) with 1.5% potassium ferrocyanide (w/v) for 90 minutes on ice (EM step 2). Next, the coverslips were incubated with 1% thiocarbohydrazide (TCH) in dH_2O (w/v) for 15 min. After the samples were washed in dH_2O , a second staining with osmium was performed by incubation with 1% osmium tetroxide in dH_2O for 90 or 30 minutes. The samples were en-bloc stained with 2% uranyl acetate in dH_2O for 30 minutes (EM step 3) and stained with Walton lead aspartate for 30 min at 60°C (EM step 4). In between and after the final staining and incubation steps, the samples were washed 5 times in dH_2O . Finally, dehydration was performed using a graded ethanol series and samples were embedded in Spurr's resin and polymerized for 48-60 h at 65°C (EM step 5).

4.2.3 Osmium exposure experiments

A large drop of fluorescence intensity of the endocytosed fiducial markers is typically observed when the cellular samples are stained with osmium. A possible way to improve on this, is to reduce the osmium staining time. To test this whether this approach could be successful, the fluorescence intensity of the fiducial markers is determined after exposing the particles to an osmium tetroxide solution for various amounts of time.

To do so, glass substrates with a homogeneously distributed layer of fiducial markers were prepared by diluting a solution of the fiducial markers in ethanol 10.000 times in a solution of polyvinyl alcohol in water (10 mg/mL). The polymer, polyvinyl alcohol,

was added here to prevent drying effects that would otherwise result in the formation of aggregates of particles on the substrate [118]. 20 μL of this solution was drop casted on twelve 1 cm diameter spherical glass substrates. A pipette tip was used to spread the solution so that it uniformly covered the glass substrates and the water was evaporated on air.

Next, an osmium tetroxide solution was prepared by transferring aqueous solutions of 6.5 mL sodium cacodylate (0.1 M), 1 mL potassium ferrocyanide (15 wt%) and osmium tetroxide (4 wt%) to a vial. The substrates were transferred to twelve separate vials and osmium exposure was started by the addition of 1 mL of the osmium tetroxide solution ($t=0$) to ten of these vials. After this addition, the vials were transferred to an ice bath that was placed on a shaker. After 5 minutes ($t=5$), the first two samples were removed from the ice bath, the osmium tetroxide solution was removed with a pipette and 1 mL water was added to the vials. This cleaning procedure was repeated five more times with time intervals of five minutes before samples were dried on air. The same procedure was repeated to obtain samples that were exposed to the osmium tetroxide solution for 15, 30, 60 and 90 minutes ($t=15/30/60/90$). The two substrates that were not exposed to the solution were cleaned following the same procedure. These samples were used to determine the fluorescence intensity of the fiducial markers that were not exposed to the osmium tetroxide solution ($t=0$).

Fluorescence imaging and radiative decay measurements

Widefield fluorescence microscopy measurements were carried out on a Nikon Eclipse Ti widefield microscope. A mercury arc lamp in conjunction with a 510-560 nm excitation filter, a 565 nm long pass dichroic mirror and a 590 nm long pass emission filter ensured well defined illumination and detection wavelength bands. The same objective, excitation intensity and diaphragm settings were used in all experiments. Finally, an Andor NEO sCMOS camera was used to record images.

For the endocytosed particles, it was not possible to determine the single particle intensity of the fiducial markers as clusters of particles were present in the cells. Therefore, the average intensity throughout a large set of cells was taken as a measure for the intensity. The values that are determined here, can only be used as a rough indication for the fluorescence intensity as the particles are not homogeneously distributed throughout the cells.

For the osmium exposure experiments, single particle intensities were estimated with the ThunderSTORM [50] and Otsu [119] plugins in ImageJ.

Radiative decay measurements were carried out on a Nikon Eclipse TiE microscope equipped with a 40x 0.75 NA Nikon air objective. The fluorescence lifetime module (LiMO) of the Confocal Laser Scanning Microscope (CLSM) [51] was used to record average fluorescence decay times. An NKT laser set at 525 nm was used for pulsed (10ps, 80 MHz) excitation. Before reaching the sample, the excitation light was filtered with a 535/40 bandpass filter and the intensity was further reduced with an acousto optical tunable filter (AOTF). A GaAsP photomultiplier tube (PMT) in combination

with a 50x Philips preamplifier and a 532 nm long-pass filter (RazorEdge) were used for detection. To obtain average fluorescence lifetimes, the obtained time traces were fitted with double-exponential decay curves in commercially available Becker & Hickl GmbH software

4.2.4 3D iCLEM measurements by the integration of a CLSM with a FIB-SEM

3D iCLEM measurements were performed using an integrated setup that was developed within this project by Loginov and co-workers [120]. In this setup, a Confocal Laser Scanning Microscope (CLSM) equipped with a high numerical aperture (NA) objective is integrated in a commercial FIB-SEM. The FIB-SEM and the CLSM in the integrated setup observe the sample from the same direction and switching between the modalities is accomplished by shuttling the specimen using an accurate mechanical stage. In figure 4.3 a schematic representation of the iCLEM setup is included. This section continues with a brief description of the setup. Details of the process of integration and a full characterization of the performance of the iCLEM microscope are presented in the work by Loginov et al. [120].

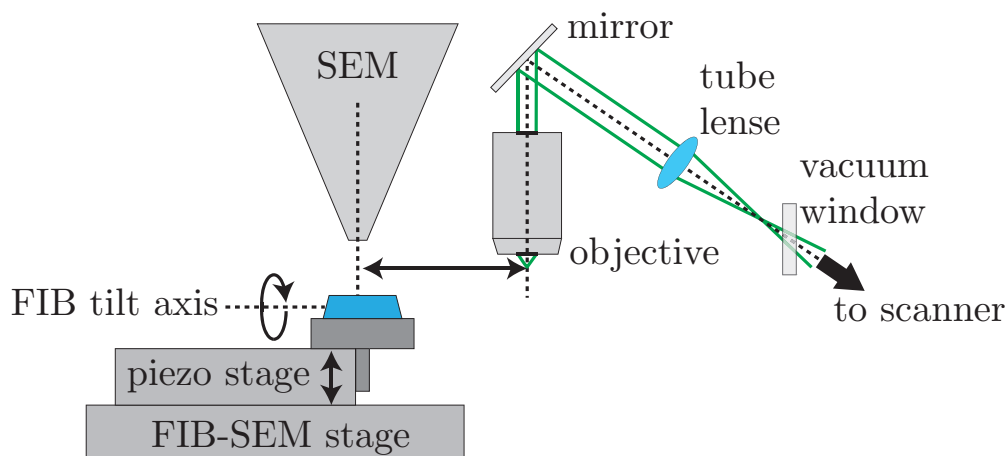


Figure 4.3: A schematic representation of the integrated CLSM FIB-SEM setup. The CLSM scan area is situated roughly 90 mm from the SEM working point. The objective lens, the mirror and the tube lens are situated inside the vacuum chamber. The confocal scanner is located behind the vacuum window. A 1D-piezo stage is mounted on top of the FIB-SEM stage for sub-micrometer axial positioning. Adapted from ref [120].

For EM imaging, a Scios FIB-SEM (ThermoFischer) with an Everhard-Thorley Detector (ETD), an in-lens detector of Back Scattered Electrons (BSE), and an in-column detector of Secondary Electrons (SE) was used. For FIB milling, The Scios was equipped with a Ga-ion source. Control of 3D EM acquisition was performed with the Slice&View version 3 software.

For confocal imaging, a Nikon industrial inspection objective lens (ELWD series, Plan Apo 100x NA 0.9), a mirror and a tube lens were placed inside the vacuum

chamber of the Scios. The other compartments of the CLSM setup were placed outside the vacuum by passing the optical path through a vacuum window, see figure 4.3. For lateral scanning, a Yanus scan-head (FEI Munich) equipped with a 50 mm focal length scan-lens was used. A single axis piezo-stage (E-601.1SL, Physik Instrumente) was mounted on top of the FIB-SEM stage to achieve sub-micrometer axial positioning and scanning.

For excitation of the specimen, a 532 nm laser (LightHUB with an AOM, Omicron) was used. A fiber was used to guide the light to a stand-alone detection module. Here, a dichroic mirror was used to split the light into a fluorescence and a reflection signal. The reflection signal was detected by a PMT operating in current mode (PMMA01, Thorlabs). The fluorescence signal was, after bandpass filtering (ET585pxr-65, Chroma), detected by a photon counting PMT (H7422P-40, Hamamatsu).

The integrated measurements were performed on the extremely thin layer plastified samples described in section 4.2.2. For the iCLEM experiments included in this chapter, HeLa cells incubated for 3 hours with a 10 $\mu\text{g}/\text{mL}$ solution of fiducial markers with a total diameter of 90.8 nm were used. After polymerization, the coverslips containing ETLF samples were mounted on aluminium stubs using conductive carbon tape and coated with 10 nm carbon in a Leica ACE600 sputter coater to ensure conductivity.

After mounting the sample in the FIB-SEM and pumping the system down to vacuum, confocal fluorescence and reflection images were recorded. Next, the sample surface was imaged with the SEM in 2D. This data shows great similarities with the CLSM reflection data and was used to create a first rough overlay. This overlay was then used to navigate over the sample and to select a region of interest for further FIB-SEM processing based on the fluorescence data.

After identification of region(s) of interest, automated serial imaging was performed according to a previously described workflow [84]. Briefly, trenches were prepared surrounding the region of interest using the FIB, after which automated serial imaging was performed using 5 nm isotropic voxels. All SEM images were collected at an acceleration voltage of 2 kV and a current of 0.2 nA, using the T1 backscattered electron detector.

4.3 Results

4.3.1 Endocytosis of the fiducial markers

A first set of cellular uptake experiments was performed to determine whether the fiducial markers are endocytosed by the macrophages and HeLa cells. These experiments were also used to determine which conditions (i.e. concentration and incubation time) should be used to obtain cells that are properly labelled in three dimensions. To this end, different concentrations (0, 5, 15 and 50 $\mu\text{g}/\text{mL}$) of particles dispersed in cell culture medium were added to cells grown on gridded glass coverslips that were placed on well plates. Live cell widefield imaging was used to follow endocytosis over time and cells were fixated when endocytosis of the particles was clearly visible. Following fixation, confocal images were recorded to determine how well the particles were distributed throughout the cells.

Live-cell data

In the live-cell data successful uptake of the fiducial markers by both cell types and at all concentrations of fiducial markers was observed. To illustrate this, live-cell data of two macrophages and of a HeLa cell after three hours incubation with 15 respectively 5 $\mu\text{g}/\text{mL}$ fiducial markers are included in figure 4.4a and b. The fluorescent rhodamine B spots observed in these images indicate that (groups of) fiducial markers are present. This assumption is justified by the absence of fluorescent spots in live-cell data of cells that were not incubated with the fiducial markers.

In the live-cell data of the macrophages (figure 4.4a), one can see a rough outline of two cells. Over time, movement of the cell as well as the fluorescent spots within the cells is observed. This indicates the presence of endocytosed fiducial markers within the cells. Within the observation time, also live endocytosis of the group of particles encircled in green is observed. This group of particles crosses the boundary of the cell (60 s) and gradually moves from the exterior to the interior of the cell.

For the HeLa cell in figure 4.4b, similar observations were made. To visualize how the endocytosed fiducial markers are moving inside the cell, some of the fluorescent spots were tracked within the live-cell data. In the final panel, the trajectories of these fluorescent spots and a rough outline of the cell are included. In this data set, live uptake is observed as well. The fiducial markers indicated by the white trajectory are for example moving from the exterior to the interior of the cell.

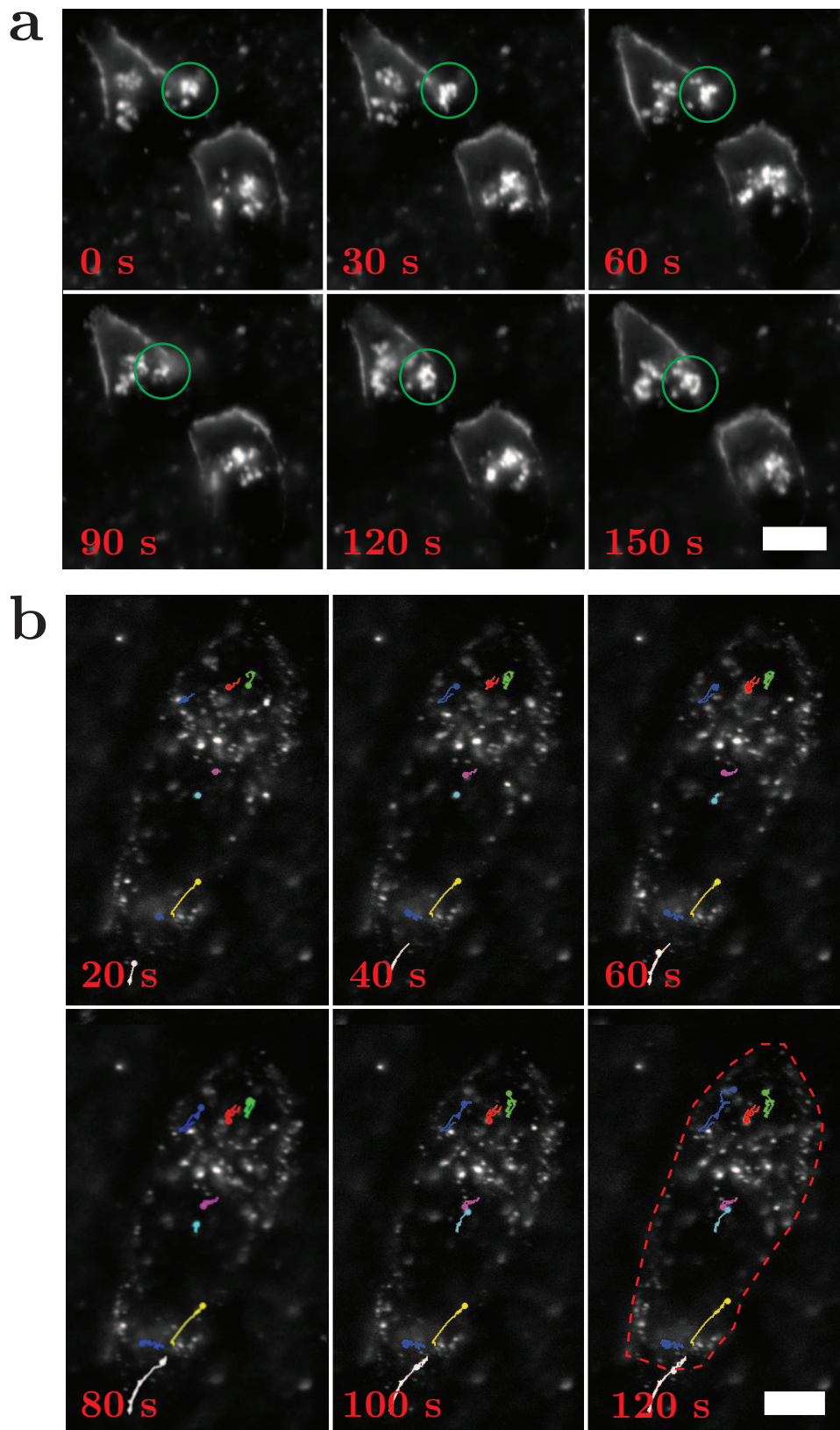


Figure 4.4: Live-cell FM images of (a) macrophages and (b) a HeLa cell after three hours incubation with 15 $\mu\text{g}/\text{mL}$ and 5 $\mu\text{g}/\text{mL}$ fiducial markers. In the green circles in (a) a group of particles is observed that is endocytosed by one of the macrophages within this time frame. In (b) particles are followed over time, trajectories and a rough outline of the cell are included in the final panel. Scale bars indicate 10 μm .

Widefield data after primary fixation

In figure 4.5 fluorescence and DIC images of the macrophages and HeLa cells after three hours of incubation with different concentrations of fiducial markers are shown. Figure 4.5a shows macrophages incubated with 0 $\mu\text{g}/\text{mL}$ fiducial markers; here, no fluorescent spots are observed. The DIC images on the other hand prove that cells are present within the imaged region. For the HeLa cells, similar observations were made when no fiducial markers were added during incubation. Therefore, it can be concluded that the fluorescent spots observed in the other images can be attributed to the fiducial markers present at these positions.

For the macrophages, significant uptake of the fiducial markers is observed after incubation with the lowest concentration of fiducial markers, 5 $\mu\text{g}/\text{mL}$. The DIC images are used here to verify that fluorescence is observed within the cells as the outline of cells is clearly visible in these images.

For the HeLa cells, uptake of the fiducial markers is also observed after incubation with 5 $\mu\text{g}/\text{mL}$ fiducial markers. However, uptake is not as distinct as for the macrophages. When the concentration of fiducial markers during uptake is increased, no pronounced increase of endocytosed particles is observed. When comparing the images after incubation with 5 and 15 $\mu\text{g}/\text{mL}$, the distribution and number of fluorescent spots within the cells seems to be more or less constant. Additionally, more fluorescence of non-endocytosed fiducial markers around the cells is observed. When the cells are incubated with a fiducial marker concentration of 50 $\mu\text{g}/\text{mL}$, the cells are surrounded by (clusters) of non-endocytosed fiducial markers. Again, no increase in endocytosis is observed. An explanation for this can be the increased probability of clustering of the fiducial markers with increasing concentration. The increased size of clusters of particles compared to the original size of the particles is expected to hinder uptake by the HeLa cells. For the iCLEM measurements it is best to reduce the number of non-endocytosed particles to reduce the signal by clusters which can be considered as background.

The results presented here show that the optimum concentration of fiducial markers is between 5 and 15 $\mu\text{g}/\text{mL}$ when an incubation time of 3 hours is used. Therefore, it was decided to use a concentration of 10 $\mu\text{g}/\text{mL}$ fiducial markers and an incubation time of 3 hours for further experiments.

Confocal data after primary fixation

For successful labelling in three dimensions, it is important that the fiducial markers are well distributed throughout the cells after endocytosis. To determine whether this is the case, confocal stacks of the macrophages (figure 4.6a and b) and HeLa cells (figure 4.6c and d) were recorded after three hours incubation with 10 $\mu\text{g}/\text{mL}$ fiducial markers. These measurements demonstrate that (groups of) particles are present throughout the entire volume of the cell that is not occupied by the nucleus which proves that labelling was successful.

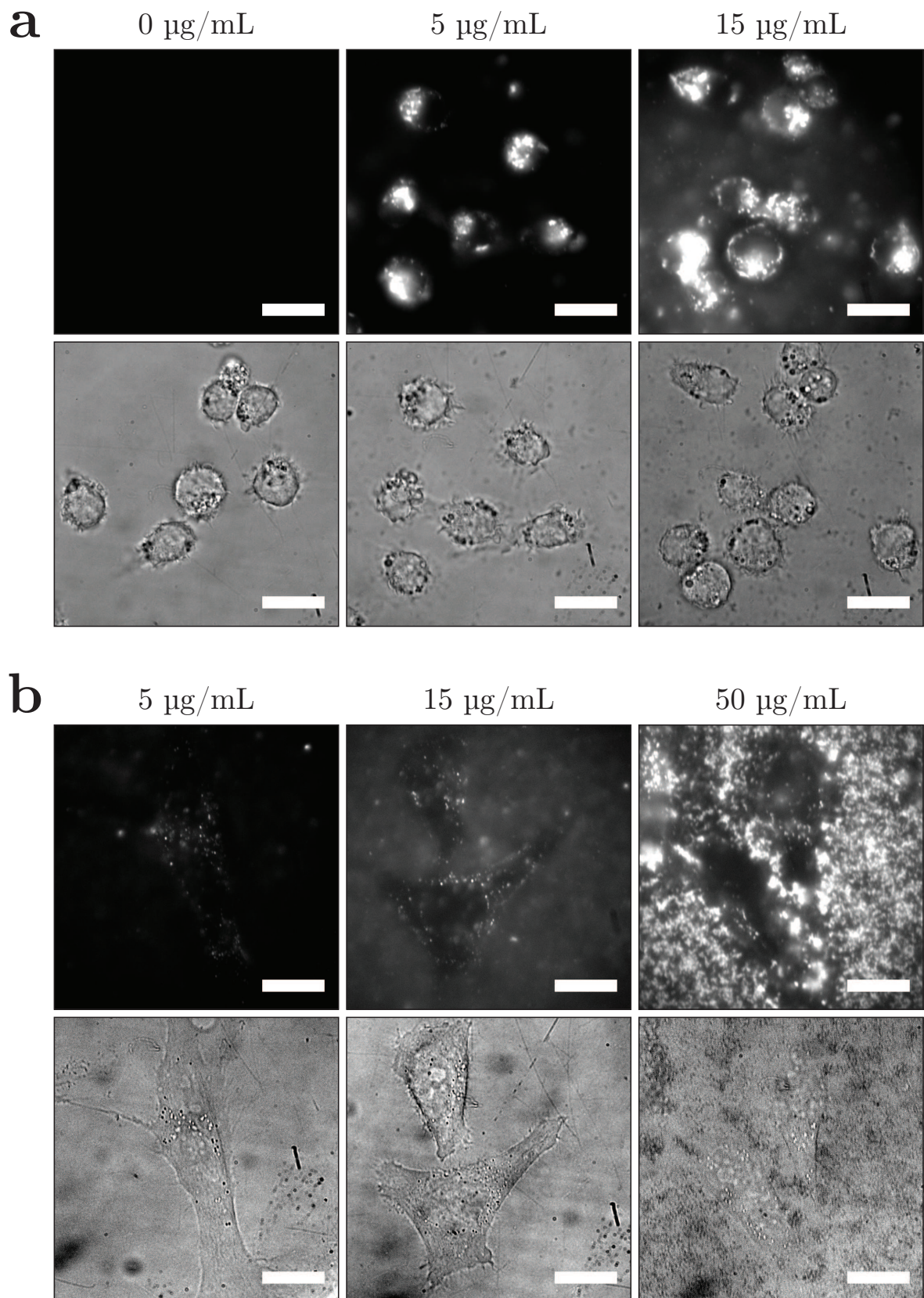


Figure 4.5: Fluorescence (top) and DIC (bottom) images of (a) P388D1 macrophages and (b) HeLa cells after incubation with different concentrations of fiducial markers. The concentration of fiducial markers during incubation is indicated above the images, all scale bars indicate 20 μm .

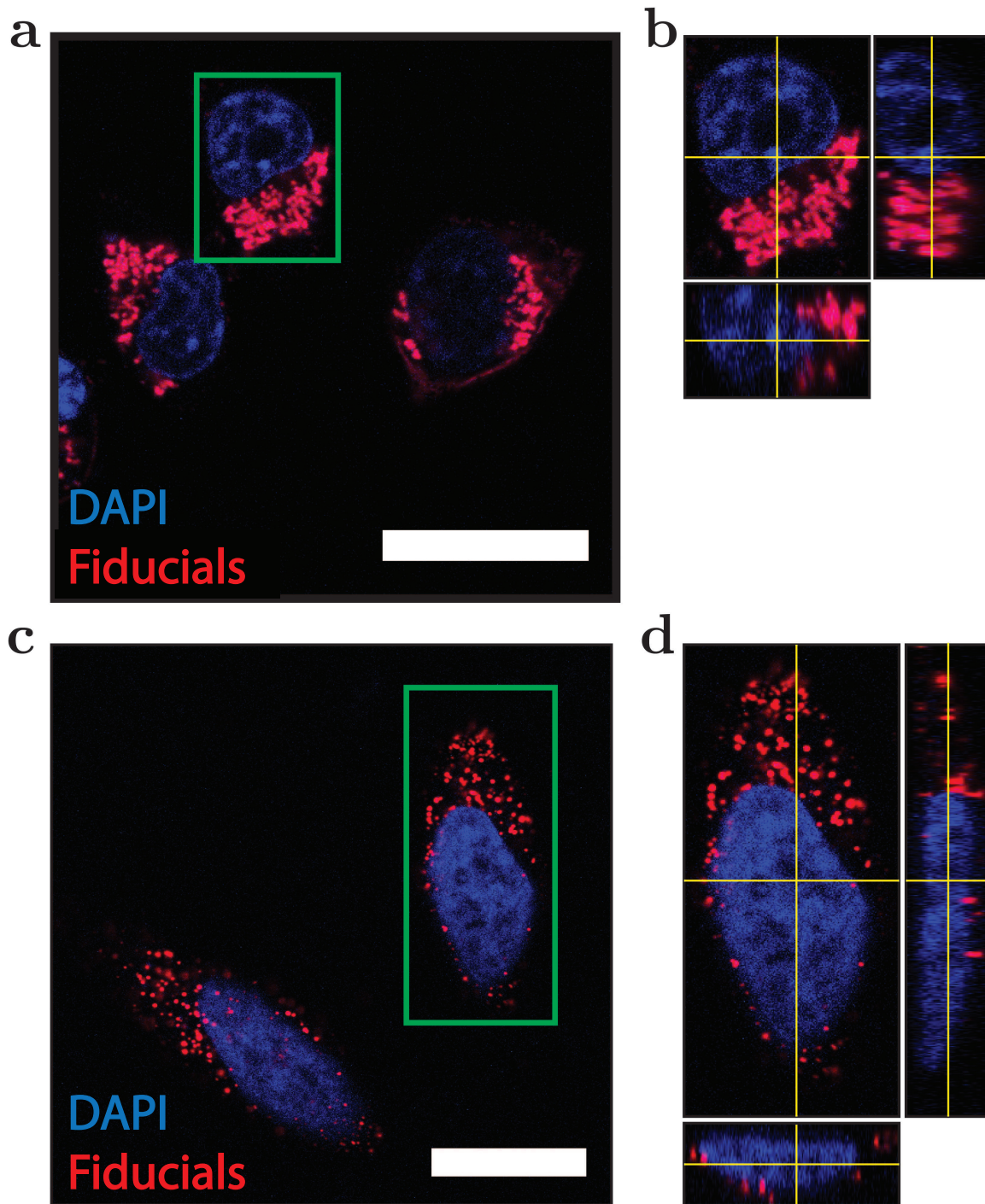


Figure 4.6: In (a) and (b) a confocal slice of HeLa cells and P388D1 macrophages after three hours incubation with 10 $\mu\text{g}/\text{mL}$ fiducial markers. In (c) and (d) an orthogonal view of the areas encircled area in (a) and (b) are included. Both scale bars indicate 20 μm .

4.3.2 Fluorescence preservation during EM sample preparation

To use the fiducial markers in iCLEM experiments, it is important that (enough of) the fluorescence is preserved after the samples are prepared for EM. To study whether this is the case, the fluorescence intensity of the endocytosed fiducial markers was monitored after the different EM sample preparation steps (also indicated in section 4.2.2). To this end, five sets of samples were prepared throughout the EM sample preparation procedure as follows:

1. After fixation;
2. After the first osmium staining;
3. After the second osmium staining and staining with uranyl acetate;
4. After lead staining;
5. After resin embedding.

In figure 4.7 representative FM images of samples prepared after the aforementioned steps of endocytosed particles are included. The fluorescence intensity decreases gradually from (1) to (4) for the macrophages and from (1) to (3) for the HeLa cells. After the final EM sample preparation step(s) a small increase in fluorescence is observed in (5).

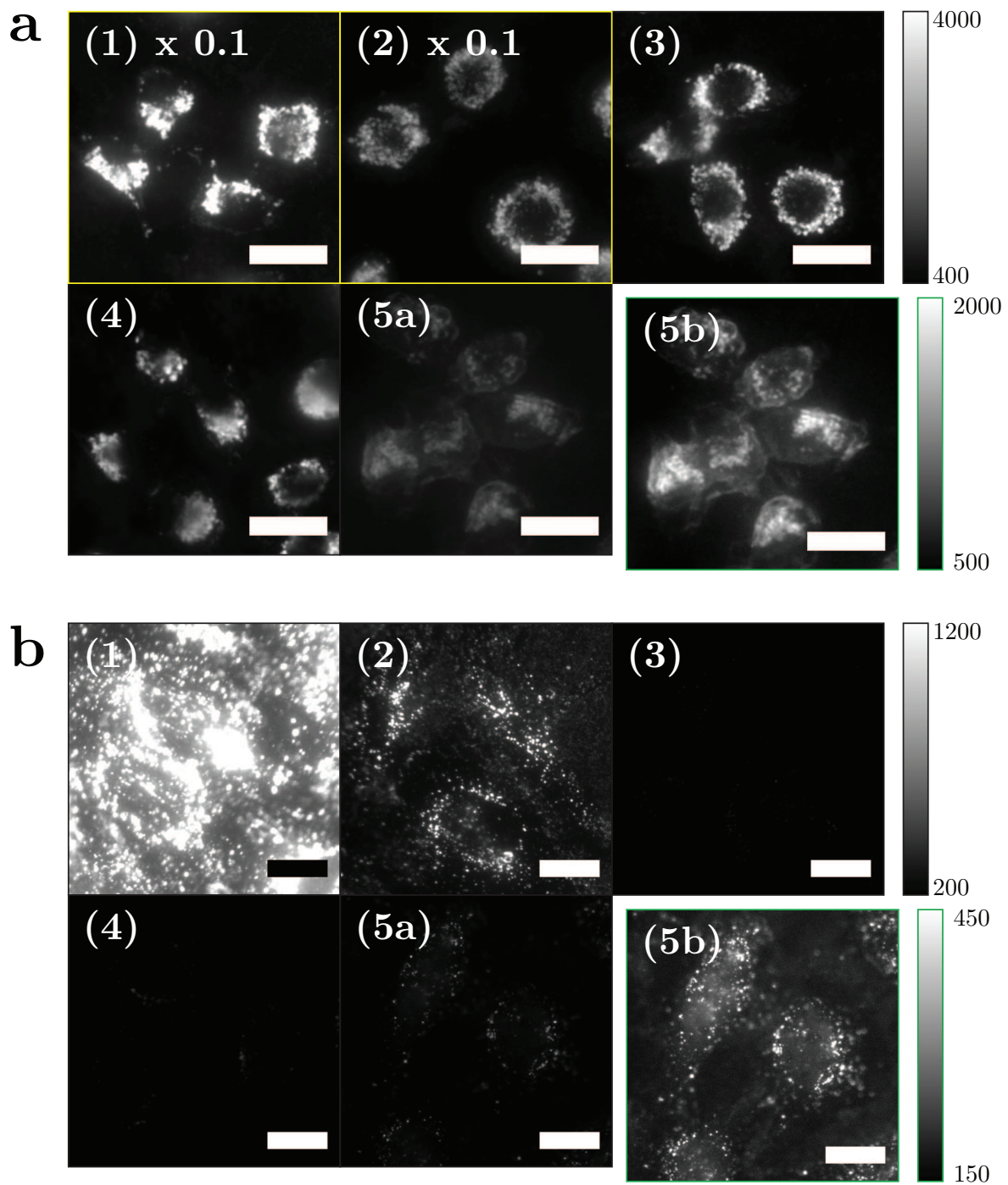


Figure 4.7: Wide field fluorescence images of (a) macrophages after cellular uptake of 128.8 nm diameter fiducial markers and (b) HeLa cells after cellular uptake of 90.8 nm diameter recorded after EM sample preparation steps (1)-(5). In both subfigures, the intensity of the first five images is scaled identically as indicated by the intensity scaling in the top right corner. Panel (5b) shows the same image as panel (5a), but rescaled to better show the fluorescent spots present in this image. All scale bars indicate 20 μm.

Both observations are confirmed when the estimated normalized fluorescence intensity of the fiducial markers is plotted as a function of the number of the EM sample preparation step, see figure 4.8a.

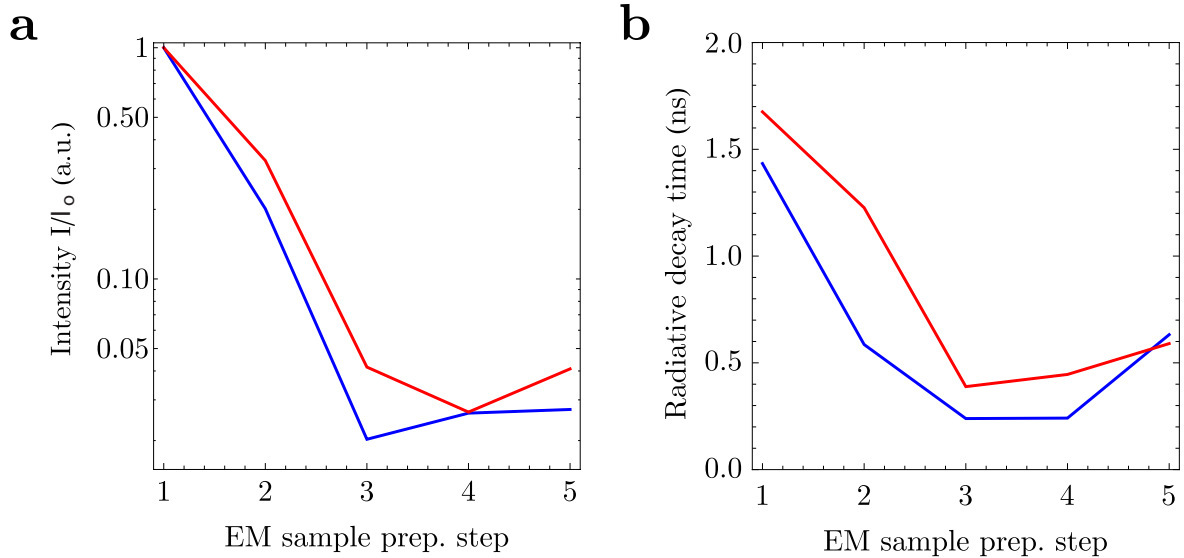


Figure 4.8: In (a) estimated values of the normalized fluorescence intensity and in (b) average radiative decay times are plotted versus the number of the EM sample preparation step. Red and blue lines correspond to data of particles endocytosed by macrophages and HeLa cells respectively.

To gain more insight in the severity of quenching, a plot of the average radiative decay time of the particles versus the number of the EM sample preparation step is included in figure 4.8b. This radiative decay time or fluorescence lifetime is related to the quantum yield of a fluorophore (see section 4.1) and corresponds to the time that a fluorophore remains (on average) in its excited state before decaying back to the ground state. Figure 4.8b also confirms earlier the observed trends: from (1) to (4) for the macrophages and from (1) to (3) for the HeLa cells, the fluorescence lifetimes becomes shorter which is indicative of increased quenching. A small recovery of the fluorescence lifetime is observed after the final EM sample preparation step(s). However, these measurements do not only reveal quenching effects. The fluorescence lifetime only drops to approximately two-thirds of its original value where the fluorescence intensity drops to below 5% of its original value.

An explanation for this underestimation is that fully quenched fluorophores do not contribute to these measurements as they no longer emit photons. In addition, excitation of fluorophores and the detection of emitted photons is less efficient for more heavily stained samples. Staining darkens the samples which makes them less transparent. Photons that could enter or exit the sample before staining are now blocked or absorbed by the heavy metals that are introduced throughout the staining procedure. The wide field transmission images recorded after the first four EM sample preparation steps shown in figure 4.9 confirm this. The cells clearly become darker and darker

(i.e. less transparent) after each EM sample preparation steps. The biggest decrease in transparency is observed after the second osmium staining and staining with uranyl acetate in (3). After this step, also the largest decrease in fluorescence intensity is observed.

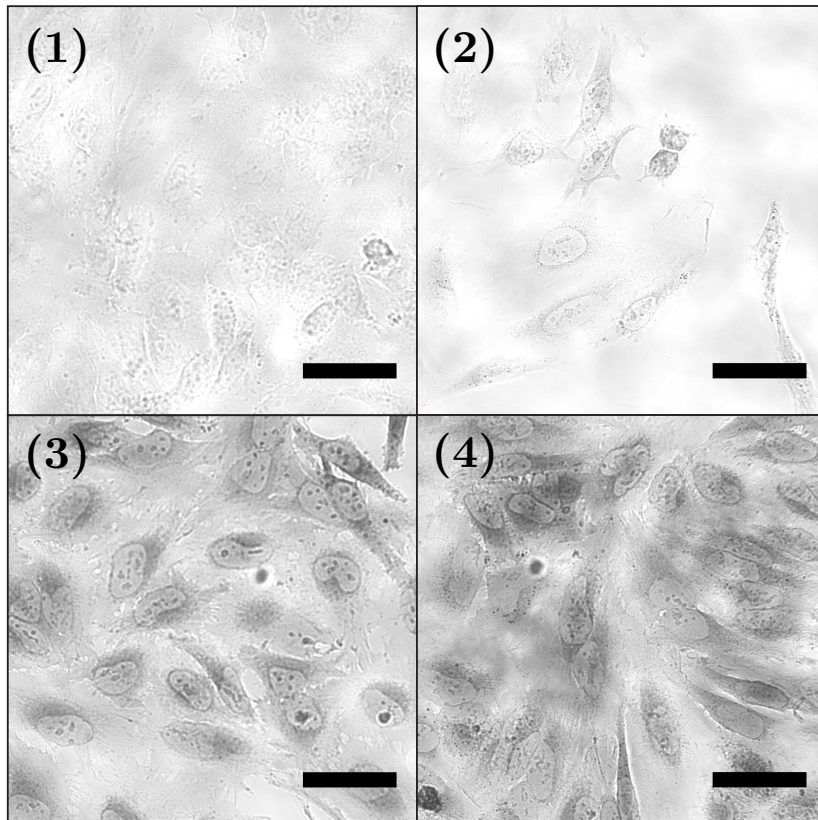


Figure 4.9: Wide field transmission images of HeLa cells after cellular uptake of fiducial markers recorded after EM sample preparation steps (1)-(4). The intensity scaling is identical for all four images and all scale bars indicate 50 μm

4.4 Osmium exposure experiments

In the previous experiments it was observed that most of the fluorescence intensity of the particles is lost in the first three steps of the ETLP procedure to prepare samples for EM. Both, the second and third step, involve exposure of the sample to a solution of osmium tetroxide in water. Therefore, it is hypothesized that the loss in fluorescence intensity can be reduced by reducing the time that the samples are exposed to this solution. To test this hypothesis, the fluorescence intensity of fiducial markers on a glass substrate is measured as a function of the osmium tetroxide exposure time. The results of this experiment are summarized in figure 4.10.

The data in figure 4.10 confirms that the loss in fluorescence intensity of the fiducial markers can be reduced by reducing the osmium exposure time. The largest decrease in fluorescence intensity is observed between 30 and 60 minutes exposure time. Therefore, the osmium staining time to prepare samples for EM is reduced from 90 to 30 minutes.

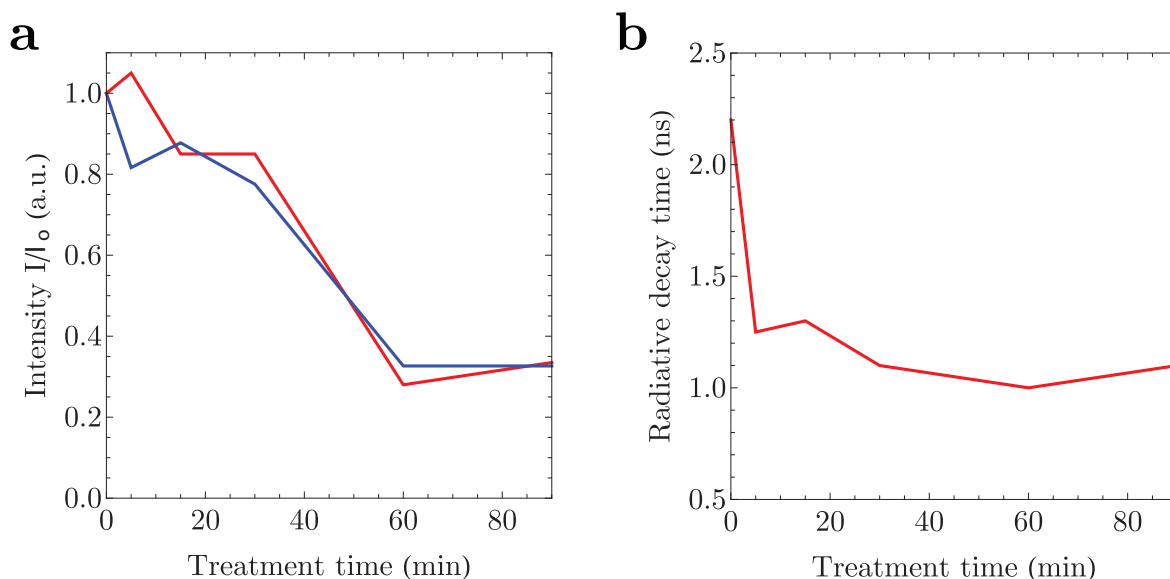


Figure 4.10: In (a) normalized single particle fluorescence intensities determined with Thunderstorm (red) and Otsu (blue) and in (b) average radiative decay times are plotted versus the osmium treatment time.

To determine whether this approach is successful, a representative SEM image of HeLa cells prepared following to the ETLP procedure with the reduced osmium staining time of 30 minutes is included in figure 4.11. This image shows that membranes and morphological details are clearly visible throughout the entire volume that was imaged. No differences in contrast are observed when comparing regions that are closer to the glass coverslip and regions that are further away from it. This indicates that 30 minutes of heavy metal staining is enough to uniformly penetrate the entire specimen. An explanation for this can be the limited thickness of this sample. The HeLa cells are only a few micrometers thick and are only covered by a very thin layer of Spurr's resin after thin-layer embedding.

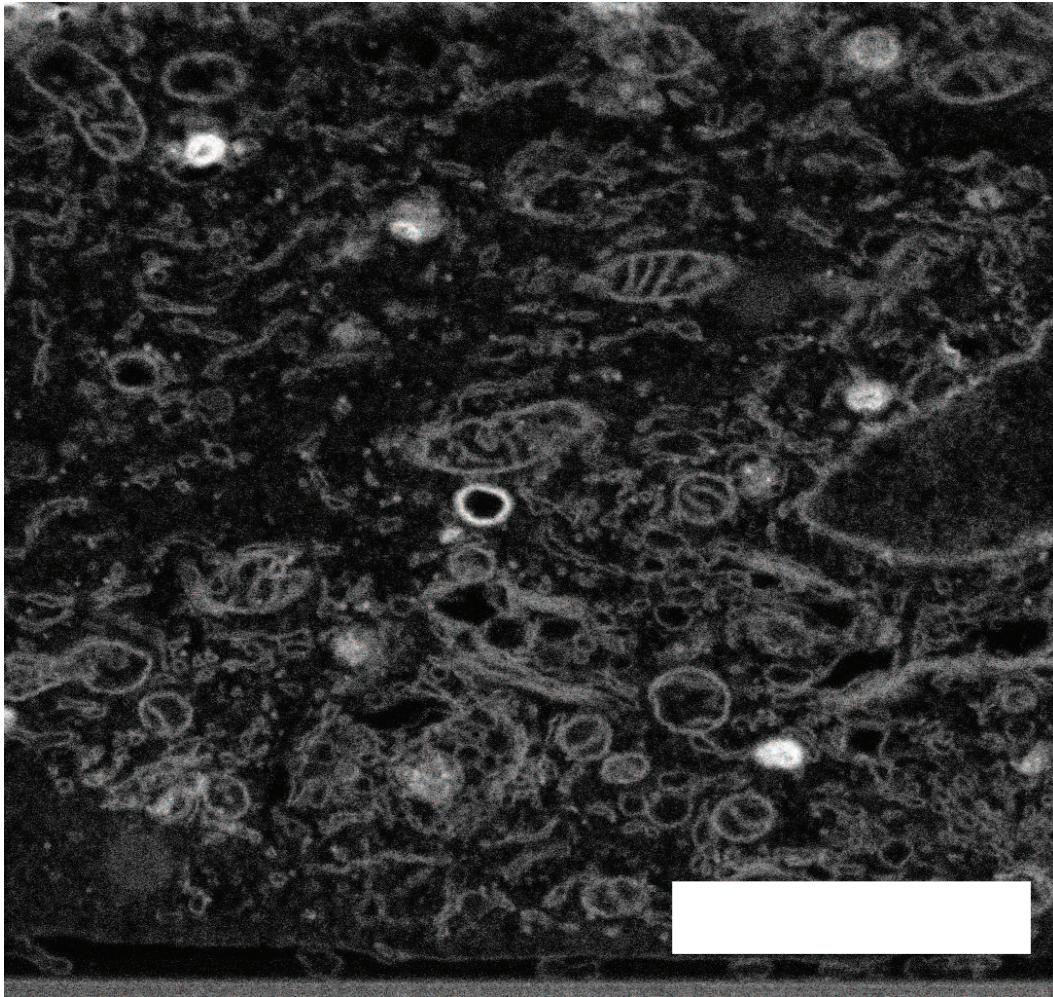


Figure 4.11: HeLa cells imaged in the FIB-SEM prepared according to the ETLF protocol with a reduced osmium staining time of 30 minutes. The glass coverslip is at the bottom of this image and the scale bare indicates 2 μm .

4.5 Fiducial markers in 3D iCLEM

In figure 4.12 2D projections of the fluorescence (a) and reflection (b) images of the endocytosed fiducial markers in HeLa cells are included. These images are constructed from a 3D stack that was recorded with the earlier presented iCLEM setup where the CLSM is integrated into the Scios FIB-SEM chamber. The measurements were performed under the vacuum conditions required for SEM operation to test whether the particles remain fluorescent under these conditions. In the fluorescence data, distinct fluorescent spots indicating the presence of (groups of) particles are observed. This proves that fluorescence is preserved throughout the final EM sample preparation steps and that the particles remain fluorescent under the vacuum conditions that are required for SEM.

In the fluorescence images, only the particles are visible and information about cellular structures or the outline of cells is absent as no other fluorescent labels are present. In the reflection image in (b) on the other hand, the outline of a cell is clearly visible. Therefore, this data can be used to navigate over the sample. Within the cell, the $3 \times 3 \mu\text{m}$ region of interest indicated by the green square in (a) and (b) is selected for further EM processing. Based on the fluorescence image, this region should contain (at least) three (groups of) particles.

In figure 4.12c a SEM image of the same cell is included. Before this image was recorded, the sample was transferred between the CLSM and SEM positions. Typically, this transfer has an accuracy of $2 \mu\text{m}$. To select which $3 \times 3 \mu\text{m}$ region should be imaged in FIB-SEM it is therefore necessary to first improve the correlation accuracy. As there are great similarities between the reflection data in (b) and the SEM image in (c), the reflection data could be used to correct for this transfer error. Finally, the region of interest that was originally selected in the fluorescence data could be identified in the corrected SEM image.

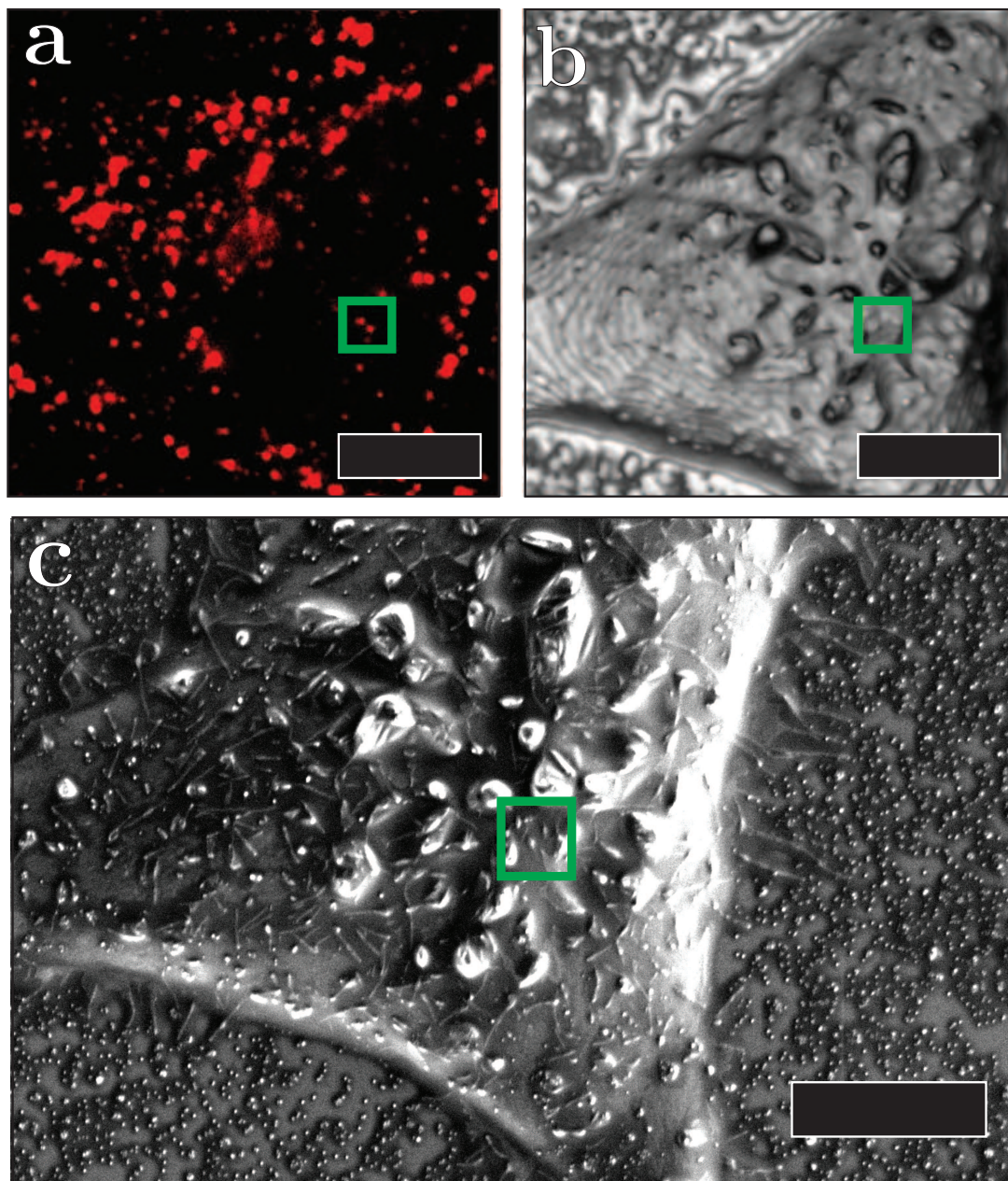


Figure 4.12: 2D projections of a 3D stack of fluorescence (a) and reflection (b) images of HeLa cells after 3 hours incubation with fiducial markers. The stack was recorded under vacuum conditions using the iCLEM setup. The area indicated by the green square is chosen as the region of interest for further FIB-SEM investigation.

In figure 4.13a, a representative 2D slice (X,Y) through the 3D FIB-SEM data stack selected in figure 4.12 is included. In this slice, three groups of particles can be recognized as indicated in (b). In (c) a magnified image of the fluorescence data of the same region is included, also showing that three fluorescence spots are present within this region. Finally, in (d) an overlay of the fluorescence and FIB-SEM data is created, here the fluorescence signal perfectly overlaps with the position of the fiducial markers.

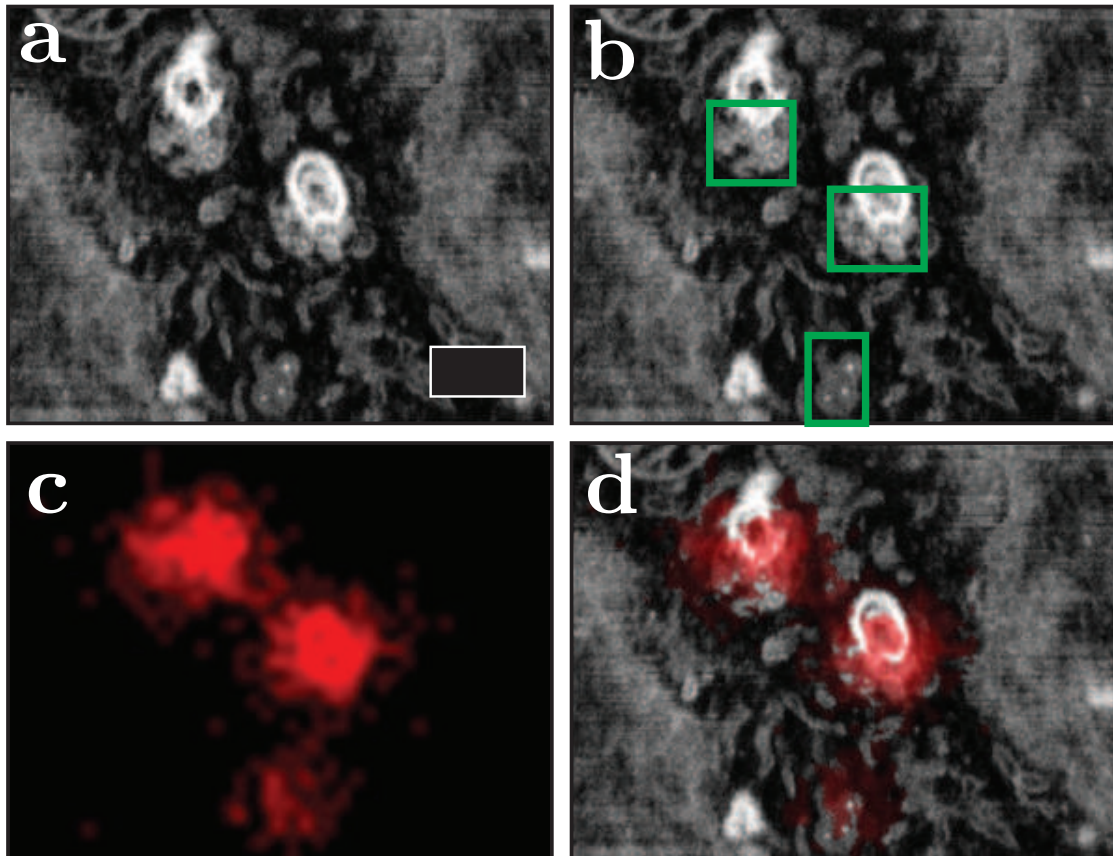


Figure 4.13: Correlation between the fluorescence and the 3D FIB-SEM data. (a) A virtual 2D slice (X,Y) through the 3D FIB-SEM data stack. Three groups of particles can be identified in the virtual FIB-SEM slice. The groups are indicated by the green squares in (b). (c) shows a magnified view of the region of interest in the fluorescence image 4.12a. In (d) an overlay of the fluorescence and FIB-SEM data is shown.

4.6 Conclusion and Outlook

In this chapter the use of the fiducial markers presented in chapter 3 is explored in 3D (i)CLEM experiments. To this end, first, the possibility to label cells with the fiducial markers via cellular uptake is investigated. 3D labelling proved to be possible for both cell lines that were tested; P338D1 mouse macrophage cells and HeLa cells were successfully labelled with 129 nm and 91 nm diameter particles respectively. For both cell lines, good three-dimensional labelling was achieved by incubation of the cells with 10 $\mu\text{g}/\text{mL}$ of fiducial markers dispersed in cell culture medium.

After labelling and fixation, the cells were prepared for EM following the extremely thin layer plastification or ETLT protocol developed by van Donselaar et al. [98]. Following this procedure, the cells were stained with heavy metals (osmium, uranyl and lead) and embedded in a thin layer of Spurr's resin. Throughout this procedure a large drop in fluorescence intensity of the fiducial markers was observed. Less than 5% of the original fluorescence intensity was preserved after carrying out all steps of the protocol. The largest drop in fluorescence intensity was observed when samples were stained with osmium. A similar drop in intensity was also observed when the fiducial markers were exposed to an osmium tetroxide solution for an increasing amount of time. Therefore, the osmium staining time in the ETLT protocol was shortened from 90 to 30 minutes to prepare the final iCLEM samples. This did not lead to any observable decrease in the image quality of the FIB-SEM images; all morphological features of the cells remained visible and well-contrasted.

The next step was to test the particles in a realistic cellular iCLEM experiments. To this end, HeLa cells with 90 nm fiducial markers were studied with the iCLEM setup that was developed by co-workers within this project. In this setup, a CLSM is integrated into the Scios FIB-SEM chamber. The measurements prove that the ~ 100 nm particles can be used as fiducial markers in cellular experiments. The particles can be clearly recognized in the FIB-SEM images by their distinct core-shell structure. And more importantly, enough fluorescence was preserved to detect the particles in fluorescence images. This observation shows that the particles are very promising for biological iCLEM experiments.

The workflow presented here can be expanded to also include fluorescence labelling steps for the recording of fluorescence images of, for instance, specific proteins in cells. The fluorescence of these labels in general do not survive EM sample preparation. However, fluorescence images recorded both before and after EM sample preparation will show the fiducial markers. As the fiducial markers are also visible in the EM images they can be employed as a set of reliable reference points in both FM images and the EM image. They can help to mitigate the effect of distortions of the specimen due to EM preparation but also due to shrinkage by the e-beam of the EM and transfer of the specimen. The use of these fiducial markers offers the potential to greatly enhance the accuracy and reliability of the correlative analyses, both in integrated and non-integrated CLEM approaches.

Despite the (commercial) availability of integrated CLEM setups, the majority of CLEM measurements is still performed in a non-integrated fashion. An explanation for this is that the easiest way to circumvent the trade-off between FM and EM compatibility of samples is simply by recording FM data before preparing samples for EM [64]. In non-integrated CLEM, the particles can be used to detect and correct sample distortions that are easily introduced as samples are very fragile before fixation and plastification.

There is plenty of room to improve the results presented in this chapter. A very heavy staining protocol was employed in the EM preparation. For many experiments, milder staining suffices. Therefore, it would be interesting to test milder staining conditions as this can increase the fluorescence signal of the particles. Additionally, strategies to protect the fiducial markers from the added heavy metals are worthwhile to explore. The addition of an outer non-fluorescent silica shell can, for example, prevent quenching of fluorophores. In the current situation, excited state migration allows the excited state to move from fluorophores inside the particles towards fluorophores closer to the outer surface (see chapter 2). As the particles are surrounded by heavy metals, this increases the probability of fluorescence quenching. The addition of a non-fluorescent outer shell could prevent this as this shell acts as a quenching barrier. If the fiducial markers are fully penetrated by the heavy metals, this approach does not work. If this is the case, it might be necessary to explore methods to make the particles less permeable for the heavy metals. The particles presented here can be used as fiducial markers but are too big for fluorescent labelling. By protecting the particles from the heavy metals and by reducing the amounts of heavy metals that are added for staining it may be possible to drastically reduce the size of the fiducial markers and employ them for labelling.

Up to this point, all SEM images of endocytosed fiducial markers were based on the detection of backscattered electrons. In these images, the gold core appears as a distinct bright spot as the heavy gold atoms scatter electrons very efficiently. The shape of the surrounding silica core can also be recognized and it is this distinct core-shell structure that enables a user to reliably identify the fiducial markers, see figure 4.14a. In figure 4.14b an image of the same cellular region is obtained by the detection of secondary electrons with the in-column detector. There are great differences in contrast between these two images and apparently, a large number of secondary electrons are produced by the glass coverslip and the silica shell of the fiducial markers with respect to the surrounding cellular tissue. This observation is of great interest as the high contrast opens up possibilities for automated detection of the fiducial markers within the FIB-SEM data which turned out to be problematic when only backscattered electrons were taken into consideration.

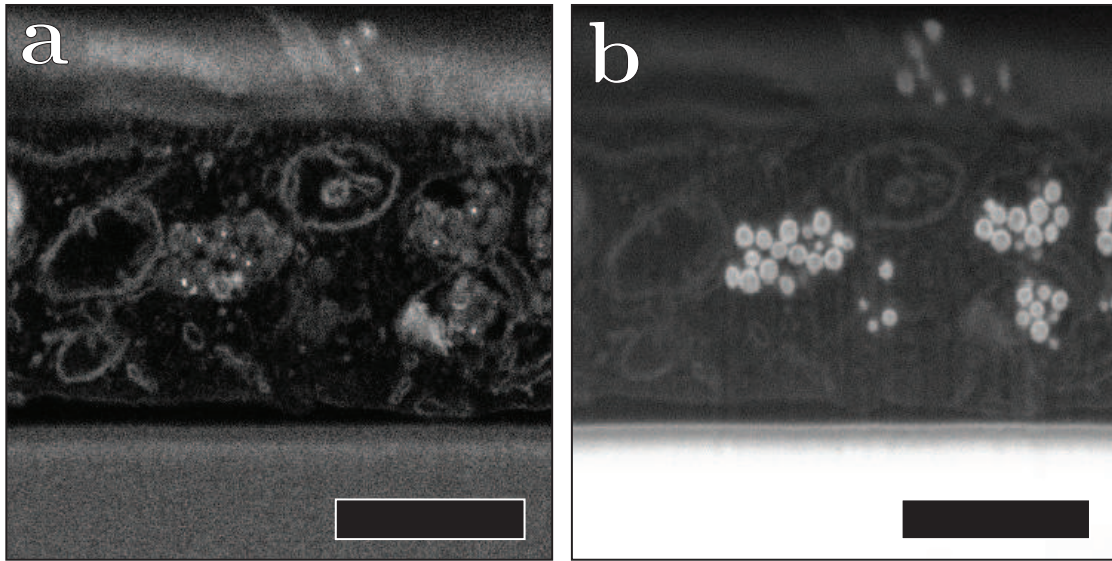


Figure 4.14: SEM images of a FIB polished cross-section of the endocytosed particles in HeLa cells imaged in backscattered electron (a) and secondary electron (b) mode.

4.7 Acknowledgments

The work presented in this chapter was a collaboration with Job Fermie and Sergey Loginov. I would like to thank and acknowledge the following persons for their contributions: Job Fermie for his help on the cellular uptake and osmium exposure experiments and the accompanying live cell, widefield and confocal measurements; Maaïke Nederend from the Laboratory for Translational Immunology of the University Medical Center Utrecht for providing the P388D1 cells; Job Fermie and Elly van Donselaar for the FIB-SEM sample preparation and Sergey Loginov, Sasha Agronskaia and Dave van den Heuvel for the wide field and radiative decay measurements that were collected throughout this procedure. The iCLEM and FIB-SEM measurements included in this chapter were performed by Sergey Loginov. Finally, I would like to thank Job Fermie, Gerhard Blab and Hans Gerritsen for critical reading of the chapter.

A Single Sample to Check the Performance of a Light Microscope

At present, a multitude of samples is required to monitor and optimize the quality and reliability of quantitative measurements of 3D (super-resolution) light microscopes. In this work, one sample is presented to substitute this multitude of samples. The sample is composed of a refractive index matched colloidal crystal of silica beads with fluorescent and gold cores and can be optimized for different objectives. The microscope can be calibrated in three dimensions using the periodicity of the crystal; the alignment of the laser lines can be checked using the reflection of the gold cores; and the point spread function (PSF) can be measured at multiple positions and depths using the fluorescent cores. It is demonstrated how this sample can be used to visualize and improve the quality of confocal and super-resolution images. In addition, it is discussed how the sample can be adjusted to meet different requirements and how it can be used to evaluate refractive index mismatches as a function of depth quantitatively.

5.1 Introduction

Reliable quantitative 3D light microscopy measurements require a well calibrated setup. Moreover, proper alignment of the microscope contributes to a higher resolving power, thereby enabling analysis at a smaller scale [121]. Calibration and alignment have become even more critical with the advent of super-resolution microscopy techniques, such as stimulated emission depletion (STED) microscopy [122, 123, 124]. Additionally, it has been demonstrated that image restoration with an experimentally measured 'point response function', referred to as the point spread function (PSF), allows for better image restoration than deconvolution with a theoretical PSF [23, 24, 121, 125, 126, 127]. Therefore, it is also important to be able to reliably measure the PSF of a setup.

Currently, a multitude of different samples and methods are needed for a complete evaluation of a light microscopy setup. First of all, calibration of the microscope in the lateral directions can be performed with commercially available stage micrometers. For calibration in the axial direction various methods have been reported [21, 128, 129, 130]. Secondly, the alignment of excitation beams is commonly checked with ~ 100 nm gold beads [131]. For STED, the same gold beads can be used to check the alignment of the depletion beam with the excitation beam, which is crucial to maximize the performance of the system. Finally, measurements of the PSF of a confocal microscope can be performed by imaging sub-diffraction sized (< 175 nm in diameter) fluorescent beads [22] or larger beads in combination with deconvolution software [21] in 3D. For STED this is more challenging, since smaller fluorescent probes (< 50 nm in diameter) are required, as the size of the probe needs to be close to, or below, the resolving power of the technique. Some suitable probes are available: DNA origami techniques for example have been demonstrated to produce sub-30-nm fluorescent beads that can be used as fluorescent probes for PSF measurements and as rulers for the calibration of a STED microscope [132, 133]. In addition, it has been demonstrated that photostable quantum dots can be imaged with STED [134, 135] and could therefore be used as fluorescent probes for PSF measurements of a STED microscope. However, to the best of our knowledge, a simple method to ensure enough separation between the probes in 2D or a method to produce 3D samples is not yet available.

While the PSF measurement and alignment methods used so far are good tools to check the performance of a microscope, these methods usually only apply to measurements close to the cover glass. With recent work using (3D) STED in combination with glycerol objectives, sub-resolution imaging far from the cover glass was demonstrated in life science specimens, where the refractive index is close to 1.45 [25, 121, 136]. In addition, knowledge of the depth dependent PSF has shown to be important for accurate 3D image reconstruction [127].

In this work, a sample for the 3D calibration and alignment, as well as the PSF measurement of a confocal (STED) microscope is presented. The sample is composed of a colloidal crystal consisting of a mixture of highly monodisperse silica beads with a gold or fluorescently labelled silica core. The crystal is refractive index matched with an embedding solvent mixture, resulting in optimal imaging and an effective refractive

index similar to life science specimens optimized for glycerol objectives. The periodicity of the crystal in the lateral and axial directions is used to perform calibrations. The gold cores are used to image the excitation and depletion spots in reflection and to align the STED microscope. The fluorescent cores are individually resolvable as they are separated by a non-fluorescent silica shell and can therefore be used for PSF measurements at different positions and depths in the sample.

We will first show how the sample can be used for the calibration of lateral and axial distances of a microscope. Second, we demonstrate the alignment and PSF measurement of a confocal and STED microscope, also at different depths. Next, we demonstrate the importance of proper alignment of the excitation and depletion lasers of a STED microscope and how this can be achieved using the presented sample. In addition, we will discuss how the sample can be tailored by adjusting the synthesis of the silica beads and composition of the sample for different objectives. We will discuss how the sample can also be used to study the effects of refractive index mismatching on the PSF by intentionally mismatching the particles and the solvent mixture, as well as between the sample, cover glass and the immersion liquid of the objective.

5.2 Experimental details

5.2.1 Synthesis of the particles

In this section, a description of the synthesis of the particles two types of core-shell particles that were used for the calibration sample is described. The synthesis was performed in various steps that were partially performed in parallel as illustrated in figure 5.1.

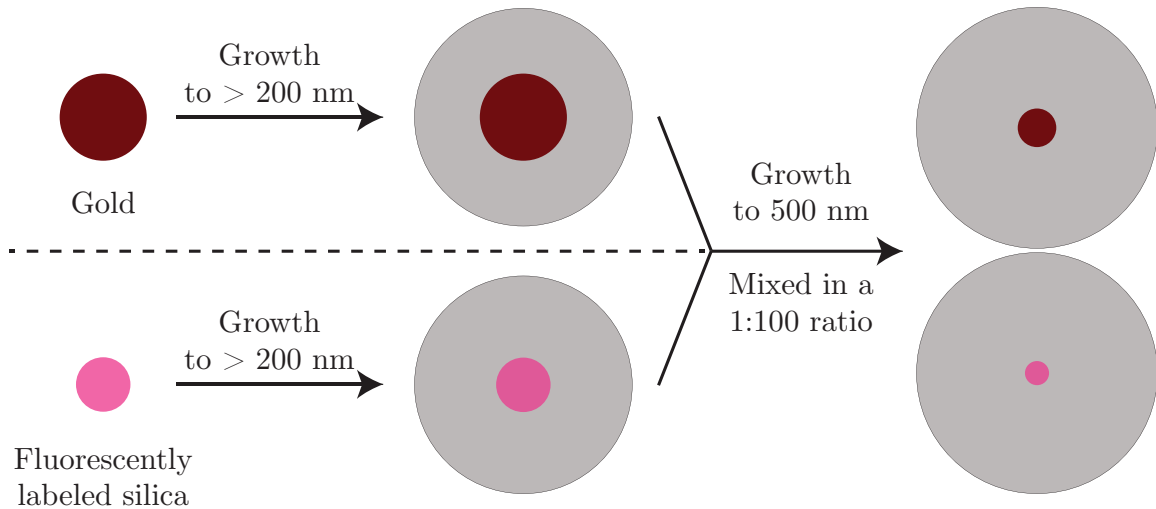


Figure 5.1: A schematic representation of the synthesis of the particles that were used to grow a colloidal crystal. Gold and fluorescently labelled silica cores were coated with silica to obtain 200 nm diameter particles. Next, the aforementioned particles were mixed in a 1:100 ratio and silica growth was continued to reach a final size of 500 nm.

In the first step, 80 nm diameter citrate stabilized gold nanoparticles were functionalized with PVP, transferred to ethanol and coated with silica [79]. In parallel, fluorescently labelled silica spheres were synthesized in a reverse micro-emulsion. This method was chosen because of its simplicity, its reproducibility and because of the high monodispersity in shape and size of the particles obtained via this method. Covalent incorporation of the fluorophore was ensured by linking a fluorophore that contains an active amine reactive group such as an isothiocyanate group, with an aminosilane; (3-aminopropyl)triethoxysilane or APTES [27, 81, 137]. This procedure was originally used by van Blaaderen, Imhof and Verhaegh to synthesize fluorescently labelled silica spheres via the traditional Stöber method. However, it is demonstrated that fluorophores and nanoparticles are also successfully incorporated in the particles when the spheres are synthesized in a reverse micro-emulsion [138, 139, 140]. These fluorescent cores are also coated with a layer of non-fluorescent silica via seeded growth. Silica growth of both types of particles was continued to obtain particles with a final diameter of at least 200 nm.

To obtain the 500 nm diameter particles that were used to grow the colloidal crystal, a second growth step was performed. This growth can be divided into two steps: first silica coating of the fluorescent cores was continued until a total diameter close to the diameter of the silica coated gold particles was reached. Once this size was reached, the silica coated gold particles were added to the reaction mixture to obtain a 1 to 100 ratio of particles with a gold versus particles with a fluorescent core. After homogenization of the reaction mixture, silica growth was continued until the particles have a total diameter of ~ 500 nm.

Materials

A stabilized suspension of 80 nm diameter gold nanoparticles in citrate buffer (OD 1), tetraethyl orthosilica or TEOS (reagent grade, 98%), polyvinylpyrrolidone or PVP (average Mw 10.000 g mol⁻¹), ammonium hydroxide (ACS reagent, 28-30 w% NH₃ basis) Cyclohexane (laboratory reagent, 99.8%), Igepal CO-520, *N,N*-dimethylformamide or DMF (anhydrous, 99.8%), Rhodamine B isothiocyanate (mixed isomers) or RITC and 99% (3-Aminopropyl)triethoxysilane or APTES were purchased from Sigma-Aldrich and used as received. Absolute ethanol was purchased from Merck.

Silica coating of 80 nm diameter gold nanoparticles

PVP functionalization of the gold nanoparticles was performed by transferring 20 mL of the gold nanoparticle solution and 400 μ L of a 10% (w/v) PVP solution (1 g in 10 mL water) to a vial. The obtained solution was stirred for 16 hours to ensure functionalization of the particles. Next, the solution was transferred to 5 mL eppendorf tubes and centrifuged 5 minutes at 5.000 rcf. The supernatant was removed as much as possible with a glass pipette and the gold nanoparticles were redispersed in 2.5 mL ethanol and collected in a 4 mL glass vial.

Silica coating was performed in a closed 4 mL vial under constant stirring at 600 rpm and was initiated by the addition of 250 μ L ammonia and 25 μ L of a 10 vol% solution of TEOS in ethanol. These additions were followed by the addition of 50, 100 and 200 μ L of 10 vol% after 90, 270 and 360 minutes. 90 minutes after the final addition, the solution was transferred to a 20 mL vial and diluted with ethanol to obtain a total volume of 20 mL. This solution was centrifuged 15 minutes at 1.000 rcf and after removal of the white turbid supernatant the particles were redispersed in 20 mL ethanol by sonication. Centrifugation and redispersion of the particles was repeated to remove empty silica spheres formed by secondary nucleation. After the final centrifugation step, the particles were redispersed in 10 mL ethanol.

Synthesis of fluorescent cores coated with a non-fluorescent silica shell

Dye-APTES coupling was performed prior to the synthesis by transferring 6,00 mg RITC, 500 μ L absolute ethanol and 12 μ L APTES to a vial. The vial was wrapped in aluminium foil and stirred for 5 hours. A reverse micro-emulsion was prepared by transferring 50 mL cyclohexane and 6.5 mL Igepal CO-520 to a vial under vigorous stirring (700 rpm). As soon as a clear solution was obtained, 400 μ L TEOS was added to the solution. After 2 minutes stirring, 50 μ L of dye-APTES solution was added resulting in the formation of a colourless solution. After an additional 5 minutes of

stirring to ensure complete homogenisation, 750 μL ammonia was added to initiate the reaction. Immediately after this addition, the solution turned pink. After an additional minute of stirring the solution was stored in dark place for the reaction to proceed.

After 24 hours, the reaction mixture was transferred to a round bottomed flask. The cyclohexane was evaporated under reduced pressure (~ 10 mbar) using a rotary evaporator. Evaporation was performed under vacuum and the flask was placed in a room temperature water bath. After 20 minutes, a very viscous, pink solution of fluorescent silica particles dispersed in the non-ionic surfactant, Igepal CO-520, was obtained. 10 mL DMF and 10 mL absolute ethanol were added to this liquid which resulted in the formation a clear, non-scattering, pink solution.

Further silica coating of the fluorescent cores was performed by transferring 5 mL of the fluorescent core solution, 3.45 mL absolute ethanol, 1.11 mL water and 0.45 mL ammonia to a three necked round bottomed flask. Under gentle stirring (200 rpm) and nitrogen flow a 3 times diluted solution of TEOS in ethanol was added to the solution using a syringe pump. A water/ammonia/ethanol solution was added simultaneously to keep the water and ammonia concentrations constant. The addition rate was set at 0.32 mL/h. After 20 hours (6.54 mL added), the addition rate was doubled. After 10.98 mL of TEOS solution was added, the syringes were refilled and the addition of TEOS and water/ammonia/ethanol was continued until a total volume of 30.13 mL was added.

After silica growth, the solution was transferred to two 50 mL eppendorf tubes and centrifuged 30 minutes at 2000 rcf. Particles were redispersed in 20 mL absolute ethanol by sonication, collected in one vial and stored in the fridge.

Further silica growth of a mixture of the two types of particles

93 mL ethanol, 1.8 mL of silica coated fluorescent cores and 12.4 mL water were transferred to a 250 mL round bottomed flask. The obtained solution was sonicated for an hour before growth was started. Under gentle stirring (200 rpm) and nitrogen flow, 3 mL of a 3 times diluted solution of TEOS in ethanol was added to the solution using a syringe pump with an addition rate of 0.65 mL/h. A water/ammonia/ethanol solution was added simultaneously to keep the water and ammonia concentrations constant.

After this first growth step, a TEM sample was prepared to determine whether the size of the particles matched the size of the silica coated gold particles. The TEM measurements showed a good match: the diameter of the the particles was determined to be 313.3 ± 5.8 nm while the silica coated gold particles have an average diameter of 321.5 ± 13.7 nm (see section 5.3). 8.8 mL of the solution of silica coated gold particles was sonicated for an hour and added to the reaction mixture. The concentration of gold particles and the weight fraction of the fluorescently labelled silica cores was used here to determine how much of this solution should be added to obtain the desired 1:100 ratio between the two types of particles. Next, growth was continued by the simultaneous addition of 17.16 mL of the diluted 3 times dilutes solution of TEOS in ethanol and the water/ammonia/ethanol solution with an addition rate of 1.00 mL/h.

After silica growth, the solution was transferred to three 50 mL eppendorf tubes and centrifuged 30 minutes at 500 rcf. After repeated centrifugation and redispersion of the particles, all particles were redispersed in 40 mL absolute ethanol by sonication, collected in one vial and stored in the fridge.

5.2.2 Colloidal crystal growth and characterization

Colloidal crystals growth is performed following a procedure based on the method developed by Jiang *et al.* [141]. In the work by Jiang *et al.* it is demonstrated that colloidal crystals of silica spheres can be obtained by placing a microslide vertically in a diluted solution of colloids in ethanol. During the controlled evaporation of ethanol at room temperature, the silica spheres spontaneously crystallize onto the microslide into long range (~ 1 cm) close-packed arrays. It is demonstrated that the thickness, or number of layers, of these colloidal crystals can be controlled from two to several hundreds of layers by varying the particle size and the concentration of particles in the solution used for colloidal crystal growth. Typically, for higher volume fractions and smaller particles, thicker (i.e. more layers) crystals are obtained. It is also demonstrated that thicker crystals can be obtained by repeating the growth procedure, i.e. by performing multiple dipping's.

The method of Jiang *et al.* is very successful for small particles. However, when larger particles, such as the 500 nm diameter particles in this work, are used and when it is desired to grow thick crystals, adjustments are necessary. The main reason for this is that sedimentation of the particles happens already in the first (few) hours of the colloidal crystal growth making it impossible to grow thick colloidal crystals in one dipping. Various methods to overcome this problem can be found in literature, key point in these methods is to speed up the evaporation of the process by increasing the evaporation speed, either by increasing temperature [142, 143] or decreasing the pressure of the surrounding medium [144]. In this work, colloidal crystal growth was performed at elevated temperature by performing the growth inside a preheated oven.

Materials

Absolute ethanol was purchased from Merck. 24×50 mm #1.5H cover glasses were ordered from Marienfeld Superior and cleaned with soap and rinsed with water and ethanol prior to use.

Methods

For crystal growth, 8.00 mL of a 1.0 vol% solution of the ~ 500 nm diameter particles in ethanol were transferred to a 20 mL glass vial. This vial and a 100 mL beaker filled with ethanol were placed inside a 50°C preheated oven (RS-IF-203 Incufridge, Revolutionary Science) and covered with a large beaker. After approximately 16 hours, the cover glass was removed from the solution. An opaque deposition of particles was observed on one side of the cover glass. Under the right illumination angle Bragg reflections were observed which indicates the formation of a crystalline structure. For the growth of thicker crystals, growth steps were performed by repeating this process up to three times.

FIB-SEM to study the crystal structure

Focused ion beam scanning electron microscopy (FIB-SEM) tomography measurements were used to characterize the structure of the colloidal crystal [145]. For this, a colloidal crystal with slightly larger particles ($d = 531$ nm, $< 2\%$ PDI) then used in the calibration sample was studied. After growth, the colloidal crystal was infiltrated with the resin Lowicryl HM20. Infiltration of the crystal improves the finish of the milling process. Moreover, embedding the individual particles into a matrix prevents the particles to fall out of the crystal whilst slicing. The resin was composed of a 3:17 weight ratio mixture of Crosslinker D (Electron Microscopy Sciences) and Monomer E (Electron Microscopy Sciences). As initiator 0.5 w% dibenzoyl peroxide (Merck) was added. The crystal was infiltrated with resin which was subsequently cured at 65°C in an oven overnight.

The glass slide with the embedded crystal was attached to an aluminium SEM stub with carbon tape. A strip of carbon tape made contact between the crystal on top of the glass slide and the SEM stub to create an electrically conductive pathway. Subsequently, the ensemble was coated with a 5 nm thick layer of platinum, using a Cressington HQ280 sputter coater.

A standard FIB-SEM tomography (Scios, AutoSliceAndViewG3 1.7.2, Thermo Fisher, former FEI) routine was carried out after protecting an area of interest with in-situ platinum deposition (~ 1 μm thickness) and preparing side trenches and an alignment marker. Milling conditions during the tomography run were 30 kV, 300 pA. The slice thickness was 75 nm. Images were recorded in BSE mode with 3.5 kV, 25 pA. The scan resolution was 3904×4096 which corresponded to a (horizontal) pixel size of 6.2 nm. The pixel dwell time was 10 μs . The series were recorded with the build-in autofocus routine to ensure a high quality focus during the series. The coordinates of the particles in the crystal were determined from the FIB-SEM tomogram as described in ref. [146].

5.2.3 Refractive index matching to minimize scattering

To optimize the imaging conditions, the colloidal crystals should be infiltrated with a liquid with the same refractive index as the silica spheres. This refractive index matching minimizes scattering by the silica spheres as can be seen from the formula below for backward reflection of a dielectric material [147]. In this formula, R is the ratio of reflected beam power to incident beam power, n_1 is the refractive index of the liquid that is used for immersion, and n_2 is the refractive index of the dielectric solid (i.e. the silica spheres). When $n_1 = n_2$, $R = 0$ indicating that no light is reflected by the silica spheres.

$$R = \left| \frac{1 - \frac{n_1}{n_2}}{1 + \frac{n_1}{n_2}} \right|^2 \quad (5.1)$$

A study was carried out to determine the refractive index of the particles. Because this refractive index is temperature and wavelength dependent [148] this study was carried out under the same conditions as used during confocal/STED measurements. Therefore, all measurements were carried out at 21°C, the estimated temperature in the confocal/STED setup, and transmittance is determined at 550 nm, the excitation wavelength used for confocal measurements.

The refractive index of the particles is determined by dispersing a fixed amount of particles in solutions with increasing refractive index. These solutions are prepared by mixing two solvents with different refractive indices in various ratios [149]. Next, the transmittance of these solutions is determined because it will reach a maximum when the refractive index of the particles and the solution match. The region of refractive indices that was studied, was chosen to be around $n_D = 1.45$ because for Stöber silica, n_D values ranging from 1.43 to 1.462 are reported in literature [137, 150]. Two non-volatile solvent with refractive indices above and below 1.45 were selected for this: dimethyl sulfoxide or DMSO ($n_D^{25} = 1.4768$ [151]) and 1-pentanol ($n_D^{20} = 1.4100$ [152])

Materials

Dimethylsulfoxide or DMSO (99.99%) and 1-pentanol (99%) were purchased from Sigma Aldrich and used as received.

Methods

First, the relationship between the vol% DMSO in 1-pentanol and the refractive index at 550 nm and 21°C (n_{550}^{21}) was determined. To do so, a range of solutions going from 0 to ~85 vol% DMSO in 1-pentanol to pure DMSO was prepared. With an Atago 3T refractometer, the n_D^{21} and the corresponding Cauchy's equations of these solutions were determined. The Cauchy's equations were used to calculate the refractive index at 550 nm (n_{550}^{21}) [148].

For refractive index matching of the particles, 6.51 mL of a 1.92 vol% solution of particles in ethanol was transferred to a 20 mL glass vial and the ethanol was evaporated by placing this vial in a 50°C preheated oven for 16 hours. Next, the particles were redispersed in 5 mL 1-pentanol by by sonication to obtain a 2.5 vol%

stock solution of particles in 1-pentanol. 0.5 mL of the stock solution of particles and various volumes of DMSO and 1-pentanol were transferred to separate vials to obtain a range of 0.25 vol% solutions of particles dispersed in different 1-pentanol/DMSO ratios (0-85 vol%). Absorption spectra of these solution were measured at 21°C to determine the transmittance at 550 nm.

5.2.4 Assembling the calibration and alignment sample

Using the colloidal crystal, the calibration and alignment sample was prepared as depicted in figure 5.2. Two spacers (Menzel #00 cover glass) were glued onto a microscope slide using UV-glue (Norland 68 Optical Adhesive), about 5 mm apart. Next, the cover glass containing the crystal was glued onto the spacers, such that the crystal was inside the created channel. This channel was then infiltrated with a mixture of *n*-butanol and glycerol ($n_D^{21} = 1.4286$, measured using a Atago 3T refractometer) in order to refractive index match the particles to the surrounding liquid, to reduce scattering and optimize the imaging conditions. The use of water in the matching solvent mixture was omitted, as it has been reported to change the refractive index of silica particles [150], because it is small enough to enter the interior of the silica network, while molecules larger than 0.3 nm cannot. Finally, the channel was closed using UV-glue. While curing the glue, the crystal was covered with aluminum foil as protection from the UV radiation to prevent bleaching of the dye in the particles.

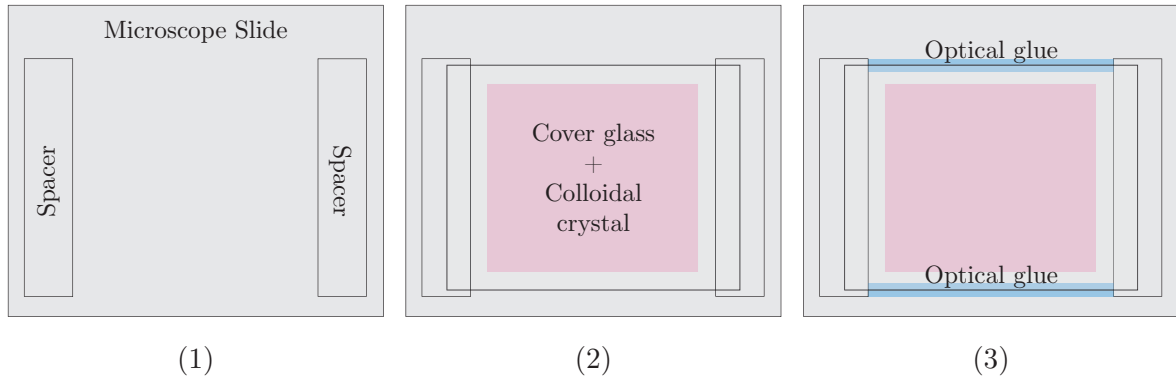


Figure 5.2: A schematic representation of sample assembly; (1) spacers are glued onto a microscope slide; (2) the cover glass containing the colloidal crystal is glued onto the spacers; (3) the channel is infiltrated and closed with optical glue.

5.2.5 Confocal and STED measurements

Calibration and alignment measurements were performed on an inverted Leica TCS SP8 STED 3X confocal microscope, equipped with a Leica HC PL APO 100 \times /1.40 OIL STED WHITE or a Leica HC PL APO 93 \times /1.30 GLYC motCORR STED WHITE objective with a correction collar. In case of the oil objective Type F immersion oil ($n_{546}^{23} = 1.518$, Leica Microsystems) was used as immersion liquid, while for the glycerol objective a 85 w% glycerol/water mixture ($n_D^{20} = 1.452$) was used.

To image the fluorescent cores of the particles, a pulsed (80 MHz) supercontinuum white light laser (SuperK, NKT Photonics) was tuned at 543 nm, while the emission was detected using a gated (0.3-6.0 ns) HyD detector (553-650 nm). For STED imaging of the fluorescent beads a continuous wave (CW) depletion laser with a wavelength of 660 nm was used. The depletion laser was either fully focused into a 'donut'-shaped spot (2D STED) or into an axial depletion spot (3D STED). The gold cores were imaged by detecting the reflection of the excitation or depletion laser using a photomultiplier tube (PMT). The correction collar of the glycerol objective was used to compensate for the refractive index mismatch between the sample (1.43) and the objective (1.45), and allowed to fine tune the depletion laser pattern, as discussed in more detail in the supplementary information of [136].

A HeLa cell sample (Active Motif/Leica Microsystems) was used for evaluation of the alignment of 2D STED imaging of a realistic biological sample, where the α -tubulin was stained with BD Horizon V500-streptavidin (BD Biosciences) for imaging. The cells in the sample were mounted using Mowiol 4-88 on a 170 ± 10 μm thick cover glass (Hecht Assistent #1014), resulting in a sample refractive index of $n \approx 1.52$.

Acquisition parameters of the confocal and STED images are listed in Table 5.1.

The confocal 3D stack of the fluorescent beads was deconvoluted using Huygens Software (Scientific Volume Imaging, 17.04). Any image filtering was done using Fiji [153] (ImageJ 1.52d).

Calibration measurements

For the lateral calibration Fast Fourier transforms of the XY slices were calculated using iTEM (Soft Imaging System GmbH, 5.0) and a 1 pixel Gaussian blur was applied using Fiji [153] to reduce noise. To measure the ΔX and ΔY distances (see Fig. 5.7e) intensity profiles parallel to the direction of interest were drawn through the origin. Using OriginPro (v8.0891, OriginLab Corporation) Gaussian functions were fitted to the peaks nearest to the origin in the intensity profiles, to obtain the distance of these peaks to the origin ΔX and ΔY .

For the axial calibration Fiji was used to plot the intensity of the deconvoluted confocal z-stack as a function of Z-height. Using OriginPro the peaks in the profile were fitted with Gaussian functions. The peak positions were plotted as a function of peak number and fitted using a linear function using OriginLab. The slope of this function was used as interlayer distance.

Measuring the scaling factor of a $93\times/1.3$ NA glycerol objective for $n=1.43$ samples

To determine the scaling factor of the axial distances in our sample as measured by confocal microscopy, we used the method described by Besseling *et al.* [21]. A sample cell was constructed by gluing two Menzel #00 cover glasses as spacers on a microscope slide, after which a channel was created by bridging the spacers with a Menzel #1.5 cover glass. The Fabry-Pérot fringes were measured using a Fourier-transform infrared (FTIR) spectrometer (Vertex 70, Bruker) and fitted to determine the cell height: 94.257 ± 0.008 μm . Next, rhodamine B dyed poly(methyl methacrylate) spheres (70 nm diameter) were deposited from hexane on the inside of the cell and the height of the cell was measured in fluorescent mode on a confocal microscope equipped with a $20\times/0.7$ NA air objective: 98.0 ± 0.2 μm , resulting in a miscalibration of the microscope stage of $4.0 \pm 0.2\%$. After filling the cell with the glycerol/*n*-butanol mixture ($n_D^{21} = 1.4286$) and closing it with UV-glue a height of 99.9 ± 0.2 μm was measured, which was corrected for the mis-calibration of the microscope stage: 96.0 ± 0.3 μm . This gives a scaling factor of 0.982 ± 0.003 for axial distances in a sample with a refractive index of 1.43 recorded with a 1.3 NA glycerol objective.

| Figure | imaging mode ^{&} | objective* | pinhole (Airy units) | pixel sizes (nm) X / Y / Z | pixel dwell time (μs) | line accumulation | frame accumulation | frame averaging |
|----------|-------------------------------|--------------|----------------------|----------------------------|-----------------------|-------------------|--------------------|-----------------|
| 5.7a | Confocal | 93× glycerol | 0.7 | 35 / 35 / 50 | 2.0 | 2 | 4 | 1 |
| 5.9a | Confocal | 100× oil | 0.7 | 31.4 / 31.4 / 50 | 7.8 | 6 | 6 | 1 |
| 5.9b (l) | Reflection | 100× oil | 4.7 | 15 / 15 / - | 6.5 | 1 | 1 | 10 |
| 5.9b (r) | 2D STED | 100× oil | 1.0 | 20.5 / 20.5 / - | 4.3 | 6 | 4 | 1 |
| 5.9c (l) | Reflection | 93× glycerol | 4.7 | 17 / - / 17 | 3.9 | 1 | 1 | 10 |
| 5.9c (r) | 3D STED | 93× glycerol | 1.0 | 41 / - / 41 | 4.3 | 4 | 12 | 1 |
| 5.9d (l) | Reflection | 93× glycerol | 4.7 | 20 / - / 20 | 6.5 | 1 | 1 | 10 |
| 5.9d (r) | 3D STED | 93× glycerol | 1.0 | 41 / - / 41 | 4.3 | 4 | 12 | 1 |
| 5.10a | 2D STED | 100× oil | 1.0 | 11.3 / 11.3 / - | 2.2 | 2 | 1 | 8 |
| 5.10b | 2D STED | 100× oil | 1.0 | 11.3 / 11.3 / - | 2.2 | 4 | 1 | 8 |
| 5.10c | Reflection | 100× oil | 1.0 | 19.2 / 19.2 / - | 4.3 | 2 | 1 | 12 |
| 5.10e | 2D STED | 100× oil | 1.0 | 11.3 / 11.3 / - | 2.2 | 2 | 1 | 8 |
| 5.10f | 2D STED | 100× oil | 1.0 | 11.3 / 11.3 / - | 2.2 | 4 | 1 | 8 |
| 5.10g | Reflection | 100× oil | 1.0 | 19.1 / 19.1 / - | 4.3 | 2 | 1 | 12 |

Table 5.1: Acquisition parameters of microscope images in figures 5.7, 5.9 and 5.10. 6*93× glycerol = Leica HC PL APO 93×/1.30 GLYC motCORR STED WHITE, 100× oil = Leica HC PL APO 100×/1.40 OIL STED WHITE.

5.3 Results

5.3.1 Synthesis of the particles

TEM images of the particles after the different steps in the synthesis are included in figure 5.3. The silica coated gold nanoparticles in (b) have an average diameter of 321.5 ± 13.7 nm after silica coating. The fluorescent cores in (c) have an average diameter of 44.7 ± 2.3 nm and the particle size after silica coating in (d) was found to be 240.1 ± 4.1 nm. Sizes were obtained by measuring the diameter of 100 particles.

In (e) and (f) TEM images after the final silica growth step of the mixture of core-shell particles are included. By adjusting the contrast of the images it was possible to demonstrate that a gold core is present in some of the particles (see insets). From the TEM pictures, the final particle size was determined to be 505.1 ± 9.2 nm. This demonstrates that the particles are very monodisperse in size (st.dev. $<2\%$) which is critical to grow high quality colloidal crystals. This value was obtained by measuring the diameter of 368 particles.

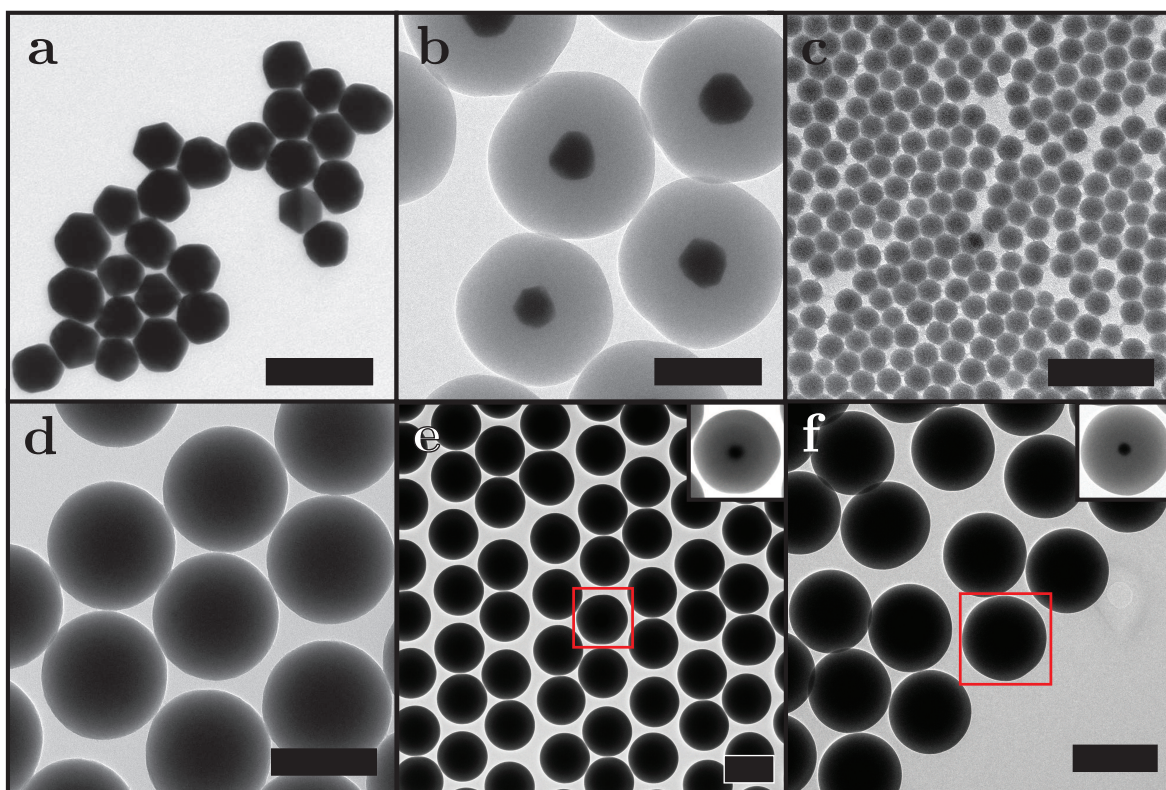


Figure 5.3: Representative TEM images of the synthesized particles. (a,b) 80 nm gold nanoparticle before and after silica coating. (c,d) Fluorescently labelled silica cores before and after further silica coating. (e,f) Images after the final growth step to ~ 500 nm of the mixture of the two types of core-shell particles, in the inset the contrast of the area encircled in red is adjusted to show that some particles contain a gold core. Scale bars represent 200 nm in (a-d) and 500 nm in (e,f).

5.3.2 Refractive index matching

In the left side of figure 5.4 the refractive index at 550 nm and 21°C (n_{550}^{21}) is plotted as a function of the vol% DMSO in 1-pentanol. A linear equation is used to fit this data. This linear relationship was used to calculate the refractive index of the particle suspensions that were used for the refractive index matching study. On the right side of the figure, the outcome of this study is presented. In this graph the transmittance at 550 nm and 21°C of suspensions of particles with different refractive indices is plotted. By fitting a quadratic equation to this data, the refractive index of maximum transmittance was determined: $n_{550}^{21} = 1.43025$.

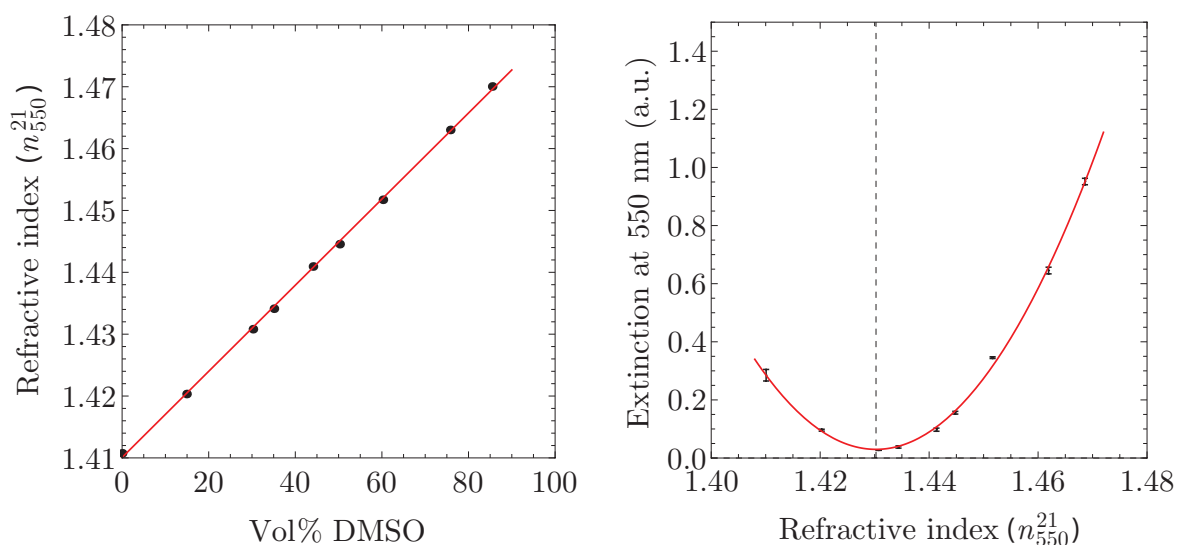


Figure 5.4: In the left image, the refractive index at 550 nm and 21°C (n_{550}^{21}) is plotted as a function of the vol% of DMSO in 1-pentanol. A linear equation is fitted to the data (red line). In the right image, the percentage of light transmitted at 550 nm is plotted as a function of the refractive index measured at 21°C (n_{550}^{21}). The black dots correspond to measurements of dispersions of particles in DMSO/1-pentanol mixtures with various refractive indices. A quadratic equation is fitted to the data (red line) to determine the refractive index of maximum transmittance: $n_{550}^{21} = 1.43025$.

5.3.3 Colloidal crystal growth and sample preparation

In figure 5.5a pictures of the final calibration and alignment are included. From figure (a) it becomes apparent that bright Bragg reflections are observed when the sample is illuminated from the side. This is a first indication of the crystallinity of the colloidal crystal. Another important observation is that the sample is fully transparent under available light which is an indication for successful refractive index matching of the crystal.

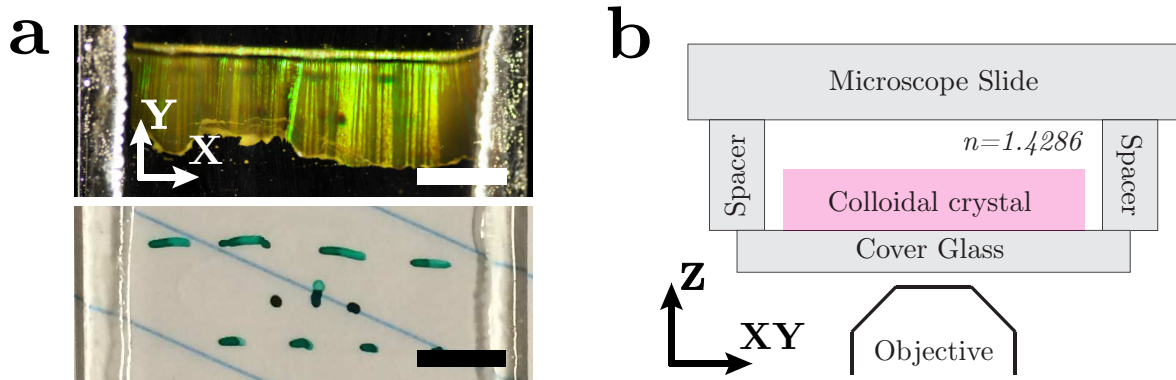


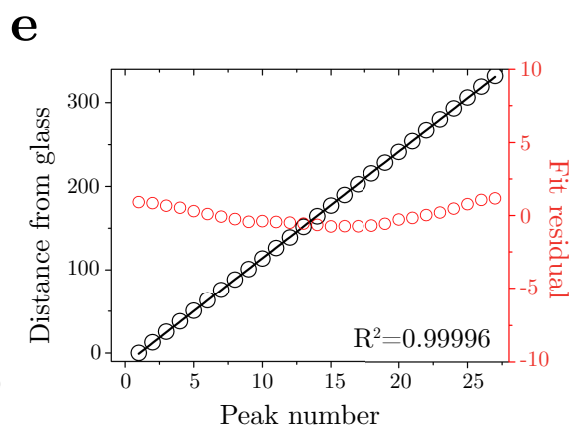
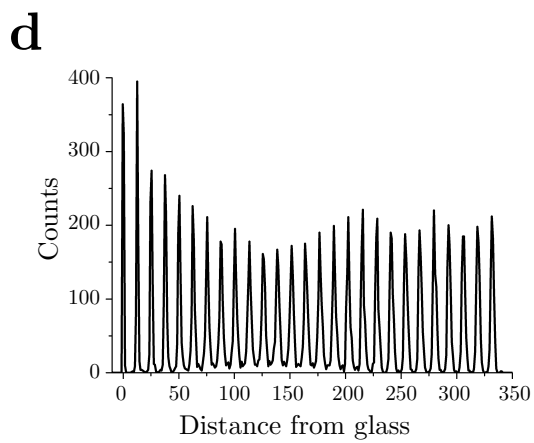
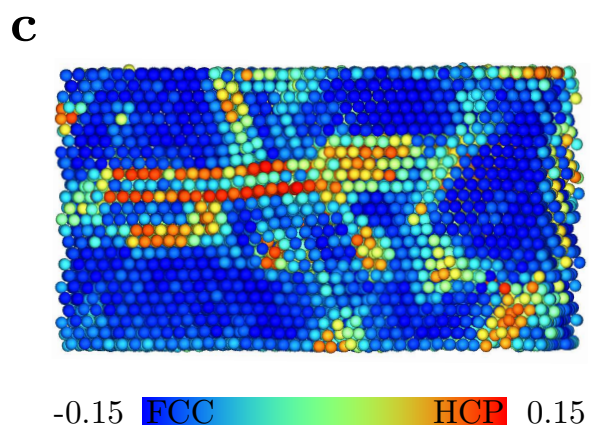
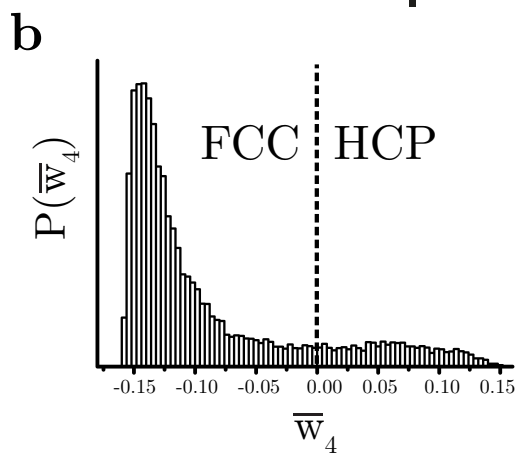
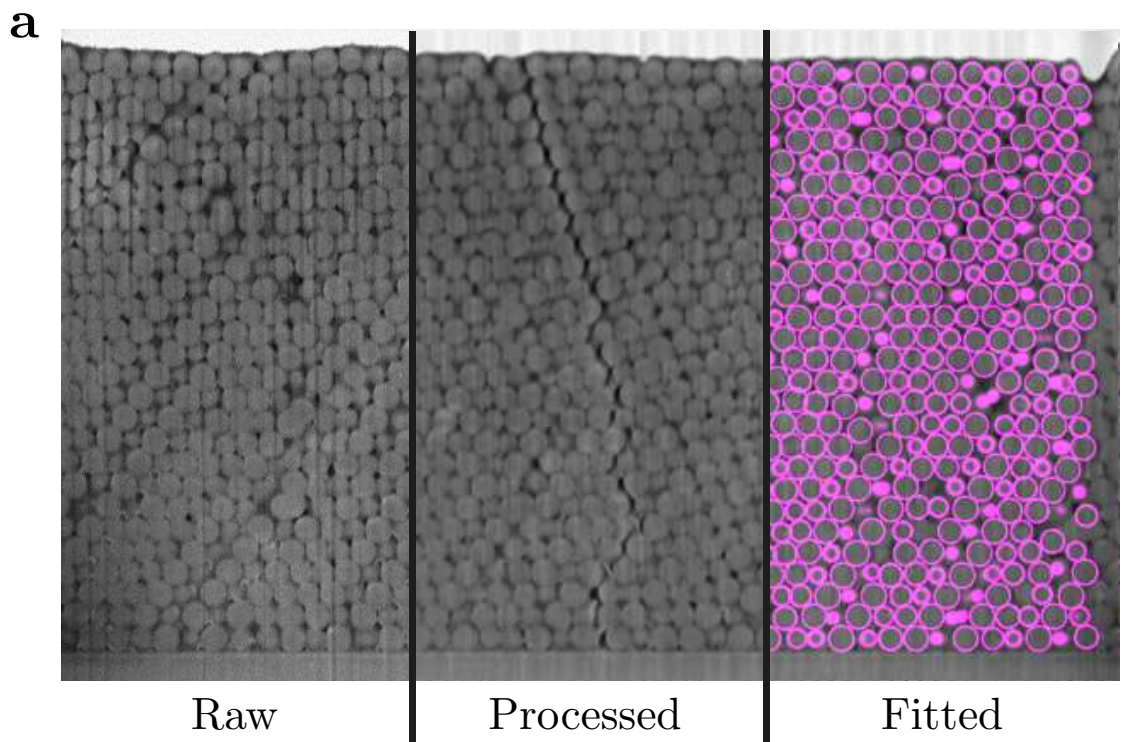
Figure 5.5: Calibration and alignment sample after assembly. (a) Top view of the sample illuminated from the side (top) and under available light (bottom), scale bars indicate 0.5 cm. (b) Schematic side view of the sample.

FIB-SEM characterization of the colloidal crystal

As mentioned in section 5.2.2 FIB-SEM tomography measurements were used to characterize the structure of colloidal crystals obtained via the crystal growth method used in this work. In figure 5.6a example data of a FIB-SEM slice is included. The raw data was processed for optimal particle identification. Next, the coordinates of the particles were determined using recently developed particle tracking routines as described by van Hoeven *et al.* [146].

From the coordinates of the particles it was possible to identify the crystal structure of the colloidal crystal using bond orientation order parameters [154], see figure 5.6b and c. The colloidal crystal structure was found to be face-centered cubic (FCC) with hexagonal close-packed (HCP) stacking faults. It was also observed that the hexagonal arrangement of the particles in the (111) plane of the FCC crystal is not perfectly hexagonal. In the direction of the crystal growth (Y in figure 5.6a) the distance to the nearest neighbour was $\sim 4\%$ smaller than in the two other nearest neighbour directions of the hexagon. This is in agreement with earlier studies using X-ray diffraction where a similar crystal growth method was used [155].

Figure 5.6: FIB-SEM tomogram of the colloidal crystal. (a) A slice from the FIB-SEM tomogram as recorded (left), after filtering (middle) and with overlay of fitted particle coordinates (right). (b) Histogram of the \bar{w}_4 bond orientational order parameter values calculated from the FIB-SEM coordinates. (c) Computer rendering of particles from coordinates obtained by particle identification is included. The particles are coloured according to their \bar{w}_4 value. (d) Histogram of the distances of the identified particles from the glass substrate. (e) Linear fit of the peak positions in (d) conforming close to perfect linearity.



For calibration purposes, it is important that the spacing between layers is constant throughout the entire colloidal crystal. To study this, a histogram of the distances of the identified particles from the glass substrate is plotted in figure 5.6d. The distinct peaks observed in this plot corresponds to the different layers of particles of the crystal perpendicular to the (111) plane. In figure 5.6e the peak number is plotted versus the peak position. This data can be fitted with a linear fit almost perfectly ($R^2 = 0.99996$) which proves that the linear spacing is constant throughout the crystal.

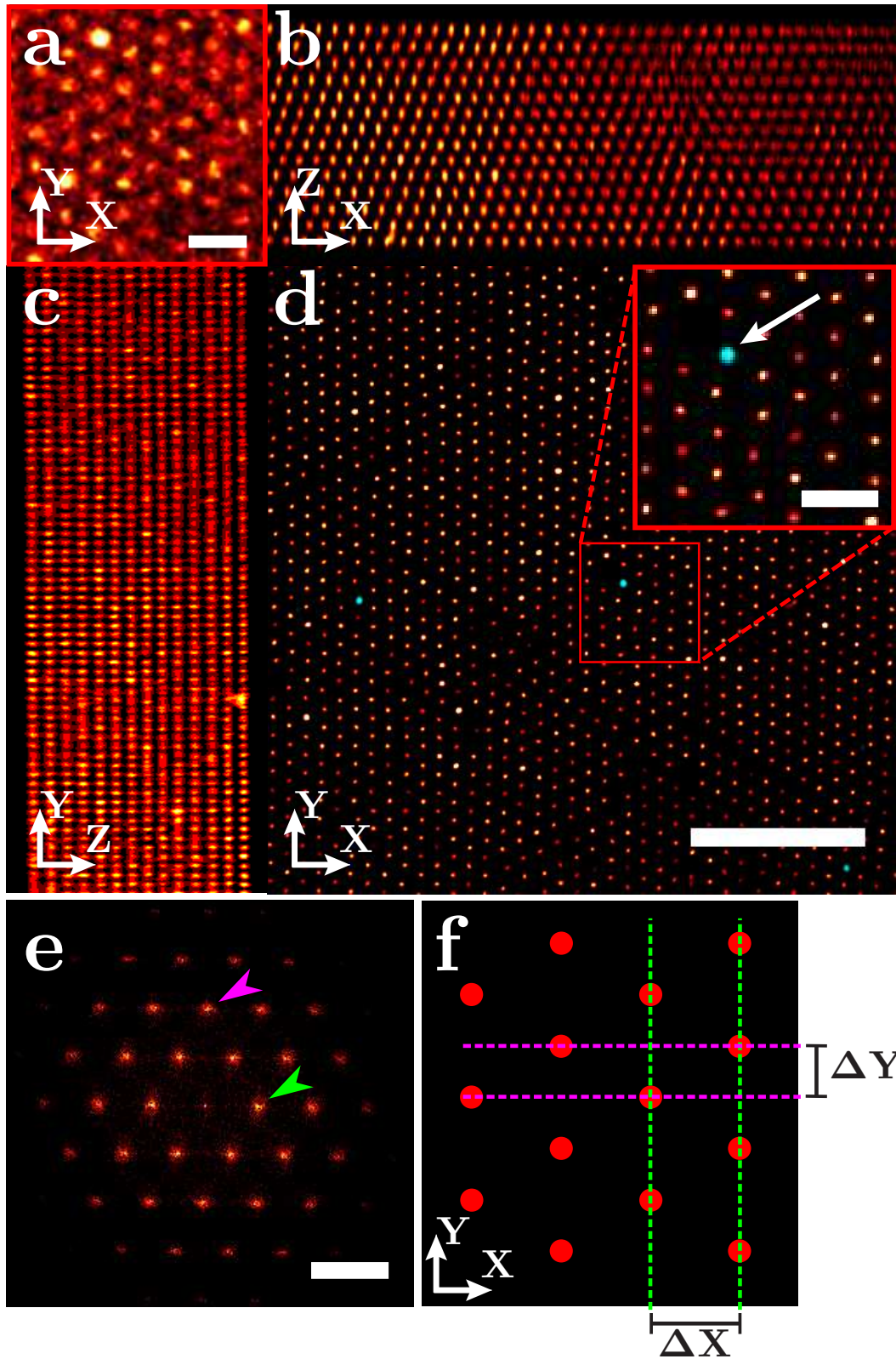
5.3.4 Lateral and axial calibration

A z-stack of the silica beads with rhodamine B labelled cores was recorded in fluorescent mode using a HC PL APO 93 \times /1.30 GLYC motCORR STED WHITE objective (Fig. 5.7a). The periodicity of the crystal in both the lateral as well as the axial direction becomes visible after deconvolution of the z-stack (Fig. 5.7b-d). The (111) plane of the FCC crystal is parallel to the lateral plane, while the $(\bar{1}10)$ and $(11\bar{2})$ planes are parallel to the XZ and YZ directions, respectively, of the confocal z-stack. The growth direction of the crystal was parallel to the Y scanning direction of the confocal microscope.

For calibration in the lateral direction the Fast Fourier transforms (FFT) were calculated of three XY slices from the deconvoluted 3D confocal stack, respectively 1.3, 3.6 and 5.9 μm away from the cover glass. Figure 5.7e shows the FFT of the XY slice 3.6 μm away from the cover glass, with the arrows pointing at the two characteristic distances of the crystal in both the X (green) and Y (magenta) directions (see inset). From the three slices the characteristic distances ΔX and ΔY were determined to be 481 ± 4 nm and 269 ± 2 nm, respectively. These values can be used to calibrate the two lateral directions of the microscope.

Figure 5.7: Images recorded for the calibration of a confocal microscope.

(a) Close-up of a slice 3.6 μm from the cover glass from a confocal stack of the colloidal crystal (1 pixel gaussian blur) acquired using a HC PL APO 93 \times /1.30 GLYC motCORR STED WHITE objective and a pinhole of 0.7 Airy units. The scale bar is 1 μm . (b) Average projection of the XZ planes of the confocal z-stack shown in (a) after deconvolution, showing the ABC stacking in the $(\bar{1}10)$ plane of the FCC crystal. (c) Average projection of the XY planes of the deconvoluted confocal z-stack, showing the $(11\bar{2})$ plane of the FCC crystal. (d) Overlay of an XY slice of the confocal stack of both reflection (cyan) and deconvoluted fluorescence (red) 3 μm from the cover glass. The arrow points at a gold core bead imaged in reflection mode. The scale bars are 5 and 1 (inset) μm . (e) Fast Fourier transform of the confocal image included in (d) demonstrating long range hexagonal order. The arrowheads in (e) point to the peaks in the FFT image used for calibrating distances in the X (green) and Y (magenta) direction. The scale bar is 3 μm^{-1} . In (f) the characteristic distances ΔX (green) and ΔY (magenta) in the real space crystal corresponding to the peaks in the FFT image are shown.



Since the hexagonal arrangement is slightly distorted by a shrinkage in the direction of crystal growth, Y in this case, the orientation of the hexagonal arrangement (and therefore the crystal growth direction) with respect to the confocal scanning direction should be taken into account during the calibration.

As the particles are touching in the Y direction the effective particle diameter σ_{eff} can be estimated by $2\Delta Y$. We find that $\sigma_{eff} = 538 \pm 4$ nm and therefore $\sigma_{eff} \sim 1.07 \sigma_{TEM}$. This slightly larger effective diameter compared to the diameter as measured in TEM is expected because the particles shrink due to electron beam exposure during the TEM measurements [156].

For axial calibration of the setup, the intensity of the deconvoluted confocal z-stack is plotted as a function of the Z height (Fig. 5.8a). The relative positions of the peaks in this intensity profile display almost perfect linearity ($R^2 = 0.9998$, Fig. 5.8b) and a linear fit results in a distance of 448 ± 2 nm between the lateral layers of the crystal. It should be noted that axial distances, as recorded by confocal microscopy using high NA objectives, are sensitive to refractive index mismatches between the sample medium and the immersion medium of the objective. This results in an elongation or shrinkage of measured distances [21, 157]. The presented sample has a slightly lower refractive index (1.43) than the refractive index of the immersion liquid (1.45). Therefore, the axial scaling factor was determined using the method described by Besseling *et al.* [21] (see section 5.2.5). A scaling factor of 0.982 ± 0.003 was determined, resulting in a (111) layer spacing d_{111} of the sample of 440 ± 2 nm. For a perfect FCC crystal d_{111} can be calculated using: $d_{111} = \sqrt{6}\sigma/3$, where σ is the particle diameter [155]. Using σ_{eff} as estimated before, a value of d_{111} of 439 ± 3 nm is found, which corresponds to the measured value.

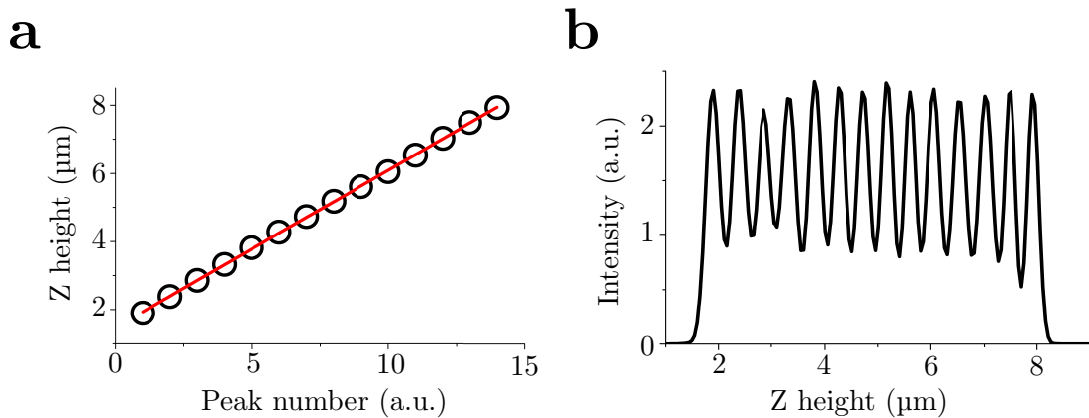


Figure 5.8: Axial calibration of the microscope. In (a) the intensity profile in the z -direction is plotted, demonstrating the periodicity in the axial direction. (b) Shows a linear fit of the peak positions in (a).

5.3.5 PSF measurements and laser alignment

Using the fluorescent cores of the beads in the colloidal crystal, the PSF of a confocal microscope can be recorded. Figure 5.9a shows the sub-resolution fluorescent cores close to the cover slip, imaged in confocal mode with a HC PL APO 100 \times /1.40 OIL STED WHITE objective and the pinhole set to 0.7 Airy units. The PSF of this microscope has an expected ellipsoidal shape in the axial planes, but is slightly rotated in the YZ plane.

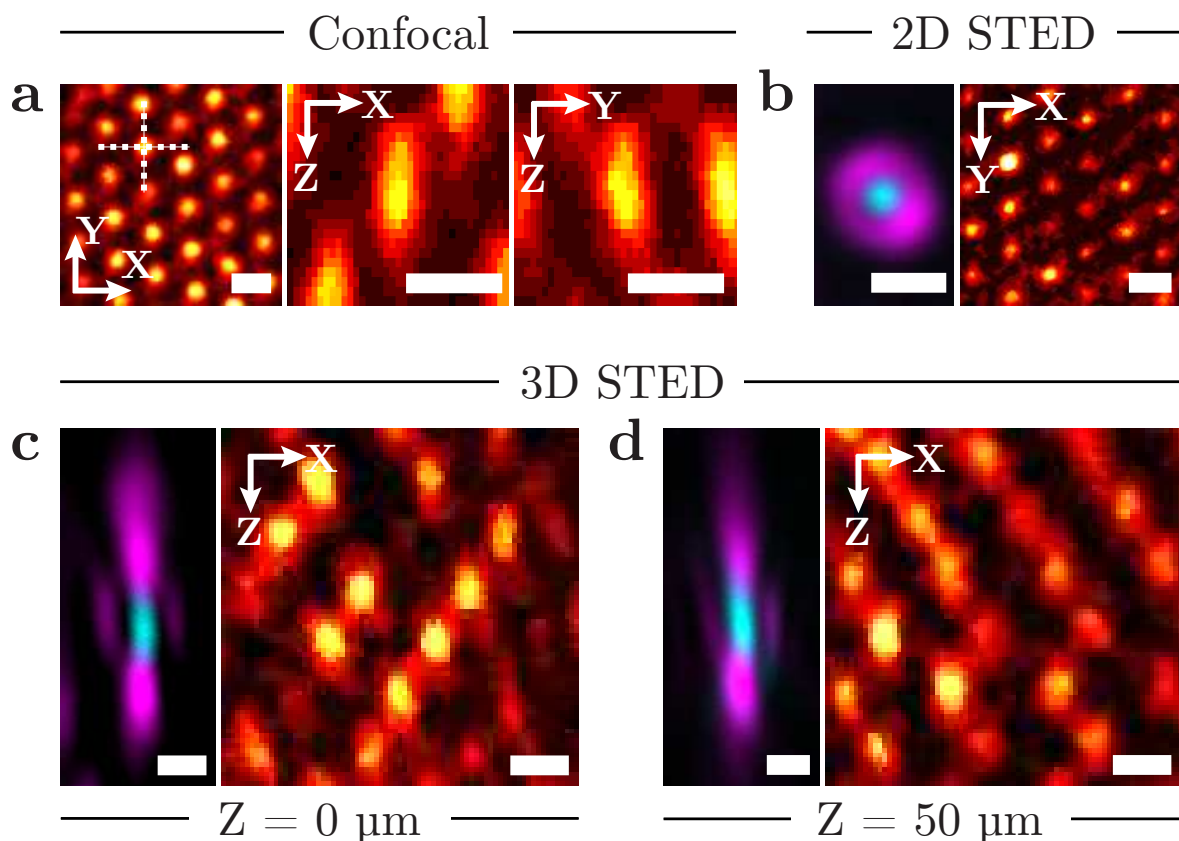


Figure 5.9: Alignment of confocal STED microscope. (a) Slices from confocal z-stack of fluorescent cores in colloidal crystal close to the cover glass, recorded with a HC PL APO 100 \times /1.40 OIL STED WHITE objective (2 pixel 3D median filter), showing the response function of the microscope in the lateral plane (left), XZ plane (middle) and YZ plane. The two axial planes are marked by the dashed lines in the lateral plane (left). Alignment of 2D (b) and 3D (c,d) STED excitation (cyan) and depletion (magenta) lasers in the lateral plane, as imaged using a HC PL APO 93 \times /1.30 GLYC motCORR STED WHITE objective in reflection mode (left) using a gold core particle close to (b,c) and 50 μm (d) from the cover glass, and the resulting STED images (2 pixel median filter) of the fluorescent cores in the crystal (right), showing increased resolvability of the particles in the crystal as compared to a). All scale bars indicate 500 nm.

The gold cores in the crystal were used to check the shape of the depletion laser spot and the overlap with the excitation laser spot, which are both critical for an optimal STED resolution. Figure 5.9b shows the excitation spot (cyan) and the 2D STED 'donut'-shaped depletion spot (magenta) imaged in reflection mode using a HC PL APO 93 \times /1.30 GLYC motCORR STED WHITE objective with the pinhole set to 4.7 Airy units. Subsequent imaging of the fluorescent cores with the pinhole set to 1 Airy unit shows an increase in lateral resolution of the STED microscope as compared to confocal (Figure 5.9a), even when using a lower NA objective. Since 2D STED microscopy only improves the resolution in the lateral plane compared to confocal microscopy, it is primarily employed on thin samples, close to the cover glass. 3D STED, however, enables imaging at sub-diffraction resolution in both lateral and axial directions, which allows imaging of samples at sub-diffraction resolutions also far away from the cover glass [158]. Figure 5.9 shows the excitation and depletion laser spots of a 3D STED confocal microscope equipped with a HC PL APO 93 \times /1.30 GLYC motCORR STED WHITE objective as imaged in reflection mode close to the cover glass (Fig. 5.9c) and ~ 50 μm away from the cover glass (Fig. 5.9d). The correction collar of the objective was used to keep the intensity of the top and bottom depletion spots balanced when imaging more than ~ 30 μm from the cover slip. This was necessary because the refractive index of the sample (1.43) is slightly lower than the ideal index for a glycerol objective (1.45). To check the results of the alignment of the lasers, the fluorescent cores were imaged using our confocal microscope in 3D STED imaging mode at a pinhole size of 1 Airy unit (Figure 5.9c,d). The improved axial resolution is visible from the decreased aspect ratio of the ellipsoidal fluorescent spots as compared to the confocal PSF (Figure 5.9a).

To show the importance of a proper alignment of the excitation and depletion spots in STED microscopy, fluorescently labelled α -tubulin in HeLa-cells was imaged using 2D STED microscopy using a HC PL APO 100 \times /1.40 OIL STED WHITE objective (Figure 5.10). When the two laser spots were properly aligned using our sample, an increase of the lateral resolution is visible (Figure 5.10a-d). When the minimum of the depletion spot is slightly off-center with respect to the maximum of the excitation spot, the depletion of the fluorophores by the depletion beam results in a higher level of noise in the resulting image and no improvement in the resolution compared to the confocal image (Figure 5.10f-h).

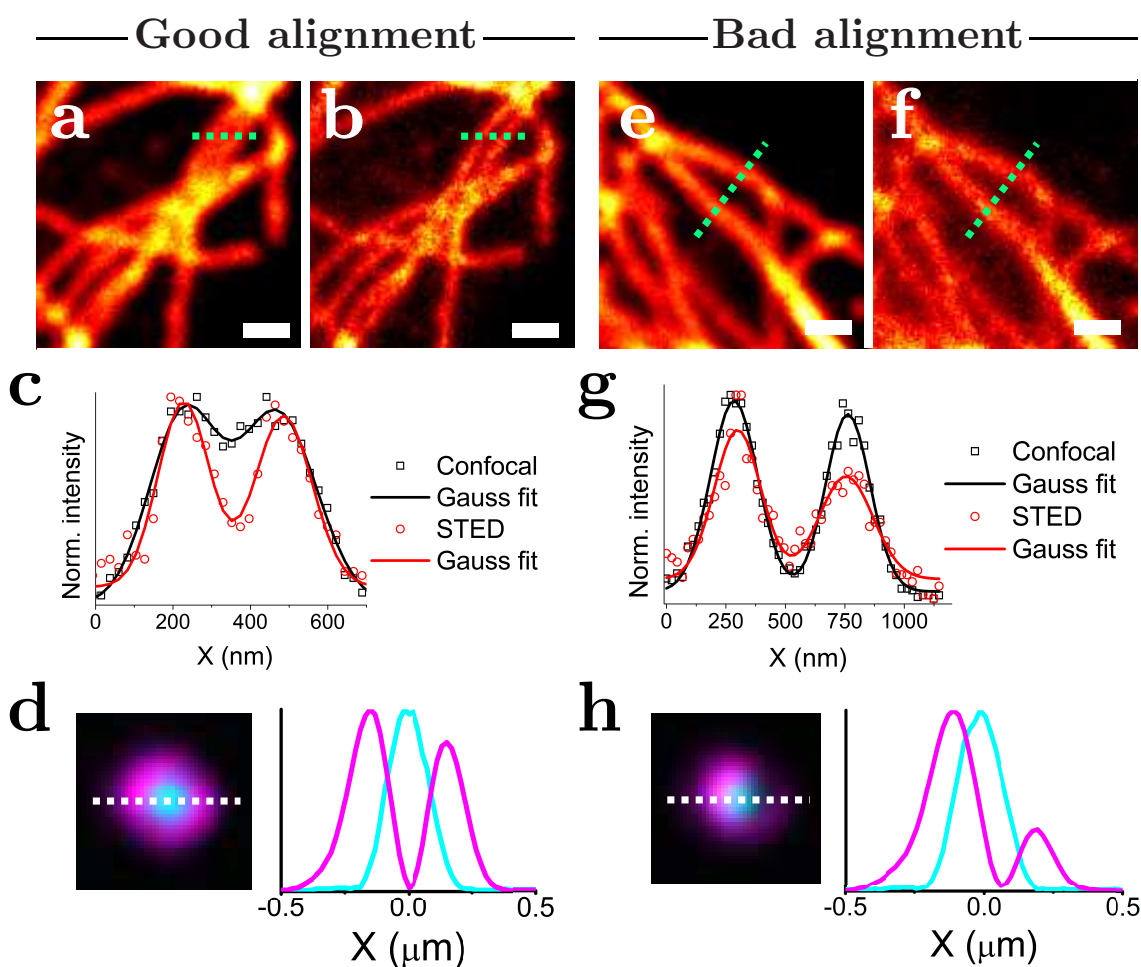


Figure 5.10: The importance of a proper alignment of the STED microscope. Results of alignment of the laser beams in STED microscopy on imaging of α -tubulin (HeLa-cell) with a HC PL APO 100 \times /1.40 OIL STED WHITE objective. (a) Confocal micrograph. (b) 2D STED image at same region as (a) after aligning the minimum of the ‘donut’-shaped depletion laser spot to the maximum of the excitation laser spot. (c) Intensity profiles along the lines in (a) and (b), showing the increased resolving power of the STED compared to confocal microscopy. (d) Alignment of excitation (cyan) and STED (magenta) lasers in b). (e) Confocal micrograph. (f) 2D STED image at same region as (e) with slightly misaligned excitation and depletion laser spots. (g) Normalized intensity profiles along the lines in (e) and (f), showing no increase in the resolving power of the (2D) STED compared to confocal microscopy. (h) Alignment of excitation (cyan) and STED (magenta) lasers in (f). All Scale bars indicate 500 nm.

5.4 Discussion

The test sample as presented here is a robust standard for the quality control of a laboratory's confocal and STED microscopes. By the time of writing the shelf life of the sample is on the order of months. Although the small fluorescent cores tend to bleach upon prolonged excitation the sample can be used repeatedly because the crystal contains over 10^{10} particles due to its larger size (close to 2 cm^2 see Fig. 5.5a).

In the measurement of the characteristic lateral length scales ΔX and ΔY an error below 1% is found (obtained by measuring at three depths). In addition, for the axial interlayer spacing an error of less than 0.5% is found (obtained from a linear fit of the intensity peaks of the crystal layers). This low error is supported by the perfect linearity of the axial interlayer spacing as found by FIB-SEM tomography and particle tracking. These low errors make the sample suitable for the calibration of microscopes at a high precision.

Due to the bottom-up assembly, the sample is highly tunable. This makes it possible to adjust the sample to for example meet the requirements for different high NA lenses (e.g. oil immersion) and/or different techniques. This can be achieved by changing the core, the ratio between different types of cores, the shell and the total size of the particles, which will be discussed below.

While it was demonstrated that rhodamine labelled silica cores can be used, the synthesis method of these cores allows for the incorporation of a wide variety of dyes [27, 81, 159, 160, 161, 162, 163]. This can be useful because by mixing cores with different dyes in the non-fluorescent silica growth step, to accommodate microscope setups with multiple laser lines. This can also be used to produce a sample where fluorescent cores labelled with two different dyes are combined at a strongly asymmetric number ratio. Within such a geometry, one of the two fluorescent particles can be used for the calibration measurements whereas the other core allows for PSF measurements. The axial tails of the PSFs can then be well separated by ensuring that the ratio of the second type of core particle is low enough compared to the first type. This separation is required for some restoration routines as e.g. used in commercial software often used in biology (see methods). Depth dependent PSFs are important for accurate 3D image reconstruction, especially if the index of the mounting medium does not exactly match that for the objective used.

Instead of keeping the gold and dye separated within the sample, the two can also be combined within a single particle, by growing a fluorescent layer around the gold core. Another option is to use a silver core instead of a gold core. This flexibility opens up the possibility to design nanocomposite particles where the fluorescence is enhanced by the presence of the metal core [87], which has recently been demonstrated to be compatible with STED microscopy [164].

The possibility to exchange the fluorescent cores with quantum dots is also worthwhile exploring, since quantum dots have excellent photostability, are only a few nanometer in size and have shown to be compatible with STED microscopy [134, 135]. As the absorption and emission wavelengths of quantum dots are size dependent [165], they can be tailored to the wavelength of the excitation and STED lasers. When mea-

suring a PSF using quantum dots, the challenge is to ensure there is enough separation between them which can be achieved by coating the quantum dots with silica [166, 167]. This seeded growth method is directly compatible with the work presented here, because silica coating is performed in the same reverse micro-emulsion system used to synthesize the fluorescent cores. The most promising quantum dots to use are so-called CdS/CdSe/CdS quantum well dots, as these can be coated with silica while maintaining a high photoluminescence quantum yield [168, 169].

Next to quantum dots, a variety of nanometer sized probes have been put to use in STED imaging [170], such as fluorescent nanodiamonds [171], upconversion nanocrystals [172] and carbon dots [173]. Although these probes can be coated with silica [174, 175, 176], and could be integrated in our demonstrated sample, to the best of our knowledge, no STED microscopy has been demonstrated on these probes after silica coating.

Another method to tune the sample is by tuning the silica shell that is used to ensure separation between the cores. While in this work the focus was on a refractive index of 1.43 compatible with glycerol objectives, it can also be tuned to a higher refractive index. This can be achieved by synthesizing a shell of titania/silica composite with a higher refractive index [177, 178, 179]. Doing so, the refractive index can easily be increased to match the refractive index of oil objectives (1.52), or any other intermediate refractive index that is comparable to the refractive index of life science specimens of interest. Another option is to increase the size of the shell to increase the spacing between the probes. This makes the sample compatible with lower NA objectives, where the axial resolving power is smaller. For this, the assembly method needs to be adjusted due to a faster settling rate of the particles, as has been demonstrated for close to 1 μm silica particles [180].

Finally, by introducing a refractive index mismatch between the particles and the embedding solvent, the effect of the mismatch on the PSF can be measured as a function of the distance to the cover glass. Moreover, the periodicity of the crystal in the axial direction and the known refractive indices of the beads and the embedding mixture can be used to test effective refractive index theories developed in the photonic crystal community.

5.5 Conclusion and Outlook

In this chapter we demonstrated a robust sample that can be used as a standard to assure the quality of (STED) confocal microscopes equipped with high NA objectives. The sample is composed of a crystal of fluorescently labelled silica colloids, mixed with a small amount of gold core silica colloids. As the sample is infiltrated with a refractive index matched solvent mixture, it is perfect for imaging with (STED) confocal microscopy, far from the cover glass. The periodicity of the crystal in all three dimensions can be used to calibrate the microscope setup. In addition, the gold cores can be used to align the excitation and depletion lasers of a STED microscope. The effect of the alignment can then be checked on the fluorescent cores by measuring the point spread function (PSF). As the sample has a refractive index of $n = 1.43$, the sample is optimized for glycerol objectives, which have been shown to be ideal for deep super-resolution imaging of life science specimens [136].

The bottom-up assembly of the sample allows for tailoring of the sample to its users needs. As the reported labelling method is compatible with a wide variety of dyes, the sample can be made suitable for different laser lines. Moreover, the synthesis methods allows for the incorporation of different metal cores, as well as quantum dots. Next to modification of the cores of the particles, the particles themselves can be grown larger to make the sample compatible with lower NA objectives. In addition, by incorporating Titania into the particle shells and matching with higher refractive index solvents, the sample can be tailored for use with oil objectives. Finally, by introducing a mismatch between the particles and the embedding solvent mixture, the sample can be used to test effective refractive index theories and the effect of the mismatch on the PSF.

5.6 Acknowledgements

The work presented in this chapter was a collaboration with Ernest van der Wee, Alfons van Blaaderen, Peter Speets and Marc del Pozo Puig. I would like to thank and acknowledge the following persons for their contributions: Dave van den Heuvel for his help with confocal measurements; Peter Helfferich for his help with confocal (STED) measurements; Job Fermie for his assistance in the FIB-SEM sample preparation; Matthijs de Winter for the FIB-SEM measurements and Michiel Hermes for the particle localization in the FIB-SEM data. Finally, I would like to thank Alfons van Blaaderen, Matthijs de Winter, Gerhard Blab and Hans Gerritsen for critical reading of the chapter.

Bibliography

- [1] J. W. Lichtman and J. A. Conchello, “Fluorescence microscopy,” *Nature Methods*, vol. 2, no. 12, pp. 910–919, 2005.
- [2] I. Serdyuk, N. Zaccai, and J. Zaccai, *Methods in Molecular Biophysics - Structure, Dynamics, Function*. Cambridge University Press, 2007.
- [3] I. Watt, *The Principles and Practice of Electron Microscopy*. Cambridge University Press, 1997.
- [4] J. Lackowicz, *Principles of fluorescence spectroscopy*. Springer, 2006.
- [5] M. A. Karreman, L. Mercier, N. L. Schieber, G. Solecki, G. Allio, F. Winkler, B. Ruthensteiner, J. G. Goetz, and Y. Schwab, “Fast and precise targeting of single tumor cells in vivo by multimodal correlative microscopy,” *Journal of Cell Science*, vol. 129, no. 2, pp. 444–456, 2016.
- [6] Y. Olmos, L. Hodgson, J. Mantell, P. Verkade, and J. G. Carlton, “ESCRT-III controls nuclear envelope reformation,” *Nature*, vol. 522, no. 7555, pp. 236–239, 2015.
- [7] D. J. Stephens and V. J. Allan, “Light Microscopy Techniques for Live Cell Imaging,” *Science*, vol. 300, pp. 82–86, 2003.
- [8] S. W. Hell and J. Wichmann, “Breaking the diffraction resolution limit by stimulated emission: stimulated-emission-depletion fluorescence microscopy,” *Optics Letters*, vol. 19, no. 11, p. 780, 1994.
- [9] W. E. Moerner, “Microscopy beyond the diffraction limit using actively controlled single molecules,” *Journal of Microscopy*, vol. 246, no. 3, pp. 213–220, 2012.
- [10] M. Wahl, “PicoQuant, Technical Note: Time-Correlated Single Photon Counting,” pp. 1–14, 2014.
- [11] P. de Boer, J. P. Hoogenboom, and B. N. G. Giepmans, “Correlated light and electron microscopy: ultrastructure lights up!,” *Nature Methods*, vol. 12, no. 6, pp. 503–513, 2015.
- [12] C. Wouters and H. Koerten, “Combined Light Microscope and Scanning Electron Microscope, a New Instrument for Cell Biology,” *Cell Biology International Reports*, vol. 6, no. 10, pp. 955–959, 1982.

- [13] F. J. Timmermans and C. Otto, "Contributed Review: Review of integrated correlative light and electron microscopy," *Review of Scientific Instruments*, vol. 86, no. 1, 2015.
- [14] T. Ando, S. P. Bhamidimarri, N. Brending, H. Colin-York, L. Collinson, N. De Jonge, P. J. de Pablo, E. Debroye, C. Eggeling, C. Franck, M. Fritzsche, H. Gerritsen, B. N. G. Giepmans, K. Grunewald, J. Hofkens, J. P. Hoogenboom, K. P. F. Janssen, R. Kaufmann, J. Klumpermann, N. Kurniawan, J. Kusch, N. Liv, V. Parekh, D. B. Peckys, F. Rehfeldt, D. C. Reutens, M. B. J. Roeffaers, T. Salditt, I. A. T. Schaap, U. S. Schwarz, P. Verkade, M. W. Vogel, R. Wagner, M. Winterhalter, H. Yuan, and G. Zifarelli, "The 2018 correlative microscopy techniques roadmap," *Journal of Physics D: Applied Physics*, vol. 51, p. 443001, nov 2018.
- [15] A. V. Agronskaia, J. A. Valentijn, L. F. van Driel, C. T. Schneijdenberg, B. M. Humbel, P. M. van Bergen en Henegouwen, A. J. Verkleij, A. J. Koster, and H. C. Gerritsen, "Integrated fluorescence and transmission electron microscopy," *Journal of Structural Biology*, vol. 164, no. 2, pp. 183–189, 2008.
- [16] F. C. Hendriks, S. Mohammadian, Z. Ristanović, S. Kalirai, F. Meirer, E. T. Vogt, P. C. Bruijninx, H. C. Gerritsen, and B. M. Weckhuysen, "Integrated Transmission Electron and Single-Molecule Fluorescence Microscopy Correlates Reactivity with Ultrastructure in a Single Catalyst Particle," *Angewandte Chemie - International Edition*, vol. 57, no. 1, pp. 257–261, 2018.
- [17] A. C. Zonneville, R. F. C. Van Tol, N. Liv, A. C. Narvaez, A. P. J. Effting, P. Kruit, and J. P. Hoogenboom, "Integration of a high-NA light microscope in a scanning electron microscope," *Journal of Microscopy*, vol. 252, no. 1, pp. 58–70, 2013.
- [18] N. Liv, A. C. Zonneville, A. C. Narvaez, A. P. Effting, P. W. Voorneveld, M. S. Lucas, J. C. Hardwick, R. A. Wepf, P. Kruit, and J. P. Hoogenboom, "Simultaneous Correlative Scanning Electron and High-NA Fluorescence Microscopy," *PLoS ONE*, vol. 8, no. 2, pp. 1–9, 2013.
- [19] M. T. Haring, N. Liv, A. C. Zonneville, A. C. Narvaez, L. M. Voortman, P. Kruit, and J. P. Hoogenboom, "Automated sub-5 nm image registration in integrated correlative fluorescence and electron microscopy using cathodoluminescence pointers," *Scientific Reports*, vol. 7, no. March, pp. 1–9, 2017.
- [20] "URL, Thorlabs - Grid Distortion Test Targets," July 2019.
- [21] T. H. Besseling, J. Jose, and A. V. Blaaderen, "Methods to calibrate and scale axial distances in confocal microscopy as a function of refractive index," *Journal of Microscopy*, vol. 257, no. 2, pp. 142–150, 2015.

- [22] R. W. Cole, T. Jinadasa, and C. M. Brown, “Measuring and interpreting point spread functions to determine confocal microscope resolution and ensure quality control,” *Nature Protocols*, vol. 6, no. 12, pp. 1929–1941, 2011.
- [23] W. Wallace, L. H. Schaefer, and J. R. Swedlow, “A workingperson’s guide to deconvolution in light microscopy,” *BioTechniques*, vol. 31, no. 5, pp. 1076–1097, 2001.
- [24] Y. Li, M. Mund, P. Hoess, J. Deschamps, U. Matti, B. Nijmeijer, V. J. Sabinina, J. Ellenberg, I. Schoen, and J. Ries, “Real-time 3D single-molecule localization using experimental point spread functions,” *Nature Methods*, vol. 15, no. 5, pp. 367–369, 2018.
- [25] C. Fouquet, J. F. Gilles, N. Heck, M. D. Santos, R. Schwartzmann, V. Cannaya, M. P. Morel, R. S. Davidson, A. Trembleau, and S. Bolte, “Improving axial resolution in confocal microscopy with new high refractive index mounting media,” *PLoS ONE*, vol. 10, no. 3, pp. 1–17, 2015.
- [26] Á. Szabó, T. Szendi-Szatmári, L. Ujlaky-Nagy, I. Rádi, G. Vereb, J. Szöllösi, and P. Nagy, “The Effect of Fluorophore Conjugation on Antibody Affinity and the Photophysical Properties of Dyes,” *Biophysical Journal*, vol. 114, no. 3, pp. 688–700, 2018.
- [27] A. Imhof, M. Megens, J. J. Engelberts, D. T. N. de Lang, R. Sprik, and W. L. Vos, “Spectroscopy of Fluorescein (FITC) Dyed Colloidal Silica Spheres,” *Journal of Physical Chemistry B*, vol. 103, no. 9, pp. 1408–1415, 1999.
- [28] L. Linck and U. Resch-Genger, “Identification of efficient fluorophores for the direct labeling of DNA via rolling circle amplification (RCA) polymerase ϕ 29,” *European Journal of Medicinal Chemistry*, vol. 45, no. 12, pp. 5561–5566, 2010.
- [29] R. I. Nooney, C. M. N. McCahey, O. Stranik, X. Le Guevel, C. McDonagh, and B. D. MacCraith, “Experimental and theoretical studies of the optimisation of fluorescence from near-infrared dye-doped silica nanoparticles,” *Analytical and Bioanalytical Chemistry*, vol. 393, pp. 1143–1149, 2009.
- [30] W. Chen, L. J. Young, M. Lu, A. Zaccone, F. Strohl, N. Yu, G. S. Schierle, and C. F. Kaminski, “Fluorescence self-quenching from reporter dyes informs on the structural properties of amyloid clusters formed in vitro and in cells,” *Nano Letters*, vol. 17, no. 1, pp. 143–149, 2017.
- [31] I. Johnson, *Molecular Probes Handbook: A Guide to Fluorescent Probes and Labeling Technologies*. Life Technologies Corporation, 2010.
- [32] A. Margineanu, J. J. Chan, D. J. Kelly, S. C. Warren, D. Flatters, S. Kumar, M. Katan, C. W. Dunsby, and P. M. French, “Screening for protein-protein interactions using Förster resonance energy transfer (FRET) and fluorescence lifetime imaging microscopy (FLIM),” *Scientific Reports*, vol. 6, no. June, 2016.

- [33] E. Haas, "The study of protein folding and dynamics by determination of intramolecular distance distributions and their fluctuations using ensemble and single-molecule FRET measurements," *ChemPhysChem*, vol. 6, no. 5, pp. 858–870, 2005.
- [34] W. A. Eaton and B. Schuler, "Protein folding studied by single-molecule FRET," *Current Opinion in Structural Biology*, vol. 18, no. 1, pp. 16–26, 2008.
- [35] D. L. Dexter, "A Theory of Sensitized Luminescence in Solids," *The Journal of Chemical Physics*, vol. 21, pp. 836–850, may 1953.
- [36] J. Canning, G. Huyang, M. Ma, A. Beavis, D. Bishop, K. Cook, A. McDonagh, D. Shi, G.-D. Peng, and M. Crossley, "Percolation Diffusion into Self-Assembled Mesoporous Silica Microfibres," *Nanomaterials*, vol. 4, no. 1, pp. 157–174, 2014.
- [37] G. H. Ning, Z. Chen, Q. Gao, W. Tang, Z. Chen, C. Liu, B. Tian, X. Li, and K. P. Loh, "Salicylideneanilines-Based Covalent Organic Frameworks as Chemosselective Molecular Sieves," *Journal of the American Chemical Society*, vol. 139, no. 26, pp. 8897–8904, 2017.
- [38] T. Jiao, Y. Liu, Y. Wu, Q. Zhang, X. Yan, F. Gao, A. J. Bauer, J. Liu, T. Zeng, and B. Li, "Facile and Scalable Preparation of Graphene Oxide-Based Magnetic Hybrids for Fast and Highly Efficient Removal of Organic Dyes," *Scientific Reports*, vol. 5, no. June, pp. 1–10, 2015.
- [39] T. Bernas, J. P. Robinson, E. K. Asem, and B. Rajwa, "Loss of image quality in photobleaching during microscopic imaging of fluorescent probes bound to chromatin," *Journal of Biomedical Optics*, vol. 10, no. 6, p. 064015, 2006.
- [40] Invitrogen, Thermo Fisher Scientific, *Molecular Probes Handbook*. Invitrogen, 11 ed., 2010.
- [41] C. E. Aitken, R. A. Marshall, and J. D. Puglisi, "An oxygen scavenging system for improvement of dye stability in single-molecule fluorescence experiments," *Biophysical Journal*, vol. 94, no. 5, pp. 1826–1835, 2008.
- [42] L. Guo and F. Gai, "Simple method to enhance the photostability of the fluorescence reporter R6G for prolonged single-molecule studies," *Journal of Physical Chemistry A*, vol. 117, no. 29, pp. 6164–6170, 2013.
- [43] M. Swoboda, H.-m. Cheng, D. Brugger, D. Haltrich, N. Plumere, and M. Schlierf, "Enzymatic Oxygen Scavenging for Photostability without pH Drop in Single-Molecule Experiments," *ACS Nano*, no. 7, pp. 6364–6369, 2012.
- [44] D. Genovese, E. Rampazzo, N. Zaccheroni, M. Montalti, and L. Prodi, "Collective Properties Extend Resistance to Photobleaching of Highly Doped PluS NPs," *European Journal of Inorganic Chemistry*, no. c, pp. 5094–5097, 2017.

- [45] P. J. Verveer and P. I. Bastiaens, *FRET analysis of signaling events in cells*, vol. 2. Elsevier Inc., second edition ed., 2010.
- [46] M. Karg, S. Wellert, S. Prevost, R. Schweins, C. Dewhurst, L. M. Liz-Marzán, and T. Hellweg, “Well defined hybrid PNIPAM core-shell microgels: Size variation of the silica nanoparticle core,” *Colloid and Polymer Science*, vol. 289, no. 5-6, pp. 699–709, 2011.
- [47] S. Reculosa, C. Mingotaud, E. Bourgeat-Lami, E. Duguet, and S. Ravaine, “Synthesis of daisy-shaped and multipod-like silica/polystyrene nanocomposites,” *Nano Letters*, vol. 4, no. 9, pp. 1677–1682, 2004.
- [48] H. Giesche, “Synthesis of monodispersed silica powders I. Particle properties and reaction kinetics,” *Journal of the European Ceramic Society*, vol. 14, pp. 189–204, jan 1994.
- [49] H. Giesche, “Synthesis of monodispersed silica powders II. Controlled growth reaction and continuous production process,” *Journal of the European Ceramic Society*, vol. 14, pp. 205–214, jan 1994.
- [50] M. Ovesný, P. Krížek, J. Borkovec, Z. Svindrych, and G. M. Hagen, “ThunderSTORM: a comprehensive ImageJ plug-in for PALM and STORM data analysis and super-resolution imaging,” *Bioinformatics*, vol. 30, no. 16, pp. 2389–2390, 2014.
- [51] H. C. Gerritsen, M. A. H. Asselbergs, A. V. Agronskaia, and W. G. J. H. M. Van Sark, “Fluorescence lifetime imaging in scanning microscopes: acquisition speed, photon economy and lifetime resolution,” *Journal of Microscopy*, vol. 206, pp. 218–224, jun 2002.
- [52] C. V. Bindhu, S. S. Harilal, G. K. Varier, and R. C. Issac, “Measurement of the absolute fluorescence quantum yield of rhodamine B solution using a dual-beam thermal lens technique,” *Journal of Physics D: Applied Physics*, vol. 29, pp. 1074–1079, 1996.
- [53] D. Setiawan, A. Kazaryan, M. A. Martoprawiro, and M. Filatov, “A first principles study of fluorescence quenching in rhodamine B dimers: how can quenching occur in dimeric species?,” *Physical Chemistry Chemical Physics*, vol. 12, no. 37, pp. 11238–11244, 2010.
- [54] M. Enoki and R. Katoh, “Estimation of quantum yields of weak fluorescence from eosin Y dimers formed in aqueous solutions,” *Photochemical & Photobiological Sciences*, vol. 17, pp. 793–799, 2018.
- [55] A. Penzkofer and Y. Lu, “Fluorescence Quenching of Rhodamine 6G in Methanol At High Concentration,” *Chemical Physics*, vol. 103, pp. 399–405, 1986.

- [56] F. L. Arbeloa, P. R. Ojeda, and I. L. Arbeloa, "Dimerization and trimerization of rhodamine 6G in aqueous solution. Effect on the fluorescence quantum yield," *Journal of the Chemical Society, Faraday Transactions 2*, vol. 84, no. 12, p. 1903, 1988.
- [57] A. S. Kristoffersen, S. R. Erga, B. Hamre, and Ø. Frette, "Testing fluorescence lifetime standards using two-photon excitation and time-domain instrumentation: Rhodamine B, coumarin 6 and lucifer yellow," *Journal of Fluorescence*, vol. 24, no. 4, pp. 1015–1024, 2014.
- [58] L. Arbeloa and P. R. Ojeda, "Dimeric states of rhodamine B," *Chemical Physics*, vol. 87, no. 6, pp. 556–560, 1982.
- [59] M. Grabolle, R. Brehm, J. Pauli, F. M. Dees, I. Hilger, and U. Resch-Genger, "Determination of the Labeling Density of Fluorophore Biomolecule Conjugates with Absorption Spectroscopy," *Bioconjugate Chemistry*, vol. 23, no. 2, pp. 287–292, 2012.
- [60] T. Fujii, H. Nishikiori, and T. Tamura, "Absorption spectra of rhodamine B dimers in dip-coated thin films prepared by the sol-gel method," *Chemical Physics Letters*, vol. 233, no. 4, pp. 424–429, 1995.
- [61] M. Karimi Gofar, K. Moradi, and N. M. Kor, "Spectroscopic studies on aggregation phenomena of dyes," *European Journal of Experimental Biology*, vol. 4, no. 2, pp. 72–81, 2014.
- [62] M. E. Gál, G. R. Kelly, and T. Kurucsev, "Derivation and interpretation of the spectra of aggregates. Part 2. Dimer of Rhodamine B in aqueous solutions," *Journal of the Chemical Society, Faraday Transactions 2: Molecular and Chemical Physics*, vol. 69, pp. 395–402, 1973.
- [63] W. West and S. Pearce, "The dimeric state of cyanine dyes," *The Journal of Physical Chemistry*, vol. 566, no. 1956, pp. 1894–1903, 1965.
- [64] K. Narayan and S. Subramaniam, "Focused ion beams in biology," *Nature Methods*, vol. 12, no. 11, pp. 1021–1031, 2015.
- [65] W. Kukulski, M. Schorb, S. Welsch, A. Picco, M. Kaksonen, and J. A. G. Briggs, "Correlated fluorescence and 3D electron microscopy with high sensitivity and spatial precision," *Journal of Cell Biology*, vol. 192, no. 1, pp. 111–119, 2011.
- [66] P. Schellenberger, R. Kaufmann, C. A. Siebert, C. Hagen, H. Wodrich, and K. Grünewald, "High-precision correlative fluorescence and electron cryo microscopy using two independent alignment markers," *Ultramicroscopy*, vol. 143, pp. 41–51, 2014.
- [67] M. Schorb and J. A. G. Briggs, "Correlated cryo-fluorescence and cryo-electron microscopy with high spatial precision and improved sensitivity," *Ultramicroscopy*, vol. 143, pp. 24–32, 2014.

- [68] S. Masich, T. Östberg, L. Norlén, O. Shupliakov, and B. Daneholt, “A procedure to deposit fiducial markers on vitreous cryo-sections for cellular tomography,” *Journal of Structural Biology*, vol. 156, no. 3, pp. 461–468, 2006.
- [69] E. Brown and P. Verkade, “The use of markers for correlative light electron microscopy,” *Protoplasma*, vol. 244, no. 1, pp. 91–97, 2010.
- [70] B. N. G. Giepmans, T. J. Deerinck, B. L. Smarr, Y. Z. Jones, and M. H. Ellisman, “Correlated light and electron microscopic imaging of multiple endogenous proteins using Quantum dots,” *Nature Methods*, vol. 2, no. 10, pp. 743–749, 2005.
- [71] V. Oorschot, H. de Wit, W. G. Annaert, and J. Klumperman, “A Novel Flat-embedding Method to Prepare Ultrathin Cryosections from Cultured Cells in Their In Situ Orientation,” *Journal of Histochemistry & Cytochemistry*, vol. 50, no. 8, pp. 1067–1080, 2002.
- [72] B. T. Miles, A. B. Greenwood, D. Benito-Alifonso, H. Tanner, M. C. Galan, P. Verkade, and H. Gersen, “Direct Evidence of Lack of Colocalisation of Fluorescently Labelled Gold Labels Used in Correlative Light Electron Microscopy,” *Scientific Reports*, vol. 7, no. February, p. 44666, 2017.
- [73] D. M. van Elsland, E. Bos, J. B. Pawlak, H. S. Overkleeft, A. J. Koster, and S. I. van Kasteren, “Correlative light and electron microscopy reveals discrepancy between gold and fluorescence labelling,” *Journal of Microscopy*, vol. 267, no. 3, pp. 309–317, 2017.
- [74] M. A. Karreman, A. V. Agronskaia, E. G. van Donselaar, K. Vocking, F. Fereidouni, B. M. Humbel, C. T. Verrips, A. J. Verkleij, and H. C. Gerritsen, “Optimizing immuno-labeling for correlative fluorescence and electron microscopy on a single specimen,” *Journal of Structural Biology*, vol. 180, no. 2, pp. 382–386, 2012.
- [75] N. Billinton and A. W. Knight, “Seeing the Wood through the Trees: A Review of Techniques for Distinguishing Green Fluorescent Protein from Endogenous Autofluorescence,” *Analytical Biochemistry*, vol. 291, no. 2, pp. 175–197, 2001.
- [76] J. Turkevich, P. C. Stevenson, and J. Hillier, “A study of the nucleation and growth processes in the synthesis of Colloidal Gold,” *Discussions of the Faraday Society*, vol. 11, no. c, pp. 55–75, 1951.
- [77] S. D. Perrault and W. C. W. Chan, “Synthesis and surface modification of highly monodispersed, spherical gold nanoparticles of 50–200 nm.,” *Journal of the American Chemical Society*, vol. 131, pp. 17042–17043, dec 2009.
- [78] L. Liz-Marzán, M. Giersig, and P. Mulvaney, “Synthesis of nanosized gold-silica core-shell particles,” *Langmuir*, vol. 7463, no. 5, pp. 4329–4335, 1996.

- [79] C. Graf, D. L. J. Vossen, A. Imhof, and A. van Blaaderen, "A General Method To Coat Colloidal Particles with Silica," *Langmuir*, vol. 19, pp. 6693–6700, aug 2003.
- [80] W. Stöber, A. Fink, and E. Bohn, "Controlled growth of monodisperse silica spheres in the micron size range," *Journal of Colloid and Interface Science*, vol. 69, pp. 62–69, 1968.
- [81] N. A. M. Verhaegh and A. van Blaaderen, "Dispersions of Rhodamine-Labeled Silica Spheres: Synthesis, Characterization, and Fluorescence Confocal Scanning Laser Microscopy," *Langmuir*, vol. 10, no. 5, pp. 1427–1438, 1994.
- [82] J. W. Slot and H. J. Geuze, "Cryosectioning and immunolabeling," *Nature Protocols*, vol. 10, no. 2, pp. 2480–2491, 2007.
- [83] P. Paul-Gilloteaux, X. Heiligenstein, M. Belle, M.-C. Domart, B. Larijani, L. Collinson, G. Raposo, and J. Salamero, "eC-CLEM: flexible multidimensional registration software for correlative microscopies," *Nature Methods*, vol. 14, no. 2, pp. 102–103, 2017.
- [84] J. Fermie, N. Liv, C. ten Brink, E. G. van Donselaar, W. H. Müller, N. L. Schieber, Y. Schwab, H. C. Gerritsen, and J. Klumperman, "Single organelle dynamics linked to 3D structure by correlative live-cell imaging and 3D electron microscopy," *Traffic*, vol. 19, no. March, pp. 354–369, 2018.
- [85] T. J. Deerinck, E. A. Bushong, A. Thor, and M. H. Ellisman, "NCMIR methods for 3D EM: A new protocol for preparation of biological specimens for serial block-face SEM," *Microscopy (Online)*, no. January, pp. 6–8, 2010.
- [86] P. Reineck, D. Gómez, S. Ng, M. Karg, T. Bell, P. Mulvaney, and U. Bach, "Distance and wavelength dependent quenching of molecular fluorescence by Au-SiO₂ core-shell nanoparticles," *ACS Nano*, 2013.
- [87] O. G. Tovmachenko, C. Graf, D. J. van den Heuvel, A. van Blaaderen, and H. C. Gerritsen, "Fluorescence Enhancement by Metal-Core/Silica-Shell Nanoparticles," *Advanced Materials*, vol. 18, pp. 91–95, jan 2006.
- [88] E. Dulkeith, a. Morteani, T. Niedereichholz, T. Klar, J. Feldmann, S. Levi, F. van Veggel, D. Reinhoudt, M. Möller, and D. Gittins, "Fluorescence Quenching of Dye Molecules near Gold Nanoparticles: Radiative and Nonradiative Effects," *Physical Review Letters*, vol. 89, p. 203002, oct 2002.
- [89] H. Mertens, a. F. Koenderink, and a. Polman, "Plasmon-enhanced luminescence near noble-metal nanospheres: Comparison of exact theory and an improved Gersten and Nitzan model," *Physical Review B - Condensed Matter and Materials Physics*, vol. 76, no. 11, pp. 1–12, 2007.

- [90] Y. Jin, S. Kannan, M. Wu, and J. X. Zhao, “Toxicity of Luminescent Silica Nanoparticles to Living Cells,” *Chemical Research in Toxicology*, vol. 20, no. July, pp. 1126–1133, 2007.
- [91] J. Zhu, L. Liao, L. Zhu, P. Zhang, K. Guo, J. Kong, C. Ji, and B. Liu, “Size-dependent cellular uptake efficiency, mechanism, and cytotoxicity of silica nanoparticles toward HeLa cells,” *Talanta*, vol. 107, pp. 408–415, 2013.
- [92] Z. Chu, Y. Huang, Q. Tao, and Q. Li, “Cellular uptake, evolution, and excretion of silica nanoparticles in human cells,” *Nanoscale*, vol. 3, no. 8, pp. 3291–3299, 2011.
- [93] I.-L. Hsiao, A. M. Gramatke, R. Joksimovic, M. Sokolowski, M. Grazielski, and A. Haase, “Size and Cell Type Dependent Uptake of Silica Nanoparticles,” *Journal of Nanomedicine & Nanotechnology*, vol. 5, no. 6, 2014.
- [94] C. Kizilyaprak, A. Bittermann, J. Daraspe, and B. Humbel, “FIB-SEM tomography in biology,” *Methods in molecular biology*, vol. 1117, pp. 547–558, 2014.
- [95] V. Lešer, D. Drobne, Ž. Pipan, M. Milani, and F. Tatti, “Comparison of different preparation methods of biological samples for FIB milling and SEM investigation,” *Journal of Microscopy*, vol. 233, no. 2, pp. 309–319, 2009.
- [96] R. Pandithage, “EM Sample Preparation,” *Leica Microsystems*, pp. 3–16, 2013.
- [97] Y. Hua, P. Laserstein, and M. Helmstaedter, “Large-volume en-bloc staining for electron microscopy-based connectomics,” *Nature Communications*, vol. 6, pp. 1–7, 2015.
- [98] E. G. van Donselaar, B. Dorresteijn, D. Popov-Čeleketić, W. J. van De Wetering, T. C. Verrips, T. Boekhout, C. T. Schneijdenberg, A. T. Xenaki, T. P. van Der Krift, and W. H. Müller, “Extremely thin layer plastification for focused-ion beam scanning electron microscopy: an improved method to study cell surfaces and organelles of cultured cells,” *Journal of Microscopy*, vol. 270, no. 3, pp. 359–373, 2018.
- [99] D. Williams and C. Carter, *Transmission Electron Microscopy: A Textbook for Materials Science*. Springer, 2nd ed., 2009.
- [100] A. M. Seligman, H. L. Wasserkrug, and J. S. Hanker, “A New Staining Method (Oto) for Enhancing Contrast of Lipid-Containing Membranes and Droplets in Osmium Tetroxide-Fixed Tissue with Osmiophilic Thiocarbonylhydrazide (Tch),” *Journal of Cell Biology*, vol. 30, no. 2, pp. 424–432, 1966.
- [101] A. Odriozola, J. Llodrá, J. Radecke, C. Ruegsegger, S. Tschanz, S. Saxena, S. Rohr, and B. Zuber, “High contrast staining for serial block face scanning electron microscopy without uranyl acetate,” *bioRxiv*, p. 207472, 2017.

- [102] A. Khan, J. Riemarsma, and H. Booij, "The reactions of osmium tetroxide with lipids and other compounds," *Journal of Histochemistry and Cytochemistry*, vol. 9, pp. 560–563, 1961.
- [103] D. White, J. Mazurkiewicz, and B. R.J., "A Chemical Mechanism for Tissue Staining by Osmium Tetroxide-Ferrocyanide containing Mixtures," *Journal of Histochemistry and Cytochemistry*, vol. 27, pp. 1084–1091, 1979.
- [104] G. Thiery, J. Bernier, and M. Bergeron, "A Simple Technique for Staining of Cell Membranes with Imidazole and Osmium Tetroxide," *Journal of Histochemistry and Cytochemistry*, vol. 43, no. 10, pp. 1079–1084, 1995.
- [105] S. Angermüller and H. D. Fahimi, "Imidazole-buffered osmium tetroxide: an excellent stain for visualization of lipids in transmission electron microscopy," *The Histochemical Journal*, vol. 14, no. 5, pp. 823–835, 1982.
- [106] J. Walton, "Lead Aspartate, an en Bloc Contrast Stain Particularly Useful for Ultrastructural Enzymology," *Journal of Histochemistry and Cytochemistry*, vol. 27, no. 10, pp. 1337–1342, 1979.
- [107] M. A. Karreman, A. V. Agronskaia, A. J. Verkleij, F. F. Cremers, H. C. Gerritsen, and B. M. Humbel, "Discovery of a new RNA-containing nuclear structure in UVC-induced apoptotic cells by integrated laser electron microscopy," *Biology of the Cell*, vol. 101, no. 5, pp. 287–299, 2008.
- [108] M. S. Lucas, M. Günthert, P. Gasser, F. Lucas, and R. Wepf, *Bridging Microscopes: 3D Correlative Light and Scanning Electron Microscopy of Complex Biological Structures*, vol. 111. Elsevier, 2012.
- [109] D. Kim, T. J. Deerinck, Y. M. Sigal, H. P. Babcock, M. H. Ellisman, and X. Zhuang, "Correlative stochastic optical reconstruction microscopy and electron microscopy," *PLoS ONE*, vol. 10, no. 4, pp. 1–20, 2015.
- [110] C. J. Peddie, K. Blight, E. Wilson, C. Melia, J. Marrison, R. Carzaniga, M. C. Domart, P. O'Toole, B. Larijani, and L. M. Collinson, "Correlative and integrated light and electron microscopy of in-resin GFP fluorescence, used to localise diacylglycerol in mammalian cells," *Ultramicroscopy*, vol. 143, pp. 3–14, 2014.
- [111] E. Brama, C. J. Peddie, M. L. Jones, M. C. Domart, X. Snetkov, M. Way, B. Larijani, and L. M. Collinson, "Standard fluorescent proteins as dual-modality probes for correlative experiments in an integrated light and electron microscope," *Journal of Chemical Biology*, vol. 8, no. 4, pp. 179–188, 2015.
- [112] H. Terada and K. Hirota, "Endocytosis of Particle Formulations by Macrophages and Its Application to Clinical Treatment," *Molecular Regulation of Endocytosis*, 2012.

- [113] A. C. Allison, "An Examination of the Cytotoxic Effects of Silica on Macrophages," *Journal of Experimental Medicine*, vol. 124, pp. 141–154, aug 1966.
- [114] E. Witasp, N. Kupferschmidt, L. Bengtsson, K. Hultenby, C. Smedman, S. Paulie, A. E. Garcia-Bennett, and B. Fadeel, "Efficient internalization of mesoporous silica particles of different sizes by primary human macrophages without impairment of macrophage clearance of apoptotic or antibody-opsonized target cells," *Toxicology and Applied Pharmacology*, vol. 239, pp. 306–319, sep 2009.
- [115] L. Sanchez, Y. Yi, and Y. Yu, "Effect of partial PEGylation on particle uptake by macrophages," *Nanoscale*, vol. 9, no. 1, pp. 288–297, 2017.
- [116] R. Rahbari, T. Sheahan, V. Modes, P. Collier, C. Macfarlane, and R. M. Badge, "A novel L1 retrotransposon marker for HeLa cell line identification," *BioTechniques*, vol. 46, pp. 277–284, apr 2009.
- [117] J. Blechinger, A. T. Bauer, A. a. Torrano, C. Gorzelanny, C. Bräuchle, and S. W. Schneider, "Uptake kinetics and nanotoxicity of silica nanoparticles are cell type dependent.," *Small*, vol. 9, pp. 3970–80, 3906, dec 2013.
- [118] B. Michen, C. Geers, D. Vanhecke, C. Endes, B. Rothen-Rutishauser, S. Balog, and A. Petri-Fink, "Avoiding drying-artifacts in transmission electron microscopy: Characterizing the size and colloidal state of nanoparticles.," *Scientific reports*, vol. 5, p. 9793, 2015.
- [119] N. Otsu, "A threshold selection method from gray-level histograms," *IEEE Transactions on Systems, Man, and Cybernetics*, vol. 9, pp. 62–66, Jan 1979.
- [120] S. Loginov, A. Agronskaia, G. Blab, and H. Gerritsen, "Integrated 3D Light and Electron Microscopes: 3D CLEM via CLSM inside FIB/SEM," -To be published-.
- [121] J. Pawley, *Handbook of Biological Confocal Microscopy*. Springer, 2010.
- [122] G. Vicidomini, P. Bianchini, and A. Diaspro, "STED super-resolved microscopy," *Nature Methods*, vol. 15, no. 3, pp. 173–182, 2018.
- [123] M. Booth, D. Andrade, D. Burke, B. Patton, and M. Zurauskas, "Aberrations and adaptive optics in super-resolution microscopy," *Microscopy*, vol. 64, no. 4, pp. 251–261, 2015.
- [124] S. Deng, L. Liu, Y. Cheng, R. Li, and Z. Xu, "Effects of primary aberrations on the fluorescence depletion patterns of STED microscopy," *Optics Express*, vol. 18, no. 2, p. 1657, 2010.
- [125] P. J. Shaw and D. J. Rawlins, "The point spread function of a confocal microscope: its measurement and use in deconvolution of 3D data," *Journal of Microscopy*, vol. 163, no. 2, pp. 151–165, 1991.

- [126] M. Bierbaum, B. D. Leahy, A. A. Alemi, I. Cohen, and J. P. Sethna, “Light microscopy at maximal precision,” *Physical Review X*, vol. 7, no. 4, pp. 1–10, 2017.
- [127] Y. Chen, M. Chen, L. Zhu, J. Y. Wu, S. Du, and Y. Li, “Measure and model a 3-D space-variant PSF for fluorescence microscopy image deblurring,” *Optics Express*, vol. 26, no. 11, p. 14375, 2018.
- [128] F. R. Boddeke, L. J. Van Vliet, and I. T. Young, “Calibration of the automated z-axis of a microscope using focus functions,” *Journal of Microscopy*, vol. 186, no. 3, pp. 270–274, 1997.
- [129] H. Bornfleth, K. Sätzler, R. Eils, and C. Cremer, “High-precision distance measurements and volume-conserving segmentation of objects near and below the resolution limit in three-dimensional confocal fluorescence microscopy,” *Journal of Microscopy*, vol. 189, no. 2, pp. 118–136, 1998.
- [130] K. E. Jensen, D. A. Weitz, and F. Spaepen, “Note: A three-dimensional calibration device for the confocal microscope,” *Review of Scientific Instruments*, vol. 84, no. 1, pp. 2011–2014, 2013.
- [131] P. F. G. Rodríguez, Y. Wu, H. Singh, H. Zhao, L. Toro, and E. Stefani, “Building a fast scanning stimulated emission depletion microscope : a step by step guide,” *Current Microscopy Contributions to Advances in Science and Technology*, pp. 791–800, 2012.
- [132] J. J. Schmied, M. Raab, C. Forthmann, E. Pibiri, B. Wünsch, T. Dammeyer, and P. Tinnefeld, “DNA origami-based standards for quantitative fluorescence microscopy,” *Nature Protocols*, vol. 9, no. 6, pp. 1367–1391, 2014.
- [133] F. Göttfert, T. Pleiner, J. Heine, V. Westphal, D. Görlich, S. J. Sahl, and S. W. Hell, “Strong signal increase in STED fluorescence microscopy by imaging regions of subdiffraction extent,” *Proceedings of the National Academy of Sciences*, vol. 114, no. 9, pp. 2125–2130, 2017.
- [134] J. Hanne, H. J. Falk, F. Görlitz, P. Hoyer, J. Engelhardt, S. J. Sahl, and S. W. Hell, “STED nanoscopy with fluorescent quantum dots,” *Nature Communications*, vol. 6, no. May, p. 7127, 2015.
- [135] X. Yang, K. Zhanghao, H. Wang, Y. Liu, F. Wang, X. Zhang, K. Shi, J. Gao, D. Jin, and P. Xi, “Versatile Application of Fluorescent Quantum Dot Labels in Super-resolution Fluorescence Microscopy,” *ACS Photonics*, vol. 3, no. 9, pp. 1611–1618, 2016.
- [136] N. T. Urban, K. I. Willig, S. W. Hell, and U. V. Nägerl, “STED nanoscopy of actin dynamics in synapses deep inside living brain slices,” *Biophysical Journal*, vol. 101, no. 5, pp. 1277–1284, 2011.

- [137] A. V. Blaaderen and A. Vrij, "Synthesis and characterization of colloidal dispersions of fluorescent, monodisperse silica spheres," *Langmuir*, vol. 81, no. 2, pp. 2921–2931, 1992.
- [138] K. Osseo-Asare and F. Arriagada, "Preparation of SiO₂ nanoparticles in a non-ionic reverse micellar system," *Colloids and surfaces*, vol. 50, pp. 321–339, 1990.
- [139] a. van Blaaderen and a.P.M. Kentgens, "Particle morphology and chemical microstructure of colloidal silica spheres made from alkoxysilanes," *Journal of Non-Crystalline Solids*, vol. 149, pp. 161–178, nov 1992.
- [140] F. Arriagada and K. Osseo-Asare, "Synthesis of Nanosize Silica in a Nonionic Water-in-Oil Microemulsion: Effects of the Water/Surfactant Molar Ratio and Ammonia Concentration.," *Journal of colloid and interface science*, vol. 211, no. 2, pp. 210–220, 1999.
- [141] P. Jiang, J. F. Bertone, K. S. Hwang, and V. L. Colvin, "Single-Crystal Colloidal Multilayers of Controlled Thickness," *Chemistry of Materials*, vol. 11, no. 8, pp. 2132–2140, 1999.
- [142] S. Wong, V. Kitaev, and G. A. Ozin, "Colloidal Crystal Films: Advances in Universality and Perfection," *Journal of the American Chemical Society*, vol. 125, no. 50, pp. 15589–15598, 2003.
- [143] J. M. Meijer, F. Hagemans, L. Rossi, D. V. Byelov, S. I. R. Castillo, A. Snigirev, I. Snigireva, A. P. Philipse, and A. V. Petukhov, "Self-assembly of colloidal cubes via vertical deposition," *Langmuir*, vol. 28, no. 20, pp. 7631–7638, 2012.
- [144] J. Zhang, H. Liu, Z. Wang, and N. Ming, "Assembly of high-quality colloidal crystals under negative pressure," *Journal of Applied Physics*, vol. 103, no. 1, pp. 8–12, 2008.
- [145] M. D. Uchic, L. Holzer, B. J. Inkson, E. L. Principe, and P. Munroe, "Three-Dimensional Microstructural Characterization Using Focused Ion Beam Tomography," *MRS Bulletin*, vol. 32, pp. 408–416, may 2007.
- [146] J. E. S. van der Hoeven, E. B. van der Wee, D. A. M. de Winter, M. Hermes, Y. Liu, J. Fokkema, M. Bransen, M. A. van Huis, H. C. Gerritsen, P. E. de Jongh, and A. van Blaaderen, "Bridging the gap: 3D real-space characterization of colloidal assemblies via FIB-SEM tomography," *Nanoscale*, 2019.
- [147] R. Budwig, "Refractive index matching methods for liquid flow investigations," *Experiments in Fluids*, vol. 17, no. 5, pp. 350–355, 1994.
- [148] F. A. Jenkins and H. E. White, *Fundamentals op Optics*. McGraw Hill Education, 1976.

- [149] S. Wiederseiner, N. Andreini, G. Epely-Chauvin, and C. Ancey, “Refractive-index and density matching in concentrated particle suspensions: A review,” *Experiments in Fluids*, vol. 50, no. 5, pp. 1183–1206, 2011.
- [150] F. García-Santamaría, H. Míguez, M. Ibisate, F. Meseguer, and C. López, “Refractive index properties of calcined silica submicrometer spheres,” *Langmuir*, vol. 18, no. 5, pp. 1942–1944, 2002.
- [151] R. G. Lebel and D. A. Goring, “Density, Viscosity, Refractive Index, and Hygroscopicity of Mixtures of Water and Dimethyl Sulfoxide,” *Journal of Chemical and Engineering Data*, vol. 7, no. 1, pp. 100–101, 1962.
- [152] V. Alonso, J. A. González, I. García De La Fuente, and J. C. Cobos, “Dielectric and refractive index measurements for the systems 1-pentanol + octane, or + dibutyl ether or for dibutyl ether + octane at different temperatures,” *Thermochimica Acta*, vol. 543, pp. 246–253, 2012.
- [153] J. Schindelin, I. Arganda-Carreras, E. Frise, V. Kaynig, M. Longair, T. Pietzsch, S. Preibisch, C. Rueden, S. Saalfeld, B. Schmid, J. Y. Tinevez, D. J. White, V. Hartenstein, K. Eliceiri, P. Tomancak, and A. Cardona, “Fiji: An open-source platform for biological-image analysis,” *Nature Methods*, vol. 9, no. 7, pp. 676–682, 2012.
- [154] W. Lechner and C. Dellago, “Accurate determination of crystal structures based on averaged local bond order parameters,” *Journal of Chemical Physics*, vol. 129, no. 11, 2008.
- [155] J. Thijssen, *Characterization of photonic colloidal crystals in real and reciprocal space*. PhD thesis, University of Utrecht, 2007.
- [156] E. Mackovic, M., Niekieł, F., Wondraczek, L. & Spiecker, “Direct observation of electron-beam-induced densification and hardening of silica nanoballs by in situ transmission electron microscopy and finite element method simulations,” *Acta Materialia*, vol. 79, pp. 363–373, 2014.
- [157] Hell, S. and Reiner, G. and Cremer, C. and Stelzer, E.H.K., “Aberrations in confocal fluorescence microscopy induced by mismatches in refractive index,” *Journal of Microscopy*, vol. 169, pp. 391–405, 2013.
- [158] D. Wildanger, R. Medda, L. Kastrup, and S. W. Hell, “A compact STED microscope providing 3D nanoscale resolution,” *Journal of Microscopy*, vol. 236, no. May, pp. 35–43, 2009.
- [159] S. W. Bae, W. Tan, and J.-I. Hong, “Fluorescent dye-doped silica nanoparticles: new tools for bioapplications,” *Chemical communications (Cambridge, England)*, vol. 48, pp. 2270–82, feb 2012.

- [160] R. P. Bagwe, C. Yang, L. R. Hilliard, and W. Tan, "Optimization of dye-doped silica nanoparticles prepared using a reverse microemulsion method.," *Langmuir*, vol. 20, pp. 8336–42, sep 2004.
- [161] W. Wang, P. D. Nallathamby, C. M. Foster, J. L. Morrell-Falvey, N. P. Mortensen, M. J. Doktycz, B. Gu, and S. T. Retterer, "Volume labeling with Alexa Fluor dyes and surface functionalization of highly sensitive fluorescent silica (SiO₂) nanoparticles.," *Nanoscale*, vol. 5, pp. 10369–75, 2013.
- [162] X. Zhao, R. Bagwe, and W. Tan, "Development of Organic-Dye-Doped Silica Nanoparticles in a Reverse Microemulsion," *Advanced Materials*, vol. 16, pp. 173–176, jan 2004.
- [163] R. Boonsin, G. Chadeyron, J.-P. Roblin, D. Boyer, and R. Mahiou, "Silica encapsulated fluorescein as a hybrid dye for blue-LED based lighting devices," *Journal of Materials Chemistry C*, vol. 4, no. 27, pp. 6562–6569, 2016.
- [164] N. T. Urban, M. R. Foreman, S. W. Hell, and Y. Sivan, "Nanoparticle-Assisted STED Nanoscopy with Gold Nanospheres," *ACS Photonics*, vol. 5, no. 7, pp. 2574–2583, 2018.
- [165] C. de Mello Donegá, "Synthesis and properties of colloidal heteronanocrystals.," *Chemical Society reviews*, vol. 40, pp. 1512–46, mar 2011.
- [166] R. Koole and M. van Schooneveld, "On the incorporation mechanism of hydrophobic quantum dots in silica spheres by a reverse microemulsion method," *Chemistry of Materials*, vol. 20, no. 7, pp. 2503–2512, 2008.
- [167] M. Darbandi, R. Thomann, and T. Nann, "Single quantum dots in silica spheres by microemulsion synthesis," *Chemistry of materials*, vol. 3, no. 5, pp. 5720–5725, 2005.
- [168] B. G. Jeong, Y. S. Park, J. H. Chang, I. Cho, J. K. Kim, H. Kim, K. Char, J. Cho, V. I. Klimov, P. Park, D. C. Lee, and W. K. Bae, "Colloidal Spherical Quantum Wells with Near-Unity Photoluminescence Quantum Yield and Suppressed Blinking," *ACS Nano*, vol. 10, no. 10, pp. 9297–9305, 2016.
- [169] N. Wang, S. Koh, B. G. Jeong, D. Lee, W. D. Kim, K. Park, M. K. Nam, K. Lee, Y. Kim, B. H. Lee, K. Lee, W. K. Bae, and D. C. Lee, "Highly luminescent silica-coated CdS/CdSe/CdS nanoparticles with strong chemical robustness and excellent thermal stability," *Nanotechnology*, vol. 28, no. 18, p. 185603, 2017.
- [170] D. Jin, P. Xi, B. Wang, L. Zhang, J. Enderlein, and A. M. van Oijen, "Nanoparticles for super-resolution microscopy and single-molecule tracking," *Nature Methods*, vol. 15, no. 6, pp. 415–423, 2018.
- [171] Y. K. Tzeng, O. Faklaris, B. M. Chang, Y. Kuo, J. H. Hsu, and H. C. Chang, "Superresolution imaging of albumin-conjugated fluorescent nanodiamonds in cells

- by stimulated emission depletion,” *Angewandte Chemie - International Edition*, vol. 50, no. 10, pp. 2262–2265, 2011.
- [172] Y. Liu, Y. Lu, X. Yang, X. Zheng, S. Wen, F. Wang, X. Vidal, J. Zhao, D. Liu, Z. Zhou, C. Ma, J. Zhou, J. A. Piper, P. Xi, and D. Jin, “Amplified stimulated emission in upconversion nanoparticles for super-resolution nanoscopy,” *Nature*, vol. 543, no. 7644, pp. 229–233, 2017.
- [173] G. Leménager, E. De Luca, Y. P. Sun, and P. P. Pompa, “Super-resolution fluorescence imaging of biocompatible carbon dots,” *Nanoscale*, vol. 6, no. 15, pp. 8617–8623, 2014.
- [174] A. Bumb, S. K. Sarkar, N. Billington, M. W. Brechbiel, and K. C. Neuman, “Silica encapsulation of fluorescent nanodiamonds for colloidal stability and facile surface functionalization,” *Journal of the American Chemical Society*, vol. 135, no. 21, pp. 7815–7818, 2013.
- [175] H. S. Qian, H. C. Guo, P. C. L. Ho, R. Mahendran, and Y. Zhang, “Mesoporous-silica-coated up-conversion fluorescent nanoparticles for photodynamic therapy,” *Small*, vol. 5, no. 20, pp. 2285–2290, 2009.
- [176] Y. Lin, C. Wang, L. Li, H. Wang, K. Liu, K. Wang, and B. Li, “Tunable Fluorescent Silica-Coated Carbon Dots: A Synergistic Effect for Enhancing the Fluorescence Sensing of Extracellular Cu^{2+} in Rat Brain,” *ACS Applied Materials and Interfaces*, vol. 7, no. 49, pp. 27262–27270, 2015.
- [177] A. F. Demirörs, A. Jannasch, P. D. Van Oostrum, E. Schäffer, A. Imhof, and A. Van Blaaderen, “Seeded growth of titania colloids with refractive index tunability and fluorophore-free luminescence,” *Langmuir*, vol. 27, no. 5, pp. 1626–1634, 2011.
- [178] A. Jannasch, A. F. Demirörs, P. D. J. van Oostrum, A. van Blaaderen, and E. Schäffer, “Nanonewton optical force trap employing anti-reflection coated, high-refractive-index titania microspheres,” *Nature Photonics*, vol. 6, no. 7, pp. 469–473, 2012.
- [179] A. F. Demirörs, A. van Blaaderen, and A. Imhof, “Synthesis of Eccentric Titania#Silica Core#Shell and Composite Particles,” *Chemistry of Materials*, vol. 21, pp. 979–984, mar 2009.
- [180] J. P. Hoogenboom, C. Rétif, E. de Bres, M. van de Boer, A. K. van Langen-Suurling, J. Romijn, and A. van Blaaderen, “Template-Induced Growth of Close-Packed and Non-Close-Packed Colloidal Crystals during Solvent Evaporation,” *Nano Letters*, vol. 4, no. 2, pp. 205–208, 2004.

Summary

The field of Correlative Light and Electron Microscopy (CLEM), has expanded rapidly in the last decade. Especially in biology it turns out to be very useful to combine these two techniques. Light microscopy, or more specifically Fluorescence Microscopy (FM), is used to visualize, localize, and track specific fluorescent molecules in cells over large areas with high sensitivity, while Electron Microscopy (EM) provides high resolution ultrastructural information of cells and materials. At present, most CLEM experiments are performed in a non-integrated fashion; FM and EM data is collected sequentially using two dedicated setups. The biggest advantage of this approach is that the great variety of well-developed labelling agents, protocols and commercially available setups for FM and EM is accessible without having to compromise on one of them.

To gain additional information from CLEM experiments, it is very important to properly overlay or register (stacks of) images obtained in the two modalities. This process is complicated by the vastly different fields of view of FM and EM, as well as the different contrast mechanisms of these techniques. FM requires bright and stable fluorophores, while EM relies on differences in electron density for contrast, and frequently requires heavy metal staining to visualize biological structures. Since fluorescent probes (i.e. molecules, proteins) are typically not electron dense, fluorescent labels can generally not be used for correlation. Particles, or fiducial markers, that are visible in both modalities can be used to overcome this problem. In this work, nanocomposite core-shell particles based on a gold core and a fluorescently labelled silica shell are deployed as fiducial markers. Within this particle, the gold core provides contrast for EM while fluorophores covalently incorporated in the silica shell provide fluorescence for FM.

For FM, it is important that the fiducial markers are bright as their signal should be well above any background signal present. In addition, the particles should remain fluorescent over a longer period of time, so the bleaching behaviour is of importance as well. As both properties are strongly influenced by the fluorophore labelling density this topic is addressed in **Chapter 2**. In this chapter, theory, measurements and simulations are included to get a better understanding of the effects of fluorophore labelling density on brightness and bleaching of fluorescently labelled particles. For the theoretical model, it seems reasonable to assume that the brightness of a fluorescently labelled particle scales with the number of fluorophores within the particles. This assumption would hold if fluorophores can be viewed as independent molecules but in reality the situation is much more complex as interactions between fluorophores come into play when the distances between fluorophores become short enough. Generally speaking, interactions can result in energy transfer between fluorophores at intermedi-

ate distances ($\sim 1\text{-}10$ nm) or fluorescence quenching at even shorter distances (< 1 nm). As a result, increasing the number of fluorophores does not result in the expected (linear) increase of the fluorescence intensity.

To study how labelling density and the brightness and bleaching behaviour relate to each other, silica particles labelled with different fluorophore densities (rhodamine B) were synthesized. A combination of absorption, spectral, radiative decay and single particle measurements was used to fully characterize the particles. From there on, simulations were performed to proof that a combination of energy transfer and quenching can be used to explain the observed trends in the experimental data. For future research it is recommended to expand the simulations included in this chapter. Ideally, this results in the development of a generic model that can be used to predict labelling density effects of a great variety of fluorophores.

Chapter 3 is the first chapter that solely focuses on the development of the fiducial markers. In this chapter, the synthesis of 15 nm gold nanoparticles coated with a rhodamine B labelled silica shell is optimized to obtain homogeneous, spherical and (photo)stable particles. From there on, the particles are tested in 2D and 3D CLEM experiments. In the 2D CLEM experiment, 81.9 nm diameter fiducials are added to a 70 nm thick cryosection of HT1080 cells stably expressing LAMP-1-GFP. Next, wide field FM and Transmission Electron Microscopy (TEM) images of selected regions of interest are collected. For the 3D CLEM experiment HeLa cells are labelled in three dimensions by endocytosis of 99.2 nm diameter fiducial markers. Next, 3D FM (confocal) and EM (Focused Ion Beam Scanning Electron Microscope (FIB-SEM)) data of selected regions of interest is collected. Both examples demonstrate that the particles are clearly visible in both modalities and, more importantly, that it is possible to use the particles for correlation. Additionally, the core-shell structure of the fiducials proves to be very useful in electron microscopy: it makes it possible to irrefutably identify the particles and makes it easy to accurately determine the center of the fiducials.

So far, all CLEM experiments in this work were performed in a non-integrated fashion. An obvious disadvantage of this approach is the need to transfer specimen from the first to the second microscope. During this transfer, specimens are easily contaminated or damaged. If a sample is successfully transferred, another challenge appears. Retrieving a region of interest in EM that was first imaged in FM is not always straightforward and can be time consuming as the orientation of the samples changes when the sample is transferred. To tackle these challenges, various alternative routes were developed by the integration of a fluorescence microscope in an electron microscope. As all commercially available integrated CLEM (iCLEM) setups are based on 2D EM techniques, Loginov and co-workers within this project focused on the development of the first 3D iCLEM setup. This was achieved by integrating a confocal microscope in a FIB-SEM. In this setup, the confocal microscope is used to obtain 3D FM data that can be used to rapidly locate regions of interest. Next, high resolution 3D EM images of these regions are obtained by repetitively removing layers by ion-beam milling and recording scanning electron microscopy images (slice and view). As this allows the user to only image predefined regions of interest in EM, this significantly speeds-up the 3D CLEM workflow.

The success of iCLEM experiments not only depends on the availability of good performing integrated setups. The compatibility of samples, labels and the procedures to prepare samples for both FM and EM is also of great importance. It is not straightforward to prepare samples that can be imaged with both modalities. Extensive protocols involving many steps are required to prepare biological samples for EM. Often there is a trade off between FM and EM compatibility of samples as the heavy metals that are required for EM staining quench most fluorescence of standard fluorophores and other FM labels. Despite this contradiction it has been demonstrated that it is possible to produce biological samples that are suitable for iCLEM measurements. This was achieved by choosing the right fluorophores and/or fluorescent proteins and labelling procedure and by minimizing heavy metal staining to yield maximum fluorescence.

In **Chapter 4** the possibility to use the fiducial markers in three dimensional iCLEM measurements is explored. For iCLEM it is important that (enough) fluorescence of the fiducial markers is preserved after samples are prepared for EM. In this experiments, HeLa cells and P388D1 mouse macrophages are labelled in 3 dimensions with the fiducial markers via endocytosis of the particles. Next, the cells were embedded in an extremely thin layer of plastic, and heavily stained with heavy metals to yield optimal imaging conditions for EM. Throughout this procedure a large drop in fluorescence intensity of the fiducial markers was observed. Despite this large drop, it remained possible to detect the particles in FM. As there is plenty of room for improvement, the particles are very promising for biological iCLEM experiments. Suggestions for improvement include the exploration of milder staining conditions or the addition of an additional silica layer to protect the fiducial markers from the added heavy metals.

This work closes with **Chapter 5** where a single sample based on core-shell nanocomposite particles is presented to check and optimize the full performance of a high-end 3D super-resolution (STED) light microscope. The sample is composed of a colloidal crystal consisting of a mixture of highly monodisperse ~ 500 nm diameter silica beads with a gold (1%) or a fluorescently labelled silica core. The crystal is refractive index matched with an embedding solvent mixture, resulting in optimal imaging and effective refractive index similar to life science specimens optimized for glycerol objectives. It is demonstrated that the periodicity of the crystal in the lateral and axial directions can be used to calibrate the microscope. The gold cores can be used to image and align the excitation and depletion lasers of the STED microscope. Finally, the fluorescent cores that are individually resolvable as they are separated by a non-fluorescent silica shell can be used for PSF measurements at different positions and depths of the sample.

Samenvatting voor een breder publiek

In de laatste jaren is de interesse in Correlatieve Licht en ElektronenMicroscopie (CLEM) sterk toegenomen. Met name in de biologie blijkt het waardevol te zijn om deze twee technieken te combineren. Licht of fluorescentiemicroscopie (FM) wordt daarbij gebruikt om fluorescente moleculen of fluorescent gelabelde structuren in cellen zichtbaar te maken, te lokaliseren of over grote afstanden te volgen. Vervolgens wordt elektronenmicroscopie (EM) gebruikt om de structurele details van cellen en omliggende materialen met hoge resolutie te bekijken. Nagenoeg alle CLEM metingen worden vandaag de dag niet geïntegreerd uitgevoerd: FM en EM data wordt apart van elkaar opgenomen op twee speciaal daarvoor bestemde microscopen. Een groot voordeel van deze aanpak is dat er op deze manier gebruik gemaakt kan worden van de grote verscheidenheid aan doorontwikkelde fluorescente labels en labelingsprotocollen voor zowel FM als EM. Bovendien kan gebruik worden gemaakt van de hoogwaardige commercieel beschikbare standaardopstellingen voor beide technieken.

Om de maximale hoeveelheid informatie uit CLEM experimenten te kunnen halen is het van groot belang dat FM en EM afbeeldingen of data met hoge precisie over elkaar heen wordt gelegd. In de praktijk blijkt dit niet eenvoudig te zijn. Een eerste oorzaak hiervan is het grote verschil in de grootte van het blikveld, ook wel de field-of-view genoemd, en resolutie van beide technieken. Dit verschil ontstaat doordat EM data bij een veel hogere vergroting wordt opgenomen dan FM data. Een tweede oorzaak is dat de zichtbaarheid van materialen erg verschillend is in beide technieken. In FM wordt fluorescentie gedetecteerd. De zichtbaarheid van materialen en structuren hangt daarom af van de helderheid en fotostabiliteit van fluoroforen of fluorescente eiwitten en ongelabelde, niet fluorescente structuren zijn niet zichtbaar. De zichtbaarheid van structuren in EM aan de andere kant wordt bepaald door verschillen in elektronendichtheid. Biologische materialen en structuren zijn daardoor pas zichtbaar na aankleuring met zware metalen. Fluorescente materialen hebben meestal geen hoge elektronendichtheid en materialen met een hoge elektronendichtheid zijn bijna nooit fluorescent. Door deze tegenstrijdigheid zijn er vaak weinig goed gedefinieerde structuren zichtbaar in FM en EM die gebruikt kunnen worden voor de correlatie van data. Deeltjes, of markers, die goed zichtbaar zijn in zowel FM als EM kunnen worden gebruikt om dit probleem op te lossen. In dit werk wordt het gebruik van nanodeeltjes met een goud kern en een fluorescent gelabelde silica schil onderzocht. De goud kern in deze deeltjes zorgt voor voldoende contrast in EM terwijl fluoroforen in de silica schil ervoor zorgen dat de deeltjes ook zichtbaar zijn in FM.

Voor FM is het belangrijk dat de markers helder zijn zodat de deeltjes goed zichtbaar zijn, ook wanneer metingen vervuild worden door de aanwezigheid van achtergrondsignaal. Het blekingsgedrag van de deeltjes is ook van belang omdat het belangrijk is dat de deeltjes lang genoeg zichtbaar zijn. Omdat beide eigenschappen worden beïnvloed door de concentratie of labelingsdichtheid van de fluoroforen in de deeltjes komt dit onderwerp in **Hoofdstuk 2** aan bod. Dit hoofdstuk bevat theorie, experimenteel werk en simulaties om meer inzicht te krijgen in het verband tussen de labelingsdichtheid en de helderheid en het blekingsgedrag van fluorescent gelabelde deeltjes. Voor het theoretische model zou een eerste optimistische aanname kunnen zijn dat de helderheid van fluorescent gelabelde deeltjes schaalst met het aantal fluoroforen dat aanwezig is in de deeltjes. De situatie blijkt echter veel complexer te zijn doordat er interacties tussen fluoroforen mogelijk zijn wanneer de afstand tussen fluoroforen afneemt. Zo kan er energieoverdracht plaatsvinden tussen fluoroforen ($\sim 1-10$ nm) en kunnen fluoroforen die zich te dicht op elkaar bevinden (< 1 nm) elkaar uitdoven.

Om te bestuderen hoe de labelingsdichtheid de helderheid en het blekingsgedrag van deeltjes beïnvloedt werden silica deeltjes gelabeld met een toenemende hoeveelheid rhodamine B gesynthetiseerd en gekarakteriseerd. Vervolgens werden simulaties uitgevoerd waarmee kon worden aangetoond dat de trends in de experimentele data kunnen worden verklaard middels een combinatie van de hiervoor beschreven energie overdracht tussen en de uitdoving van fluoroforen. Een belangrijke aanbeveling in dit hoofdstuk is de uitbreiding van de gepresenteerde simulaties. Idealiter resulteert dit in de ontwikkeling van een model dat kan worden gebruikt om het effect van labelingsdichtheid op bijvoorbeeld helderheid en blekingsgedrag voor een groot scala aan verschillende fluoroforen te voorspellen.

Hoofdstuk 3 is het eerste hoofdstuk dat zich volledig focust op de ontwikkeling van CLEM markers. In dit hoofdstuk wordt de synthese van deeltjes met een 15 nm goud kern en een rhodamine B gelabelde silica schil geoptimaliseerd om homogene, sferische en (foto)stabiele markers van een gewenste grootte te verkrijgen. De geschiktheid van deze deeltjes als markers wordt vervolgens getest in 2D en 3D CLEM experimenten. In het 2D CLEM experiment werden deeltjes toegevoegd aan 70 nm dikke cryosecties van HT1080 cellen waarna FM en transmissie elektronenmicroscopie (TEM) metingen werden uitgevoerd. In het 3D CLEM experiment werden HeLa cellen driedimensionaal gelabeld middels endocytose van de deeltjes waarna confocale FM metingen en 3D EM (FIB-SEM) metingen werden uitgevoerd. Beide voorbeelden laten zien dat de deeltjes zichtbaar zijn in FM en EM en dat de deeltjes gebruikt kunnen worden voor de correlatie van de verzamelde data. De data laat bovendien zien dat de herkenbare “core-shell” structuur van de deeltjes gebruikt kan worden om de deeltjes in EM te herkennen. De kern kan daarnaast gebruikt worden om de positie van het midden van de deeltjes vast te stellen.

Alle CLEM experimenten die tot nu toe zijn opgenomen in dit werk zijn uitgevoerd volgens de niet geïntegreerde aanpak. Een voor de hand liggend nadeel van deze aanpak is dat monsters of weefsels verplaatst moeten worden van de eerste naar de tweede microscoop. Veel CLEM monsters zijn erg kwetsbaar waardoor ze in deze

stap gemakkelijk beschadigd kunnen raken en ook de introductie van vervuilingen kan niet altijd voorkomen worden. Daarnaast blijkt het bovendien niet altijd eenvoudig om de gebieden waarvan FM data is opgenomen terug te vinden in EM. Er zijn daarom verschillende integratedCLEM of iCLEM alternatieven ontwikkeld waarbij een fluorescentie microscoop wordt geïntegreerd in een elektronenmicroscoop. Alle commercieel beschikbaar iCLEM opstelling maken gebruik van 2D EM technieken. Daarom heeft Loginov zich met enkele collega's binnen dit project gericht op de ontwikkeling van de eerste 3D iCLEM opstelling. Dit werd bereikt door de integratie van een confocale fluorescentiemicroscoop in een Focused Ion Beam Scanning Electron Microscope (FIB-SEM). In deze opstelling wordt de confocale microscoop gebruikt om in FM snel interessante gebieden te identificeren waarvan vervolgens 3D EM data kan worden opgenomen. Opname van deze data wordt gedaan door het herhaaldelijk verwijderen van plakjes materiaal met de ionenbundel van de FIB waarna de SEM wordt gebruikt voor het maken van een EM afbeelding. Omdat nu alleen interessante gebieden worden bestudeerd in EM kan in kortere tijd een grotere hoeveelheid bruikbare data worden verzameld.

In **Hoofdstuk 4** wordt getest of de hier gepresenteerde deeltjes ook gebruikt kunnen worden als markers voor de correlatie van 3D iCLEM data. Het is daarbij van belang dat (genoeg) fluorescentie van de deeltjes overblijft nadat monsters klaar zijn gemaakt voor EM. Voor dit experiment worden HeLa cellen en P388D1 muis macrofagen driedimensionaal gelabeld via endocytose van de deeltjes. De cellen worden daarna geïmpregneerd en ingebed in een zeer dunne laag plastic en zwaar aangekleurd met zware metalen om weefsels maximaal zichtbaar te maken in EM. Tijdens deze procedure wordt een sterke afname van de helderheid van de deeltjes waargenomen maar blijft genoeg fluorescentie bewaard om de deeltjes in FM te lokaliseren. Ook zijn de deeltjes goed te herkennen in de EM data. Omdat er veel ruimte is voor verdere optimalisatie zijn de deeltjes daarmee geschikt als marker voor biologische iCLEM experimenten. Voor verdere optimalisatie kunnen monsters bijvoorbeeld minder zwaar aangekleurd worden met zware metalen of kan onderzocht worden of het helpt om een extra beschermende laag om de deeltjes heen te groeien.

In het laatste hoofdstuk, **Hoofdstuk 5**, wordt onderzocht of soortgelijke deeltjes met een kern en een schil gebruikt kunnen worden om de uitlijning van een hoogwaardige 3D superresolutie (STED) lichtmicroscoop te controleren en optimaliseren. Het gepresenteerde kalibratiemonster bestaat uit een colloïdaal kristal van een mengsel van monodisperse, sferische silica deeltjes met een totale diameter van ~ 500 nm. Een deel van deze deeltjes (1%) heeft een goud kern, de rest van de deeltjes heeft een fluorescent gelabelde kern. Alle holle ruimtes van het colloïdale kristal zijn opgevuld met een oplossing met een brekingsindex gelijk aan de brekingsindex van de deeltjes. Daarmee wordt verstrooiing binnen het kristal geminimaliseerd en kan het kristal onder ideale omstandigheden bekeken worden met de lichtmicroscoop. De brekingsindex van het gehele kalibratiemonster is bovendien bijna gelijk aan de brekingsindex van veel biologische monsters en is optimaal wanneer gebruik wordt gemaakt van een glycerol objectief. In het hoofdstuk wordt gedemonstreerd dat de periodieke structuur van

het kristal gebruikt kan worden voor kalibratie van de laterale en axiale assen van de microscoop. De goud kern kan vervolgens gebruikt worden om de uitlijning van de excitatie en depletie lasers van de STED microscoop te bekijken en verbeteren. De fluorescente kern kan tot slot gebruikt worden om de point-spread-functie, of PSF, van de microscoop te bestuderen.

Dankwoord

Er zijn heel wat mensen geweest die mij hebben geholpen om deze thesis af te ronden. Hier wil ik graag iedereen bedanken die mij heeft gesteund in de afgelopen jaren.

Ik start met het bedanken van mijn promotor, **Hans Gerritsen**. Jij hebt mij de mogelijkheid geboden om dit onderzoek binnen de groep te doen. Toen na anderhalf jaar de financiering van het project weg viel heb jij alles op alles gezet om er voor te zorgen dat ik verder kon. Je hebt me in de afgelopen jaren alle ruimte gegeven om te doen wat ik leuk en interessant vond. Iets wat kon, omdat je deur altijd open stond voor het uitwisselen van ideeën, theorieën en resultaten en je daar waar het nodig was bijstuurde. Je hebt me vaak moeten vertellen dat niet alles te plannen is en dat het wel goed zou komen en dit boekje laat zien dat dat inderdaad zo is. **Gerhard Blab**, mijn co-promotor, ook jou wil ik graag bedanken. Aan de start van mijn onderzoek heb jij een groot deel van de begeleiding op je genomen. We zijn toen samen gestart met simulaties, iets wat helemaal nieuw voor mij was. Ik bewonder je passie voor het geven van onderwijs, het begeleiden van studenten en het overdragen van kennis. Ook toen ik begon met schrijven heb ik veel aan je gehad. Als ik een stuk tekst had geproduceerd en naar je opstuurde ontving ik dat altijd binnen een mum van tijd inclusief waardevolle feedback terug, bedankt daarvoor.

Van de Biofysica groep zijn er nog een aantal mensen die ik hier graag wil bedanken. Allereerst **Dave**; jij hebt me in de afgelopen jaren geholpen met zo ongeveer alles wat ik maar nodig had. Dat ging van een nieuwe computer en het creëren van een werkplek op het lab tot het organiseren van koffiemomenten, groepsuitjes en koekjes op donderdag. Mijn kennis over fluorescentie metingen en microscopie heb ik voor een groot deel aan jou te danken. Je nam (steeds weer) de tijd om mij de basis uit te leggen en was altijd bereid om mee te helpen en denken. Als ik met inhoudelijke vragen over mijn onderzoek of syntheses naar je toe kwam wees je me er regelmatig op dat je geen expert bent. Toch wist je me door te luisteren, vragen te stellen en hardop mee te denken altijd verder te helpen. **Sergey, Sajjad & Sasha**; we did a lot of work together within the Microscopy Valley project. Despite our different backgrounds and many technical challenges we achieved a lot within the project. **Helena**; jij was aan het afronden toen ik startte met mijn onderzoek en ik wil je bedanken voor de gezelligheid op kantoor in de eerste maanden. **Imaad**; I was really impressed by your persistence. You were the colleague that was always present on the occasional Saturday that I decided to go to the University to finish some of my work.

Er zijn in de afgelopen jaren binnen de groep heel wat studenten geweest waarvan ik er hier een aantal wil noemen. **Marc**; you are the only student that I supervised

within my project and I was really impressed by your hard work and eagerness to learn. We peacefully shared a fume hood for months and I really enjoyed working with you on the lab. I still remember the first time you ran into my office to tell me that your beautiful red solution of gold particles somehow turned blue. Luckily, you managed to solve this problem together with all the other problems related to the stability of the particles and mastered the synthesis of beautiful particles and colloidal crystals within a couple of months. Chapter 5 is a continuation of your project and I am grateful for your input and hard work. **Anton & Kyo**; bedankt voor jullie hulp met het programmeren wat ik heb gedaan. **Tom**; jij hebt met Gerhard een belangrijk deel van de data-analyse voor mijn paper opgezet en was de eerste die het over de “Jantina Particles” ook wel de “JPs” had. Dit bleek een hardnekkige verwijzing die ik daarna binnen de groep nog heel wat keren tegen ben gekomen. **Querijn, Jacob, Johannes, Anne, Stefan, Sander & Marita** ook jullie wil ik graag bedanken voor jullie inbreng en gezelligheid in de groep.

Er zijn ook heel wat mensen van de Cell Biology groep in het UMC die ik hier graag wil bedanken. Allereerst **Judith Klumperman**, professor van de groep. Bedankt voor je gastvrijheid en de prettige samenwerking binnen het Microscopy Valley project. Je gaf altijd aan dat ik het moest laten weten als ik ergens hulp nodig had en alle biologische experimenten in dit proefschrift laten zien dat er vanuit de groep veel hulp gekomen is. **Nalan Liv**; thanks a lot for your support and your help with the CLEM experiments included in this thesis. You were always full of ideas and you were always showing me that there were plenty of possibilities to finish my thesis. Your enthusiasm, honesty and organizational skills make you a great researcher and it was a pleasure to work with you. **Job**; ook jou wil ik graag bedanken voor je hulp en vriendschap in de afgelopen jaren. We spraken regelmatig af om samen te lunchen en ik kon altijd bij je terecht als ik ergens vast was gelopen. Mijn eerste CLEM experimenten heb ik samen met jou gedaan en ik ben dankbaar voor de tijd die je altijd nam om me te helpen en dingen uit te leggen. Jij hebt me geholpen om de hele biologische kant van het verhaal beter te begrijpen en samen hebben we mijn deeltjes voor het eerst “gevoerd” aan verschillende soorten cellen. Ik weet nog hoe blij ik was toen jij mij na het eerste uptake experiment in de avond een filmpje stuurde waarin te zien was dat de cellen mijn deeltjes aan het “opeten” waren. Ik wil ook **Carlinda, Tineke, Suzanne, Cilia, George** en **Elly** graag bedanken voor hun bijdrage.

Een groot deel van mijn tijd heb ik doorgebracht op het Soft Condensed Matter laboratorium. Van deze groep wil ik graag **Alfons van Blaaderen** bedanken. Alfons, ik was altijd onder de indruk van de enorme hoeveelheid kennis die jij paraat hebt. Jouw kritische blik en inbreng hebben veel bijgedragen aan het verzamelen van de data gepresenteerd in hoofdstuk 5. **Arnout Imhoff**; al mijn onderwijs heb ik met veel plezier samen met jou gegeven waarvoor dank. **Wessel**; aan de start van mijn PhD heb ik mijn eerste silica deeltjes met jou gemaakt. In de jaren die volgden heb je nog heel wat silica gerelateerde vragen beantwoord en was je altijd in voor een gezellig praatje op het lab. **Fabian**; op het lab, waar je eigenlijk altijd te vinden was, was je altijd bereid om te helpen. Je bracht daar een hoop gezelligheid en ook onze

fietstochtjes richting het station kon ik altijd erg waarderen. **Ernest**; jij was de eerste die mijn deeltjes onder de lichtmicroscopie bekeek en ik was dolblij toen ze goed te zien waren. Vanaf dat moment zijn we steeds meer gaan samenwerken wat resulteerde in prachtige beelden van (ontploffende) colloïdale kristallen. Zelfs op de conferentie in Bordeaux vond je een manier om die beelden te delen met het aanwezige publiek. Ik heb met veel plezier met je samengewerkt en wil je graag bedanken dat je de tijd nam om de vele aspecten van lichtmicroscopie en Fabry-Pérot fringes aan me uit te leggen. **Matthijs**; jou heb ik beter leren kennen tijdens de uurtjes die we samen met Ernest achter de FIB-SEM hebben doorgebracht. Bedankt voor je gezelligheid en humor, ook tijdens de koffiemomentjes en al het heen-en-weer gemail over ons manuscript dat daarna volgde. **Frankje**; met onze gedeelde Friese roots hadden we vrij snel een klik. Bizar genoeg bleek ook jij Wyckel te kennen omdat ook jouw Pake daar vandaan komt. Je kwam zelfs met een oude schoolfoto waarop onze Pakes samen te bewonderen zijn. We hebben samen heel wat gemopperd, koffie gedronken in het Koningsberger en het vooral ook heel gezellig gehad. Je hebt me zo vaak bemoedigend laten weten dat ik "bijna klaar" was, maar toen ook jouw contract op zijn einde liep begreep je waarom ik daar kriebels van kreeg. Als we er eindelijk tijd voor kunnen maken moeten we nog heel wat pizza's inhalen voor de publicaties die er inmiddels zijn. Speciaal voor jou: "Tige tank foar dyn help!". Ook **Peter, Patrick, Jessi, Maarten, Albert, Chris, Wiebke, Henriëtte, Nina, Pepijn, Srivatssan, Harini & Berend** wil ik graag bedanken voor hun gezelligheid op en rond het lab.

Ook van de Condensed Matter and Interfaces groep wil hier graag een aantal mensen noemen. **Andries Meijerink**; jij hebt me samen met Gerhard begeleid toen ik net was gestart met mijn PhD. Ook mijn eerste kennismaking met het doen van onderzoek was tijdens mijn bachelor onder jouw begeleiding, bedankt daarvoor. **Robin**; een trip naar Spanje is het niet geworden maar we hebben samen wel hele mooie deeltjes gemaakt en ik vond het fijn om met je samen te werken. **Jacobine**; jou heb ik al tijdens mijn masteronderzoek leren kennen en toen hadden we het altijd al gezellig. Ook toen we samen voor een conferentie naar Brugge gingen hebben we ons tussen alle lezingen door als toeristen in de stad goed vermaakt. **Elleke**; onze reis naar Venetië is één van de hoogtepunten van de afgelopen jaren. Toen we samen het vliegtuig instapten kenden we elkaar nog niet heel goed maar daar heeft die week wel verandering in gebracht. Met het voornemen om onze werkdagen eerder te beginnen zijn we nog een tijd gestart met een kop thee in de ochtend, een afspraak waarvoor we allebei op tijd op de Universiteit moesten zijn. Ik kon altijd bij je terecht voor advies, en als ik weer eens laat thuis kwam was dat regelmatig omdat wij nog een tijd na hadden staan praten op kantoor. Van de groep wil ik ook **Annelies & Carlo** hier nog noemen en bedanken voor hun bijdrage.

Het onmisbare ondersteunende personeel wil ik hier ook graag noemen. **Hans & Chris**; bedankt voor jullie hulp bij de vele TEM metingen die ik heb gedaan. Jullie konden het altijd oplossen als ik achter de TEM zat en weer eens geen idee had waarom ik geen beeld had. **Marion, Linda, Dianne & Hester**; bedankt voor alle gezelligheid en het organiseren van allerlei praktische zaken om het promoveren heen.

Ook mijn paranimfen ben ik dankbaar. **Relinde**; jij bent vanaf de dag dat ik begon met het doen van onderzoek al betrokken geweest. Tijdens mijn bacheloronderzoek bij CMI hebben we kort een kantoor gedeeld en een jaar later, tijdens mijn master, was jij daar één van mijn begeleiders. In die tijd hebben we elkaar tijdens de vele uren die je voor mij achter de TEM hebt doorgebracht beter leren kennen. Ik weet nog heel goed dat we in de donkere TEM ruimte beiden een gat in de lucht sprongen toen we zagen dat het na heel wat pogingen was gelukt om een laag silica om onze goud deeltjes heen te groeien. Iets wat ik later tijdens mijn PhD nog heel vaak gedaan heb. Ik wil je graag bedanken voor onze vriendschap, je openheid en je behulpzaamheid in al die jaren. Ik kon in de afgelopen jaren niet alleen bij je terecht met al mijn vragen over quantum dots of nanodeeltjes maar kon privé ook (dag en nacht) bij je terecht met al mijn baby-, peuter- en kleutervragen. Toen ik op zoek ging naar werk richting het einde van mijn PhD ben je ook van grote waarde geweest. Dit heeft er in geresulteerd dat ik nu een kantoor deel met je man, Tom, op de Hogeschool Rotterdam. **Josine**; wij zijn heel wat jaren geleden gelijktijdig begonnen aan de Scheikunde opleiding en deelden tijdens ons bacheloronderzoek een kantoor. Nadat we in een gekke bui meededen met een belspelletje op de radio, waardoor we een paar uur later bij een concert van Gers Pardoel stonden, kon de vriendschap niet meer stuk. Tijdens ons masteronderzoek leek het ons handiger om aangrenzende kantoren te bezetten maar dat weerhield ons er niet van om, bij voorkeur onder het genot van chocolade op de Protonkamer, heel wat plannen te maken voor festivals en allerlei andere leuke dingen. Iets wat we sinds die tijd zijn blijven doen.

Ik wil graag afsluiten met het bedanken van mijn familie voor hun onvoorwaardelijke steun in de afgelopen jaren. Allereerst mijn ouders, **Sytze & Janneke**. Zolang ik me kan herinneren moedigen jullie mij al aan om het beste uit mezelf te halen en steunen jullie mij in de keuzes die ik maak. Ik ben er dankbaar voor dat jullie altijd voor mij, en ons, klaar staan en hoop zelf ook zo'n ouder te kunnen zijn. Tijdens de afronding van mijn PhD hebben jullie heel wat dagen op de kinderen gepast zodat ik kon uitrusten of (eindelijk) even ongestoord kon schrijven. Mijn broer en zusje wil ik hier ook graag noemen: **Gerlof**, bedankt voor het aanhoren van al mijn verhalen over nanodeeltjes en het kleine beetje "programmeren" wat ik heb gedaan; **Sonja**, bedankt voor de oneindige hoeveelheid positieve energie die je altijd met je mee brengt. Mijn schoonouders, **Joke & Leendert**, wil ik hier ook graag bedanken. Ook vanuit Middelharnis staan jullie altijd voor ons en onze kinderen klaar.

Als laatste wil ik graag mijn lieve man, **Ruben**, bedanken. We kregen verkering vlak voor ik begon aan mijn PhD en ondanks dat het niet altijd leuk was heb je me altijd gesteund en geholpen waar je kon. Zelf vind je dat, ondanks dat je roept dat het je wel wat grijze haren heeft gegeven, de normaalste zaak van de wereld. We hebben in de afgelopen jaren samen heel wat opgebouwd en ik ben dankbaar voor iedere dag met jou, **Teske & Ibbe** om me heen.

List of Publications

This thesis is based on the following publications

- J.Fokkema, J. Fermie, N. Liv, D.J. van den Heuvel, T.O.M. Konings, G.A. Blab, A. Meijerink, J. Klumperman & H.C. Gerritsen, “Fluorescently Labelled Silica Coated Gold Nanoparticles as Fiducial Markers for Correlative Light and Electron Microscopy”, *Scientific Reports*, vol. 8 (13625), pp. 1-10, 2018 (Chapter 3)
- E.B. van der Wee*, J. Fokkema* (*equal contributions), C.L. Kennedy, M. del Pozo-Puig, D.A.M. de Winter, P.N.A. Speets, H.C. Gerritsen & A. van Blaaderen, “3D test sample for the calibration and quality control of super-resolution and confocal microscopes”, *in preparation* (Chapter 5)

Other work:

- S. Mohammadian, J.Fokkema, A.V. Agronskaia, N. Liv, C. de Heus, E. van Donselaar, G.A. Blab, J. Klumperman & H.C. Gerritsen, “High accuracy, fiducial marker-based image registration of correlative microscopy images”, *Scientific Reports*, vol. 9 (3211), pp. 1-10, 2019 (Chapter 3)
- S. Loginov, J. Fermie, J. Fokkema, A.V. Agronskaia, G.A. Blab, J. Klumperman, H.C. Gerritsen & N. Liv, “Targeted Correlative Imaging of Organelles in Volume Electron Microscopy”, *in preparation* (Chapter 4)
- K. Buerger, K.N. Schmidt, J. Fokkema, H.C. Gerritsen, O. Maier, U. de Vries, Y. Zaytseva, R. Rachel & R. Witzgall, “Three-dimensional on-section correlative light and electron microscopy of large cellular volumes using STEM tomography”, *accepted for publication in Methods in Cell Biology*
- J.J.H.A. van Hest, A.V. Agronskaia, J.Fokkema, F. Montarella, A. Gregorio Puig, C. de Mello Donega, A. Meijerink, G.A. Blab & H.C. Gerritsen, “Towards robust and versatile single nanoparticle fiducial markers for correlative light and electron microscopy”, *Journal of Microscopy*, vol. 274 pp. 13-22, 2019
- J.E.S. van der Hoeven, E.B. van der Wee, D.A.M. de Winter, M. Hermes, Y. Liu, J. Fokkema, M. Bransen, M.A. van Huis, H.C. Gerritsen, P.E. de Jongh & A. van Blaaderen, “Bridging the gap: 3D real-space characterization of colloidal assemblies via FIB-SEM tomography”, *Nanoscale*, vol 11, pp. 5304-5316, 2019

About the Author



Jantina Fokkema was born in Leeuwarden, the Netherlands, on the 29th of January 1991. She attended secondary school (Atheneum level) at the 'Coenecoop College' in Waddinxveen from which she graduated in 2009. In the same year, she started her studies at Utrecht University and in 2012 she obtained her bachelor degree in Chemistry. She obtained her master's degree for the master programme 'Nanomaterials: Chemistry and Physics' at the same university in 2014. She carried out her thesis project in the Condensed Matter and Interfaces group of Andries Meijerink and Daniël Vanmaekelberg of the Utrecht University under the daily supervision of Relinde van Dijk - Moes and Freddy Rabouw. The project consisted of two parts, part A is entitled 'Dye functionalised silica coated gold nanoparticles to study localized surface plasmon - dye interactions', and part B is entitled 'Local-field effects on the spontaneous emission rate of CdSe Core CdS/CdZnS/ZnS multishell quantum dots in dielectric media'. During her master she also did a six months internship at AMOLF in Amsterdam in the Nanoscale Solar Cells group of dr. E. Garnett. The project she was working on was entitled 'Surface functionalisation of cuprous oxide for PV applications'.

In September 2014, Jantina started her PhD research in the Soft Condensed Matter and Biophysics group at Utrecht University under the supervision of Hans C. Gerritsen, Andries Meijerink and Gerhard Blab. Within her project, she focused on the development of nanocomposite particles for various applications in (CLEM) microscopy. The main results, of which parts are published in scientific journals and presented at national and international conferences, are presented in this thesis.

